

UNIVERSITY OF THE

WESTERN CAPE

FLUID IDENTIFICATION WITH THE USE OF PETROPHYSICS AND ROCK PHYSICS OF BREDASDORP BASIN, SOUTH AFRICA.

By: Melvin Meyer



UNIVERSITY *of the*
WESTERN CAPE

A research proposal submitted in partial fulfilment of the requirements for the master's degree in the Department of Earth Sciences, University of the Western Cape, Bellville, South Africa.

Supervisor: Dr. Mimonitu Opuwari

2022

ABSTRACT

In the past decade, the utilization of a combined approach involving rock physics and petrophysics has emerged as a crucial tool in petroleum geoscience. This method has proven effective in reducing exploration risks and improving reservoir forecasting accuracy. This research focuses on the Cretaceous sandstone reservoirs of wells E-BT1, E-AR1, and E-AR2 in South Africa's Bredasdorp Basin. The goal of this study was to compute the clay volume, porosity, permeability, cementation factor, and fluid zones. Additionally, the fluid substitution modelling was utilized to determine the effect of different pore fluids (brine, oil, and gas) on acoustic properties (compressional velocity, shear velocity, and density) using rock frame properties. Furthermore, this research aimed to generate rock units based on core permeability and porosity using Winland R35 and Flow Zone Indicator methods.

The analysis included core logging, creation of thin sections, core porosity and permeability determination with PoroPerm, water saturation determination with an EPS-A, and finally the use of Interactive Petrophysics to model the laboratory results. Core logging analysis identified five facies within the reservoir intervals of the three wells, ranging from pure shale to massive sandstones. E-BT1 had the most comprehensive dataset of the three wells and was the primary focus for determining the rock physics parameters. The results indicate that E-BT1 has the most favourable reservoir rock types.

The fluid substitution method revealed that oil was present, with the in-situ logs closely matching those for oil for all three wells. The flow zone results showed that five flow zones Reservoir rock types (RRTs) were identified as RRT1, RRT2, RRT3, RRT4, and RRT5. The RRT5 is the best reservoir quality composed of a megaporous rock unit, with large pore throats and good reservoir quality. The RRT1 is the most reduced rock quality composed of impervious and nanoporous rock. The multi-mineral analysis showed that clay, calcite, and microcrystalline quartz cement are the primary factors affecting porosity and permeability in all three wells.

This study demonstrated the utility of integrating petrophysics and rock physics to comprehend the behaviour of rock properties in response to fluid saturation changes in the Bredasdorp Basin. The integration of these two disciplines increased the quality and reliability of results.

DECLARATION PAGE

I declare that ***Fluid Identification with the use of Petrophysics and Rock Physics of Bredasdorp Basin, South Africa***, is my work, and has not been submitted before for any degree or examination in any other University, and that all the sources I have used or quoted have been indicated and acknowledged using complete references.

Melvin Meyer

August 2023

Signed:.....

ACKNOWLEDGEMENT

It gives me a great sense of pleasure to finally give thanks to everyone who has been involved in my journey to completing this research. This research could not have been completed without the support of my family, friends, and lecturers.

First and foremost, I would like to give thanks to my wonderful parents, Anne and Norman Meyer, my siblings (Vivian, Mercia, and Nadia), and my Uncle Prof. M. Meyer, for their continuous support and guidance throughout my academic journey. Without your support, I would not have made it thus far. Thank you for giving me the necessary tools needed to complete my research.

Next, I would like to give thanks to my special friend Andrewshca Jacobs for her continuous motivation and support. Whenever I was in doubt, it was you who motivated me and uplifted me to be stronger. Thank you for being part of my journey towards success.

I would also like to give a special thanks to my supervisor Prof. M. Opuwari. Thank you for the guidance and support that you have given me throughout this research. Thank you for helping me through all the bad encounters I had during my research. Thank you for your patience and understanding during the late stages of my research.

Additionally, I would like to give thanks to Yaseen, Malcolm and Keenan for their contributions towards my analysis done at the Petroleum Agency of South Africa (PASA)

Finally, I would like to give praise and thanks to my Lord and Savior Jesus Christ. I can do all things through Christ who gives me strength. With God, all things are possible.

Thank you all, I appreciate you all.

TABLE OF CONTENTS:

TITLE PAGE	-	I
ABSTRACT	-	II
DECLARATION PAGE	-	III
ACKNOWLEDGEMENT	-	IV
CONTENT PAGE	-	V-X
LIST OF FIGURES	-	X-XIV
LIST OF TABLES	-	XIV-XV

CHAPTER 1: INTRODUCTION

INTRODUCTION	-	1-2
1.1. AIM	-	2
1.2. OBJECTIVES	-	2-3
1.3. INVESTIGATION OF WELLS & HYDROCARBON EXPLORATION	-	3-8
1.4. PROJECT ALIGNMENT WITH SOUTH AFRICA'S IMPERATIVES	-	8

CHAPTER 2: GEOLOGICAL BACKGROUND

2.1. REGIONAL GEOLOGY	-	9-10
2.2. GEOLOGICAL BACKGROUND	-	10-12
2.3. STRUCTURAL DEVELOPMENT	-	13-15
2.4. TECTONIC SETTING	-	15-17
2.4.1. TECTONOSTRATIGRAPHIC HISTORY	-	17-19
2.5. THERMAL GRADIENT & PRESSURES	-	19
2.5.1. PRESSURE & COMPRESSION	-	20
2.6. SEDIMENTARY DEPOSITIONAL ENVIRONMENT	-	20-22

CHAPTER 3: LITERATURE REVIEW

3.1. INTRODUCTION-----	23
3.2. INTRODUCTION TO PETROLEUM SYSTEMS-----	23
3.2.1. SOURCE ROCKS-----	23-24
3.2.2. RESERVOIR-----	25
3.2.3. TRAPS-----	25-26
3.2.4. SEALS-----	26
3.3. WIRELINE LOGGING-----	27
3.3.1. GAMMA RAY LOG-----	28
3.3.2. RESISTIVITY LOG-----	29
3.3.3. POROSITY LOGS-----	
3.3.3.1. SONIC LOG-----	29-30
3.3.3.2. DENSITY LOG -----	30-31
3.3.3.3. NEUTRON LOG -----	31-32

CHAPTER 4: DATASET AND METHODOLOGY

4.1. DATA COLLECTION-----	33-34
4.2. WIRELINE LOGS LOADING & EDITING-----	35
4.2.1. DEPTH SHIFTING-----	36
4.2.2. CURVE SPLICING -----	36
4.3. PETROPHYSICAL CALCULATIONS-----	
4.3.1. VOLUME OF CLAY-----	36-37
4.3.2. POROSITY-----	37-38
4.3.2.1. POROSITY FROM LOGS-----	38-39
4.3.2.2. POROSITY FROM CORE DATA-----	39-41
4.3.3. PERMEABILITY-----	41
4.3.3.1. PERMEABILITY FROM LOGS-----	42

4.4. ELECTRICAL PROPERTIES-----	43
4.4.1. ELECTRICAL PROPERTIES FROM LOGS-----	
4.4.1.1. FORMATION WATER & RESISTIVITY-----	43
4.4.1.2. WATER & HYDROCARBON SATURATION-----	44
4.4.1.3. BULK VOLUME OF WATER-----	44
4.4.1.4. IRREDUCIBLE WATER SATURATION-----	44
4.4.1.5. RESISTIVITY & SATURATION LOGS-----	44-45
4.4.2. ELECTRICAL PROPERTIES FROM CORES-----	
4.4.2.1. ARCHIE EQUATION-----	45
4.4.2.2. FORMATION FACTOR-----	45
4.4.2.3. TORTUOSITY-----	46
4.4.2.4. CEMENTATION FACT-OR-----	46
4.4.2.5. RESISTIVITY FACTOR-----	46-47
4.5. HYDRAULIC FLOW UNITS-----	48
4.5.1. CALCULATION OF HFU WITH RQI-----	48-49
4.5.2. CALCULATION OF HFU OF WINLAND-----	49
4.6. ROCK PHYSICS ANALYSIS-----	50
4.6.1. GREENBERG CASTAGNA METHOD-----	50-51
4.6.2. DENSITY ESTIMATION-----	51-52
4.6.3. GASSMANN FLUID SUBSTITUTION-----	52-53
4.7. MULTI-MINERAL AND PETROGRAPHIC STUDIES-----	54
4.7.1. SEDIMENTOLOGICAL DESCRIPTIONS-----	54
4.7.2. THIN SECTION PROCEDURE-----	55
4.7.3. X-RAY FLUORESCENCE PROCEDURE-----	56-57
CHAPTER 5: WELL LOG INTERPRETATION	
5.1. PETROPHYSICAL ANALYSIS-----	58

5.1.1. LITHOLOGICAL IDENTIFICATION-----	58-59
5.1.1.1. LITHOLOGICAL IDENTIFICATION OF WELL E-BT1-----	59-60
5.1.1.2. LITHOLOGICAL IDENTIFICATION OF WELL E-AR1-----	60-61
5.1.1.3. LITHOLOGICAL IDENTIFICATION OF WELL E-AR2-----	61-62
5.1.2. VOLUME OF CLAY-----	62-63
5.1.2.1. VOLUME OF CLAY OF ALL WELLS-----	63-64
5.1.3. FLUID IDENTIFICATION-----	65
5.1.3.1. FLUID IDENTIFICATION OF WELL E-BT1-----	65-66
5.1.3.2. FLUID IDENTIFICATION OF WELL E-AR1-----	66-67
5.1.3.3. FLUID IDENTIFICATION OF WELL E-AR2-----	67-68
5.1.4. FLUID IDENTIFICATION WITH REPEAT FORMATION TEST-----	68-69
5.1.4.1. RFT FLUID IDENTIFICATION OF ALL WELLS-----	69-71
5.1.5. POROSITY AND PERMEABILITY-----	72
5.1.5.1. POROSITY & PERMEABILITY OF WELL E-BT1-----	72-73
5.1.5.2. POROSITY & PERMEABILITY OF WELL E-AR1-----	73-74
5.1.5.3. POROSITY & PERMEABILITY OF WELL E-AR2-----	74-75
5.1.5.4. DISTRIBUTION OF POROSITY & PERMEABILITY-----	75-76
5.1.5. MULTI-WELL CORRELATION-----	76
5.1.5.1. MULTI-WELL CORRELATION FOR STRATIGRAPHIC HORIZONS-----	76-77
5.1.5.2. MULTI-WELL CORRELATION FOR FLUID ZONES-----	77-78
5.2. HYDRAULIC FLOW UNITS-----	79
5.2.1. DISTRIBUTION OF FLOW ZONE INDICATORS-----	80-81
5.2.2. RESERVOIR QUALITY INDEX HYDRAULIC FLOW UNITS-----	81-82
5.2.3. LUCIA CLASSIFICATION-----	82-84
5.2.4. RESERVOIR ROCK TYPES FOR ALL WELLS-----	84-86
5.2.5. DETAILED ANALYSIS OF RESERVOIR ROCK TYPES-----	87-89
5.3. ELECTRICAL PROPERTIES-----	90

5.3.1. DETERMINATION OF ARCHIE & CEMENTATION FACTOR OF WELL E-BT1-----	90-92
5.3.2. DETERMINATION OF ARCHIE & CEMENTATION FACTOR OF WELL E-AR1-----	92-93
5.3.3. DETERMINATION OF ARCHIE & CEMENTATION FACOTR OF WELL E-AR2-----	93-95
5.3.4. INTERPRETATION OF CEMENTATION FACTOR-----	95-96
5.4. ROCK PHYSICS ANALYSIS-----	97
5.4.1. SHEAR VELOCITY PREDICTION-----	97-99
5.4.2. FLUID SUBSTITUTION-----	99
5.4.2.1. FLUID SUBSTITUTION OF WELL E-BT1-----	100-101
5.4.2.2. FLUID SUBSTITUTION OF WELL E-AR1-----	102-104
5.4.2.3. FLUID SUBSTITUTION OF WELL E-AR2-----	104-106

CHAPTER 6: MULTI-MINERAL & PETROGRAPHIC ANALYSIS

6.1. SEDIMENTOLOGICAL DESCRIPTION-----	107
6.1.1. FACIES IDENTIFIED IN WELLS-----	107-110
6.1.2. CORED SECTIONS OF INTEREST-----	110
6.1.2.1. SEDIMENTOLOGICAL DESCRIPTION OF WELL E-BT1-----	110-112
6.1.2.2. SEDIMENTOLOGICAL DESCRIPTION OF WELL E-AR1-----	113-114
6.1.2.3. SEDIMENTOLOGICAL DESCRIPTION OF WELL E-AR2-----	115-116
6.2. THIN SECTION ANALYSIS-----	117
6.2.1. MINERALS AND CEMENTS OF INTEREST-----	117-121
6.2.1. PETROGRAPHY OVERVIEW OF WELLS-----	121-125
6.2.2. IMPLICATION OF SANDSTONE PETROGRAPHY-----	125-126
6.3. X-RAY FLUORESCENCE ANALYSIS-----	127
6.3.1. XRF ANALYSIS OF WELL E-BT1-----	128-129
6.3.2. XRF ANALYSIS OF WELL E-AR1-----	129-130
6.3.3. XRF ANALYSIS OF WELL E-AR2-----	130-131
6.4. LITHOLOGICAL AND MINERALOGICAL ANALYSIS-----	132

6.4.1. LITHOLOGICAL AND MINERALOGICAL ANALYSIS OF WELL E-BT1-----	132-133
6.4.2. LITHOLOGICAL AND MINERALOGICAL ANALYSIS OF WELL E-AR1-----	133-135
6.4.3. LITHOLOGICAL AND MINERALOGICAL ANALYSIS OF WELL E-AR2-----	135-136

CHAPTER 7: CONCLUSION AND RECOMMENDATION

7.1. CONCLUSION -----	137-138
7.2. RECOMMENDATIONS-----	138-139
REFERENCES-----	140-145
APPENDICES-----	146-148

LIST OF FIGURES:

CHAPTER 1:

FIGURE 1.1. MAP OF WELL LOCATION-----	4
FIGURE 1.2. SEISMIC PROFILES OF WELL E-AR1, E-AR2, AND E-BT1-----	6

CHAPTER 2:

FIGURE 2.1. ILLUSTRATION OF OFFSHORE BASINS IN SOUTH AFRICA-----	10
FIGURE 2.2. CREATION OF HALF-GRABEN STRUCTURES FROM NORMAL FAULTS-----	11
FIGURE 2.3. CROSS-SECTION OF THE BREDASDORP BASIN REVEALING THE SEDIMENTS PRESENT WITHIN THE WELL -----	12
FIGURE 2.4. MAP OF THE STRUCTURAL SETTING OF BREDASDORP BASIN-----	13
FIGURE 2.5. CROSS-SECTION OF BREDASDORP BASIN-----	14
FIGURE 2.6. BATHYMETRY MAP OF SOUTH ATLANTIC SHOWING THE RIFTING OF AFRICA AND SOUTH AMERICA-----	16
FIGURE 2.7. SCHEMATIC DIAGRAM OF THE THREE RIFT PHASES DURING THE BREAK-UP SYSTEM---	17
FIGURE 2.8. SEQUENCE CHRONOSTRATIGRAPHIC REPRESENTATION OF BREDASDORP BASIN-----	19
FIGURE 2.9. REPRESENTATION OF DEPOSITIONAL ENVIRONMENTS IN THE OUTENIQUA BASIN-----	21

FIGURE 2.10. EVOLUTION OF DEEP-MARINE CHANNEL DEPOSITS-----	22
---	----

Schematic diagram of the three rift phases during the break-up system.

CHAPTER 3:

FIGURE 3.1. DIAGRAM SHOWING THE MIGRATION OF HYDROCARBONS INTO THE RESERVOIR ROCKS-----	24
FIGURE 3.2. INDICATION OF THE DIFFERENT STRUCTURAL AND STRATIGRAPHIC TRAPS WITHIN EARTH-----	26
FIGURE 3.3. REPRESENTATION OF WIRELINE LOGGING OPERATIONS INDICATING THE LOGGING TRUCK, LOGGING CABLE AND LOGGING TOOLS-----	27
FIGURE 3.4. VISUAL DRAWING OF GAMMA RAY TOOL-----	28
FIGURE 3.5. REPRESENTATION OF SONIC LOGGING TOOLS-----	30
FIGURE 3.6. COMPENSATED DENSITY LOGGING TOOL-----	31
FIGURE 3.7. COMPENSATED NEUTRON TOOL-----	32

CHAPTER 4:

FIGURE 4.1. REPRESENTATION OF THE STEPS FOLLOWED FOR RESEARCH-----	34
FIGURE 4.2. CONFIGURATION OF POROPERM-----	41
FIGURE 4.3. CONFIGURATION OF EPS A-----	48
FIGURE 4.4. PETROGRAPHIC MICROSCOPE WITH DIGITAL CAMERA-----	55
FIGURE 4.5. CONFIGURATION OF THE PORTABLE XRF ANALYZER-----	57

CHAPTER 5:

FIGURE 5.1. LITHOLOGICAL LOG PLOT OF WELL E-BT1-----	60
FIGURE 5.2. LITHOLOGICAL LOG PLOT OF WELL E-AR1-----	61
FIGURE 5.3. LITHOLOGICAL LOG PLOT OF WELL E-AR2-----	62
FIGURE 5.4. LOG PLOT SHOWING THE VOLUME OF CLAY FOR ALL WELLS -----	63

FIGURE 5.5.	MULTI-WELL HISTOGRAM SHOWING THE VOLUME OF CLAY -----	64
FIGURE 5.6.	LOG PLOT SHOWING THE FLUID IDENTIFICATION OF WELL E-BT1-----	66
FIGURE 5.7.	LOG PLOT SHOWING THE FLUID IDENTIFICATION OF WELL E-AR1-----	67
FIGURE 5.8.	LOG PLOT SHOWING THE FLUID IDENTIFICATION OF WELL E-AR2-----	68
FIGURE 5.9.	FORMATION PRESSURE VS DEPTH OF WELL E-BT1-----	70
FIGURE 5.10.	FORMATION PRESSURE VS DEPTH OF WELL E-AR1-----	71
FIGURE 5.11.	FORMATION PRESSURE VS DEPTH OF WELL E-AR2-----	71
FIGURE 5.12.	POROSITY AND PERMEABILITY OF WELL E-BT1-----	73
FIGURE 5.13.	POROSITY AND PERMEABILITY OF WELL E-AR1 -----	74
FIGURE 5.14.	POROSITY AND PERMEABILITY OF WELL E-AR2 -----	75
FIGURE 5.15.	MULTI-WELL CROSS PLOT AND HISTOGRAMS SHOWING THE RELATIONSHIP BETWEEN POROSITY AND PERMEABILITY -----	76
FIGURE 5.16.	MULTI-WELL CORRELATION FOR DIFFERENT GEOLOGICAL HORIZONS IN THE THREE STUDIED WELLS -----	77
FIGURE 5.17.	MULTI-WELL CORRELATION FOR DIFFERENT FLUID FLOW ZONES IN THE THREE STUDIED WELLS -----	78
FIGURE 5.18.	HISTOGRAM OF FZI HYDRAULIC FLOW ZONE OF WELL E-BT1-----	80
FIGURE 5.19.	HISTOGRAM OF FZI HYDRAULIC FLOW ZONE OF WELL E-AR1-----	80
FIGURE 5.20.	HISTOGRAM OF FZI HYDRAULIC FLOW ZONE OF WELL E-AR2-----	81
FIGURE 5.21.	PLOT OF RQI VS PHIZ OF WELL E-BT1-----	81
FIGURE 5.22.	PLOT OF RQI VS PHIZ OF WELL E-AR1-----	82
FIGURE 5.23.	PLOT OF RQI VS PHIZ OF WELL E-AR2-----	82
FIGURE 5.24.	SUPERIMPOSITION OF RQI VS NORMALIZED POROSITY (DENSITY) ON LUCIA PLOT FOR WELL E-BT1-----	83
FIGURE 5.25.	SUPERIMPOSITION OF RQI VS NORMALIZED POROSITY (DENSITY) ON LUCIA PLOT FOR WELL E-AR1-----	83
FIGURE 5.26.	SUPERIMPOSITION OF RQI VS NORMALIZED POROSITY (DENSITY) ON LUCIA PLOT FOR WELL E-AR2-----	84

FIGURE 5.27. HYDRAULIC FLOW ZONE OF WELL E-BT1-----	85
FIGURE 5.28. HYDRAULIC FLOW ZONE OF WELL E-AR1-----	85
FIGURE 5.29. HYDRAULIC FLOW ZONE OF WELL E-AR2-----	86
FIGURE 5.30. DETERMINATION OF ARCHIE AND CEMENTATION EXPONENT OF WELL E-BT1-----	91
FIGURE 5.31. DETERMINATION OF ARCHIE AND CEMENTATION EXPONENT OF WELL E-AR1-----	92
FIGURE 5.32. DETERMINATION OF ARCHIE AND CEMENTATION EXPONENT OF WELL E-AR2-----	94
FIGURE 5.33. REPRESENTATION OF CONSOLIDATED VS UNCONSOLIDATED ROCKS-----	95
FIGURE 5.34. CROSS-PLOT SHOWING THE RELATIONSHIP BETWEEN COMPRESSIONAL AND SHEAR VELOCITY OF WELL E-BT1-----	98
FIGURE 5.35. CROSS-PLOT SHOWING THE RELATIONSHIP BETWEEN COMPRESSIONAL AND SHEAR VELOCITY OF WELL E-AR1-----	98
FIGURE 5.36. CROSS-PLOT SHOWING THE RELATIONSHIP BETWEEN COMPRESSIONAL AND SHEAR VELOCITY OF WELL E-AR2-----	99
FIGURE 5.37. ELASTIC IMPEDANCE LOG INDICATING GASSMANN FLUID SUBSTITUTION OF WELL E-BT1-----	100
FIGURE 5.38. ELASTIC IMPEDANCE LOG INDICATING GASSMANN FLUID SUBSTITUTION OF WELL E-AR1-----	103
FIGURE 5.39. ELASTIC IMPEDANCE LOG INDICATING GASSMANN FLUID SUBSTITUTION OF WELL E-AR2-----	105

CHAPTER 6:

FIGURE 6.1. HETEROLITHIC SANDY-SHALE OF WELL E-AR1-----	109
FIGURE 6.2. HETEROLITHIC AND MASSIVE SANDSTONE FACIES OF WELL E-BT1-----	110
FIGURE 6.3. SEDIMENTARY LOG OF WELL E-BT1-----	112
FIGURE 6.4. SEDIMENTARY LOG OF WELL E-AR1-----	114
FIGURE 6.5. SEDIMENTARY LOG OF WELL E-AR2-----	116
FIGURE 6.6. THIN SECTION PHOTOMICROGRAPH OF SANDSTONES SHOWING CONTACTS THAT EXISTS BETWEEN MINERAL GRAINS-----	119

FIGURE 6.7. THIN SECTION PHOTOMICROGRAPH OF SANDSTONES SHOWING THE CEMENT AND MATRIX THAT EXISTS BETWEEN MINERAL GRAINS-----	121
FIGURE 6.8. OVERVIEW OF THE THIN SECTIONS OF WELL E-BT1-----	122-123
FIGURE 6.9. OVERVIEW OF THE THIN SECTIONS OF WELL E-AR1-----	124
FIGURE 6.10. OVERVIEW OF THE THIN SECTIONS OF WELL E-AR2-----	125
FIGURE 6.11. ELEMENTAL COMPOSITION BETWEEN OIL AND WATER OF WELL E-BT1-----	129
FIGURE 6.12. ELEMENTAL COMPOSITION BETWEEN OIL AND WATER OF WELL E-AR1-----	130
FIGURE 6.13. ELEMENTAL COMPOSITION BETWEEN OIL AND WATER OF WELL E-AR2-----	131
FIGURE 6.14. LITHOLOGICAL AND MINERALOGICAL LOG PLOT OF E-BT1-----	133
FIGURE 6.15. LITHOLOGICAL AND MINERALOGICAL LOG PLOT OF E-AR1-----	135
FIGURE 6.16. LITHOLOGICAL AND MINERALOGICAL LOG PLOT OF E-AR2-----	136

LIST OF TABLES:

CHAPTER 1:

TABLE 1.1. LOCATION & VERTICAL DEPTHS OF WELLS-----	5
---	---

CHAPTER 4:

TABLE 4.1. TABLE SHOWING THE AVAILABILITY OF LOGS FOR EACH WELL-----	35
TABLE 4.2. THE TABLE BELOW SHOWS THE QUANTITATIVE EVALUATION OF POROSITY VALUES FOR RESERVOIR ROCKS-----	37-38
TABLE 4.3. TABLE SHOWING THE VARIABLES AND UNITS FOR PERMEABILITY-----	41
TABLE 4.4. TABLE SHOWING THE OUTPUT PERMEABILITY LOGS-----	42
TABLE 4.5. TABLE SHOWING THE OUPUT ELECTRICAL LOGS-----	45
TABLE 4.6. TABLE SHOWING THE VARIABLES AND UNITS USED FOR ELECTRICAL PROPERTIES-----	47

CHAPTER 5:

TABLE 5.1.	GR CLEAN, GR CLAY & AMOUNT OF CLAY CONTENT FOR RESERVOIR INTERVALS OF WELLS E-BT1, E-AR1, AND E-AR2-----	64
TABLE 5.2.	FORMATION PRESSURE & DENSITY GRADIENTS FOR HYDROCARBONS-----	68
TABLE 5.3.	REPEAT FORMATION TESTING RESULTS-----	69-70
TABLE 5.4.	SHOWS THE CORE POROSITIES (%) & PERMEABILITIES (mD) ACROSS THE RESERVOIR INTERVALS OF ALL WELLS-----	72
TABLE 5.5.	THE RANGE & MEAN FZI VALUES FOR EACH HYDRAULIC FLOW UNITS WITHIN THE THREE DIFFERENT WELLS-----	79-80
TABLE 5.6.	CALCULATED AVERAGE PETROPHYSICAL VALUES USED TO GROUP ROCKS INTO RESERVOIR ROCK TYPES-----	86-87
TABLE 5.7.	FORMATION FACTOR & POROSITY OF 19 DIFFERENT SAMPLES OF E-BT1-----	90-91
TABLE 5.8.	FORMATION FACTOR & POROSITY OF 6 DIFFERENT SAMPLES OF E-AR1-----	92
TABLE 5.9.	FORMATION FACTOR & POROSITY OF 12 DIFFERENT SAMPLES OF E-AR2-----	93-94
TABLE 5.10.	INDICATION OF ROCK TYPES CORRESPONDING TO THE SPECIFIC CEMENTATION FACTOR AS DETERMINED BY ARCHIE-----	95
TABLE 5.11.	INDICATING THE TORTUOSITY & CEMENTATION FACTOR OF ALL WELLS WITH THEIR CORRESPONDING ROCK TYPES-----	96
TABLE 5.12.	GASSMANN FLUID SUBSTITUTION RESULTS OF WELL E-BT1-----	101
TABLE 5.13.	GASSMANN FLUID SUBSTITUTION RESULTS OF WELL E-AR1-----	103-104
TABLE 5.14.	GASSMANN FLUID SUBSTITUTION RESULTS OF WELL E-AR2-----	105-106

CHAPTER 6:

TABLE 6.1.	TABLE INDICATING THE CORES TAKEN FROM THE RESERVOIRS OF EACH WELL-----	107
TABLE 6.2.	IDENTIFIED FACIES WITH THEIR RESERVOIR QUALITY & DESCRIPTION-----	108-109
TABLE 6.3.	REPRESENTATION OF COMMON MINERALS WITH CHEMICAL FORMULA-----	117
TABLE 6.4.	TABLE SHOWING THE MEASURED MAJOR AND TRACE ELEMENTS RECORDED OVER OIL AND WATER ZONES OF ALL THREE WELLS-----	127-128

Key Words:

Petrophysics,
Porosity,
Permeability,
Reservoir Quality,
Archie Constant,
Sedimentary rocks,
Well data,
Core analysis,
Flow units,
X-Ray Fluorescence,
Rock Physics,
Fluid Substitution

Abbreviations:

XRF = X-ray fluorescence
RFT = Repeat Formation Tests
DST = Drill Stem Tests
HFU = Hydraulic Flow Unit
RQI = Reservoir Quality Index
FZI = Flow Zone Indicator
Ma = Million Years
Phiz = Pore-grain Volume Ratio
Rho = Spearman's correlation coefficient
°C = degree Celsius
API = American Petroleum Institute
mD = Milli darcieS

1. Introduction:

The Bredasdorp Basin covered in this research forms part of the Outeniqua Basin, which is the second largest basin in South Africa and contributes 30% to the basin with a coverage area of about 124,000 km² (Parker 2014). The Outeniqua Basin is defined as a large composite intracratonic rift basin formed due to dextral shearing of the margin of South Africa during the early to mid-Cretaceous (Parker 2014). The basin is broken into four sub-basins, which are Bredasdorp, Gamtoos, Pletmos, and Algoa Basins. Each of these sub-basins has half-graben structures that have been separated by basement arches of Ordovician to Devonian meta-sediments (Ramiah, Trivedi and Opuwari 2019). These structures are also overlain by thick sequences of drift phase sediments that indicate cyclic sedimentation and accumulation (Ramiah, Trivedi and Opuwari 2019). The structure of these sub-basins can be explained using strike-faulting (especially in the basin closer to the Agulhas-Falkland Fracture Zone (AFFZ)) and by inversion tectonics that were caused by periodic movements (Broad, et al. 1996).

Along the South African continental shelf, the Bredasdorp Basin can be found between Mossel Bay and Cape Agulhas (Maseko 2016). Research has shown that the basin is the largest hydrocarbon-producing basin in South Africa (Parker 2014). According to (Ojongokpoko 2006), the Bredasdorp Basin has been the focus of seismic activity and drilling since 1980, and from 1981-1991, there have been approximately 181 exploration wells drilled in the Basin.

In the Bredasdorp Basin, many hydrocarbon reservoirs are encountered in the Cretaceous sandstones. It is believed that carbon-rich source rocks generated the hydrocarbons found in these sandstone reservoirs (Parker 2014). The Bredasdorp Basin is identified by sediments mainly composed of organic, clastic, and clays from marine and fluvial channel environments and detrital sediments from dead organisms (ILE 2013). The sandstone reservoirs consist of sandstones that have fine to coarse grains with some intercalations of clays, silts, and shales (Parker 2014). The hydrocarbons of the reservoirs are residues of wet gas condensates and earlier oil charges. They are composed of liquid oil and small amounts of high molecular weight hydrocarbons (Davies, C.P.N 1997). These hydrocarbons are eagerly explored, and they are commercially important.

In this research project, the focus is to develop a model that evaluates the fluid and rock properties within selected reservoirs from wells E-AR1, E-AR2, and E-BT1. An integration approach of petrophysics and rock physics is significant for evaluating field development of selected wells to generate subsurface models based on rock properties. The concepts of rock physics and petrophysics of the reservoirs will be put to work to understand the physical properties, behaviour and the type of the fluids of the reservoir rock.

Rock physics provides a link between geological reservoir parameters and elastic properties which are used to characterize the reservoir (Avseth and Bjørlykke 2010). Petrophysics is the study of the chemical and physical properties of rocks and pore fluids (ILE 2013). The petrophysical analysis is used to transform wireline logging data to reservoir properties, such as volume of clay, porosity, permeability, water saturation, and hydrocarbon saturation. Meanwhile, rock physics analysis will be used to determine the effect of different pore fluids on acoustic properties like compressional velocity, shear velocity, and density (Avseth and Bjørlykke 2010). The Gassmann fluid substitution method will be employed to predict changes in compressional and shear velocity based on changes in saturation. By combining compressional and shear velocity data, we can identify the types of fluids present in the selected reservoirs.

This research builds on the principles of geology, petrophysics and rock physics to determine the structural architecture, reservoir quality, fluid behaviour and type of fluids present within the wells.

1.1.Aim:

This project is designed to evaluate the rock and fluid properties of reservoir rocks of wells E-AR1, E-AR2, and E-BT1 through the use and comparison of petrophysics, rock physics, sedimentology, and petrographic analysis. The main aim is to quantify and evaluate the petrophysical and rock physical parameters to determine the best reservoir rock and fluid properties. Rock physics and petrophysics will mainly be investigated with the use of Interactive Petrophysics (IP) software. This software can be used to calculate both petrophysical and rock physics parameters.

1.2.Objectives:

- Computation of petrophysical properties from well logs.

- Characterization of different reservoir rock facies and sedimentary features within the reservoir zones.
- Core laboratory analysis of petrophysical properties.
- Core-log depth shifting and matching.
- Multi-mineral analysis with the use of thin sections and X-ray fluorescence.
- Use of rock physics (Gassmann fluid substitution method) to determine the effect of different pore fluid types on acoustic properties.
- Determination of rock physical properties.
- Overall: evaluation of rock and fluid properties from an integrated approach of petrophysics, rock physics and petrographic analysis.

1.3. The investigation of wells and the Hydrocarbon Exploration and Production in the region

1.3.1. Investigation of wells:

The locations of the studied wells, E-AR1, E-AR2 and E-BT1 are shown in figure 1.1 below. These wells are drilled in the southern section of the Bredasdorp Basin in Block E. The Bredasdorp Basin is located between Mossel Bay and Cape Agulhas along the South African continental shelf (Maseko 2016). The basin is identified as a SE trending rift basin that formed in between the Columbine-Agulhas and Infanta arches (Davies, C.P.N 1997). Through research, the basin has been identified as the biggest hydrocarbon-producing basin in South Africa (Parker 2014). To date, there have been more than 200 wells drilled in the basin (Parker 2014).

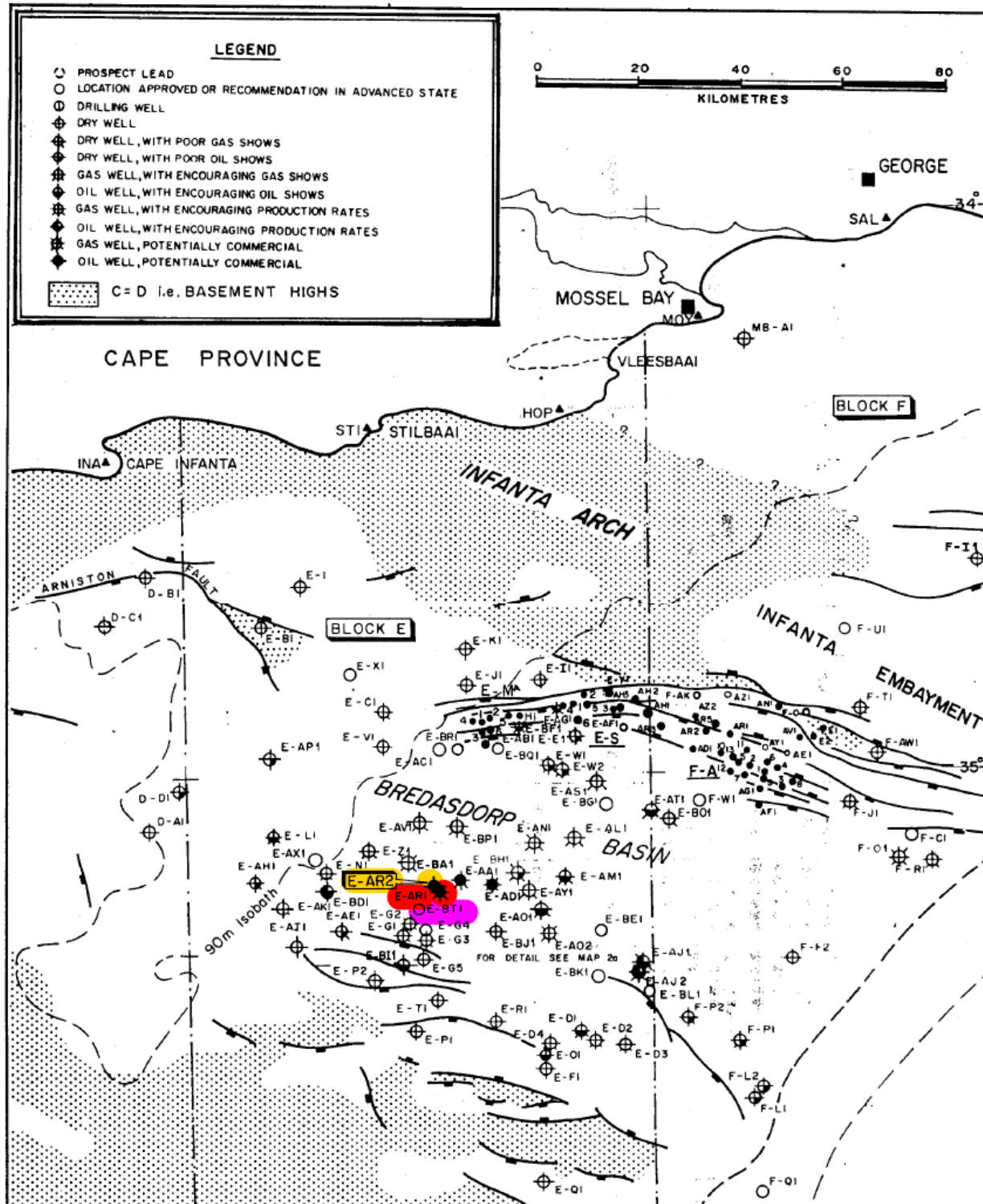


Table 1.1 below provides the coordinates and depths of wells E-AR1, E-AR2 and E-BT1 during the drilling procedure. In the table, the Kelly Bushing is identified as the distance between the Kelly Bushing on the rig and the sea floor. The water depth is identified as the distance from the sea surface to the seafloor. The total drilling depth indicates the distance between the Kelly Bushing and the bottom of the well. The cores indicate pieces of the rock formation at a specific depth below the Kelly bushing.

Table 1.1: Location and vertical depths of wells.

Well Name	Location	Kelly bushing depth (m)	Water Depth (m)	Total Drilling Depth (m)	Cores
E-AR1	Lat., 35° 12' 13.67'' S Lon., 21° 32' 41.86'' E	146	120	3455	1. 2455-2473m 2. 2849-2853m 3. 3116-3134m 4. 3212-3220m
E-AR2	Lat., 35° 11' 33.22'' S Lon., 21° 32' 17.29'' E	22	119.5	2981	1. 2442-2455.8m 2. 2445.8-2472m 3. 2803-2821m 4. 2821-2828m 5. 2828-2846.3m
E-BT1	Lat., 35° 13' 58.64'' S Lon., 21° 29' 56.48'' E	22	118	3141	1. 2384-2402m 2. 2402-2412m 3. 2412-2430m

All the wells studied in this research form part of the southern offshore Block E of the Bredasdorp Basin. Well E-AR1 has been drilled 120 km SSW of Mossel Bay following the successful tests of neighbouring wells E-AA1 and E-AD1. Well E-AR1 has therefore been drilled as a wildcat to test for hydrocarbons within the structural and stratigraphic trap between horizon F to horizon EQII intervals.

Well E-AR2 was drilled to test the extent of the hydrocarbon-bearing deep marine turbidite sands found on the 14A unconformity as well as to test for any additional hydrocarbons which may have been trapped below horizon T13AS. Well E-AR2 was drilled as a step-out well about 1.4km NNW of well E-AR1 and 125km SSW of Mossel Bay.

Well E-BT1 was drilled to test for reservoir hydrocarbons within the stratigraphic trap above horizons 14At1, 13Bt1, 13At1 and 9A sandstone sequence. The well was also drilled to see the

extent of the sandstones in Well E-AR1 above horizon 14At1. Well E-BT1 is about 95 km south of Stilbaai and 6km SW from well E-AR1.

The seismic profiles below show that all wells share the same sandstone reservoir above horizon 14At1 at different depth intervals (figure 1.2). However, it is assumed that the development of the sandstone units differs from well to well.

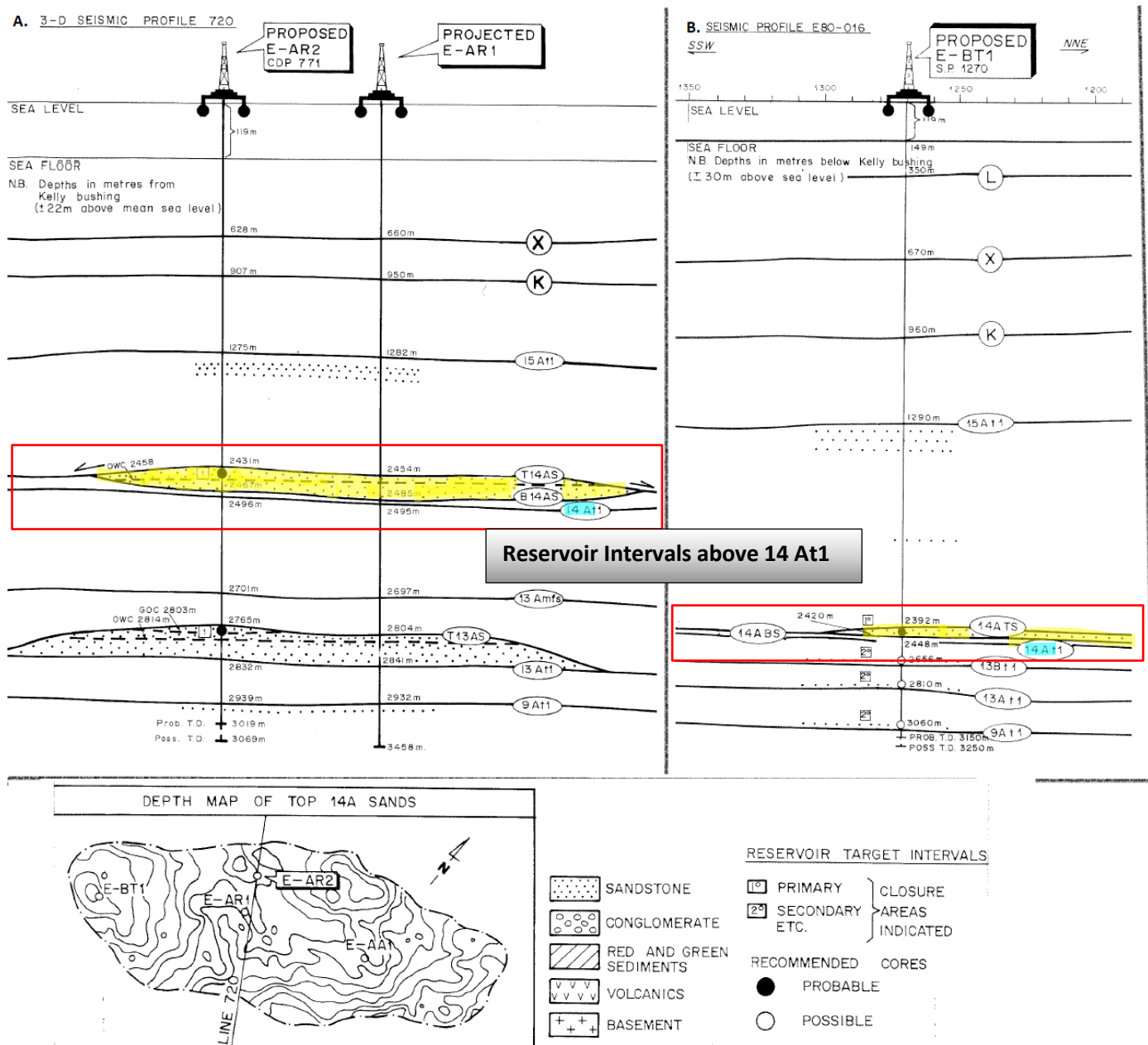


Figure 1.2: Seismic profiles of Well E-AR1, E-AR2, and E-BT1. (Revised from (Engelbrecht, Honiball, et al. 1991, Engelbrecht, Willis, et al. 1990))

1.3.2. Hydrocarbon Exploration and Production:

In the late 1960s, before the offshore exploration for hydrocarbons in South Africa, there have been no studies on the continental shelf of South Africa. Only during the past decade has the geological history become clear for exploration to improve dramatically. This has led to an increase in the understanding of the petroleum geochemistry of the basin. The studies on the nature of the offshore areas were mainly conducted by SOEKOR (Southern Oil Exploration Corporation). (Maseko 2016)

The hydrocarbon reservoirs of the Bredasdorp Basin are mainly found in the Cretaceous sandstones. It is believed that the oil and gas in the basin are produced from carbon-rich source rocks located at the edges of the basin, particularly in the western region of the Southern Outeniqua Basin (Maseko, 2016). The hydrocarbons in these reservoirs, which consist of liquid oil and small amounts of high molecular weight hydrocarbons, are remnants of wet gas condensates and previous oil charges (Davies, C.P.N, 1997).

South Africa's exploration activities are currently controlled by the Petroleum Agency of South Africa (PASA), and they are accountable for the soliciting of propositions for offshore acreage (Petroleum Agency SA 2004/2005/2010). PetroSA, which was known as SOEKOR, discovered deposits of hydrocarbons in Block 9 of the Bredasdorp Basin. In this basin, 165 wells were drilled, and 32 of them were classified as relatively small oil and gas discoveries (Parker 2014).

Many of the small oil fields were discovered in 1987 within the submarine fan complexes in porous sandstones of the Aptian and Albian ages (Wood 1995). The production within the basin started in 1992 by SOEKOR, and by 2002/2003, the company produced a daily average of 195 million cubic feet of gas per day and about 5 190 barrels of gas condensates (Broad, et al. 2006). The explored gas and condensate are transported via a 91km long pipeline to the Mossgas synfuels plant where it is converted into kerosene, petrol and diesel.

Additional deposits of hydrocarbons were discovered in the Bredasdorp Basin in blocks 9 and 11A by PetroSA. About 40% of the hydrocarbons in the sub-units surrounding the E-M and F-A oil fields within Block 9 were expected to be exploited by PetroSA (Schalkwyk 2005). This was a way to

increase the production above Oribi's current 20 000 bpd. However, the declination of the Oribi field was compensated for by the Oryx field (Parker 2014).

1.4. Project alignment with South Africa's Imperatives:

Earth & Marine:

- This research can be used to broaden the understanding of the fluid flow patterns in the exploration of hydrocarbons. An increase in the understanding of petrophysical aspects can help scientists obtain important information on marine environments.

Job Creation:

- This research can be used by environmental and petroleum companies to conduct future research. The research on fluid flow can give a better insight to determine fluid flow patterns associated with different depositional environments.
- In South Africa, the unemployment rate is at a record high of 36.0%. The country is in desperate need of job creation and this sector could be the key to South Africa's problem. When drilling commences within the Bredasdorp Basin, several jobs can be created for South Africans in various areas.

Economic Growth:

- The South African economy and GDP could see an enormous growth. The South African Government could financially benefit from income tax and royalty tax if production commences within the basin.

Energy Security:

- Oil and gas from the Bredasdorp Basin can act as a bridging fuel between coal and alternative fuels. Over the past few years, the energy crisis in South Africa has worsened. The leading company, Eskom, which supplies and manage the electricity of the country, has implemented irregular load shedding since 2013. The development of oil and gas can relieve South Africa from its energy crisis.

Chapter 2: Geological Background

2.1. REGIONAL GEOLOGY:

The coastline of South Africa is approximately 3000 km long, of which the western coast makes up 900 km stretching from the Orange River to Cape Point (Parker 2014, PASA 2017). The southern and western coastal areas appear to have a wider continental shelf and slope than the eastern coast apart from the Durban and Zululand basins (Parker 2014, PASA 2017). In South Africa, various marginal offshore basins can be separated into three tectono-stratigraphic zones (figure 2.1).

The offshore basins that form along the coasts of South Africa are the Orange Basin, Outeniqua Basin and the Durban and Zululand Basin (figure 2.1) (Parker 2014). The Orange Basin in the western region of South Africa is the largest offshore basin in South Africa with a total basinal area of 45% and a coverage area of 191 600 km² (Parker 2014, PASA 2017). The passive margin of the western basin was formed when the South Atlantic opened during the Early Cretaceous (Parker 2014). The eastern offshore basin known as the Durban and Zululand Basin is the smallest offshore basin in South Africa and has a total basinal area of 25% and a coverage area of about 107 000 km² (Parker 2014, PASA 2017). It formed due to the breakup of Africa, Madagascar and Antarctica.

The Outeniqua Basin is the second largest basin in South Africa and contributes 30% to the total basinal area with a coverage area of about 124 000 km² (Parker 2014, PASA 2017). The Outeniqua Basin is defined as a large composite intracratonic rift basin that formed due to dextral shearing of the South African margin during the early to mid-cretaceous (Parker 2014). The Basin is comprised of four sub-basins (Bredasdorp, Gamtoos, Algoa, and Pletmos Basins) with a rift half-graben structure, which is separated by basement arches of Ordovician to Devonian meta-sediments (Ramiah, Trivedi and Opuwari 2019). These half-graben structures are also overlain by thick sequences of drift phase sediments that indicate events of cyclic sedimentation and accumulation (Ramiah, Trivedi and Opuwari 2019). The structure of the Outeniqua sub-basins can be explained by the means of strike-faulting in the basin closer to the Agulhas-Falkland Fracture Zone (AFFZ) and by inversion tectonics that were caused by periodic movements (Broad, et al. 1996).

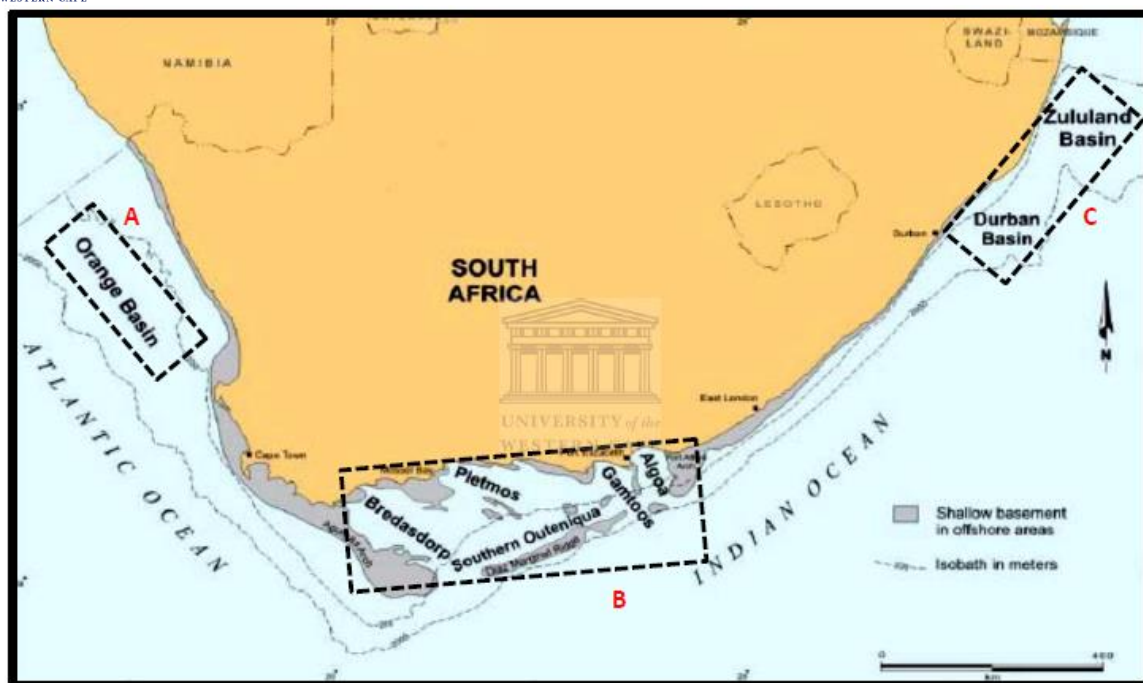


Figure 2.1: Illustration of offshore basins in South Africa (Parker 2014).

2.2. GEOLOGICAL BACKGROUND OF BREDASDORP BASIN:

The Bredasdorp Basin is one of five sub-basins that form part of the Outeniqua Basin, and it is located off the coast of South Africa on the southern continental margin (Magobiyane 2014) (figure 2.1). The continental shelf of the Outeniqua basin is approximately 50-200km wide (PASA 2017). The Bredasdorp Basin is a SE trending rift basin that formed in between the Columbine-Agulhas and Infanta arches during the breakup of Gondwana along the AFFZ (Ramiah, Trivedi and Opuwari 2019).

The faults between the Infanta and Agulhas Arches have a NW to SE trend and these faults were caused by dextral-transtensional stresses during the breakup (Ramiah, Trivedi and Opuwari 2019). The graben and half-graben basins were all caused by these normal faults (McMillan, et al. 1997) (Ramiah, Trivedi and Opuwari 2019). These half-graben structures are formed within sedimentary basins when normal faults dip in the same direction, thus causing adjacent fault blocks to slip downwards and tilt relative to the next fault (figure 2.2).

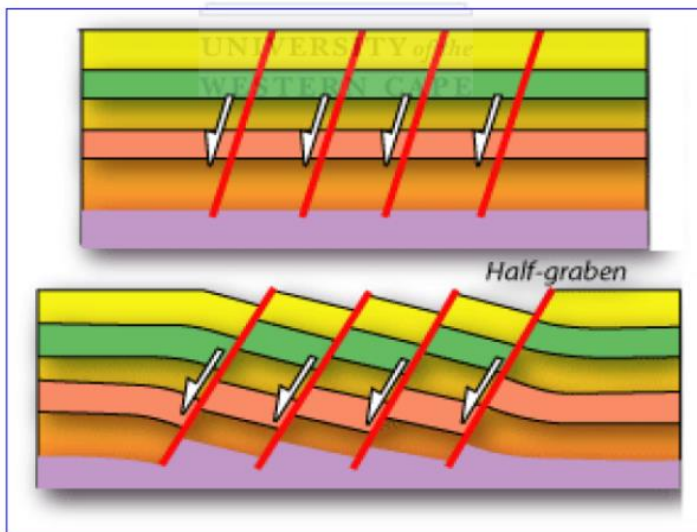


Figure 2.2: Creation of half-graben structures from normal faulting (Parker 2014)

The Bredasdorp Basin is about 200 km long and 80 km wide and covers an area of approximately 18 000 km² beneath the Indian Ocean on the Southern coast of South Africa (Parker 2014) (Ramiah, Trivedi and Opuwari 2019). The Bredasdorp Basin is believed to have formed due to extended periods during the first rifting phase in the Jurassic Age. The basin is a local depocenter that was filled with Early Cretaceous and Late Jurassic shallow marine and continental sediments (figure 2.3) (Turner, Grobber and Sontundu 2000) (Maseko 2016).

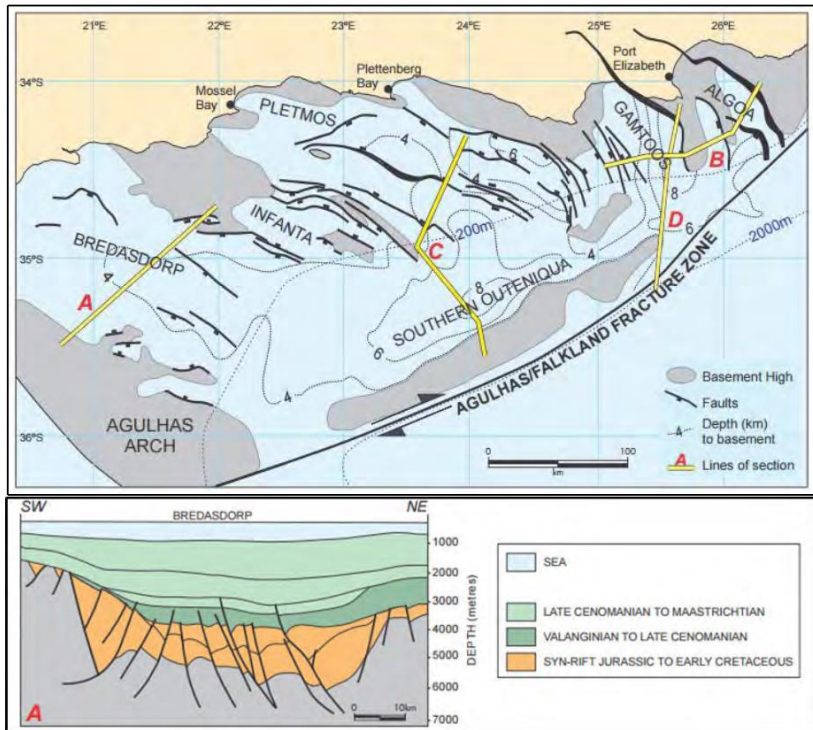
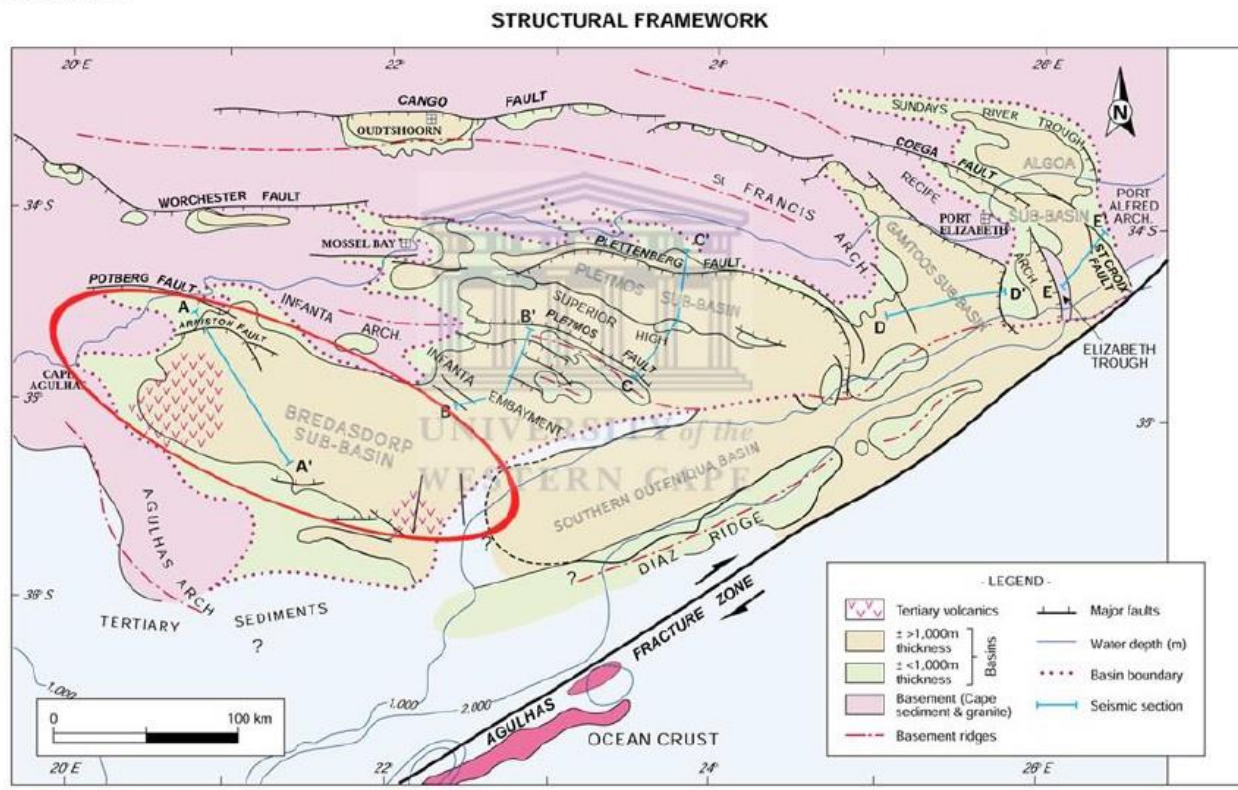


Figure 2.3: Cross section of the Bredasdorp basin revealing the sediments present within the well (PASA 2017).

The Bredasdorp Basin has a Lower Cretaceous Agulhas Falkland Fracture Zone (AFFZ) to the southeast and an E-W Permo-Triassic Cape Fold Belt to the north (figure 2.4) (Maseko 2016). The Cape Fold Belt is a thrust belt with north-verging folds (Parker 2014, Maseko 2016). On the other hand, the AFFZ is a dextral transform fault that formed when South America and Africa separated (Maseko 2016). The formation of the basin is also related to the breakup of Gondwana as previously mentioned (Ramiah, Trivedi and Opuwari 2019, Maseko 2016). The Cape Supergroup (slates and orthoquartzites) and Karoo Supergroup (sandstones and shales) also had a major impact on the sedimentation of the basin during the rift phase (Ramiah, Trivedi and Opuwari 2019, PASA 2017). The syn-rift sequence of the Bredasdorp Basin has fluvial and shallow marine sediments whereas the post-rift sequence is comprised of deep marine sediments (De Wit and Ransome 1992, Maseko 2016).



Modified after: Letellier (1992), McMillan et al., (1997)

Figure 2.4: Map of the structural setting of Bredasdorp Basin (IHS 2014).

2.3. STRUCTURAL DEVELOPMENT:

The Bredasdorp basin is identified as a widespread basement depression with an uneven cross section, located between the anticlinal basement highs of Cape Agulhas and Cape Infanta (figure 2.5) (Ojongokpoko 2006). The major structural feature of this basin is its normal faults (Ramiah, Trivedi and Opuwari 2019). The structural highs and half grabens throughout the basin are divided by these WNW-ESE trending faults (figure 2.3) (De Wit and Ransome 1992). The formation of the Outeniqua basin is attributed to extensional stress caused by the breakup of Gondwana. This further led to the formation of the half-graben sub-basins along the Agulhas Falkland Fracture Zone (Hussien 2014).

The southern section of the Bredasdorp basin was created by faulting and tilting of the northward slope side of the Agulhas arch. This can be traced to the main SE subsurface structure in the Cape Agulhas, which consists of post-Paleozoic rocks like Table Mountain quartzites and Bokkeveld

shale (Maseko 2016). The western section of the basin is dipping to the NW, and the deepest parts of the basin are closest to the northern margin. The rest of the basin floor is relatively flat (Dingle, Siesser and Newton 1983).

According to (Ojongokpoko 2006), the northern section of the basin's basement rocks descends through numerous boundary faults from the Infanta Arch. The edge linearity in the north is interrupted by small graben structures that formed embays onto the Infanta Arch. The three horst structures that are projected southwards into the basin occur above the general level of the basin floor and are confined by short, curved faults (Ojongokpoko 2006).

The western section of the basin is broken up into small, narrow, NW-SE horst grabens that extend to the coast, connecting Cape Agulhas and Cape Infanta (Dingle, Siesser and Newton 1983). However, this western section of the basin does not extend onshore (Dingle, Siesser and Newton 1983).

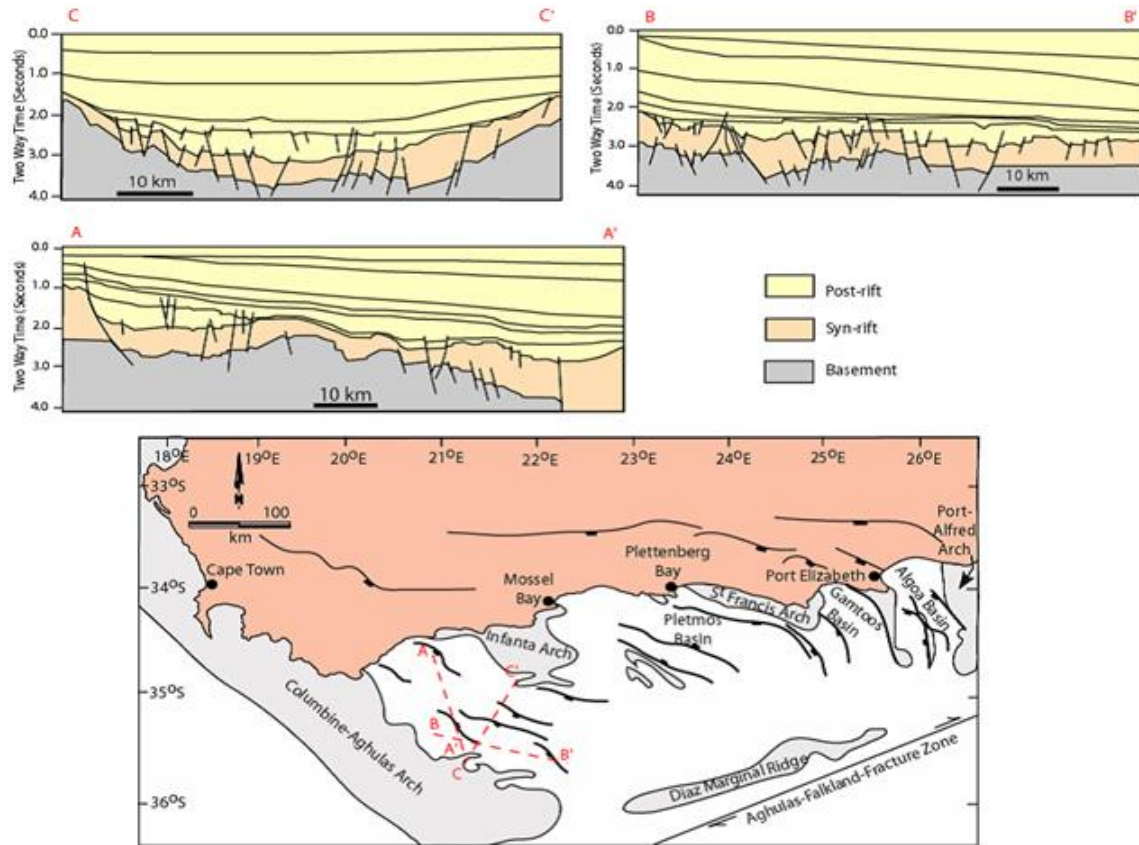


Figure 2.5: Cross-section of the Bredasdorp Basin (Thompson 1998).

The discussion below focuses on the three phases responsible for the development of the Bredasdorp Basin: “the rift phase, early drift phase, and drift phase”. These phases are described based on information from (Petroleum Agency SA; 2004/5).

1. Rift Phase (Mid Jurassic - Valaginian)

This phase is mostly controlled by extension-related subsidence and is characterized by a syn-rift basin fill. The uplift of the flanks of the basin resulted in the erosion of sediment deposited in the later stages of rifting. Isostatic uplift on the sides of the half-graben structures led to the erosion and removal of late rift sediments. The Rift Phase occurred between the Mid Jurassic to Valaginian age.

2. Early drift phase (Hauterivian- Early Barrevian)

This phase is marked by the continued uplift that caused erosion on the southern flank. The graben within the basin experienced rapid subsidence and deposition of deep-water sequence. (Petroleum Agency SA; 2004/5)

3. Drift phase (Barremian- Turonian)

This phase is characterized by the minor movements of the Arniston Fault which were caused by regional subsidence driven mainly by sediment loading and thermal cooling. The oil-prone source rocks within the half-graben reached its main stage of oil generation during the early Paleozoic. Regional subsidence ended during the early tertiary period when the southern flank of the basin experienced uplift and erosion due to alkaline-rich intrusions. (Petroleum Agency SA; 2004/5)

2.4. TECTONIC SETTING

The southern part of South Africa has classical records of dextral shear movements, that occurred when southern Africa rifted from South America along the AFFZ during the mid-late Jurassic to Early Cretaceous age (figure 2.6) (Sonibare, et al. 2014). This movement resulted in the opening of the greater South Atlantic margin which led to lithospheric stretching and the breakup of the Gondwana supercontinent into east and west during the early Mesozoic (Sonibare, et al. 2014). The dextral stresses are responsible for normal faulting in the northern AFFZ (McMillan, et al. 1997) and faulting took place during the syn-rift phase between the Agulhas and Infanta arches (McMillan, et al. 1997). The five easterly trending echelon sub-basins of the Outeniqua Basin

resulted from tectonic alignments that followed a series of lithospheric stretching and thermal relaxation (Sonibare, et al. 2014) (Davies, C.P.N 1997).

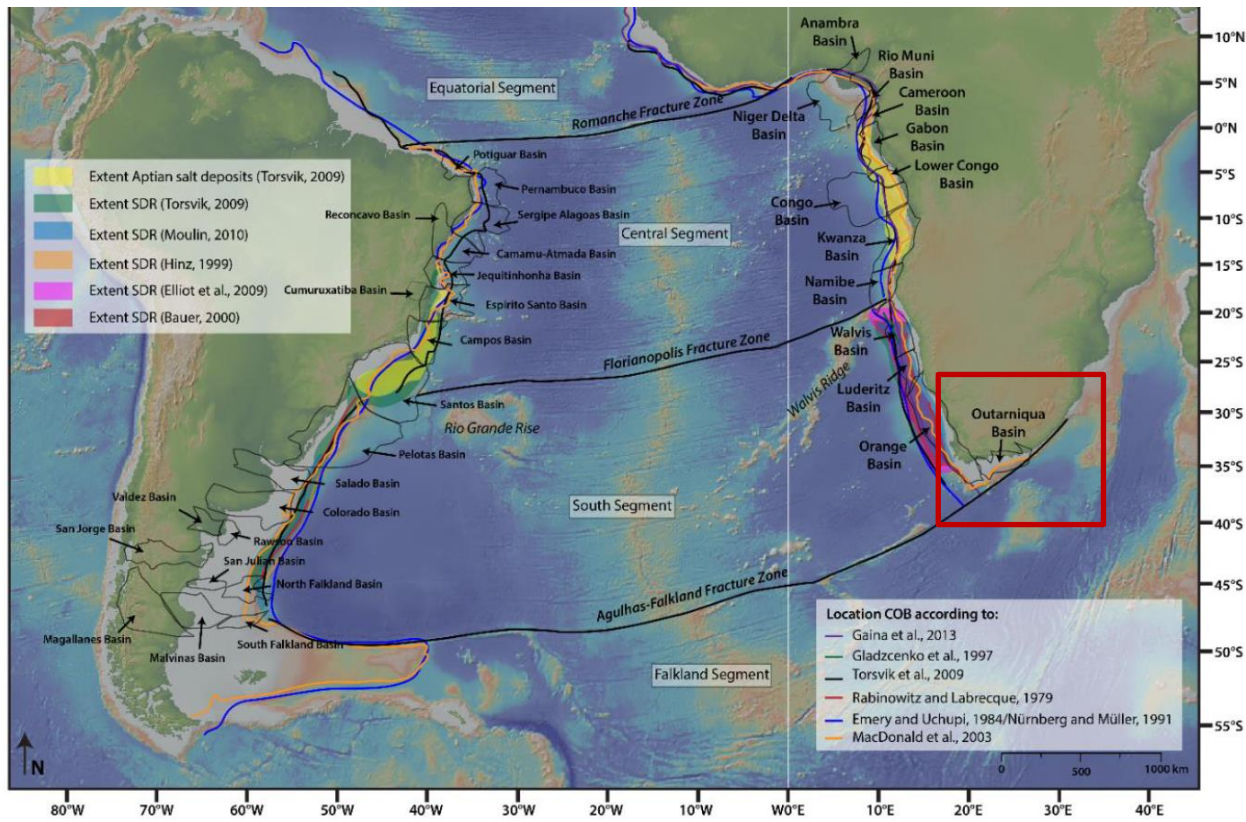


Figure 2.6: Bathymetry map of South Atlantic showing the rifting of Africa from South America and the creation of rift basins (Beniest 2017).

The Outeniqua depocentres are separated from one another through a series of oblique normal faults and basement arches (Sonibare, et al. 2014) (McMillan, et al. 1997) (Broad, et al. 1996). The sub-basin is separated from the AFFZ lineament and bounded to the south by the Diaz Marginal Ridge. The variability in the spatial distribution and strike direction of faults in the sub-basins is accompanied by the development of regional and localized unconformities. (Parker 2014)

2.4.1. Tectono-Stratigraphic History of Bredasdorp Basin:

According to the sequence chronostratigraphic below (figure 2.8), the basin-fill consists of upper Jurassic, lower and post-Cretaceous marine strata, and Cenozoic rocks that are separated into syn-rift successions covered by post-rift sediments (figure 2.7) (Magoba and Opuwari 2019). In the Bredasdorp basin, the composition of the syn-rift sequences is mostly shallow marine and fluvial-

lacustrine sediments whereas the post-rift sequences consist of deltaic and shallow to deep marine siliciclastic (Dingle, Siesser and Newton 1983) (Sonibare, et al. 2014).

In the Outeniqua Basin, several erosional and non-depositional unconformities have been identified (Brown, et al. 1995). The main regional unconformities are the 1At1 which occurred around 136 Ma (Valanginian break-up unconformity), 6At1 which occurred during the Late Hauterivian about 130 Ma, 13At1 occurring during Early Aptian about 120 Ma, 15At1 occurring during the Upper Cenomanian about 93 Ma, 17At1 which occurred during the Campanian age about 80 Ma and finally the 22At1 which occurred during the Upper Maastrichtian age about 67 Ma (figure 2.8) (Sonibare, et al. 2014).

The 1At1 unconformity is triggered by the uplifting of the arches and horst blocks which subsequently ended the active rift sedimentation about 126-117.5 Ma (McMillan, et al. 1997). The subsidence of basins through rift faulting was steady during 1At1 but declined to 5At1 (Brown, et al. 1995). The post-rift phase has 6-12 cycles and occurred between 117.5-112 Ma. The 6At1 sequence was generated by a high rate of regional subsidence.

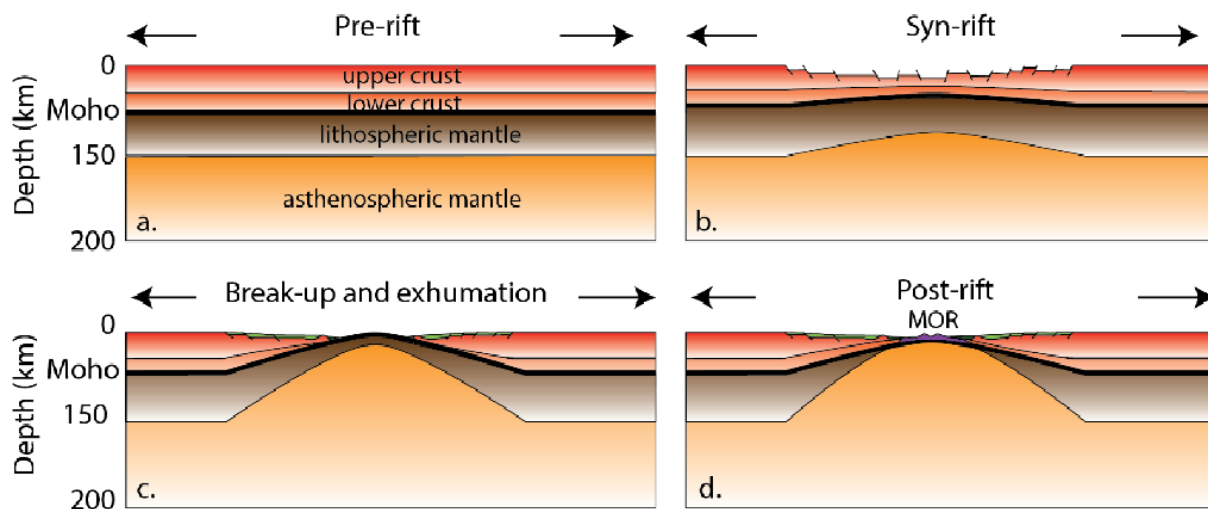


*Figure 2.7: Schematic diagram of the three rift phases during the break-up system (Beniest 2017).
 a) The pre-rift phase b) the syn-rift phase, c) the break-up and exhumation phase and d) the post-rift phase.*

During the early Aptian to mid-Albian, the drop in sea level resulted in the erosion of sediments from high-stand shelf sandstones and was deposited through turbidity currents to the basin center (Turner, Grobber and Sontundu 2000). These sediments created stacked, amalgamated channels and

fan lobes (Maseko 2016). The channels were mostly in the west and southwest areas whereas the fan lobes occurred in the eastern part of the Bredasdorp Basin (Turner, Grobber and Sontundu 2000). The area of the accumulation of oil was formed by the channel of 13At1 sequences whereas the oil-bearing reservoirs occurred in the 14At1 sequence which consists of floor-fan sandstones (McMillan, et al. 1997).

During the Late Cenomanian age, minor warping, erosion, and some uplift occurred in the 15At1 phase (McMillan, et al. 1997). Organic rich shales with some plankton occurred above the 15At1. Between the Turonian and Coniacian ages, propagation appeared. Sedimentation of shelf deposits occurred during the Tertiary era to present-time and consists of glauconitic clays, biogenic clays, and minor sands (Sonibare, et al. 2014).

Information obtained from seismic data and plate reconstruction studies has concluded that the syn-rift sequence is sub-divided into syn-rift 1 and syn-rift 2 (McMillan, et al. 1997) (Broad, et al. 2006). Syn-rift 1 is defined as a block-faulted sedimentary collection that occurred during Oxfordian and Kimmeridgian times due to rifting with extensional reactivation of the Cape Fold Belt. On the other hand, syn-rift 2 can be seen as a renewed stage of rifting following the Valanginian transformation processes along the AFFZ (Sonibare, et al. 2014).

In southern Africa, the post-break-up stage can be interpreted as the African plate moving across the Shona and Bouvet hotspots around 80-60 Ma. The period of hotspots led to episodes of regional uplifts, imbalances in thermal distribution, and the emplacement of alkaline intrusive bodies (Sonibare, et al. 2014). The structural configuration of the Bredasdorp Basin today is seen as a cumulative effect of various sedimentary and tectonic processes such as the separation of the continents, changes in elevation, mantle dynamics, volcanic activity, and the accumulation and erosion to sediment dispersal (Sonibare, et al. 2014).

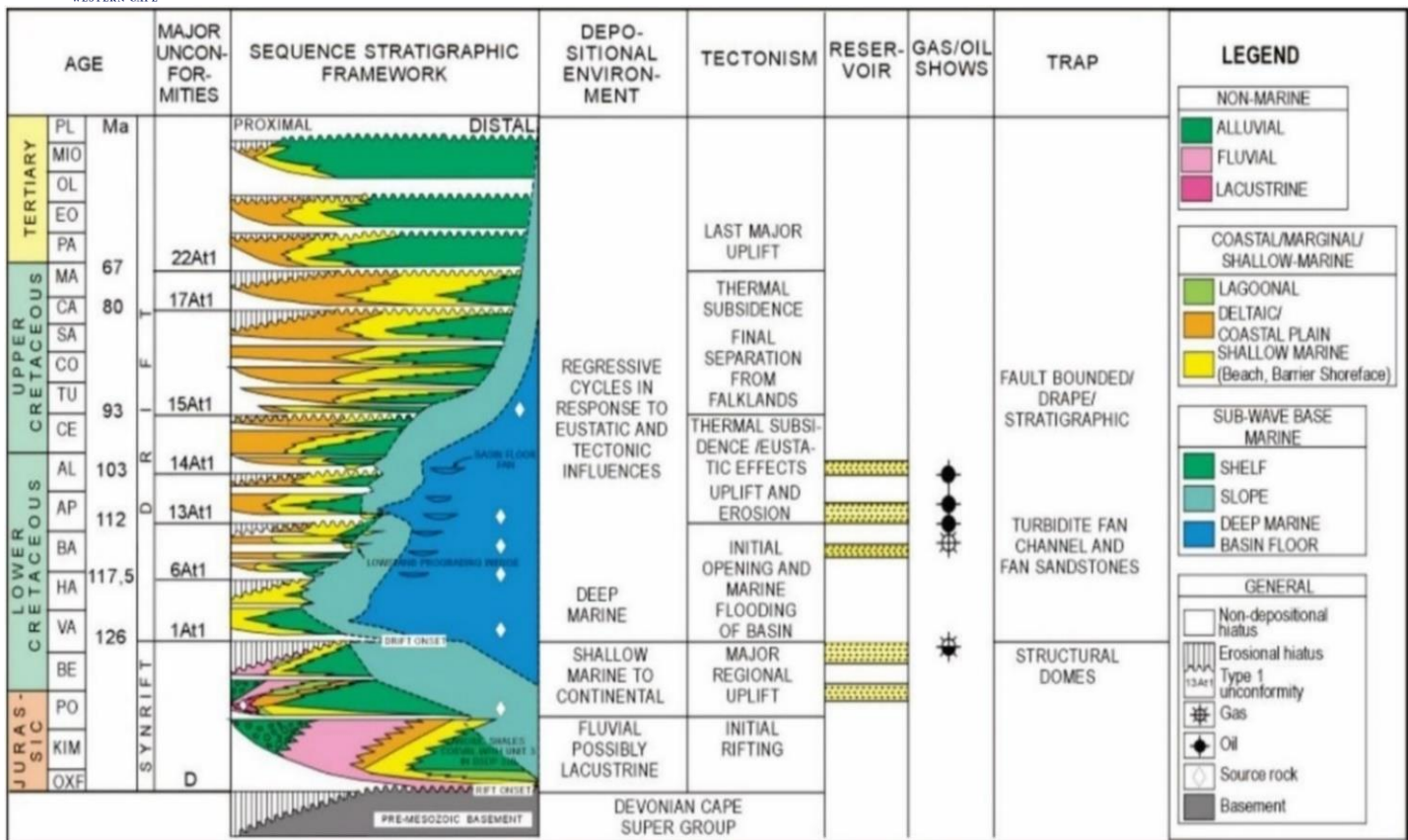


Figure 2.8: Sequence Chronostratigraphic representation of Bredasdorp Basin (Petroleum Agency SA; 2004/5).

2.5. THERMAL GRADIENT AND PRESSURES

According to (Davies, C.P.N 1997), the Bredasdorp Basin has a thermal gradient of about 35-49 °C/km. During the late Cretaceous, there was a decline in temperature that resulted from reduced flow and subsidence after rifting (Ramiah, Trivedi and Opuwari 2019). During the late Cretaceous to early tertiary, the region experienced uplift, which resulted from Africa migrating over a mantle which led to an increase in heat in the basin. The temperatures of the Bredasdorp Basin rose by more than 3°C per million years until around 80 million years ago. Sedimentation declined from approximately 80Ma to 55Ma which led to a decline in temperature to less than 0.3°C per million years (Davies, C.P.N 1997). During ~80Ma to ~55Ma, the temperature needed for oil generation in Turonian sourced rocks increased by <10°C (Davies, C.P.N 1997). The temperatures in the Bredasdorp Basin increased by 20°C due to the movement of formation waters from the Southern Outeniqua Basin (Ramiah, Trivedi and Opuwari 2019).

2.5.1. PRESSURE & COMPRESSION:

In the basin, three pressure regimes have been identified from regional pressure studies that were based on data from the Cretaceous reservoir (Ramiah, Trivedi and Opuwari 2019). The first regime is a normal pressure zone that extends to approximately 3000 m (Davies 1988). The second regime is characterized by thick Aptian source rocks that have an equivalent mud weight of 1.15 psi/ft (Ramiah, Trivedi and Opuwari 2019). The final regime is characterized by high overpressures of over 3000 psi above the hydrostatic zone. The pressures of the three regimes were obtained from petrophysical calculations as well as from DST and RFT readings (Ramiah, Trivedi and Opuwari 2019).

All offshore basins found in the area have been affected by compression that appears synonymous with the separation of the Falkland plate (Van der Merwe 1992). Due to this compression, the Karoo sedimentary rocks and Paleozoic metasediments experienced upliftment and erosion (Ramiah, Trivedi and Opuwari 2019). During the Hauterivian age, the second stage of compression occurred, and it could be related to the impact of the Falklands plate on the southern coast of Africa. The second compression led to the 6At1 angular unconformity which resulted from major uplift and erosion (Ramiah, Trivedi and Opuwari 2019). The third stage of compression resulted in the formation of the structural highs in the center of the basin. According to (Davies, C.P.N 1997), the third compression can be related to the pathway of the easterly side of the Falkland Plate past the Agulhas Arch (Ramiah, Trivedi and Opuwari 2019).

2.6. SEDIMENTARY DEPOSITIONAL ENVIRONMENT:

The deposition of sediments in the environment is explained through physical, chemical, and biological processes. It indicates the type of rocks that will form after lithification (ILE 2013). These processes are responsible for the accumulation of rich organic sediments and the prediction of hydrocarbons requires a combined understanding of the geodynamics, tectonic setting, structural development, and paleo-environmental conditions of the basin (ILE 2013).

The Outeniqua basin stretches from onshore to offshore regions and it stretches across the southern coastal line from west to east with the oldest on the eastern side and youngest on the western side.

The depositional environment of the Outeniqua basin is developed from fan deltas, and river to wave-dominated deltas, and is also related to the coastal system (figure 2.9).

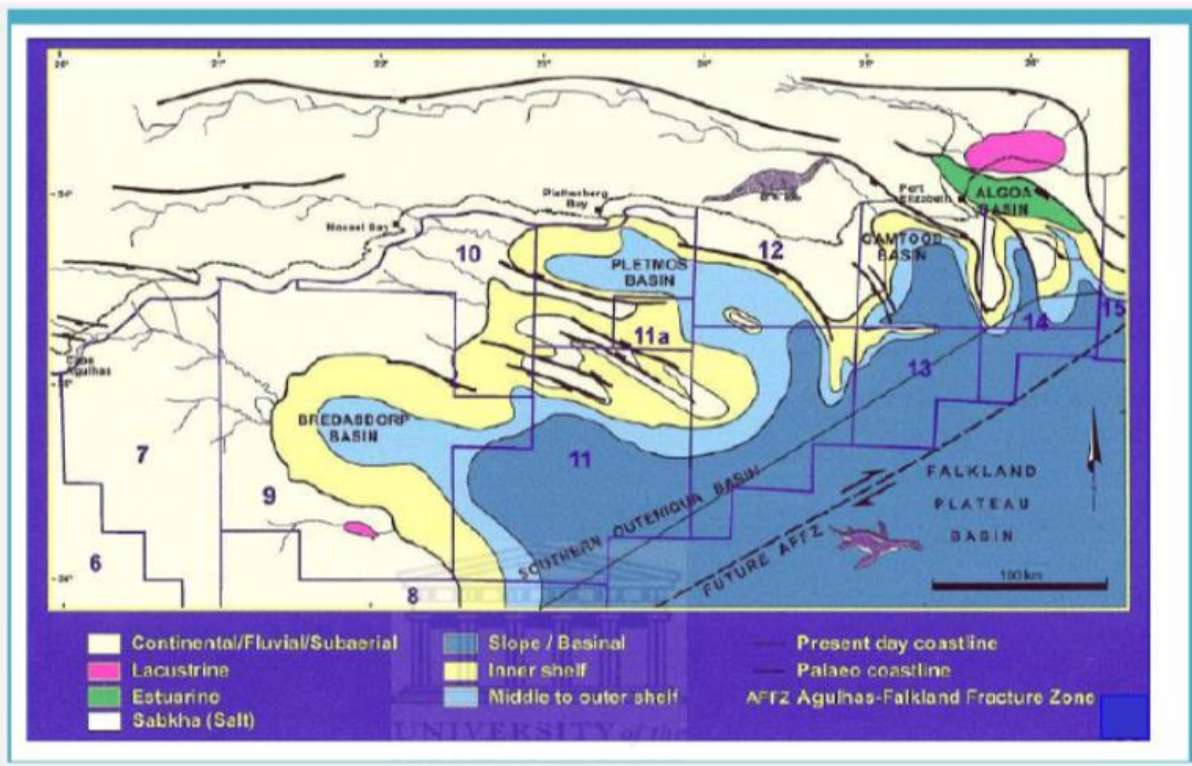


Figure 2.9: Representation of depositional environments in the Outeniqua basin (ILE, 2013).

The depositional characteristics indicate that the basin consists of sequences of sandstones with alternating clay stone beds (ILE 2013). According to the research (Emmanuel & Carey 2011), the characteristics and sequences of the beds indicate a thinning and fining upward with most of the fan channels being recorded as progressively abandoned. This provides evidence of the presence of fan deposits.

The development of basin and slope systems was caused by the deposition of fine-grained density, leveed slope deposits, and basin floor turbidite fans (figure 2.10). The second tectonic event caused depositional changes within the basin, resulting in differences in sediment supply rates, accommodation rates, and the increase of open ocean processes (Schalkwyk 2005).

During the period of the 1-5 super cycle (126 – 118 Ma), the middle part of the Bredasdorp basin was filled with sediments from the high gradient fluvial systems. During the 1-6 super cycle (118 –

112 Ma), deltaic coastal systems advanced into the basin after uplifting and erosion of the second unconformity. Fluvial sediments that eroded into the shelf edge were transported to low-stand shorelines through small canyons. The basin floors of the Upper Barremian 9A LST consist of multiple individual submarine fans.

The thickening and coarsening of the facies within the basin indicate fan progradation which portrays marine regression and transgression (ILE 2013). The third-order low-stand of the (Brown 2004) model is still used to describe the growth of highly faulted basins (ILE 2013). This model indicates that the growth of faulted, third-order low-stand sub-basins occurred off the shelf break towards the sea, where there is an accumulation of coarse-grained sediments on an unstable slope mud that was deposited during high-stand transgressive system tracts (ILE 2013).

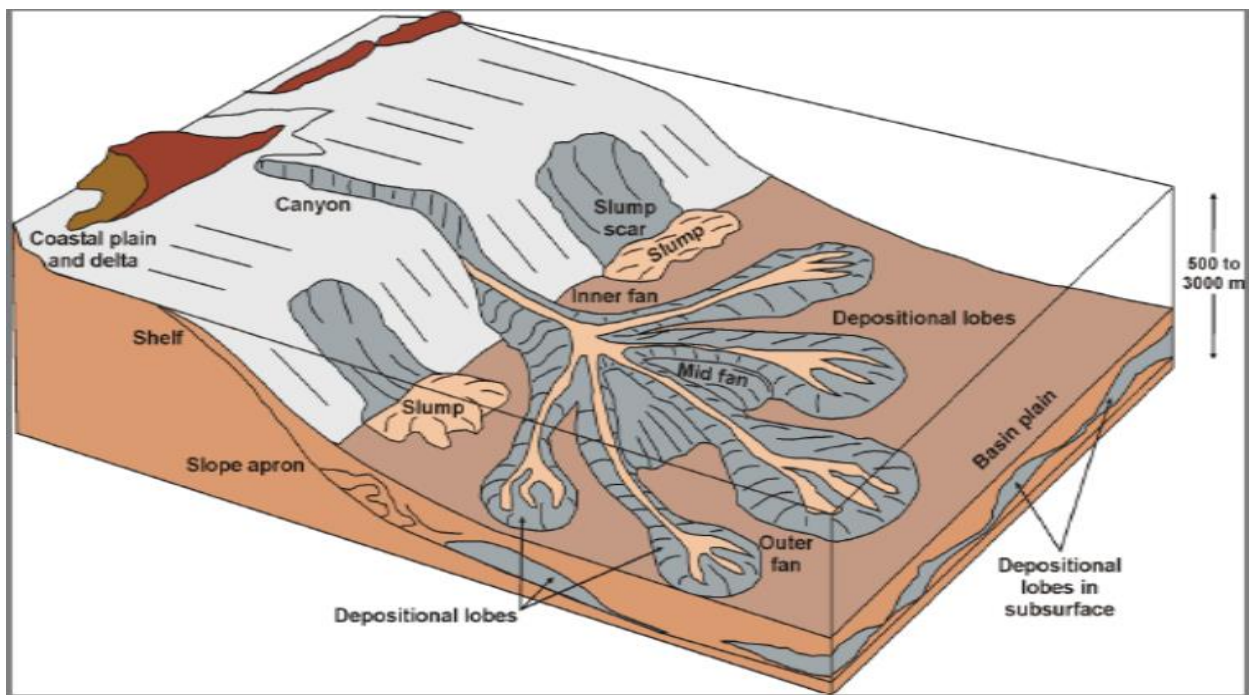


Figure 2.10: Evolution of deep-marine channel deposits (Schalkwyk 2005).

Chapter 3: Literature Review:

3.1. Introduction:

This chapter of the research project focuses on the literature review of topics in this research. These topics include an introduction to petroleum systems and wireline logging techniques. The introduction to petroleum systems was used to discuss the importance of understanding the key elements needed for the development of a petroleum system. The wireline logging techniques are critical to this research as the tools used for recording were needed for both petrophysics and rock physics analysis. These two topics help us understand the petroleum system and how data is obtained.

3.2. Introduction to Petroleum Systems:

Petroleum systems are present in reservoirs of sedimentary basins where accumulations of thick sequences of sedimentary rocks are present due to the subsidence of the earth's crust (Aminzadeh and Dasgupta 2013). Petroleum systems consist primarily of petroleum reservoir fluids which formed millions of years ago when organic material from plants and animals was mixed with sediments resulting in a build-up of different layers. These petroleum fluids are buried and trapped within the rocks of the earth either offshore or onshore due to geological shifts (Dandekar, Abhijit Y 2006). For the accumulation of hydrocarbons to be present in the subsurface, the conventional petroleum system requires four key elements namely, a source rock, a reservoir, a trap, and a seal (de Jager 2020). If any of the elements are missing, no conventionally trapped or producible hydrocarbons can be present.

3.2.1. Source Rocks:

Source rocks are fine-grained sedimentary rocks that contain sufficient organic material that was transformed through heat, time, and pressure into liquid and/or gaseous hydrocarbons (Parker 2014). The source rocks that contain hydrocarbons are normally shale or limestone. For a source rock to be productive, it needs time to mature to form oil/gas and the hydrocarbons need to migrate to the reservoir (Hyne 2012).

With time, the source rocks become buried deeper, thus causing the temperature to increase to form geochemical reactions that transform the organic material into hydrocarbons. Crude oil forms between temperatures of 65-150 °C, whereas natural gas forms at temperatures over 150 °C (Hyne 2012). The hydrocarbons migrate to the overlying reservoir rocks where they are separated based on their density with gas on top, oil below it, and water beneath the oil (Earle 2012).

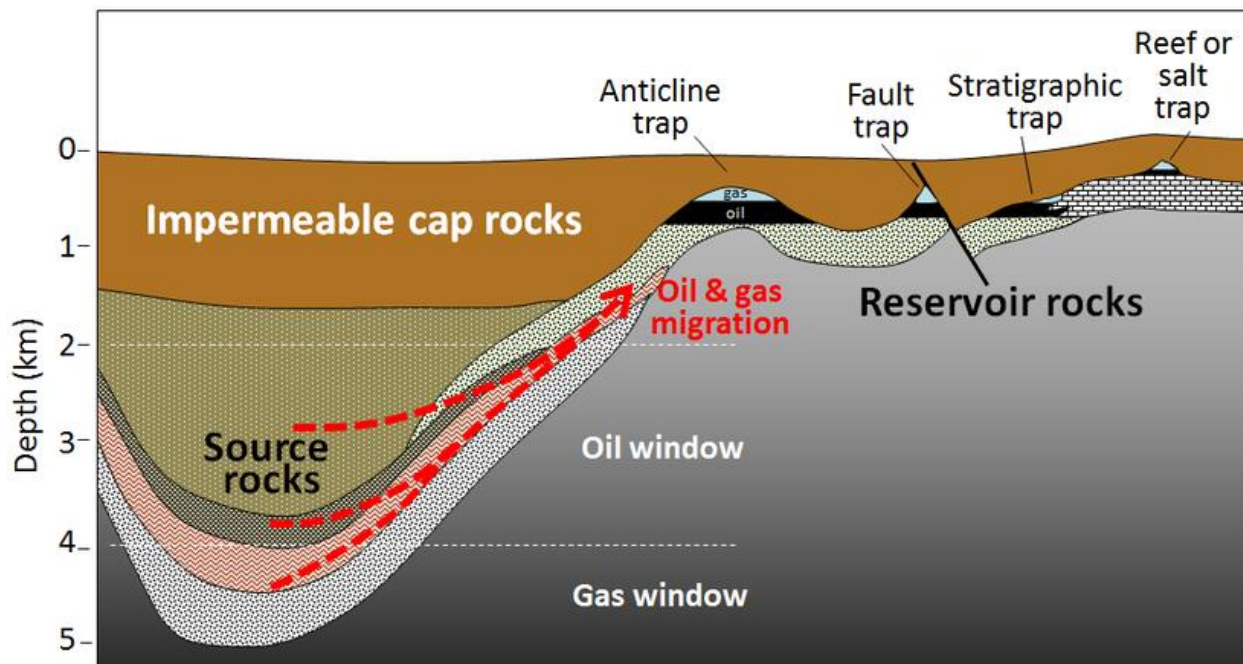


Figure 3.1: Diagram showing the migration of hydrocarbons into reservoir rocks (Sheardown and Donev 2022)

Source rocks can also be classified based on three different kerogen types which may either be oil or gas prone. The three different kerogen types are listed below:

- a. Type 1 Kerogen: This type is oil-prone and has an algal origin with a high hydrogen-to-carbon ratio.
- b. Type 2 Kerogen: This type has several origins and is mainly classified as an intermediate oil-gas ratio. It is normally found in marginal marine environments.
- c. Type 3 Kerogen: This type has a humic or lignocellulosic origin with a low hydrocarbon-to-carbon ratio. It is classified as gas-prone. (Cornford 2005, Parker 2014)

3.2.2. Reservoir:

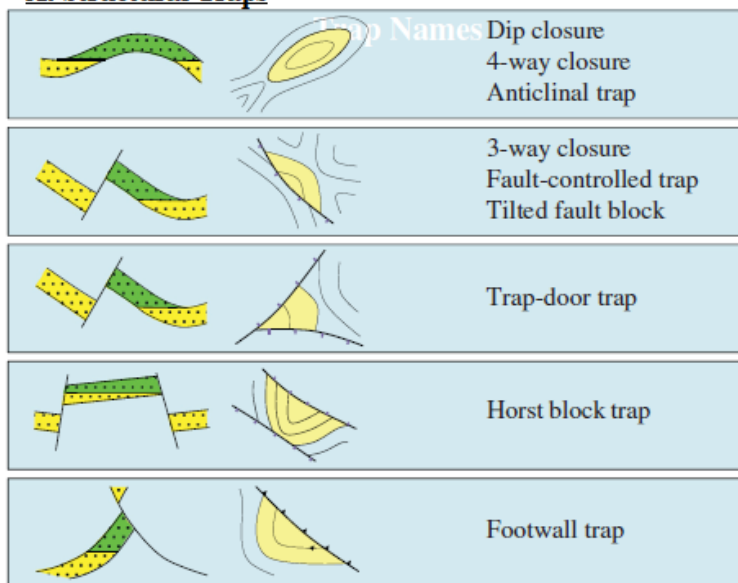
A reservoir rock is a subsurface rock that has a sufficient porous medium that can allow the accumulation and storage of hydrocarbons under adequate trapping conditions (Magoon 2004). The porosity and permeability of reservoir rocks allow a pathway for hydrocarbons to migrate from source rocks to reservoir rocks providing there's a sealing mechanism that prevents hydrocarbons from escaping (Alamooti and Malekabadi 2018). Reservoir rocks can appear in different forms, whether it's loose sands or tight and dense rocks. The most common reservoir rocks are sandstone, limestone, and dolomites, but reservoir rocks also exist through fracturing igneous and metamorphic rocks (Parker 2014).

3.2.3. Traps:

Traps are defined as 3D subsurface geometries that hold/trap an economically producible quantity of hydrocarbons. It is any barrier that prevents the upward migration of hydrocarbons, thus causing them to accumulate in the underlying reservoir (de Jager 2020). Traps include a reservoir rock and an overlying impermeable cap rock (Parker 2014). Traps are mainly classified into the following classes in order of their presence in the earth:

- i) **Structural trap**: These traps are mainly formed by deformational events such as folding and faulting (Parker 2014). They have a limitless variation of complex structural traps. More simple structural traps are shown below (figure3.2)(de Jager 2020).
- ii) **Stratigraphic trap**: These traps are formed due to changes in lithology within the reservoir (Parker 2014). They are formed without any deformational events occurring and examples of these include unconformities, coral reefs, or salt domes (de Jager 2020).
- iii) **Combination traps**: These traps are formed due to a mixture of stratigraphic and structural elements (Parker 2014).
- iv) **Hydrodynamic trap**: These are rare types of traps whereby high-water saturation of low permeable sediments reduces the permeability dramatically thus causing water to block hydrocarbons from escaping. They are formed due to the flow of water (Parker 2014).

A. Structural Traps



B. Stratigraphic Traps

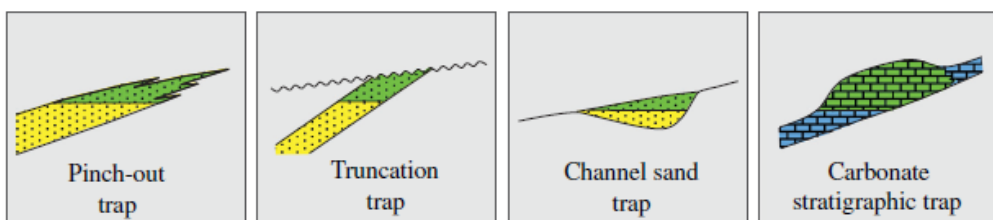


Figure 3.2: Indication of the different structural and stratigraphic traps that occur within the earth (de Jager 2020).

3.2.4. Seals:

Seals are defined as impermeable rock layers which act as a seal/cap to the reservoirs (Parker 2014). It is composed of lithologies (such as shales and evaporites) with very low permeability that prevents hydrocarbons from easily escaping from the reservoir rocks (de Jager 2020). For stratigraphic traps, the seals are mostly found above and below the trap.

3.3. Wireline Logging:

The term well logging is identified as the recording of the electrical, acoustic, and physical properties of rocks penetrated by a well. It is used to measure the in-situ rock properties that cannot be obtained from the laboratory through core samples or cutting (Halder 2018). Hydrocarbon exploration, field development, and monitoring are all areas where advanced logging is utilized (Mondol 2015). It gives information about the geology of the subsurface which includes the lithology, formation boundary, porosity, volume of clay, water saturation, permeability, and fluid content (Maseko 2016, Kadkhodaie and Kadkhodaie 2022).

The logging tools do not measure the amount of oil or gas directly but rather use the measured properties such as gamma radiation, velocity, density, and resistivity to estimate how many hydrocarbons there are (Mondol 2015). A logging operation is performed when a logging sensor is lowered into the borehole by a survey cable after the drilling tool is removed (Maseko 2016)(figure 3.3). The survey cable is used to record specific depths while the logging tools (acoustical, nuclear, electrical, thermal and dimensional) record the properties at particular depths within the borehole (Mondol 2015) (Maseko 2016).

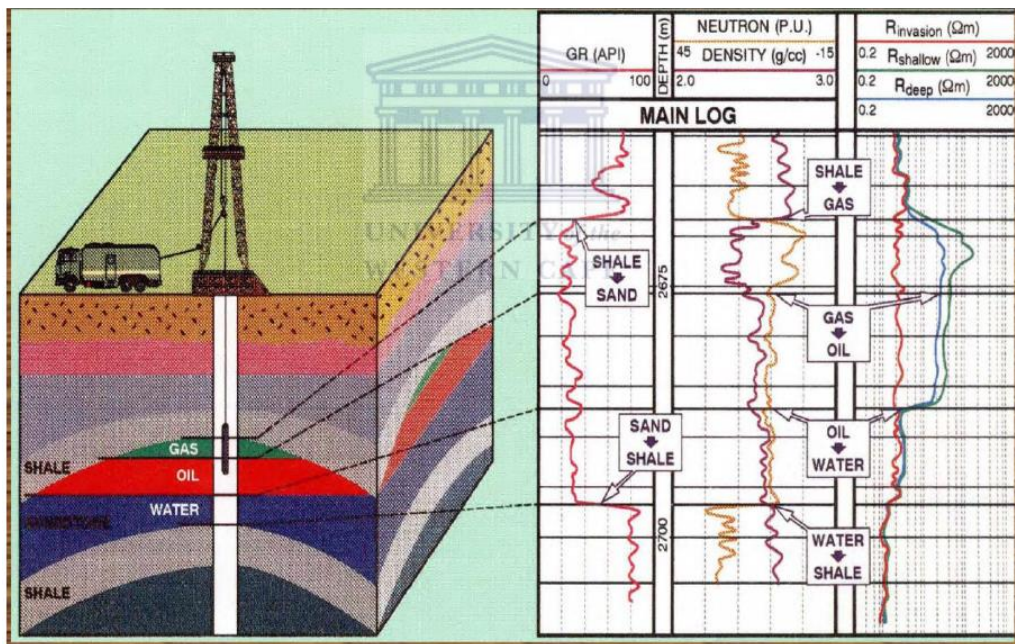


Figure 3.3: Representation of the wireline logging operation indicating the logging truck, logging cable and logging tools within the borehole (Maseko 2016)

3.3.1. Gamma Ray Logs:

Gamma-ray (GR) logs are used to record the radioactivity of a formation (figure 3.4) (Maseko 2016). The radiation originates from Potassium (the most abundant element) and the isotopes of thorium and uranium. Each of these elements releases gamma rays spontaneously (Mondol 2015). The spectral gamma-ray (SPG) logs record the individual amount of the three elements that contribute to the radioactivity, whereas the simple gamma-ray (GR) log records the radioactivity of all three elements combined (Maseko 2016). The unit used to measure gamma-ray logs is the American Petroleum Institute (API) (Fadipe 2012).

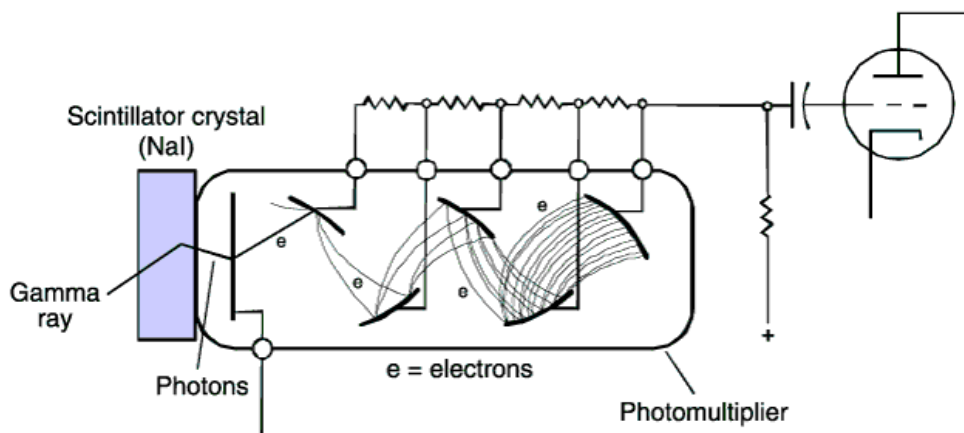


Figure 3.4 Visual drawing of the gamma-ray tool_(modified from Serra, 1984)

The Gamma-ray log can be combined with all other logging tools, and it is mostly used in combination with other logs to match the depths of the data (Mondol 2015). The gamma-ray log has the advantage over other logs because it is insensitive to drilling fluids and it can work through the cement and steel walls of cased boreholes (Mondol 2015).

Most rocks are believed to be radioactive to some degree, with shale being the most radiated rock. However, not all shales are considered radioactive and not all radioactive shales are used to derive the shale volume (Rider 2002). Qualitatively, the radiation of the shale can be used to identify lithologies, suggest sequences and facies and can be used for correlation (Rider 2002). The quantitative analysis of shale can be determined by the means of spectral gamma-ray which can derive the radioactive mineral volume and an accurate volume of shale (Rider 2002). It can also be

used to identify the clay minerals present, specify the depositional environment, and help localize the source rocks (Rider 2002).

3.3.2. Resistivity Logs:

Resistivity is an indication of how robust a material resists or opposes the flow of electric current (Mondol 2015). Most of the minerals found in rocks are insulators whereas the fluids that enclose them are conductors (Parker 2014). Most of the conductivity occurs in the liquid phase, whereas the resistance is dependent on pore fluid and its salt content with hydrocarbon fluids as an exception. A low resistivity occurs when the formation is porous and contains salty water, whereas a high resistivity occurs when the formation has very low porosity and contains hydrocarbons (Fadipe 2012).

The electrical properties of rocks are measured through the resistivity tools and induction tools which measure the resistivity and conductivity, respectively. The resistivities of rock formations are measured by allowing a known current to travel through the formation or by inducing a current distribution in the formation (Mondol 2015). Both these measurements, measure the same property of the rock and can be interconverted by Resistivity = 1/Conductivity. Resistivity of a rock formation is dependent on the amount of water present and is expressed as:

$$R = r \times A/L \quad (3.1)$$

Where R is resistivity (ohm.m), r is the resistance (ohms), A is the cross-sectional area (m^2) and L is the length (m) (ILE 2013).

The resistivity or conductivity logs can be used to detect and quantitatively analyze the hydrocarbon zone and correlate the geological strata. Formations that contain hydrocarbons are indicated by high resistivity values. These resistivity logs indicate that oil and gas have higher resistivities than water and thus these logs can be used to show the contacts between gas/oil (GOC), oil/water (OWC) and gas/water (GWC) in the reservoirs (Darling, Toby 2005). These logs are used to determine the hydrocarbon saturation.

3.3.3. Porosity Logs

3.3.3.1. Sonic Log:

Sonic logs are a measurement of how sound travels through rocks and give information about porosity (Mondol 2015, Maseko 2016). This method uses a probe to send out acoustic pulses that travel through the surrounding rocks of the well to the other end of the logging tool, where it records the sound velocity of the rock (figure 3.5). This method gives an indication of whether gas or liquid is occupied within the pore spaces. However, the velocity recorded by the sonic logs does not directly indicate porosity (Mondol 2015).

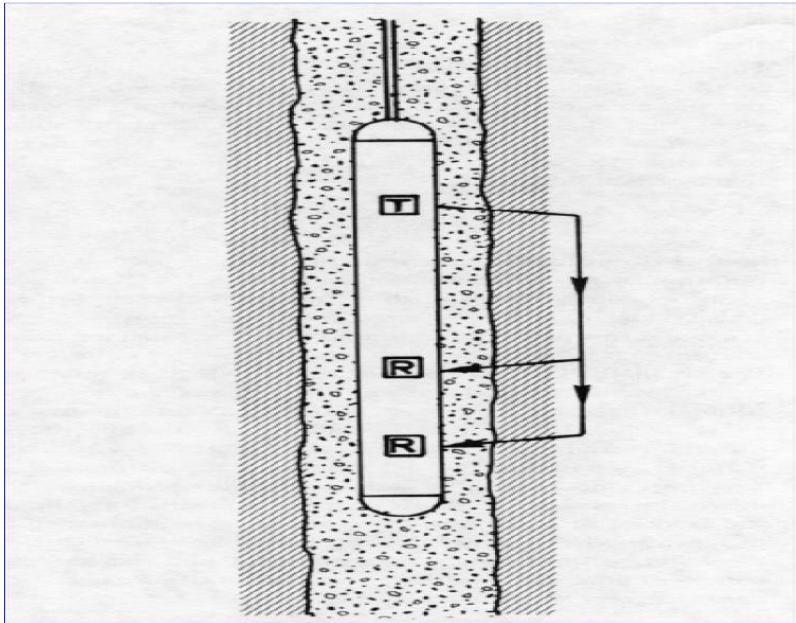


Figure 3.5: Representation of a sonic logging tool where (R) is the receiver and (T) is the transmitter (Maseko 2016).

The inverse of velocity also called the interval transit time (Δt), indicates the slowness that is presented on the log record as a scale of 40-140 us/ft ($us = 10^{-6}$) or us/m (100 us/ft corresponds to 10 000 ft/s or 3.048 m/s). The reciprocal of the sonic transit velocity is known as the interval transit time (Mondol 2015).

These sonic logs can be used to evaluate the porosity in the liquid-field holes (Maseko 2016). The interval velocities and velocity profiles of sonic logs can also be used to interpret seismic data. Geologists use sonic logs because it is very sensitive to textural variations in shales and sands (Rider 2002). These logs can be helpful in indicating the lithology, source rocks, compaction, overpressure, and fractures within the rock formation (Rider 2002).

3.3.3.2. Density Log:

The density logs are identified as induced radiation tools that consist of a radioactive source that emits medium gamma rays (Mondol 2015). It uses these gamma radiations to bombard a formation and measures the amount of returned radiation with its detectors (long and short) (figure 3.6) (Maseko 2016) (Mondol 2015). The gamma rays that return is measured through either Compton scattering or photo electric density. Compton scattering is defined as high-energy gamma rays that can determine the porosity through the bulk density, whereas the photoelectric effect is defined as low-energy gamma rays that determined the lithology of the formation (Parker 2014). The unit of the density log is indicated as g/cm³ of kg/m³ (Mondol 2015).

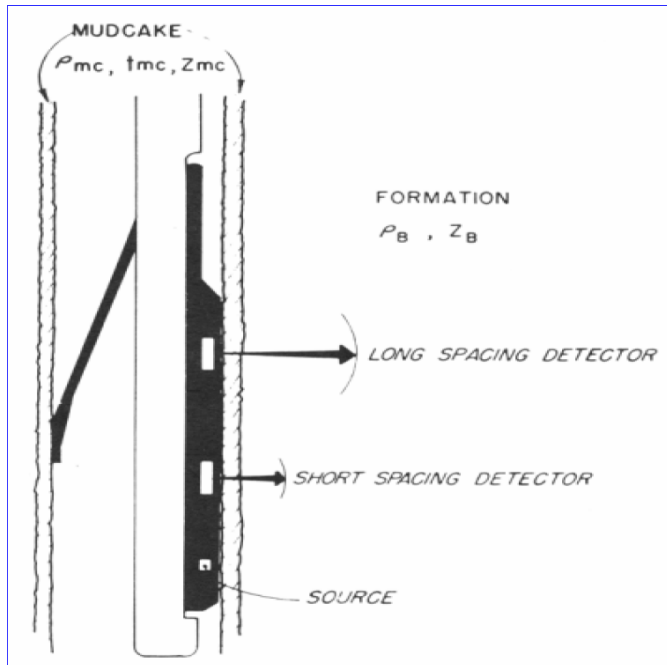


Figure 3.6: Compensated density logging tool which shows the configuration of the source and detectors (Wahl, et al. 1964).

In geology, bulk density is defined as the density of minerals in a rock and the volume of free fluid that encompasses it (Maseko 2016). These logs can calculate the acoustic impedance, indicate lithology, identify minerals, assess source rock and organic contents and it can also be used to identify fracture porosity and overpressure (Rider 2006). The formation bulk density is a function of density, porosity, matrix density and formation fluid density.

3.3.3.3. Neutron log:

Neutron logs are obtained by sending radiation into the rock formation with a neutron source. During this method, the rock formation (particularly the water) absorbs the neutron rays (Mondol 2015). This occurs when the neutron rays collide with the atomic nuclei and the absorbed neutron radiation is a function of Hydrogen atom concentrations (Acho 2015). This indicates that the neutron log is mainly a measurement of the water content within the formation, whether it's bound water, free-pore water, or water crystallization (Maseko 2016). These logs are recorded as neutron porosity and their units are p.u (porosity units, percentage, or decimal) (Mondol 2015).

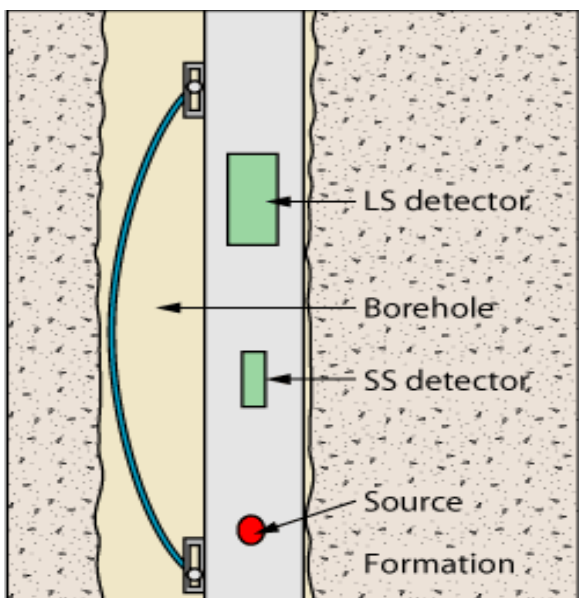


Figure 3.7: Compensated neutron tool (Acho 2015)

The neutron tool is composed of a fast neutron source and two detectors (figure 3.7). The source of the neutron tool is used to bombard the rock formation with fast neutrons, and the loss of energy of the neutrons as they collide with hydrogen atoms in the rock formation is recorded by the detectors. The most common neutron tool sources used have a peak energy of about 4Mev and they are mostly chemical, such as americium-beryllium (AmB) or plutonium-beryllium (PuBe) (Maseko 2016).

The source of the neutron tool is used to emit fast neutrons that travel through the rock formation where they are slowed down with hydrogen collision. The slow neutrons are captured by the hydrogen atoms within the formation at various energies and velocities and are then recorded by the detectors (Fadipe 2012).

Chapter 4: Dataset and Methodology

4.1. Data collection:

The data used for this study was provided by the Petroleum Agency South Africa (PASA). The data provided includes whole cores, core samples, core plugs, thin sections, geophysical wireline logs (las format) and well completion reports. The core plugs were used to perform routine core analysis to determine porosity, permeability, resistivity, and water saturation by using a PoroPerm and EPSA instrument. The data from core plugs were carefully sorted, arranged, and prepared for analysis. The data also went through processes of QC/QA, such as repeating of randomly selected samples to ensure the data is reliable. Raw data is also made available if any calculations don't add up and if the core plugs need to be rerun. The petrophysical and rock physics variables calculated from the core laboratory analysis are used to calibrate the geophysical wireline logs on Interactive Petrophysics (IP) software.

The figure gives an idea of how this research will be carried out. This research follows the following sequences outlined below complete this project (figure 4.1):

1. Review previous studies on the Bredasdorp Basin to enhance understanding of the area. The review will include the tectonic and structural history of the basin, thermal gradient and pressures, and sedimentary depositional environment.
2. Data collection. Which is the data that is collected from the Petroleum Agency of South Africa in the form of pdf files, las files, physical whole core samples and core plugs.
3. The core samples will be used for petrographic studies which include thin sections, SEM, XRD and XRF analysis.
4. Development of a Petrophysical model based on the core data and wireline logs. Calibration between core data and wireline logs will be used to calculate the petrophysical parameters.
5. Development of a rock physics model which depends on wireline logs and core plugs. The calibration between core plugs and wireline logs will be used to calculate the rock physics parameters.
6. An integration between these models will help find the best reservoir rock and fluid properties.
7. Report write-up

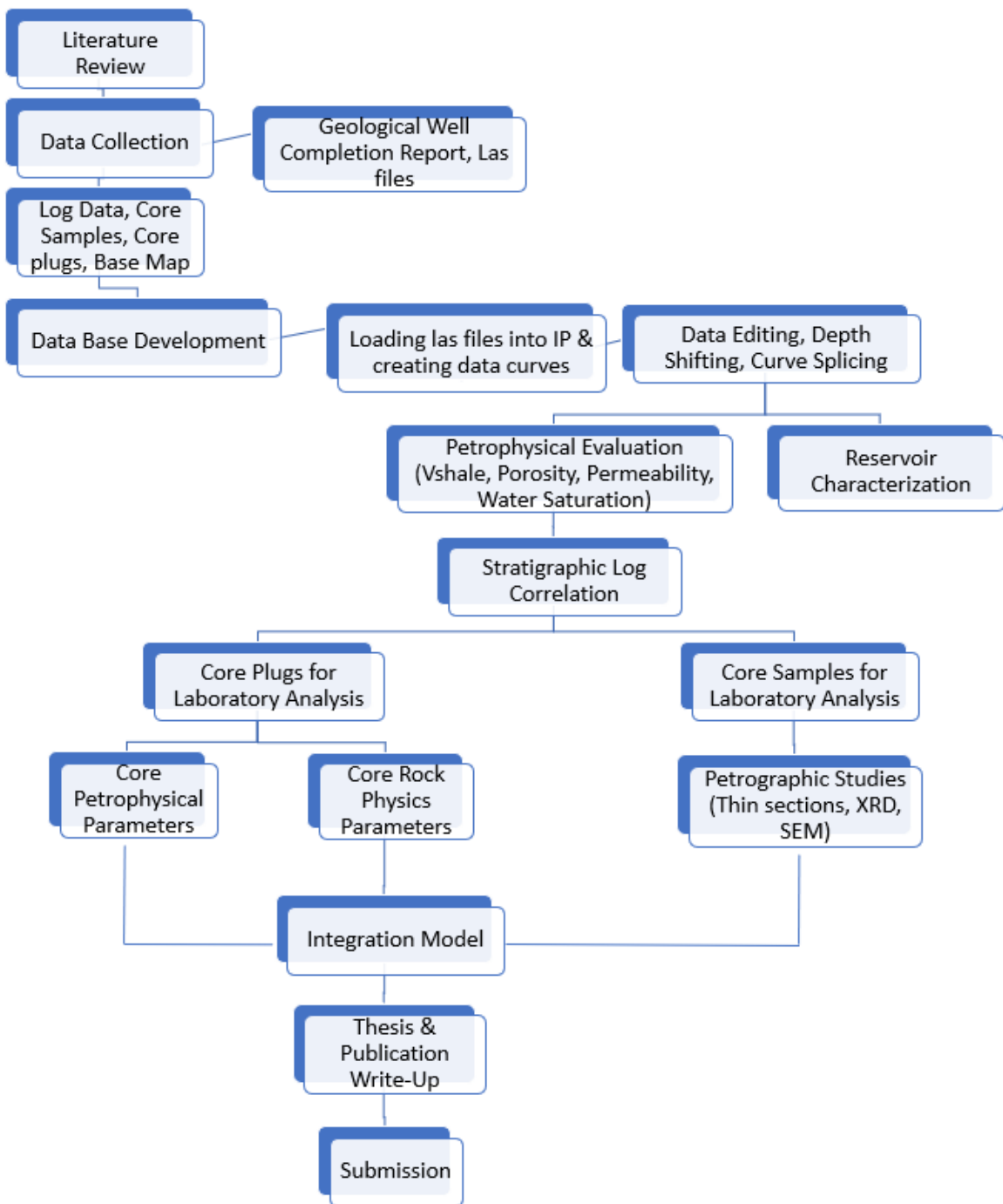


Figure 4.1: Representation of the steps followed for this research.

4.2. Wireline logs loading and editing.

Wireline logging is very important for comprehending subsurface conditions and characteristics as it is responsible for recording formation properties at a specific depth of a well. The recorded raw data from wireline logging is necessary to convert into petrophysical and geomechanical parameters. The wireline logs were collected from three wells from the reservoir sandstones of Bredasdorp Basin. The logs of the three wells were provided to me in the form of LAS files by the Petroleum Agency of South Africa (PASA).

Table 4.1: Table showing the availability of logs for each well.

Logs	E-BT1	E-AR1	E-AR2
Bit Size (BS)			
Caliper (CALI)			
Gamma Ray Logs (GR)			
Spontaneous Potential (SP)			
Deep Laterolog (LLD)			
Shallow Laterolog (LLS)			
Deep Induction (ILD)			
Microspherically Focussed (MSFL)			
Density (RHOB)		(Outside Reservoir)	(Outside Reservoir)
Neutron (NPHI)		(Outside Reservoir)	
Sonic Neutron (SPHI)			
Sonic Logs (DT)			

These logs were uploaded in the form of LAS files into Interactive Petrophysics (IP) software. As seen above, Density and Neutron logs were not available for wells E-AR1 and E-AR2 therefore reservoir porosity and saturation from the well logs could not be calculated for these wells. Other data such as core porosity and permeability that were obtained from laboratory experiments and hardcopy reports from PASA, were added to the well log database in the form of Excel spreadsheets. To interpret the uploaded data accurately and effectively, this data must be evaluated and modified

to account for any flawed borehole environments that may be encountered before progressing with any analysis. The modification of the data included depth shifting and curve splicing.

4.2.1. Depth Shifting:

The process of log editing and depth shifting is crucial in QA/QC as it helps to improve the accuracy of data interpretation. When there are inconsistencies in data sets from combining various log runs for a single borehole, depth shifting must be done for different logging tools to ensure that the formation properties are in the proper location. According to (Hussien 2014), variation in logs for the same borehole can also be caused by borehole irregularities. However, logs from the same logging run are at the correct depth and require no adjustments. In this study, the logging runs were carefully assessed for irregularities, and none were found.

4.2.2. Curve Splicing:

After carefully performing the depth shifting, the different runs that were logged in the same borehole were spliced together to produce a single continuous log.

4.3. Petrophysical Calculations:

The review of the following topics can be found in Chapter 2 under rock properties. The following literature indicates how the petrophysical parameters were obtained through the wireline logging methods and core data. These parameters include volume of clay, porosity, permeability, and fluid saturation.

4.3.1. Volume of Clay:

The volume of clay (V_{cl}) is identified as the amount of clay present in each reservoir rock volume and can be expressed as either a percentage or a decimal fraction. The presence of the clay volume in sand formations can affect the results of logging measurements for water saturation and porosity. Therefore, it is important to determine the clay volume accurately within reservoir intervals to account for the errors (Hussien 2014).

Different methods are used to determine the volume of clay, such as resistivity responses and gamma-ray, or using double curve indicators such as Neutron/Sonic, Neutron/Density or Density/Sonic logs.

For this study, we will be using gamma ray responses to determine the volume of clay. The gamma-ray log is the most common method used for determining the clay volume and it is generated by measuring the natural radiation emitted by a formation. A high gamma radiation indicates a clay-dominated formation, whereas a low gamma radiation indicates clean sand. However, these gamma rays cannot measure the presence of silts or other materials within clay. The linear gamma ray method is used to estimate the clay volume as it gives a simple and effective way to indicate the clay content (Parker 2014).

According to (Parker 2014), the mathematical formula used for this method is as follows.

$$Volume\ of\ clay\ (Vcl) = \frac{GR\ value\ (Log)-GR\ (min)}{GR\ (max)-GR\ (min)} \quad (4.1)$$

Where:

GR value = GR log value reading of formation to be evaluated

GR (minimum) = Clean formation

GR (maximum) = GR value of maximum clay reading in the formation

4.3.2. Porosity:

Porosity is the principal rock property as it describes the ability of the formation rocks to store fluids. According to (Hussien 2014), porosity is described as the ratio of pore space volumes to the total rock volume. It can be expressed either as a fraction or percentage and it is mathematically expressed as:

$$Porosity = \frac{Volume\ of\ Pore\ Spaces}{Volume\ of\ Bulk\ Rock} \quad (4.2)$$

For this study, the porosity has been determined from wireline logs such as Density (RHOB) and Neutron (NPHI, SPHI) logs as well as through laboratory experiments on core plugs using a PoroPerm that directly measures both porosity and permeability.

Table 4.2: The table below shows the quantitative evaluation of porosity values for reservoirs rocks under average operating conditions:

Porosity	Quantitative evaluation
0-5	Negligible

5-10	Poor
10-15	Fair
15-20	Good
20+	Very good

4.3.2.1.Porosity from logs:

The porosity of the selected reservoir formations of the three wells has been determined using the recorded porosity logs. The logs that were used to calculate the porosity in this research are the sonic, density, and neutron logs.

Density log:

The purpose of the density log (RHOB) is to determine the overall density of the formation, which is a key factor in determining the total porosity. The measurement of bulk density is the result of the combined effects of the matrix component of the formation and fluids occupying the pore spaces (Hussien 2014). The porosity using the density log can be calculated using the following formula:

$$\text{Porosity } (\Phi) = \frac{\rho_{ma} - \rho_b}{\rho_{ma} - \rho_f} \quad (4.3)$$

Where,

ρ_{ma} = Density of rock matrix

ρ_b = Bulk density of formation

ρ_f = Density of fluids occupying the porosity

The densities that were used for this calculation are 2.65 g/cm³ for sandstone and 2.7 g/cm³ for shale. The output log for porosity using the density log (RHOB), is Phi_Den.

Sonic log:

The sonic log (DT) records how long it takes for a sound wave to travel one foot through a formation. The recorded time, known as transit time or slowness depends on the type of rock and how porous it is. We can determine the porosity of a formation more accurately if we know the lithology.

Using a simple equation proposed by (Wyllie 1956), the equation of time average can be expressed as:

$$\text{Porosity } (\Phi) = \frac{\Delta t_{log} - \Delta t_{ma}}{\Delta t_f - \Delta t_{ma}} \quad (4.4)$$

Where,

Δt_{log} = formation transit time

Δt_{ma} = rock matrix transit time

Δt_f = fluids in pore spaces transit time

The output porosity log with the use of the sonic log (DT), is Phi_Son.

Porosity from a combination of neutron and density logs:

A common practice for calculating the total porosity in gas reservoirs is to combine neutron and density logs. This helps to offset the impact of gas on both logs (Dandekar, Abhijit Y 2006). Different formulas can be found for the combination of these logs, but the most common method is to average the apparent neutron and density porosities. This can be mathematically expressed as:

$$\text{Porosity } (\Phi) = \frac{\Phi_{density} + \Phi_{neutron}}{2} \quad (4.5)$$

As previously mentioned, the output porosity log for density is Phi_Den, whereas the output log with the use of neutron log (NPHI/SPHI), is Phi_Neu

4.3.2.2. Porosity from core data:

The porosity of a reservoir rock is comprised of three volumes namely, bulk volume (BV), pore volume (PV), and grain volume (GV) (Dandekar, Abhijit Y 2006). The relationship between these volumes can be expressed as:

$$BV = PV + GV \quad (4.6)$$

Where the bulk volume (BV) is calculated from diameter (d) and length (L) using the formula:

$$BV = \frac{\pi d^2 L}{4} \quad (4.7)$$

Two of the three volumes need to be determined to calculate the porosity of the reservoir rock sample (Dandekar, Abhijit Y 2006). The porosity of the reservoir rock can be calculated using the following equation (Magoba and Opuwari 2019):

$$\text{porosity} = \frac{PV}{BV} \quad (4.8)$$

Gas Expansion Method:

The instrument used to determine the porosity and permeability of core plugs through volumetric measurements is a PoroPerm. This instrument determines porosity from an isothermal nitrogen expansion and makes use of the principle of Boyle-Mariotte's law, which can be expressed as (Magoba and Opuwari 2019):

$$P1V1 = P2V2 \quad (4.9)$$

Nitrogen which is an ideal gas is used during the determination of porosity due to its ability to penetrate small pores within the rock sample, and its inertness to prevent adsorption on rock surfaces (Dandekar, 2006). During this technique, both the inter-particle and intra-particle pores can be determined and characterized.

The configuration of the instrument has a control console, Hassler core holder, matrix cup holder and a data acquisition computer (VINCI-Technologies 2022)(figure 4.2). The instrument consists of two chambers of equal volume called the reference chamber (core holder) and sample chamber (matrix cup) (figure 4.2) (Dandekar, Abhijit Y 2006).



Figure 4.2: Configuration of a PoroPerm that measures the porosity and permeability of core plugs and the data acquisition computer that records data.

4.3.3. Permeability

Permeability is the property of a rock that allows fluids to pass through it without causing any change in the structure of the rock (Schalkwyk 2005, Dandekar, Abhijit Y 2006). It is mainly controlled by the size of the pore throats or capillaries (Schalkwyk 2005). Permeability is mathematically expressed through Darcy's law (Alyafei 2021):

$$q = -\frac{KA}{\mu L} dP \quad (4.10)$$

Table 4.3: Table showing the variables and units for Permeability.

q	Flow rate	m ³ /s
K	Permeability	Darcies (mD)
A	Core cross sectional area perpendicular to the flow	m ²
μ	Viscosity of the injected fluid	Pa.s or N/m ² .s
L	Length of the core	M
dP	Pressure difference across the core	Pa or N/m ²

4.3.3.1. Permeability from logs

For this study, the permeability has been calculated from the water saturation (SwArch, Swi) logs and porosity logs (Phi_Son, Phi_Den, Phi_Neu). These logs have been used as input parameters along with the Schlumberger K3 chart constants to determine their respective permeabilities. The equation that has been used to calculate the permeability is as follows:

$$K = a \cdot \frac{\Phi^b}{S_w^c} \quad (4.11)$$

Where, K = Permeability (mD)

Phi = Refers to the type of porosity used.

Swi = Irreducible Water Saturation

Schlumberger constants from the K3 Chart:

$$a = 10000$$

$$b = 4.5$$

$$c = 2$$

Table 4.4: Table showing the output permeability logs:

Input Parameters for Porosity	Calculated Porosity Logs	Calculated Permeability Logs
Sonic Log (DT)	Phi_Son	Perm/PermSon
Neutron Log (NPHI/SPHI)	Phi_Neu	PermNeu
Density Log (RHOB)	Phi_Den	PermDen

4.4. Electrical Properties:

4.4.1. Electrical Properties from logs:

4.4.1.1. Formation water resistivity

True Formation resistivity (R_t) and Flushed zone water resistivity (R_{xo}) are obtained from the resistivity record of deep (ILD/LLD) and medium resistivity (MSFL) measuring devices, respectively. The estimation of the resistivity of formation water (R_w) was based on the relationship of Archie in 1941, which involves the determination of the formation factor from a shale-free water-filled formation of a clean non-shaly reservoir. In a formation filled with shale-free water, the formation factor (F) can be defined as:

$$F = \frac{R_o}{R_w} \quad (4.12)$$

or as;

$$F = \frac{a}{\Phi^m} \quad (4.13)$$

By rearranging this equation, we can determine the brine resistivity as;

$$R_w = (\Phi^{m/a} \times R_o) \quad (4.14)$$

The variables that were used for these equations are as follow:

Resistivity of brine pre-determined: $R_w = 0.16 \Omega m$

Resistivity of 100% saturated rock: R_o

Formation factor: F

Porosity: Φ

Constants:

Archie Constant: $a = 1$

Cementation factor: $m = 2$

Saturation exponent: $n = 2$

4.4.1.2. Water saturation (Sw) and Hydrocarbon saturation (Shc):

A reservoir that contains hydrocarbons is composed of empty spaces that are filled partly with formation water and hydrocarbons. The resistivity of the hydrocarbons reservoir depends on the formation factor (F), the resistivity of the formation water (R_w), and its water saturation (S_w). Archie's equation is used to determine the water saturation (S_w) in hydrocarbon-rich reservoirs and can be defined as:

$$S_w = \sqrt[0.5]{F \times \frac{R_w}{R_t}} \quad (4.15)$$

Where,

$$F = \frac{a}{\Phi^m} \quad (4.16)$$

Hydrocarbon saturation (Shc) is the part of pore space that's filled with oil and gas. This is mathematically presented as: Shc = 1 - S_w

4.4.1.3. Bulk volume of water (V_b)

The quantity of formation water within a specific rock unit can be measured by its bulk water volume. This is determined by multiplying the water saturation (S_w) and porosity (Φ) of the rock. The equation for the bulk volume of water can be expressed as:

$$V_b = S_w \times \Phi \quad (4.17)$$

4.4.1.4. Irreducible water saturation (Swir)

The irreducible water saturation (Swir) refers to the minimum saturation that reservoir water can attain when it is pushed out of a porous medium by unmixable hydrocarbons. This indicates that the part of the pore space occupied by water in the reservoir is at the highest hydrocarbon saturation. This term is used to prepare for the determination of permeability.

The irreducible water saturation can be expressed as:

$$S_{wir} = \frac{V_b}{\Phi_{eff}(1-V_{sh}^2)} \quad (4.18)$$

Where, Swir: Irreducible water saturation

Φ_{eff} : Effective porosity

V_b: Bulk volume

V_{sh}: Shale volume

Note:

Sw = Swir: hydrocarbon bearing zone

$Sw > Swir$ = production hydrocarbon with water cut.

$Sw < Swir$ = error in calculation.

4.4.1.5. Water Saturation and Resistivity from logs:

In this project, we use Archie's Method to calculate the water saturation and resistivity from logs. The following input parameters were used to calculate the Archie Water Saturation (Sw_{Arch}) and Apparent Formation Water Resistivity (R_{wa}) logs which are then used for both the fluid flow zones and the Gassmann fluid substitution method.

Table 4.5: Table showing the output electrical parameters logs:

Input Curves	Input Constants	Output Curves
Porosity Curve	Archie $a = 1$	Archie formation factor (FF)
Rt Curve	Archie $m = 2$	Formation Water Resistivity (R_{wa})
Rxo Curve	Archie $n = 2$	Flushed zone Water Resistivity (R_{mfa})
Temp Curve	$R_w = 0.16$	Water Saturation Archie (Sw_{Arch})
		Flushed zone water saturation archie (S_{xoArch})

4.4.2. Electrical Properties from core data:

4.4.2.1. Archie Equation:

The electrical resistivity log technique was developed by Archie in 1942 and is known as the Archie equation (Dandekar, Abhijit Y 2006). Archie's equation is mainly used to calculate the water saturation of clean, non-shale-bearing sandstone formations (Zhang and Xu 2016). His work can be used to calculate the conductivity of 100% water-bearing sandstones as well as those of partially saturated sandstones (Li, et al. 2021).

4.4.2.2. Formation Factor:

The formation factor (F) which is the most fundamental electrical rock property, is defined as the ratio of the resistivity of a 100% brine-saturated rock (Ro) to the resistivity of the saturating brine (Rw) and this can be expressed as (Li, et al. 2021):

$$F = \frac{R_o}{R_w} \quad (4.19)$$

4.4.2.3. Tortuosity:

There is also a strong correlation between formation factor and porosity when it is plotted on a double logarithmic coordinate. For this reason, Archie developed an equation that shows the relationship between formation factor, porosity, and tortuosity (Dandekar, Abhijit Y 2006);

$$F = \frac{\tau}{\Phi} \quad (4.20)$$

Where τ is the tortuosity is defined as $(La/L)^2$, La is the effective path length through pores and L is the length of the core.

4.4.2.4. Cementation Factor:

The relationship between formation factor, porosity and tortuosity can also be expressed (Boukadi, et al. 1998, Dandekar, Abhijit Y 2006, Li, et al. 2021);

$$F = \frac{R_o}{R_w} = \frac{a}{\Phi^m} \quad (4.21)$$

where a is related to tortuosity, and m is commonly known as the cementation factor (Li, et al. 2021, Boukadi, et al. 1998).

4.4.2.5. Resistivity Factor:

Through experimental procedures, the ratio of the true resistivity of partially saturated rocks (Rt) to that of a 100% saturated rock (Ro) can be expressed as the resistivity factor (I) (Dandekar, Abhijit Y 2006, Li, et al. 2021). The resistivity factor has a correlation with water saturation (Sw) and this can be expressed (Li, et al. 2021);

$$I = \frac{R_t}{R_o} = S_w^{-n} \quad (4.22)$$

where n is known as the saturation exponent.

With an integration approach of the above equations (3) and (4), Archie's final equation is expressed as;

$$S_w = \sqrt[n]{\frac{a R_w}{\Phi^m R_t}} \quad (4.23)$$

Table 4.6: Table showing the variables and units used for electrical properties

Formation factor	F	Dimensionless
Resistivity of 100% Brine saturated rock	R_o	Ωm
Resistivity of saturating brine	R_w	Ωm
Resistivity of partially saturated rock	R_t	Ωm
Porosity	Φ	decimal
Tortuosity	T or a	1
Cementation Factor	m	Close to 2 for sandstone
Saturation Exponent	n	2
Resistivity factor	I_r	$I > 1$ (partially saturated) $I = 1$ (100% saturated)
Water saturation	S_w	

The values of R_w , R_o , and R_t as well as their associated temperatures and weights are recorded and used as input parameters to an Excel sheet to calculate the formation factor, tortuosity, cementation factor, resistivity index and Archie saturation exponent. Archie's equation can be used to adjust and calibrate wireline logs used for drilling (VINCI-Technologies 2022).

The instrument that is used to calculate the resistivity at different water-saturated levels under different ambient conditions is known as EPS A. It is made of four electrodes which are connected to a platen. The platen is connected to the sides of the core plugs to minimize any resistance artefacts.

A plastic box is used to cover the core holder from an external environment to minimize any effects of the saturation of the core plugs. (VINCI-Technologies 2022)



Figure 4.3: Configuration of the EPS-A instrument used to record the resistivities of saturated core plugs.

4.5. Hydraulic Flow Units:

The concept of Hydraulic Flow Units (HFU) was first proposed from the Kozeny-Carmen equation of the capillary tube model for rock pore spaces which calculates the average hydraulic radius through the reservoir quality index (RQI) (Opuwari, et al. 2022). It is a dependable method that has been widely used to predict permeability in uncored wells and intervals, as well as for categorizing rock types (Hussien 2014). According to (Ebanks, Scheihing and Atkinson 1993), hydraulic flow units represent total reservoir rock volume where the rock properties that regulate the fluid flow are constant and distinctly different from other rock properties.

Typically, the formation of hydraulic flow units is the result of the environment, deposition, and diagenetic processes. These can be observed as zones within a reservoir where the hydrocarbon flow remains constant (Hussien 2014).

4.5.1. Calculation of Hydraulic Flow Units with Rock Quality Index:

The determination of hydraulic flow units within the cored intervals is calculated using the permeability-to-porosity ratio method which was first proposed by (Amaufule, et al. 1993). Porosity and permeability are the key parameters that allow fluid to flow within a reservoir. Porosity controls the hydrocarbon storage, while permeability influences the flow capacity (Hussien 2014). The permeability/porosity ratio method has been used to anticipate flow units by identifying three

petrophysical parameters, namely, the reservoir quality index (RQI), pore-grain volume ratio (Phiz), and flow zone indicator (FZI) (Opuwari, et al. 2022). These parameters are calculated as follows:

$$\text{Rock quality index (RQI)} = 0.0314\sqrt{K/\Phi} \quad (4.24)$$

$$\text{Pore - grain volume (Phiz)} = \Phi/(1 - \Phi) \quad (4.25)$$

$$\text{Flow zone indicator (FZI)} = RQI/\text{Phiz} \quad (4.26)$$

Where, K = Permeability

Φ = Porosity

The fluid zone indicator (FZI) can be determined through a log-log plot of RQI vs Phiz. This plot can be used to identify the different flow boundaries as similar FZI values would plot on a straight line. Therefore, we select hydraulic flow units according to the position of clustered points on the RQI vs Phiz plot. This procedure is applied to all three wells.

4.5.2. Calculation of Hydraulic flow units with Winland R35 method:

In 1972, Winland established a relationship between pore-throat size, porosity, and permeability within sandstone reservoirs through analysis performed on sandstone samples (Opuwari and Dominick 2021). By utilizing the Winland r35 method, the determination of pore throat radius (r_{35}) which corresponds with mercury at the 35th percentile (um) can be determined using different data sources such as well logs and core data that contain information on porosity and permeability (Opuwari, et al. 2022). Winland observed that large pores were connected to large crystals, while small pores were connected to small crystals. Hence, if the pore system between the crystals is filled with intergranular and solution pore, the smallest pore system controls the outflow and inflow into larger pores (Opuwari, et al. 2022). Winland's equation, which relates to pore sizes, porosity, and permeability is as follows:

$$WinR35 = Log (0.732) + 0.588 Log(K) - 0.864 Log(\Phi) \quad (4.27)$$

Where, WinR35 = pore throat radius (um)

K = Permeability (mD)

$$\Phi = \text{Porosity (\%)}$$

4.6. Rock Physics Calculations:

Rock physics is a multidisciplinary area of study that combines principles from geophysics, geology, and rock mechanics to investigate and comprehend the physical characteristics of rocks. This scientific field examines the connections between various rock properties, such as mineral composition, permeability, porosity, and elastic moduli. The primary objective of rock physics is to establish quantitative correlations between these properties and seismic or other geophysical observations to anticipate and interpret underground formations (Avseth and Bjørlykke 2010).

The study of rock physics entails conducting laboratory experiments on rock samples to measure their physical and mechanical attributes, which include bulk density, acoustic velocity, shear strength, and electrical resistivity. However, for this research, these measurements could not be computed and therefore they are calculated from wireline logging. The calculated measurements are utilized to develop computerized models that can aid in predicting and interpreting rock properties in real-world situations. In this research, the main goal is to employ rock physics to create geological computerized models which can investigate the behaviour of rocks and fluids under different geological conditions.

In this section of this project, rock physics will be implemented to develop a model that shows the behaviour of different fluids within the selected reservoirs from wells E-AR1, E-AR2, and E-BT1. With the use of the previously identified petrophysical parameters, we will now determine the rock physics parameters to further evaluate the reservoirs and generate subsurface models. The models that will be used for rock physics are (1) the Greenberg-Castagna Model, (2) Density Estimation Models, (3) the Gassmann Fluid Substitution Model, and (4) Elastic Impedance.

4.6.1. Greenberg-Castagna Model:

The Greenberg-Castagna empirical model is used to convert the compressional sonic log (DT) to a shear sonic log (DTS) in brine-saturated multi-mineral rocks (Johari and Niri 2020). The shear sonic log is generated as it is needed for the Gassmann Fluid Substitution method. The DTS output curve is generated using the Voit-Reuss-Hill technique. Initially, velocities for predetermined minerals are computed. Furthermore, a weighted arithmetic and weighted harmonic of the generated volume of minerals are equated to create the shear sonic log (ILE 2013).

The equation used to generate the shear sonic velocity is as follows:

$$V_s = \frac{1}{2} \left\{ \left(\sum_{i=1}^4 X_i * V_{si} \right) + \left(\sum_{i=1}^4 \frac{X_i}{V_{si}} \right)^{-1} \right\} \quad (4.28)$$

Where: DTS = Vs = shear velocity (DTS = Vs)

X_i = volume of ith mineral

V_{si} = shear velocity of ith mineral

Furthermore, the quality control of the generated shear sonic log (DTS) can also be done with the Greenberg-Castagna empirical method. This is done to investigate whether the recorded shear sonic curve is an acceptable shear curve and not a mud wave curve that is generated by improper processing of sonic logs. This can be computed by inputting both compressional (DT) and shear sonic logs (DTS) to generate their equivalent compressional and shear velocity curves (V_p and V_s) as well as the V_p/V_s Ration, Poissons ratio (PoisRatio), Shear Modulus (Mu), Bulk Modulus (KB), and Young's Modulus (E).

From the generated curves with the Greenberg-Castagna model, we can interpret the relationship between the rock physics properties listed above through cross plots and log plots.

4.6.2. Density Estimation (ILE)

In the estimation of density, the previously generated shear sonic curve (DTS) can be used to generate a density curve. The sonic curve reflects the rock's tensile response when subjected to gas forces, not liquid forces. There are several writers who have shared algorithms for determining density from sonic transit time. Their models are made available in IP, and they are as follows:

4.6.2.1. Gardner Method (Gardner, Gardner and Gregory 1974):

$$\rho = a \times V_p^b \quad (4.29)$$

Output Curve = RhoGard (kg/m³)

4.6.2.2. AGIP Bellotti Method (Bellotti, Di Lorenzo and Giacca 1979):

$$\text{Consolidated formations: } \rho = 3.28 - DTS/89 \quad (4.30)$$

Output Curve = RhoAgip (kg/m³)

4.6.2.3. Lindseth Method (Lindseth 1979):

$$\rho = (V_p - 3460) / (0.308 \times V_p) \quad (4.31)$$

Output Curve = RhoLind (kg/m³)

Where; Rho = density

V_s = compressional velocity

DTS = compressional curve

a = Constant – 0.23 (default)

b = Constant – 0.25 (default)

4.6.3. Gassmann Fluid Substitution Model:

Gassmann Fluid Substitution method is the most used method for fluid substitution (Avseth and Bjørlykke 2010). Gassmann's method establishes a connection between the rock's saturated bulk modulus and its porosity, the bulk modulus of the frame of the porous rock, the bulk modulus of the mineral structure, and the bulk modulus of the fluids filling the pores (Magoba and Opuwari 2019). His method is based on substituting the type of pore fluids in reservoir intervals to study the elastic response caused by different fluid types (Avseth and Bjørlykke 2010, Magoba and Opuwari 2019).

Gassmann's method demonstrates that the variations in compressional velocity (V_p) and shear velocity (V_s) due to variations in fluid saturations can be determined through input parameters. During the substitution modeling, V_p, V_s, and bulk density are the main variables, while the values of K_o (matrix bulk modulus), K* (frame or dry rock modulus), porosity, and the rock shear modulus remain constant (Magoba and Opuwari 2019, Khan and Rehman 2018).

Gassmann's equation assumes that the mineral modulus is uniform, and the pore space is statistically isotropic but does not make any assumptions about the shape of the pores. However, this equation can only be applied at low frequencies where the pore pressures have reached equilibrium

throughout the pores (i.e., there is enough time for pore fluid to flow and cancel wave-induced pore-pressure gradients) (Abe, Edigbe and Lawrence 2018).

The Gassmann equation is most reliable for clean sandstones with high porosity and unreliable for shale-sands or carbonate rocks with low porosity. The parameters that are used for the formulation of the fluid substitution modelling were pre-determined from the wireline log data analysis presented in previous sections. The Gassmann equation can thus be presented as:

$$K_{sat} = K^* + \frac{\left(1 - \frac{K^*}{K_o}\right)^2}{\frac{\Phi}{K_{fluid}} + \frac{(1-\Phi)}{K_o} + \frac{K^*}{K_o^2}} \quad (4.32)$$

Where the input parameters for the fluid substitution modelling are:

Φ = porosity of the rock,

K_{fluid} = bulk modulus of pore fluids,

K_o = matrix bulk modulus,

K^* = bulk modulus of porous rock frame.

The Gassmann equation utilizes the properties of the rock frame to determine how replacing fluids affects seismic properties. To accurately model the new fluid, the initial fluid effect must be accounted for. The input data needed for this procedure, including water saturation, invaded zone water saturation, Vclay, and density were obtained from petrophysical analyses of the reservoirs. On the other hand, the Vp and Vs were determined by the Greenberg and Castagna (1992) method. Three fluid substitution models (brine, oil, and gas) were determined for pure sandstone and were employed to observe the behaviour of the different sandstone saturations.

The average Gassmann fluid and matrix properties were calculated from the input data and will be presented for each well. The fluid volumes were calculated with a Reuss harmonic average formula which is believed to yield more accurate results than the fluid mixing law. The Reuss harmonic formula is also helpful in minimizing the effect of flushed zone hydrocarbons on the sonic logs. Furthermore, the dry rock properties (Bulk modulus, Shear modulus, Poisson Ratio and Modulus Ratio) are determined and used for the fluid substitution cross plots. From these cross plots, the output curves such as the AI log are created and plotted for the reservoir interval.

4.7. Multi-mineral and Petrographic Studies:

4.7.1. Sedimentological Core Description:

Core description is a critical tool that helps us to gain a thorough understanding of the drilled subsurface using both qualitative and quantitative methods. By examining the described cores to wireline logs, allows us to establish the ground truth and calibrate the results. This technique allows us to measure various formation properties directly from the cores. Prior to conducting the core description, certain materials are needed to ensure optimal working conditions. These materials include:

- Ruler
- Grain size chart
- Measuring tape
- Camera
- Hand lens
- Cloth and water bottle
- Notebook
- Safety coat

To start the procedure of core description, the wireline logs were carefully analyzed to identify any major lithological breaks and select the core boxes required for the research. Once the core boxes were selected, they were laid out in an increasing depth sequence, with three to four core sections per well and around six to eight core boxes per section. The cores were first examined as a whole to identify the lithological changes, then individually to record parameters such as rock type, colour variations, grain size, sorting, texture, sedimentary features, and fossils. The main focus was on identifying the rock type, followed by colour and grain size using the grain size chart. The sedimentary structures were recorded where possible. The cores were often washed with water to enhance the clarity and accuracy of observations. The core samples were selected from these whole cores and were further analysed for to understand the paragraph of the rocks.

4.7.2. Thin Section Procedure:

The 24 thin sections that were used in this study were initially cut from the core samples collected from the different core sections at PASA. The thin sections were made by cutting a thin piece approximately one centimeter thick from the sample with the use of a diamond saw. The piece was then mounted to a glass and further reduced in thickness with the diamond saw. It was then further reduced in size using progressively finer abrasive grit until the sample was about $30\text{ }\mu\text{m}$ thick. The method involved using the Michel-Lévy interference colour chart. Typically, quartz is used as the gauge to determine the thickness as it is one of the most abundant minerals.

Once the desired thickness is achieved, a thin cover is placed on top of the piece to finalize the thin section. The thin sections were then examined using a petrographic microscope with a polarized light which can be seen in the figure below. The interaction between polarized light and the mineral grains was studied and provided information about the atomic arrangement of the grains. The images of the thin sections were taken with a camera which is equipped on top of the microscope. These images are sent to a computer for further analysis of the mineralogy present.

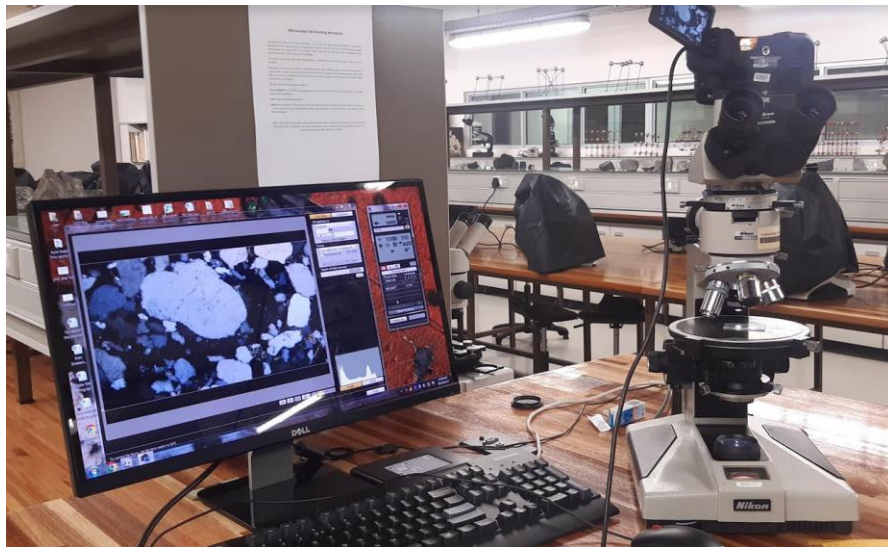


Figure 4.4: Petrographic microscope equipped with a digital camera.

4.7.3. X-ray Fluorescence:

X-ray fluorescence spectrometry (XRF) is defined as a phenomenon whereby fluorescent X-rays are emitted from a material that has been bombarded with gamma rays or X-rays. It is a non-destructive analytical technique that is used for chemical and elemental analysis within a sample (Anal.Methods 2019). At the moment, XRF is the most commonly used analytical method that determines the major and trace elements of rock samples. This technique is used in a variety of fields because it is fast, simple, and cost-effective and can be used to analyze a variety of elements (de Viguerie, Sole and Walter 2009). The main limitation of this technique is its inability to analyze elements lighter than Na (atomic number=11) (Rollinson 1993). However, it can analyze about 80 elements over a broad range of sensitivities, and it can detect concentrations from 100% down to several parts per million (Rollinson 1993).

Portable XRF procedure:

1. During XRF analysis, a sample is bombarded with polychromatic radiation from an X-ray tube within the PXRF (Figure 4.6) (Rudolf 2012).
2. When the sample is excited with gamma rays or x-rays, it becomes ionized. If the amount of radiation energy is enough to remove an inner electron, the atom becomes unstable.
3. Stability within the atom is retained when an outer electron from a higher energy replaces the inner electron (Thermo Fisher Scientific 2023).
4. During this process the element in the sample becomes excited and emits its own unique secondary radiation energy (Rudolf 2012). The secondary radiation that is emitted from the sample has a lower energy than the initial incidence radiation, and it is called fluorescence radiation. These fluorescence radiations are used to detect the amount and type of elements that occur within the sample (Thermo Fisher Scientific 2023).

The data recorded by the PXRF instrument is transferred via a portable USB drive to a data acquisition computer for further analysis. The elemental concentration is recorded in the form of an Excel sheet. The data is then converted into graphs for a visual representation of the elemental composition within the samples.

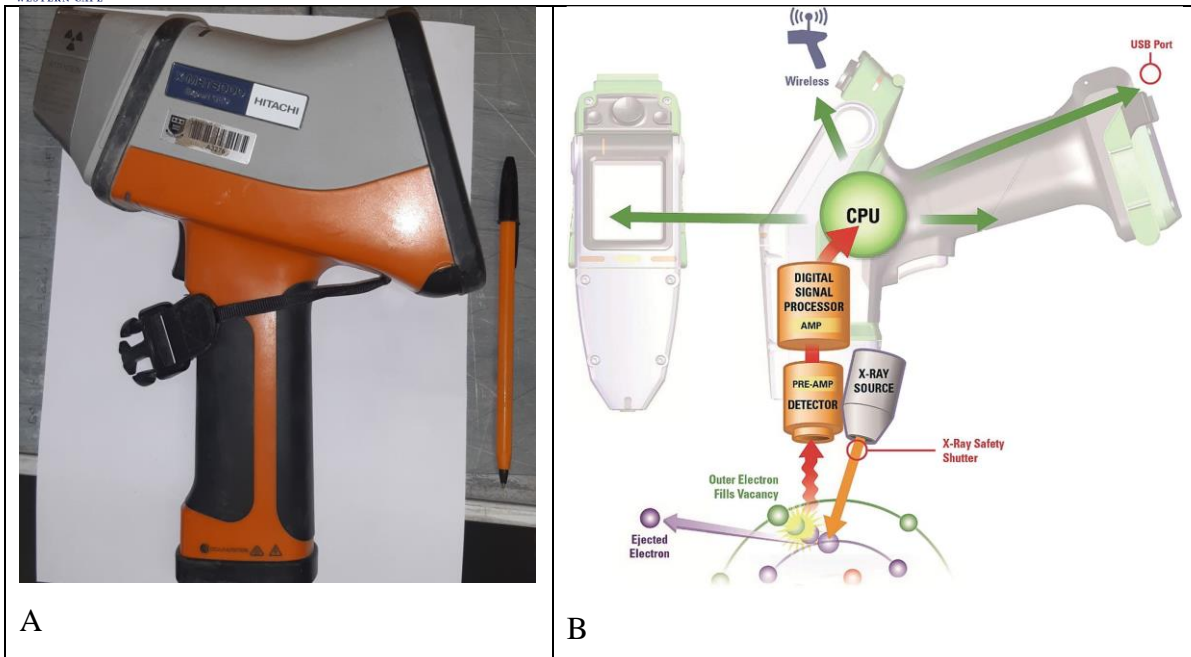


Figure 4.5: Representation showing the configuration of the portable XRF analyzer used in this research along with a schematic diagram showing the components (revised from (Thermo Fisher Scientific 2023)).

Chapter 5: Well Log Interpretation

This chapter is focused on evaluating the rock and fluid properties of each well using the available well log data. The petrophysical properties that will be determined include lithology, volume of clay, permeability, porosity, and water saturation. The logs that will be used for this analysis are caliper, bit size, spontaneous potential, gamma ray, resistivity, sonic, neutron, and density logs.

The results from petrophysics are integrated with rock physics to better understand the rock and fluid properties within the reservoir intervals. The rock physics analysis will be discussed in the following section, and it involves the creation of both shear sonic and compressional logs which are used to create an elastic impedance log through the Gassmann fluid substitution method. The generation of well logs, cross plots, and histograms as well as the calculations of both petrophysics and rock physics parameters were done on Interactive Petrophysics software.

The core data which was obtained from core laboratory experiments and PASA reports were used to calibrate the petrophysical models to get the most reliable values. The core laboratory data performed on core plugs includes porosity, permeability, water saturation, and grain density.

The limitations that exist within this study are because well E-AR1 and E-AR2 don't have all the necessary data. This means that some of the petrophysical and rock physics parameters cannot be computed due to missing data. These parameters are water saturation, permeability, sonic shear, and compressional and elastic impedance logs. Therefore, well E-BT1 are viewed as the main well and is being used for interpretations as there are few limitations for this well.

5.1. Petrophysical Analysis:

5.1.1. Lithology Identification:

The lithology of the reservoir intervals for the three wells is interpreted using the following logs: calliper (CAL), bit size (BS), gamma ray (GR), spontaneous potential (SP) and volume of clay (Vcl). These well logs will be able to give an idea of the lithology, grain size, permeability, depth, and thickness of the reservoir interval.

Calliper log readings relative to bit size can give an indication of the type of lithology that's present. The three scenarios that exist with this relationship are:

1. Caliper = Bit Size: Hard, inert rock (hole in gauge)
2. Caliper > Bit Size: Soft or brittle rocks (shales) which are indicated as a washout.
3. Caliper < Bit Size: Permeable rock (sandstone), indicated as a mud cake build-up.

Gamma-ray logs measure the amount of natural radiation from a formation. On a gamma ray log the shale formations would give a high GR reading (high radiation), whereas the sandstone formations would give a low GR reading (low radiation). The spontaneous potential measures the potential difference between voltage in the wellbore as a fraction of depth and an electrode on the surface. Low SP readings indicate shale, whereas high SP readings indicate permeable sandstones. Both these logs would deflect to the left to indicate sandstone and to the right to indicate shale. The GR and SP logs can also be used to analyse the grain size as well as the depositional environment.

The log that contains the volume of clay has been generated from the GR log to indicate the amount of clay material within the formation. Grain Density core data which is limited to well E-BT1 are used to show the average density of the formation.

5.1.1.1. Lithological Identification of Well E-BT1:

According to tracts 2 and 4, the sandstone reservoir interval that exists between horizons 14ATS, and 14ABS has a thickness of 32m (figure 5.1). Above and below these horizons, the reservoir seal that is encountered indicates argillaceous lithologies. Based on analysis done on the Gr and SP logs in track 4, it is interpreted that the reservoir interval occurring between 2384-2416m is made of good-quality submarine fan sandstones. In track 4, above the OWC the sandstones have about four sandstone fining-upward cycles. There are also some claystone interbeds within the reservoir, but these have little to no effect on the permeability of the reservoir as later discussed. According to track 4, the sands are interpreted to be fine to coarse-grained channel-fill sandstones that exist within a proximal submarine fan environment.

Track 5, which indicates the volume of clay is included in this lithological description as it indicates where there may be high or low values of clay. The volume of clay in the reservoir interval is calculated from the mean value of the VCLGR histogram below to be about 25.14%, thus indicating that only a quarter of the lithology is clay material. This indicates that the reservoir interval of well E-BT1 is made of good reservoir sandstones. The average bulk density of the reservoir interval shown in track 6 is around 2.65 which indicates a good sandstone interval.

Scale : 1 : 500

Well E-BT1

2371M - 2430M

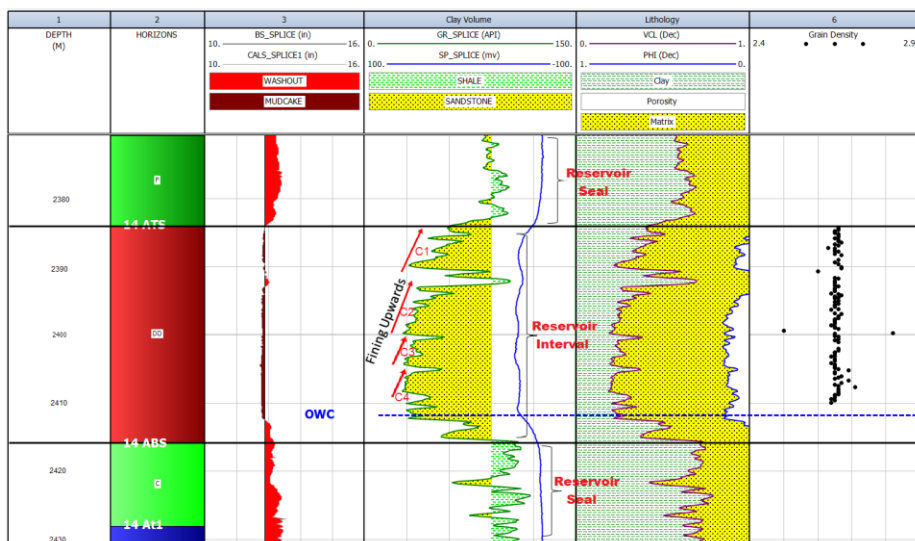


Figure 5.1: Lithological log plot of well E-BT1

5.1.1.2. Lithological Identification of Well E-AR1:

According to tracts 2 and 4, the sandstone reservoir interval that exists between horizons EQIII and EQII has a thickness of 31m (figure 5.2). Above horizon EQIII appears to be argillaceous lithologies which prograde into a coarser sandstone, thus representing a progradational sequence. Below horizon EQII are some argillaceous sequences of claystone and siltstone which are occasionally interbedded with turbidite sandstones.

The analysis of the GR and SP logs in track 4 suggests that the reservoir interval between 2454-2485m is composed of mass-flow sandstones. This can also be seen on the GR log by the irregular bedding patterns and sharp contacts that exist. These sandstones within the reservoir are coarse and poorly sorted due to turbulent flow and therefore they are known as mass flow sandstones which are good for hydrocarbon reservoirs.

Track 5 which indicates the volume of clay along with the VCLGR histogram below indicates that the volume of clay is about 23.26% over the reservoir interval, thus indicating that less than a quarter of the lithology is clay material. This indicates that the reservoir interval of well E-BT1 is made of good-quality sandstones for hydrocarbon reservoirs.

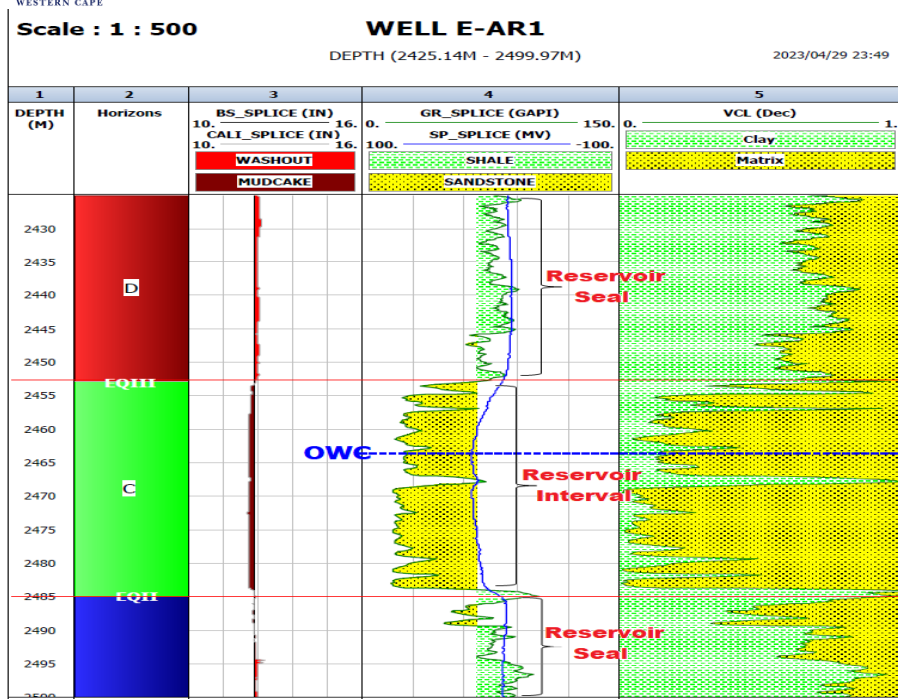


Figure 5.2: Lithological log plot of well E-AR1.

5.1.1.3. Lithological Identification of Well E-AR2:

The thickness of the sandstone reservoir interval between horizons T14AS and B14AS is 32m, as shown in tracts 2 and 4 in Figure 5.3 below. Argillaceous lithologies are present above T14AS, and claystone and siltstone suggest the existence of argillaceous sequences between B14AS and 14At1. Tract 5 also suggests that there is apparent shale with a high clay content below horizon 14At1.

Analysis of the Gr and SP logs suggests that the reservoir interval occurring between 2445-2477m is made of mass-flow sandstones, which corresponds with reservoir sandstones of well E-AR1. This is also seen in track 4 by the irregular bedding patterns and sharp contacts. These sandstones found in the reservoir are classified as mass-flow sandstones due to their fine to coarse grain size. They are considered suitable for hydrocarbon reservoirs.

The VCLGR histogram below (figure 5.5), indicates that the volume of clay is about 17.33% over the reservoir interval, this indicates a lesser clay content over the reservoir than in the other wells. This also indicates that the reservoir interval is good for hydrocarbon exploration.

Tracks 3, 5 and 6 are included in these wells to support the interpretation of the Gamma-ray log. The caliper and bit size logs in track 3 are used to support the lithological description made from track 4. If the caliper and bit size logs have an inconsistent relationship, it will show either mud cake (maroon) representing sandstone intervals or washout (red) representing shale intervals. It can be inferred from the comparison of tracks 3 and 4 that the lithology in track 4 is adequately supported in track 3.

Scale : 1 : 500

Well E-AR2

DEPTH (2435M - 2493M)

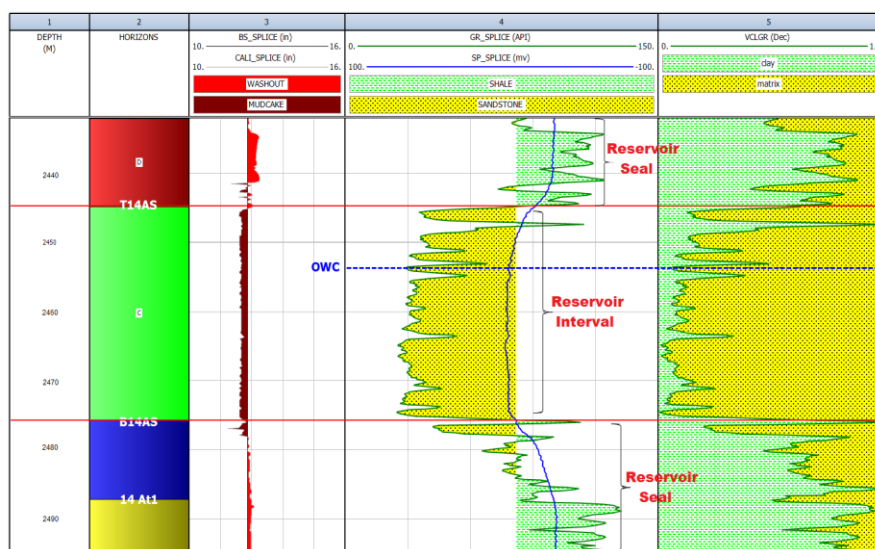


Figure 5.3: Lithological log plot of well E-AR2.

5.1.2. Volume of Clay:

The clay volume was determined by analyzing the gamma-ray log in this study (figure 5.4). The use of neutron and density logs can be considered to determine the clay volume as well, but in this research, the gamma-ray log was used. The gamma-ray log measures the radiation intensity emitted by radioactive elements present in the formation. The amount of clay radiation is influenced by the saturation of radioactive elements, namely potassium, uranium, and thorium within the reservoir interval. The relationship can be either linear or non-linear between the clay content and the measure of gamma-ray emissions.

The following formulas have been used to determine the relation between the gamma ray index and clay content:

$$V_{cl} = I_{GR}$$

$$\text{Gamma ray index (I}_{GR}\text{): } I_{GR} = \frac{GR_{log10} - GR_{clean}}{GR_{clay} - GR_{clean}} \quad (5.1)$$

I_{GR} = linear response to clay content

GR_{log} = log reading at depth of interest

GR_{clean} = GR value nearby clean zone

GR_{clay} = GR value near shale section

Non-linear methods of estimating Gamma Ray and clay volume relationship.

$$\text{Steiber: } V_{cl} = I_{GR} / 3.0 - 2.0 * I_{GR} \quad (5.2)$$

$$\text{Clavier: } V_{cl} = 1.7 * [3.38 * (I_{GR} + 0.7)^2]^{0.5} \quad (5.3)$$

$$\text{Larionov (Tertiary rocks): } V_{cl} = 0.083 * (23.7 * I_{GR} - 1) \quad (5.4)$$

$$\text{Larionov (older rocks): } V_{cl} = 0.33 * (22 * I_{GR}) - 1.0 \quad (5.5)$$

5.1.2.1. Volume of Clay for wells E-BT1, E-AR1 and E-AR2:

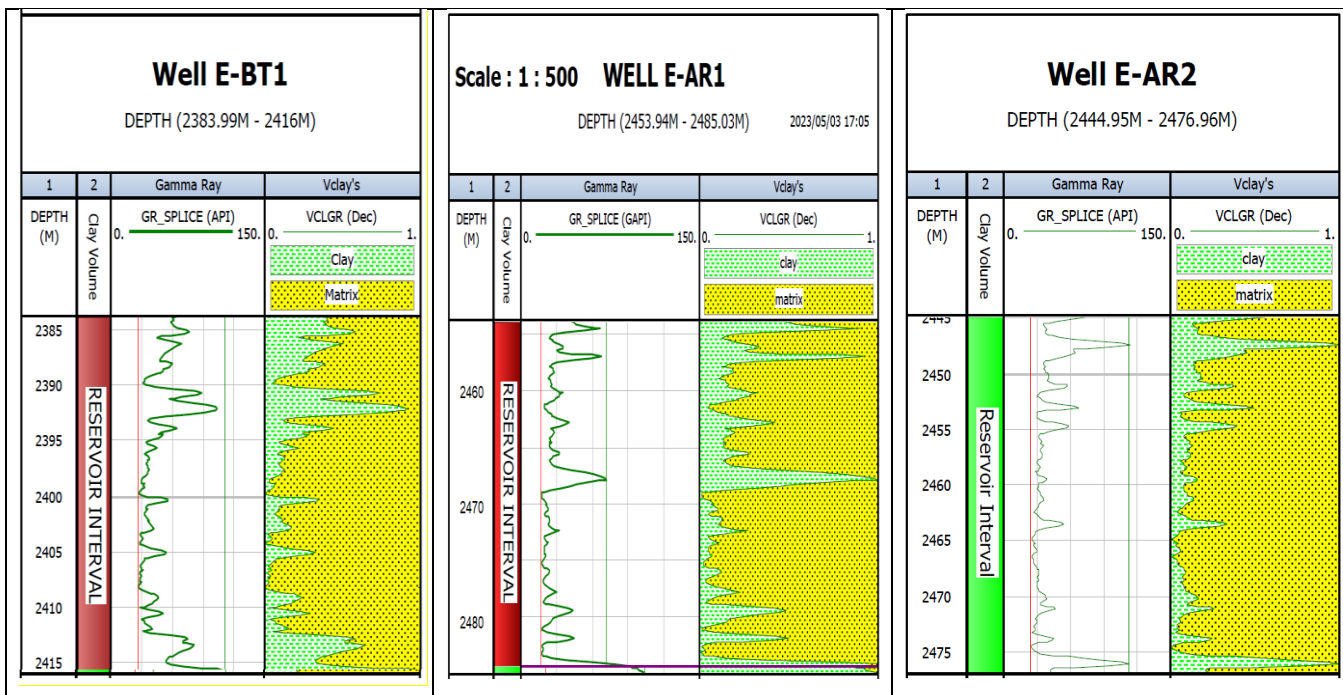


Figure 5.4: Log plot showing the volume of clay for all three wells.

Table 5.1: GR clean, GR clay and the amount of clay content for the reservoir intervals of wells E-BT1, E-AR 1 and E-AR2

Well	GRclean (minimum)	GRclay (maximum)	Average clay volume (%)
E-BT1	27	111	25.14%
E-AR1	17	75	23.26%
E-AR2	24	112	17.33%

The GRclean and GRclay were calculated on the IP software using the minimum (red) and maximum (green) line indicators on the Gamma Ray Histograms of the wells. The software uses the minimum and maximum values of radiation to determine the clay volume in the reservoir interval. The maximum value indicates the GRclay where the radiation is greatest, whereas the minimum value indicates the GRclean value where the radiation is at its lowest. Using these values of the GR log, we can compute the values of the amount of clay content within an interval.

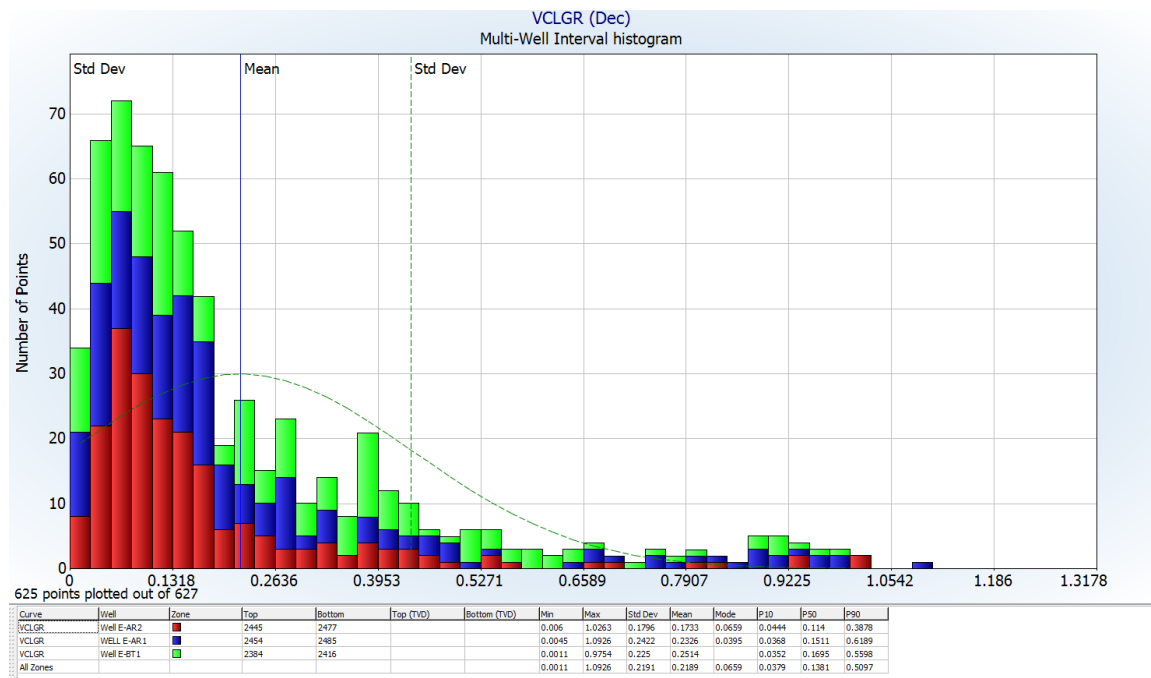


Figure 5.5: Multi-well histogram showing the volume of clay for all wells.

The multi-well histogram displays the clay volume across the reservoir intervals of the three wells (figure 5.5). The distribution of the clay volume across the three wells has a pronounced positive skew, with all three wells showing a combined average clay volume of 0.2189. This indicates that the reservoir intervals of the three wells can be considered good sandstone reservoirs as they do not contain large volumes of clay.

Understanding the distribution of clay volume is important as it can also affect the success of the drilling programme. If there is too much clay present in the well, it can lead to heaving shales which may cause pressure build-up that can lead to the borehole walls being squeezed together.

5.1.3. Fluid Identification:

Reservoir Analysis is an important part of the oil and gas industry as it enhances the ability to properly evaluate reservoirs and understand the behaviour of hydrocarbons stored within them. To date, there are several methods that can be used to identify fluids within reservoirs, with well logs being the most preferred method (Dandekar, Abhijit Y 2006).

This section uses resistivity logs, saturation core data and RFT Graphs to identify the fluid contacts and quantity of fluids that are present within the reservoir intervals. The resistivity logs are mainly used to identify where there are contacts between different fluids. When the deep resistivity log (ILD, LLD) is separated from the medium resistivity log (MSFL), it indicates the presence of hydrocarbons. When these two logs are close together, it indicates that the formation fluid is equal to the drilling fluid that is used (Darling 2005). This means that resistivity increases in the same type of rock when there is the presence of hydrocarbons and decreases when there is formation water present (Tiab and Donaldson 2012).

On the other hand, saturation core data can be used to identify the amount of fluid (oil, gas, water) that is found within the pore spaces of the formation rock (Tiab and Donaldson 2012). In all three wells, the gas saturation is higher than oil because it migrates much more easily through the rock. This means that gas fills up larger spaces in the rocks. Gas is also less dense than oil, therefore it naturally rises to the top section of the reservoir, displacing oil. This indicates that in an oil zone, the saturation of gas (S_g) is higher than the saturation of oil (S_o) (Wheaton 2016).

5.1.3.1. Fluid Identification of Well E-BT1:

The wireline logs shown below use gamma ray, resistivity, porosity, and saturation logs to indicate the presence of an oil-water contact within the reservoir interval at a depth of 2411.8m (figure 5.6). This can be confirmed by examining track 3, where there is a separation between the deep and medium resistivity logs between 2384-2411.8m, thus representing an oil zone with a thickness of 27.8m. When these resistivity logs are close together, it indicates the presence of drilling fluid (brine water). The nature of fluids in the oil column can be seen in track 4, which shows that oil accounts for roughly 18%, water for 45% and gas for 36% of the column. Despite gas being predominant, the zone is defined as an oil zone because gas travels at a faster rate and is less dense than oil. From 2411.8-2416m, the logs illustrate that the reservoir is composed of water. The shale layer at a depth of 2392m doesn't affect the fluid within the oil zone as seen from the saturation logs.

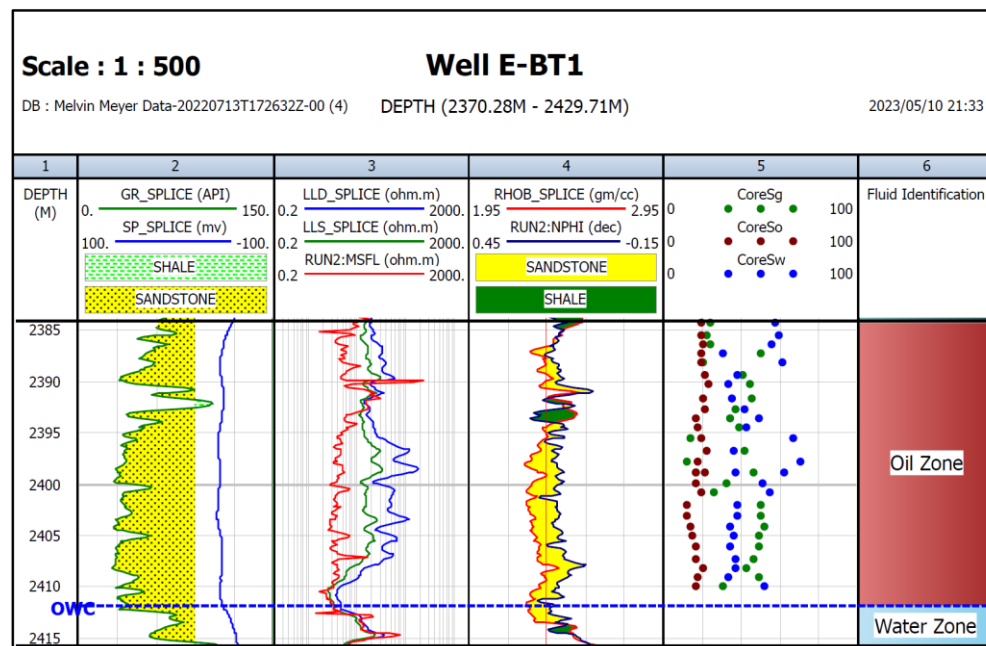


Figure 5.6: Log plot showing the fluid identification of well E-BT1.

5.1.3.2. Fluid Identification of Well E-AR1:

According to the wireline logs below (figure 5.7), we can see that there's a contact between oil and water within the reservoir interval at 2462m. This contact can be identified using track 3 where there is a separation between the deep and medium resistivity logs in the interval from 2454-2462m, thus representing an oil zone with a thickness of 8m. When these resistivity logs are closer together, they represent that drilling fluid is present which in this case is brine water. This indicates that there is a

contact between oil and water at a depth of 2462 m. The types of fluids present within the 8m oil column can be seen in track 4 (core saturation values). The reason this zone is classified as an oil zone and not a gas zone despite gas being higher is because gas migrates more quickly and is less dense than the oil. From 2462-2485 we can see that the reservoir has about 95% water present which corresponds with the deep and medium resistivity logs being closely spaced together.

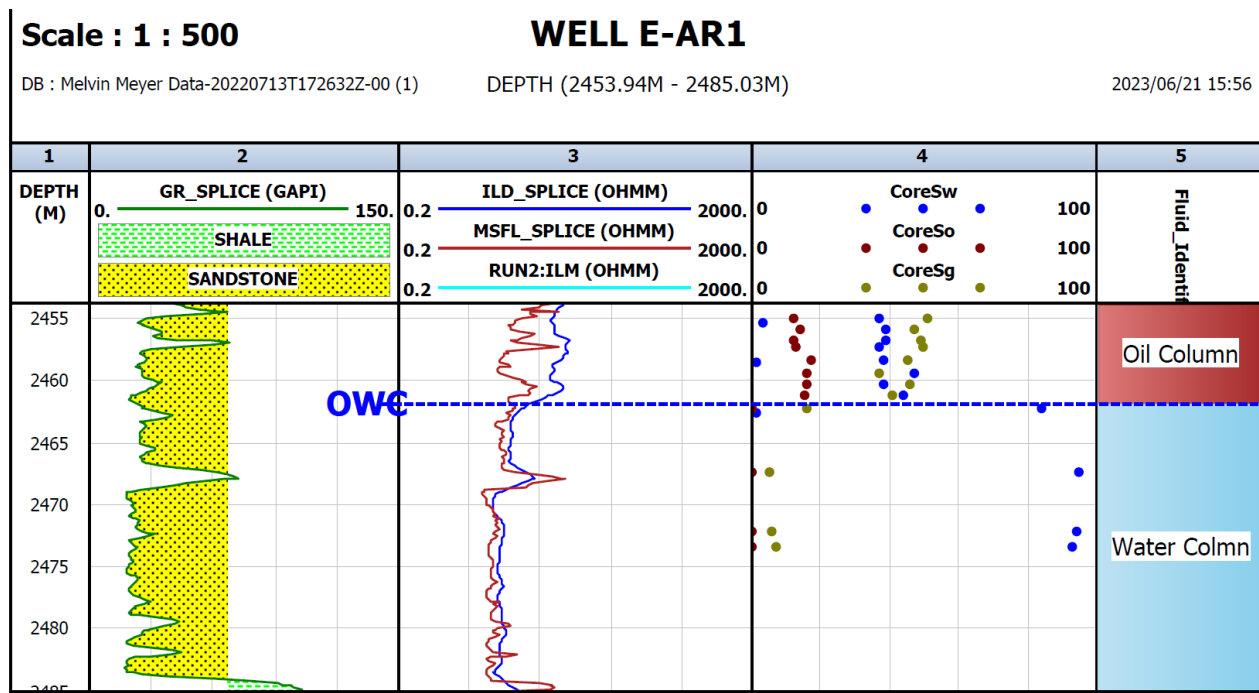


Figure 5.7: Log plot showing the fluid identification of well E-AR1.

5.1.3.3. Fluid Identification of Well E-AR2:

The wireline log below shows that at a depth of 2451.0m, there is proof of the existence of an oil-water contact within the reservoir (figure 5.8). This can be confirmed by track 3, where there is a separation between the deep and medium resistivity logs at an interval of 2445-2451.0m, thus indicating the presence of an oil zone with a thickness of 6m. When these resistivity logs are close together, it indicates that the drilling fluid is present (brine). Track 4, which shows core saturation values, reveals that the 6m oil column is made up of oil, water, and gas. From 2451-2477m, the logs indicate that the reservoir is largely composed of water, which can be confirmed by the close-spaced deep and medium resistivity logs.

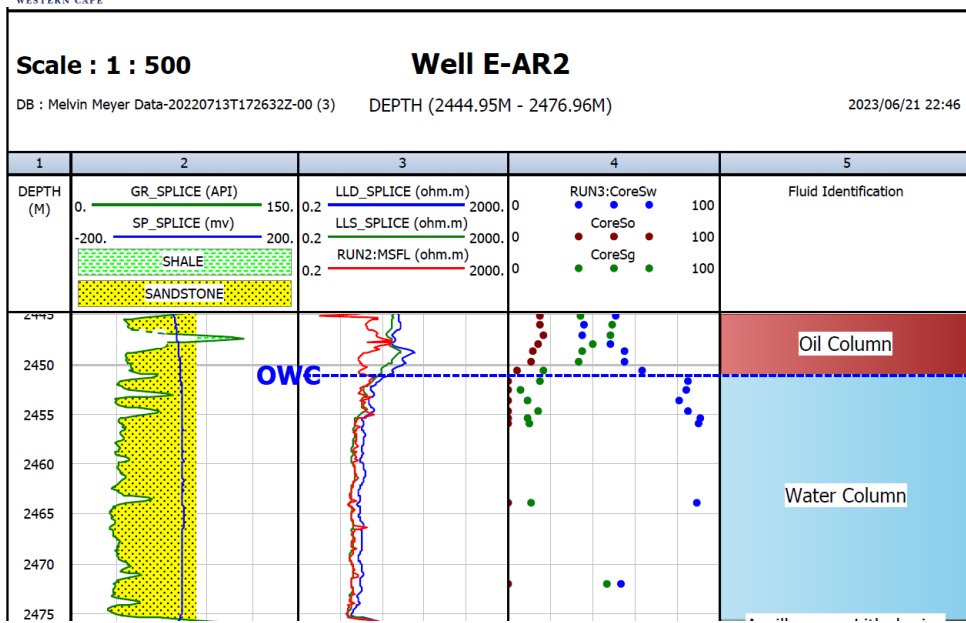


Figure 5.8: Log plot showing the fluid identification of well E-AR2.

5.1.4. Repeat formation testing for fluid identification:

The Repeat Formation Test (RFT) is a method that can be used to identify hydrocarbon contacts. The RFT test represents the relationship between formation pressure and depth. The formation pressure is mainly dependent on the density of the formation rocks and fluids contained within them (Parker 2014). In a normal hydrostatic pressure regime, the pressure would increase as depth increases. Table 5.2 below indicates the gradient ranges for density and pressure for hydrocarbons. The pressure gradients were converted to fluid densities using the following relationship:

$$1 \text{ psi/m (pressure gradient)} = 0.7034 \text{ g/cc (fluid density)}$$

Table 5.2: Formation Pressure and Density gradients for hydrocarbons (modified according to (Parker 2014)).

Fluid	Normal Density range (g/cc)	Gradient range (psi/m)
Gas (Gaseous phase)	0.007 – 0.30	0.01 – 0.43
Gas (Liquid phase)	0.20 – 0.40	0.28 – 0.57
Oil	0.40 – 1.12	0.57 – 1.60
Water	0.98 – 1.15	1.40 – 1.64

The formation pressure data were obtained from PASA reports for wells E-BT1, E-AR1, and E-AR2 to establish fluid pressure gradients within the reservoir sandstones. The visual representation of the results of the Repeat Formation Test is shown in Figures 5.9, 5.10, and 5.11. The interpretation of the data is used in the formation pressure vs. depth plot. The plot is used to visualize both the water and oil gradients for each well.

Whenever there are deflections present within the line data, it represents a different fluid line. The data from the table 5.3 has been calculated from the water and oil gradients from the PASA Reports for all three wells. All three wells indicate the presence of both water and oil, with oil accumulating on top as its density is less than water.

5.1.4.1. RFT fluid identification for all wells:

From the graphs below we can see that all three wells indicate the presence of both water and oil, with oil accumulating at a shallower depth due to smaller densities. The blue lines indicate water, whereas the red line indicates the deflected oil line. The water gradients for E-BT1 and E-AR2 are similar at 1.41psi/m thus representing a similar pressure regime for the water line. The oil gradients are different with E-BT1 having a slightly higher gradient of 0.95 psi/m in comparison with E-AR2 with 0.93 psi/m at their respective depths. On the other hand, the water line for well E-AR1 is different from E-BT1 and E-AR2, with a water gradient of 1.40 psi/m. The oil gradient for well E-AR1 is 0.81 psi/m which is much lower than the other two wells, this implies that the oil of the other two wells has a heavier API gravity than well E-AR1.

Table 5.3: Repeat Formation Testing results of wells E-BT1, E-AR1, and E-AR2.

E-BT1		E-AR1		E-AR2	
Depth (m)	Pressure (psi)	Depth (m)	Pressure (psi)	Depth (m)	Pressure (psi)
2380.8	3436.3	2387	3453.1	2374	3436.3
2383.3	2453.1	2407	3480.4	2394	3464.5
2400.8	3464.5	2427	3508.6	2414	3492.5
2412	3480.3	2447	3536.5	2434	3520.7
2420.8	3492.5	2451	3548.0	2436	3530.0

2440.8	3520.7	2462.1	3557.0	2451	3544.0
2460.8	3548.8	2467	3564.4	2454	3548.8
2480.8	3576.9	2487	3592.3	2474	3576.9
2500.8	3605.0	2507	3620.2	2494	3605.0
2520.8	3633.2	2527	3648.3	2514	3633.2
	E-BT1		E-AR1		E-AR2
Oil Gradient (psi/m)	0.95 psi/m	0.81 psi/m		0.93 psi/m	
Water Gradient (psi/m)	1.41psi/m	1.40 psi/m		1.41psi/m	

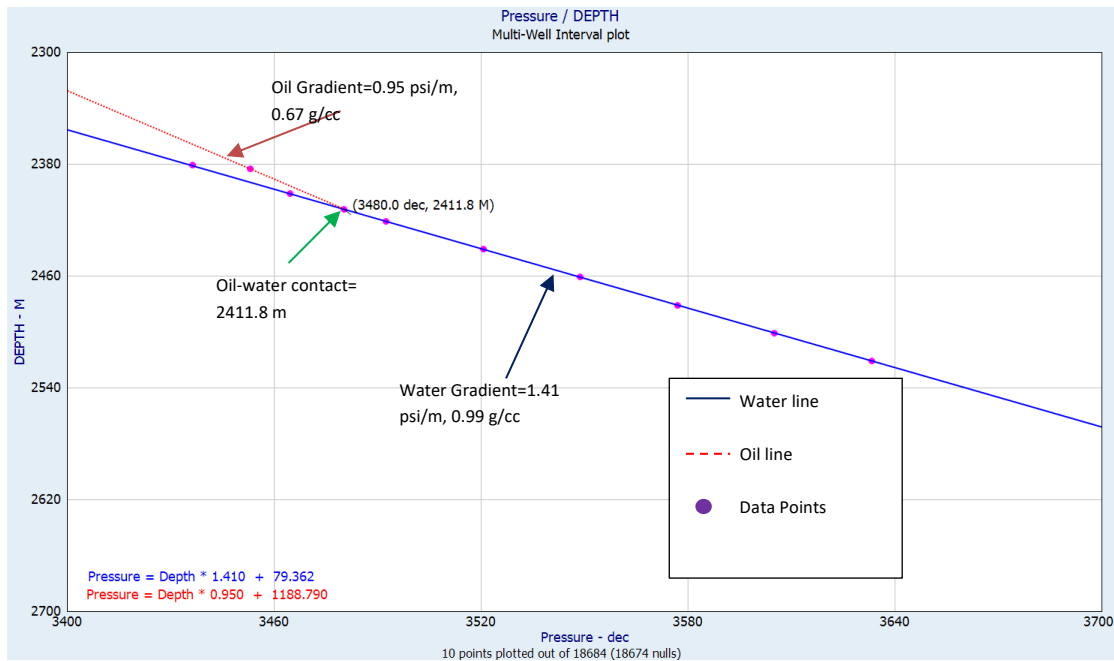


Figure 5.9: Formation pressure (psi) vs. Depth (m) of well E-BT1

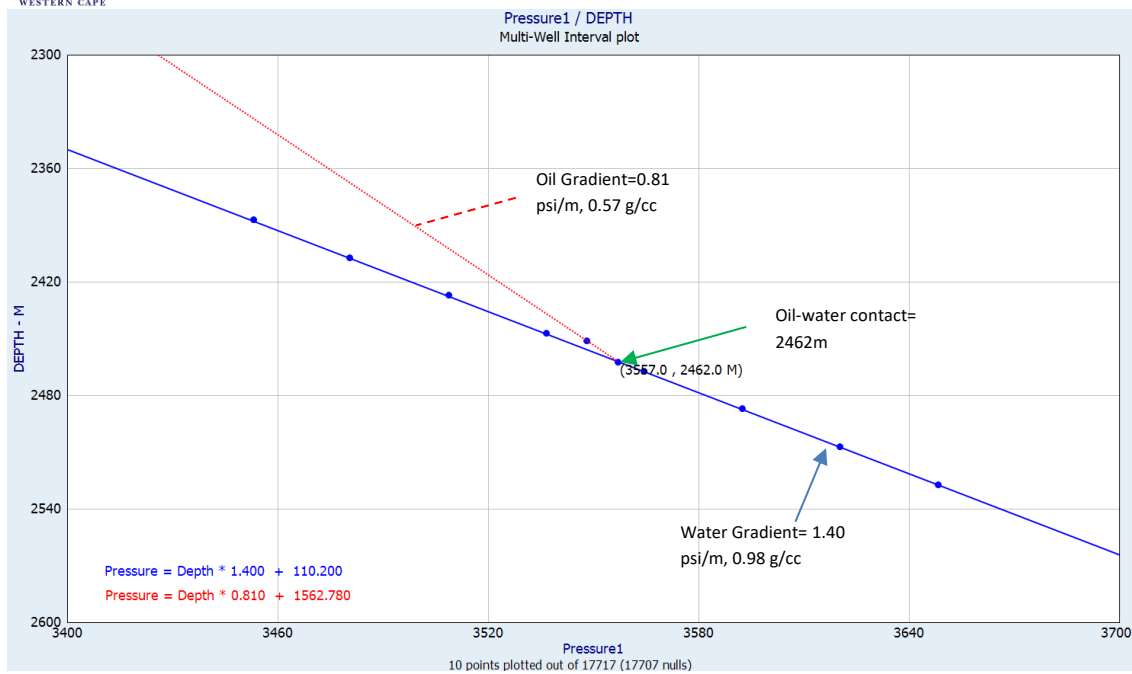


Figure 5.10: Pressure (psi) vs. Depth (m) of well E-AR1

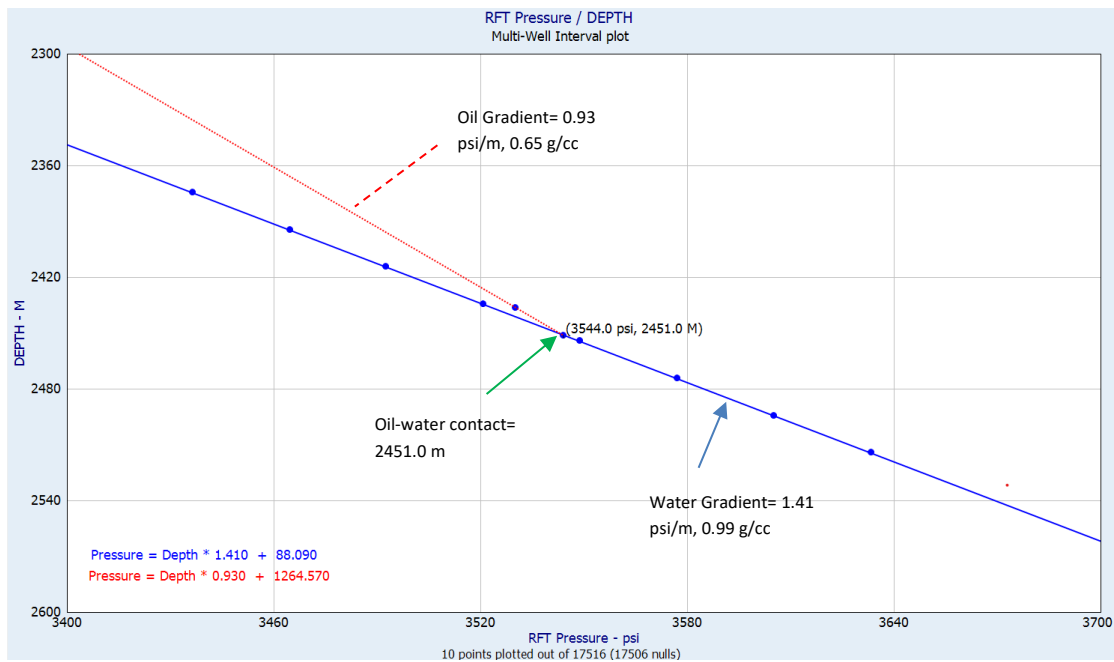


Figure 5.11: Pressure (psi) vs. Depth (m) of well E-AR2

5.1.5. Porosity and Permeability:

The porosities and permeability logs used are different over the three wells due to the availability of porosity logs (DT, SPHI and RHOB). They are also different as the porosity log that is most closely matched with their respective core porosity was used to calculate the porosity and permeability logs as in the case with well E-BT1. Both wells E-AR1 and E-AR2 are limited to only one porosity curve, with E-AR1 using a sonic curve (DT) and E-AR2 using the sonic neutron curve (SPHI).

The results of the average core porosities and permeabilities calculated over the entire reservoir intervals of the three wells are presented in the table below.

Table 5.4: Shows the core porosities (%) and permeabilities (mD) across the reservoir intervals of wells E-BT1, E-AR1 and E-AR2.

Well Name	Core Porosity (%)	Core Permeability (mD)
E-BT1	17.83	365.40
E-AR1	17.01	178.93
E-AR2	17.56	227.09

5.1.5.1. Porosity and Permeability of Well E-BT1:

For well E-BT1, the density log (RHOB) was used to calculate the porosity curve (Phi_Den) over the reservoir interval, which was then used to calculate the permeability curve (PermDen). The log below indicates that the oil zone has the highest porosity and permeability values. In contrast, the water zone near the OWC shows a noticeable decrease in both porosity and permeability. The core porosity displayed in track 3 has a consistent range of 18-19%, which indicates high reservoir quality.

The permeability presented in track 4 shows high values of 12-960 mD between 2395-2408 m, thus representing a very good sandstone interval with connected pores. At a depth of 2390.4-2394.2 m, both porosity and permeability drop to 12.93% and 1.84 mD, respectively. However, this decrease in reservoir properties over the heterolithic units does not affect the reservoir quality as both the top and bottom of this rock unit show relatively high porosity and permeability values.

The average core porosity calculated over the reservoir interval is 17.26% and the average core permeability is 365.40 mD. The core and well log data indicated in Figure 5.12 for porosity and permeability does not show much variation thus indicating that well log data can be used to accurately create subsurface models.

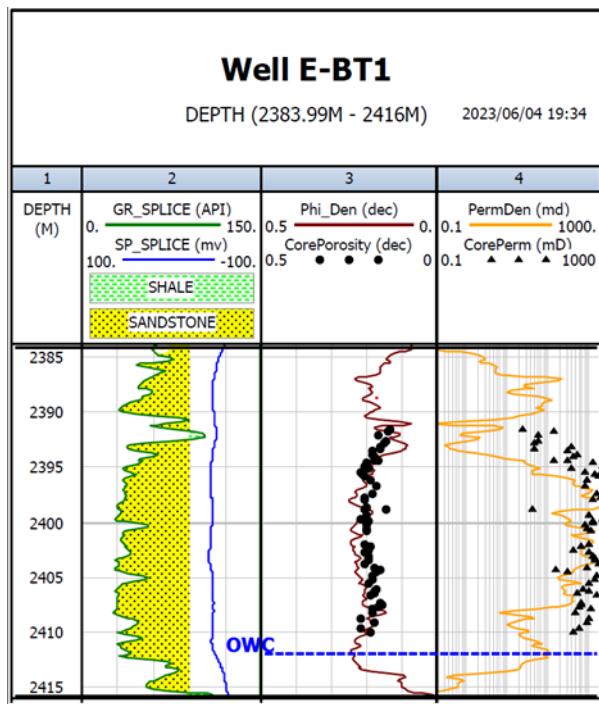


Figure 5.12: Porosity and Permeability of Well E-BT1.

5.1.5.2. Porosity and Permeability of Well E-AR1:

In well E-AR1, the porosity curve (Phi_{Son}) was calculated by using the sonic log (DT), while the permeability curve (Perm_{Son}) was calculated by using the porosity curve (Phi_{Son}). From the log below (figure 5.13), we can see that the oil zone has the highest permeability values, whereas the water zone below the OWC shows a decrease in permeability. According to both the Phi_{Son} log and core porosity data, the porosity across the reservoir seems to be constant. The core porosity shown in track 3 ranges between 18-19%, thus making it a good reservoir quality.

The core permeability presented in track 4 shows high values of 25-600 mD within the oil interval (2454-2462 m), thus representing a good sandstone interval with connected pores. Within the water zone at a depth of 2462-2485 m, the core permeability ranges from 7-350 mD. At a depth of 2467.8

m, there is a shale layer present with a porosity of 12.5% and a permeability of 7.23 mD. The quality of the reservoir is not affected by this shale layer.

The average core porosity calculated over the reservoir interval is 17.01% and the average core permeability is 178.93 mD. The core and well data indicated in Figure 5.13 do not show much variation and therefore the well log data can be used to create subsurface models.

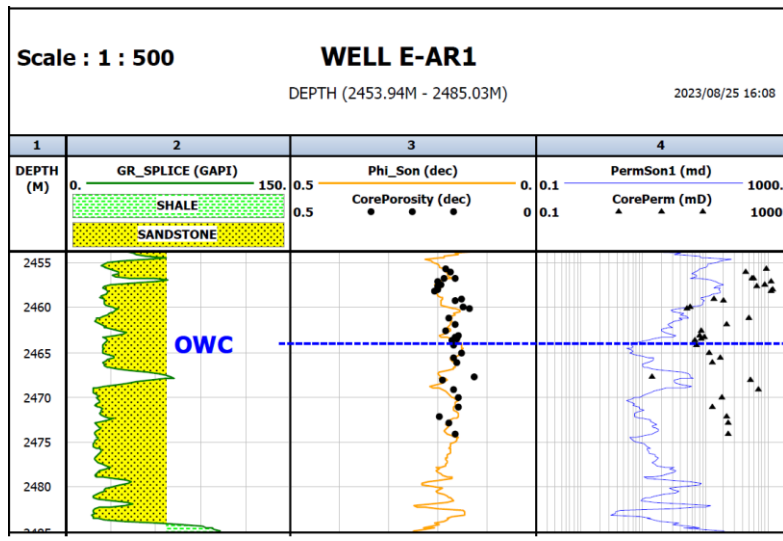


Figure 5.13: Porosity and Permeability of Well E-AR1.

5.1.5.3. Porosity and Permeability of Well E-AR2:

For well E-AR2, the neutron log (SPHI) was used to calculate the porosity curve (Phi_{Neu}) over the reservoir interval, which was then used to calculate the permeability curve (Perm_{Neu}). From the log below (figure 5.14), we can see that the oil zone has the highest permeability values, whereas the water zone shows a decrease in permeability. According to both the Phi_{Neu} log and core porosity data, the porosity over the reservoir seems to be constant. The core porosity shown in track 3, doesn't show much variation and range between 17-18%, thus making a good reservoir quality.

The permeability presented in track 4 shows high values of 75-520 mD in the oil interval of 2444-2451 m, thus indicating a good sandstone interval with connected pores. Within the water zone at a depth of 2451-2477 m, the permeability ranges from 11-450 mD. The average core porosity calculated over the reservoir interval is 17.56% and the average core permeability is 227.09 mD.

From the figure below, we can see that the core and well log porosities don't show much variation. This means that the well log data can be used to generate subsurface models.

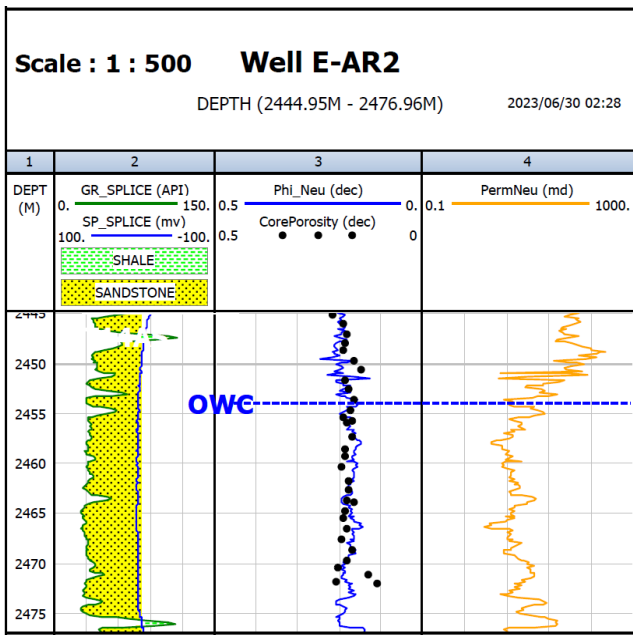


Figure 5.14: Porosity and Permeability of Well E-AR2.

5.1.5.4. Distribution of Porosity and Permeability for all wells

The multi-well cross plot and histograms in Figure 5.15, display the relationship between porosity and permeability across the reservoir intervals of the three wells. According to the cross plot below, we can see that there is a strong positive correlation between porosity and permeability over all three wells with a combined regression coefficient of 83%. This indicates that when porosity increases, permeability increases. The resultant regression equation for porosity-permeability is presented below as:

$$\text{Log (core permeability)} = 20.3564 \times \text{CorePorosity} - 1.25297 \quad (R^2 = 0.83) \quad (5.6)$$

Figure 5.15 also indicates the distribution of porosity and permeability across all three wells. The distribution of porosity is indicated on the x-axis, whereas the distribution of permeability is indicated on the y-axis.

Both porosity and permeability indicate a negatively skewed distribution where most of the data are clustered towards higher values. This indicates that all three wells have high porosity and permeability values which indicates that all three wells can be considered good reservoirs for the

storage of hydrocarbons. Understanding the distribution of porosity and permeability is important as it can also affect the success of finding hydrocarbons. If there is too little porosity or permeability present in the well, it can indicate that the reservoir is not economically viable to proceed with production.

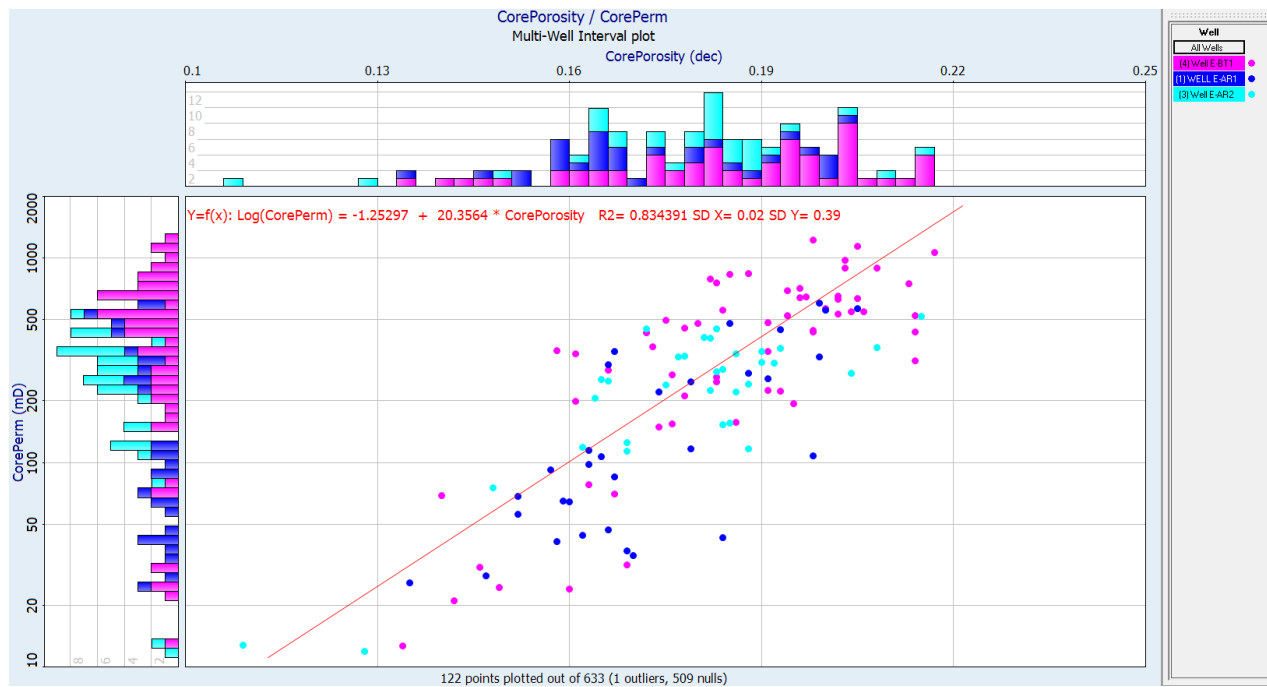


Figure 5.15: Multi-well cross-plot and histograms showing the relationship between porosity and permeability of all three wells.

5.1.5. Multi-Well Correlation:

5.1.5.1. Multi-Well Correlation for different stratigraphic horizons:

The stratigraphic correlation, which identifies different geological horizons, is based on the gamma-ray log (figure 5.16). These horizons are determined by various API values and the use of PASA reports. The horizons in well E-AR1 and E-AR2 occur at similar depths, while the horizons in well E-BT1 occur at shallower depths. The reason for this, is because well E-BT1 occurs at the proximal part of the submarine fan, whereas wells E-AR1 and E-AR2 occurs towards the distal parts of the fan.

The focus of the correlation is based on the oil-bearing reservoirs occurring between horizons 15At1 and 14At1 during the early Albian to late Cenomanian. Horizon T14AS and B14AS occurs between 15At1 and 14At1. The reservoirs of all three wells form part of the T14AS horizon, and the sandstone

within this horizon has a consistent thickness across all three wells. Directly below the T14AS horizon is the B14AS horizon, which also exhibits similar thickness across all three wells. However, the B14AS horizon does show different API values across all three wells, with E-AR1 and E-AR2 having higher API values than E-BT1.

Based on the distribution of sandstones, variation in grain size, and basin morphology, the sandstones above the 14At1 horizon have a source area located southwest of the wells. This indicates that all three wells are part of the same regressive submarine fan system, with E-BT1 being the closest to the source area. This is further supported by the presence of four cyclic channel-fill sandstones in the T14AS horizon of well E-BT1. Wells E-AR1 and E-AR2 contain mass flow sandstones with irregular bedding patterns and sharp contacts, which are commonly found in the more distant parts of submarine fans. The sandstones in wells E-AR1 and E-AR2 are predominantly coarse and poorly sorted. All three wells are considered promising for hydrocarbon accumulation, and they do correlate with one another based on their geological horizons.

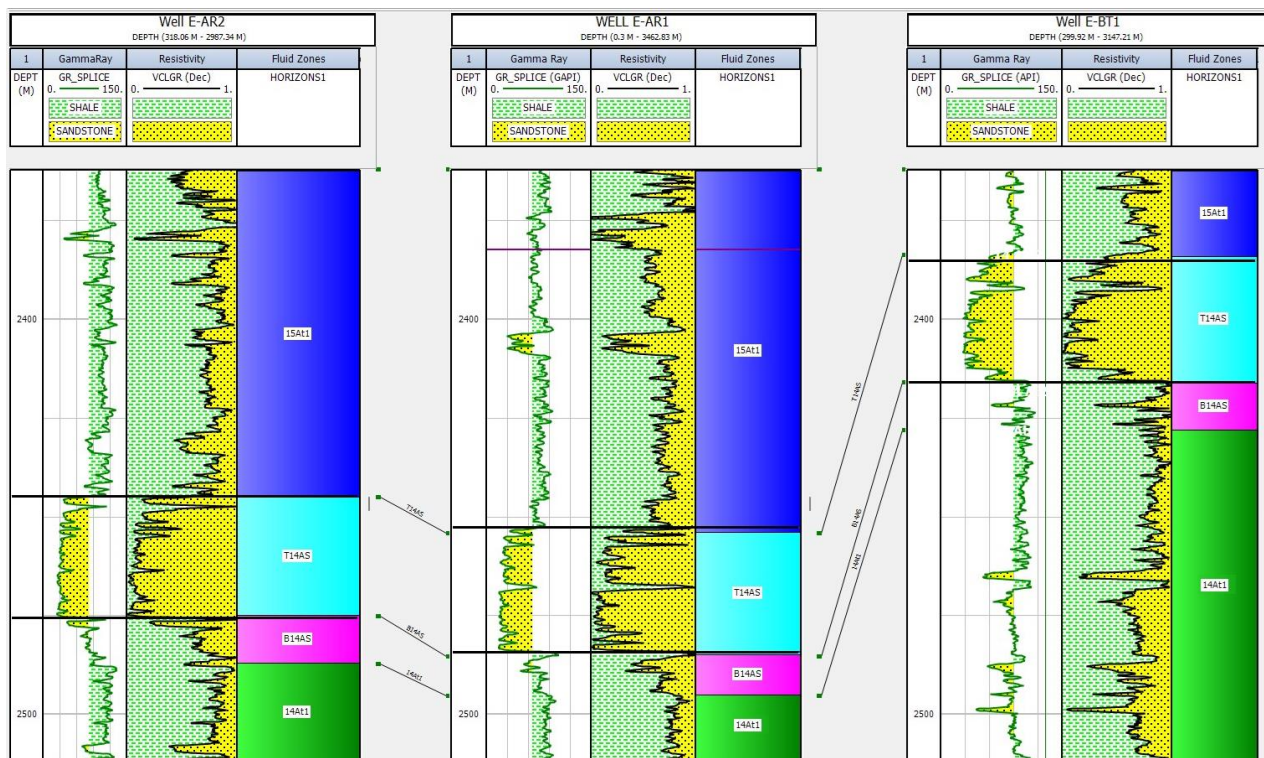


Figure 5.16: Multi-well correlation for different geological horizons in the three studied wells.

5.1.5.2. Multi-Well Correlation for fluid zones:

The following correlation is based on the fluid zones within the reservoir interval of the three wells (figure 5.17). The fluid zones and fluid contacts were previously determined using the resistivity logs and repeat formation test (RFT). When the deep resistivity is higher than the medium resistivity, oil is present, whereas if these logs are close together, it indicates drilling fluid (or water) is present.

According to the results, all three wells have an oil zone that lies above a water zone due to difference in densities. Well E-BT1 has an oil zone thickness of 27.8m and a water zone thickness of 4.2m, well E-AR1 has an oil zone thickness of 8m and a water zone thickness of 23m, and well E-AR2 has an oil zone thickness of 6m and a water zone thickness of 26m. Well E-BT1 has a larger oil zone compared to wells E-AR1 and E-AR2, which could be attributed to oil accumulating more towards the proximal part of the submarine fan.

Although all three reservoirs belong to the same pressure regime, the difference in oil water contacts occurs due to individual localized sandstone highs that were deposited due to an irregular unconformity at horizon 14At1. The difference in the oil and water contacts is also influenced by the position of each well in the submarine fan.

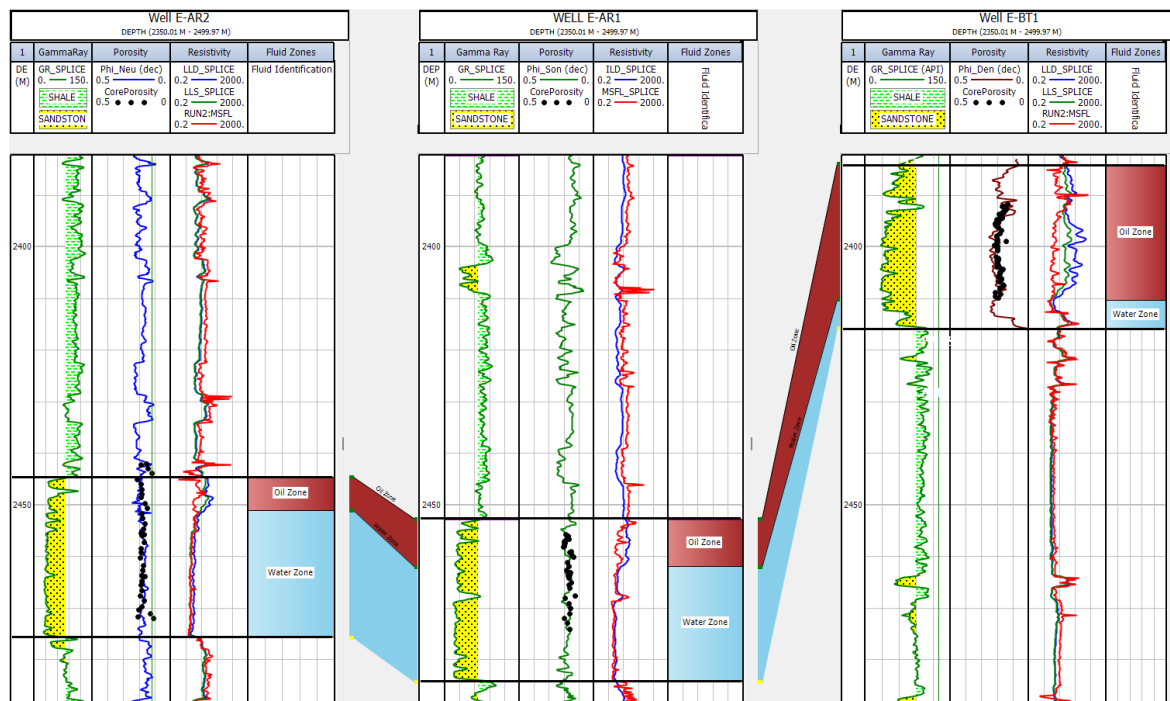


Figure 5.17: Multi-well correlation for different fluid flow zones in the three studied wells.

5.2. Hydraulic Flow Zones:

As previously discussed in Chapter 5, the hydraulic flow units for each reservoir interval of the three wells are first identified by plotting a log-log plot of the rock quality index (RQI) vs. normalized porosity ($\Phi_{\text{N}}^{\text{norm}}$). These plots for each well are shown below with their respective tables and histograms that give the range and mean for each hydraulic flow unit used for the three different wells.

From table 5.5, we can see that 5 hydraulic flow units have been identified for well E-BT1, while only 4 hydraulic flow units exist for wells E-AR1 and E-AR2. The average FZI values in the table below increase with a higher hydraulic flow unit (HFU) over each well. This indicates that HFU1 has the poorest reservoir rock quality while HFU4 and HFU5 have the best reservoir rock quality. The table also indicates that well E-BT1 has the best reservoir rock quality and well E-AR1 has the poorest reservoir rock quality.

Table 5.5: The range and mean FZI values for each hydraulic flow unit within the three different wells:

Well	FZI with RQI		
	Flow Unit	FZI Range	Mean FZI
E-BT1	HFU1	0.40 – 1.00	0.60
	HFU2	1.00 – 1.77	1.30
	HFU3	1.77 – 3.00	2.24
	HFU4	3.00 – 5.26	3.87
	HFU5	5.26 – 10.00	6.25
E-AR1	HFU1	0.28 – 0.75	0.62 (poor)
	HFU2	0.75 – 1.06	0.89
	HFU3	1.06 – 1.62	1.31
	HFU4	1.62 - 10.00	1.97 (best reservoir rock) RQI highest
E-AR2	HFU1	0.5 – 0.99	0.85
	HFU2	0.99 – 1.77	1.32

	HFU3	1.77 – 2.83	2.22
	HFU4	2.83 – 10.00	3.28

5.2.1. Distribution of FZI Hydraulic Flow Units:

We can also see from the histograms below that the distribution across wells E-AR1 and E-AR2 has a positively skewed distribution for all flow units. This indicates that the mean FZI value across all flow units for each well exceeds the median. On the other hand, well E-BT1 has a bimodal distribution with HFU1 and HFU4 indicating high values in comparison to the other flow units. The individual flow units of well E-BT1 also indicate bimodal distribution.

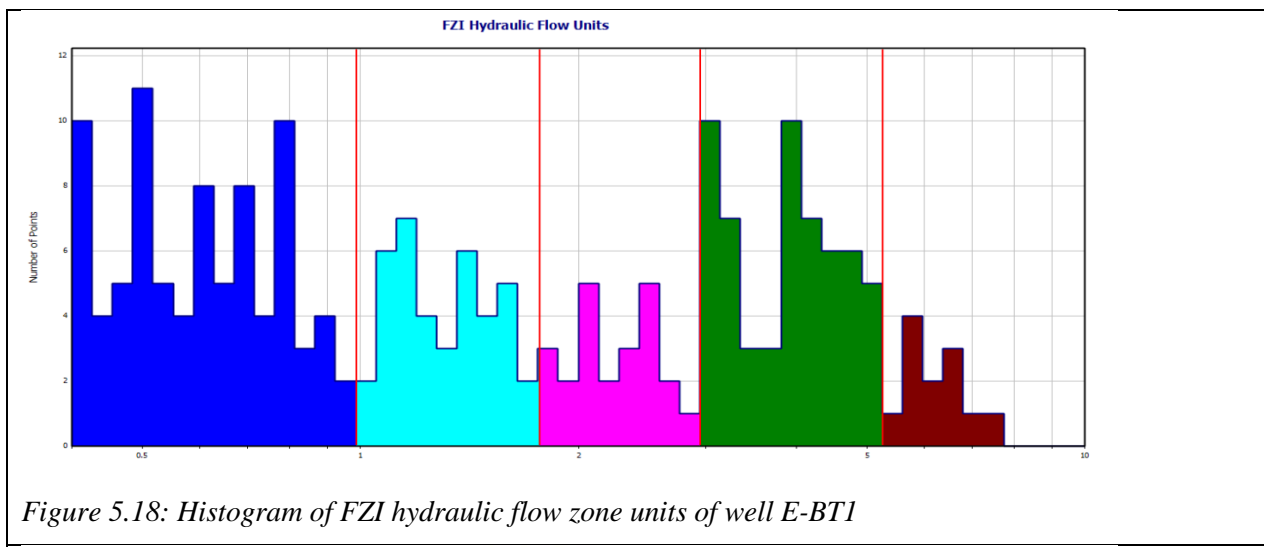


Figure 5.18: Histogram of FZI hydraulic flow zone units of well E-BT1

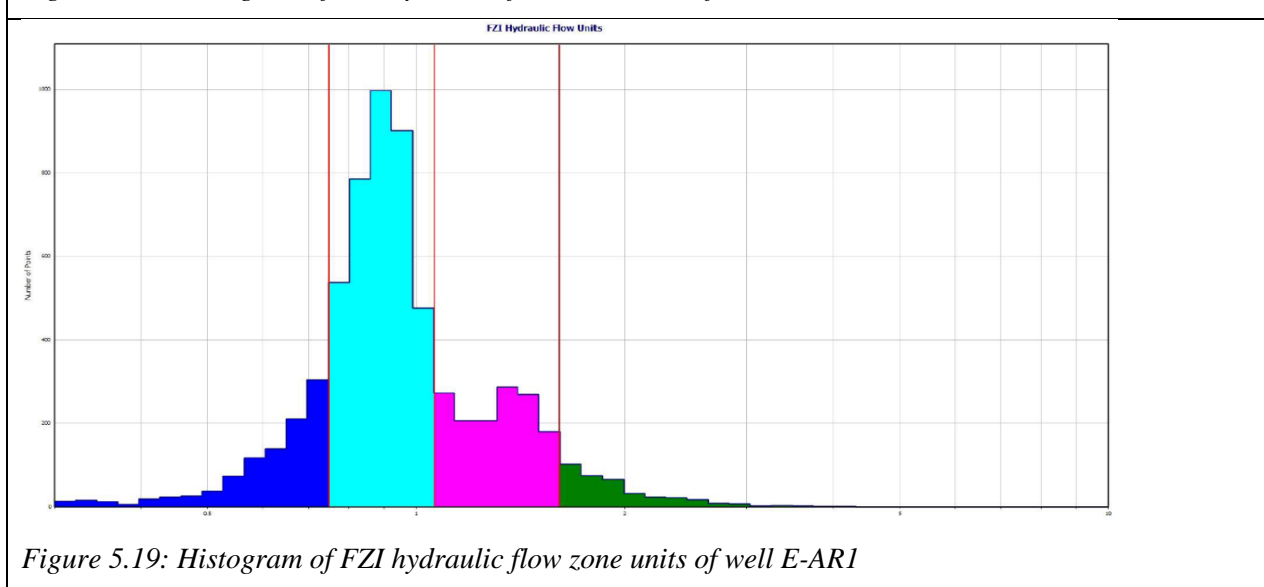


Figure 5.19: Histogram of FZI hydraulic flow zone units of well E-AR1

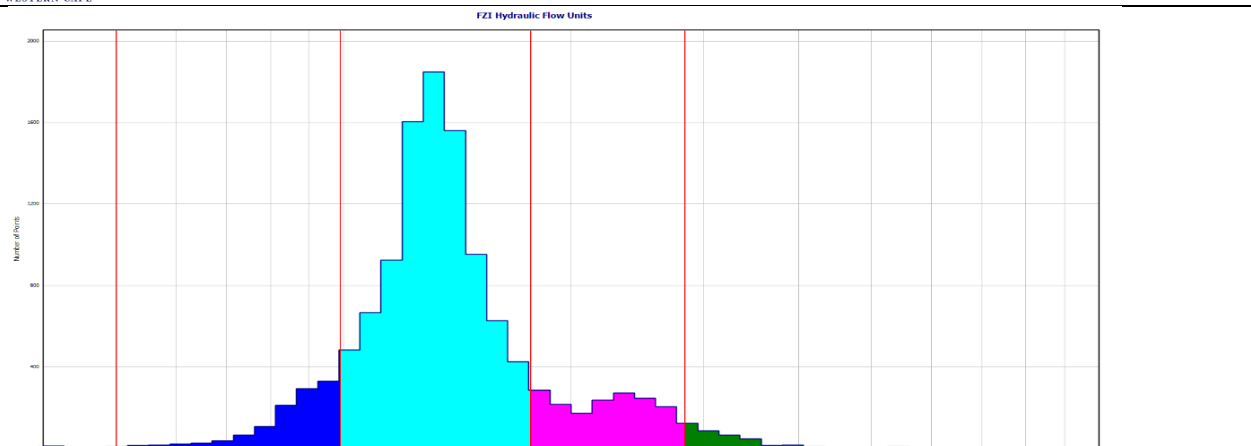


Figure 5.20: Histogram of FZI hydraulic flow zone units of well E-AR2

5.2.2. RQI Hydraulic Flow Units:

From the RQI vs. Phiz Plots below, we can see that the overall RQI values for well E-BT1 range from 0.05 – 2.0 microns, well E-AR1 range from 0.02-2.0 microns, and well E-AR2 range from 0.1-2.0 microns. Hydraulic Flow Unit (HFU1) show the lowest RQI values, whereas HFU4 and HFU5 shows the highest RQI values. As the RQI values increase, the rock quality increases thus indicating that a higher HFU indicates a better rock quality.

From figures 5.21, 5.22, and 5.23 below, we can see that HFU5 and HFU4 for well E-BT1 are clustered mostly around 1-2 microns as compared to the same HFU4 of wells E-AR1 and E-AR2 being clustered around 0.5-1 microns. This indicates that well E-BT1 have a higher RQI clustering than wells E-AR1 and E-AR2, thus representing a better rock quality.

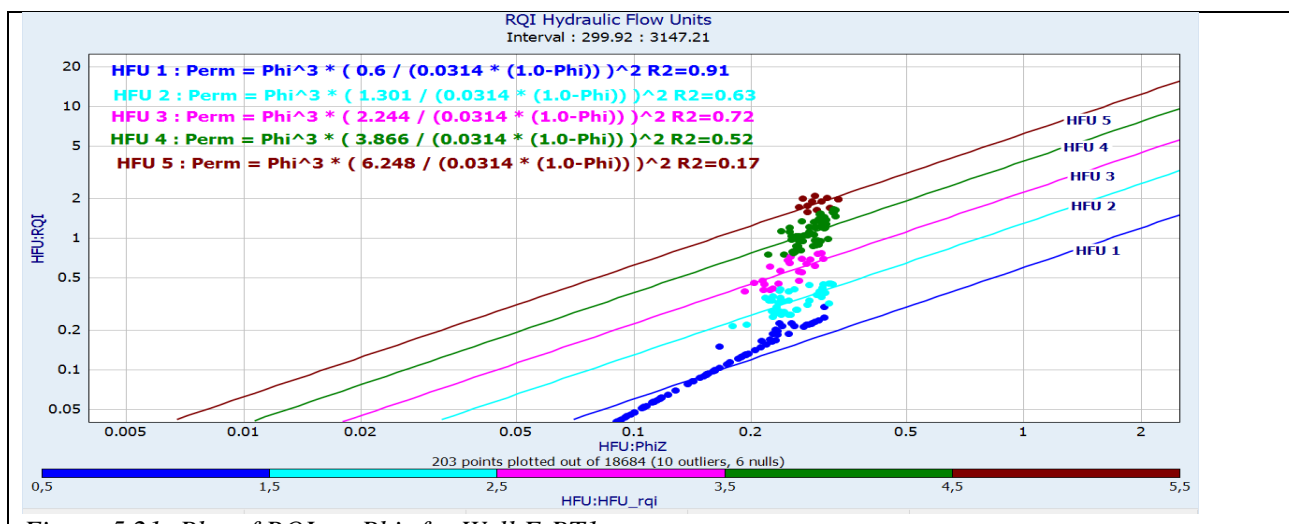


Figure 5.21: Plot of RQI vs. Phiz for Well E-BT1

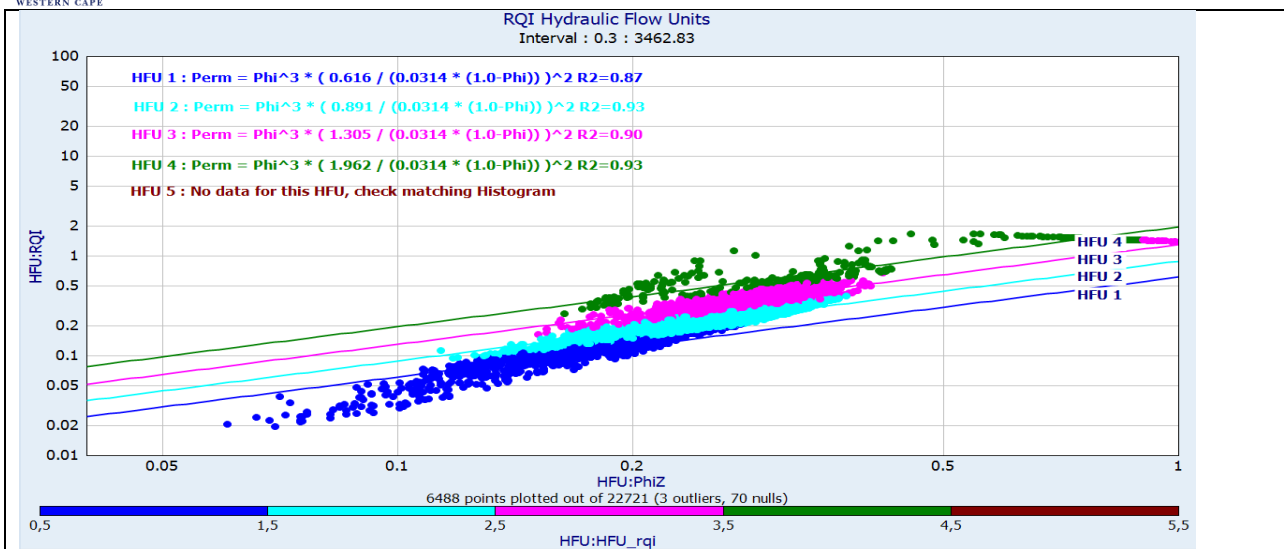


Figure 5.22: Plot of RQI vs. Φ_z for Well E-ARI

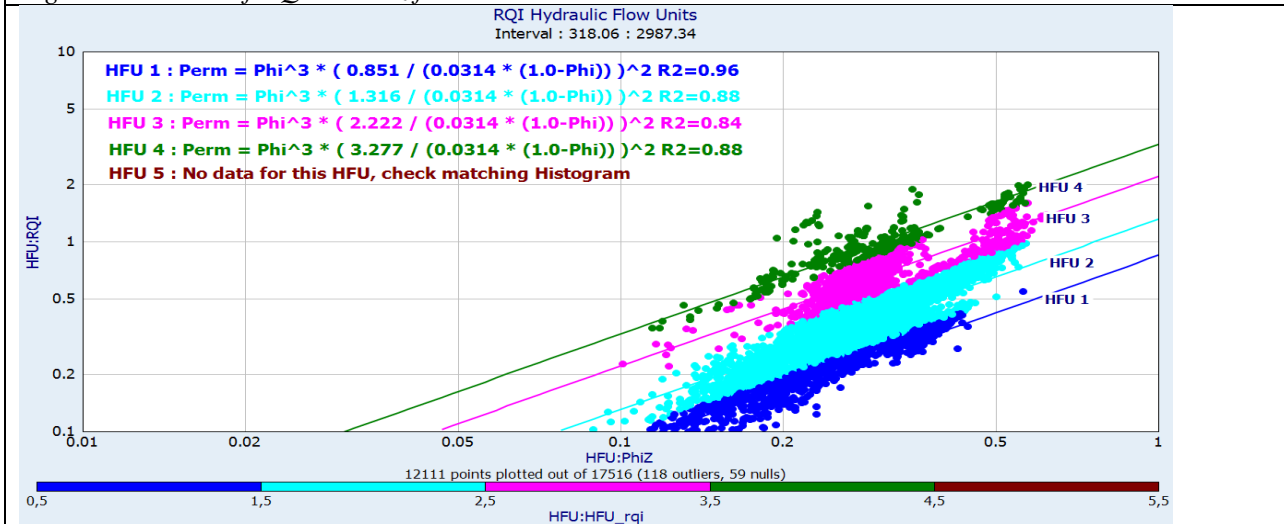


Figure 5.23: Plot of RQI vs. Φ_z for Well E-AR2

5.2.3. Lucia's Classification model for all wells:

By superimposing the FZI values on Lucia's classification model on the IP software plot, we can class the rocks from the 5 different flow units in classes of 3. Class 1 (Grain-stones) does not represent any flow units, class 2 (Grain-dominated packstones) represents HFU5, HFU4, and HFU3, and class 3 (Mud-dominated) represents HFU2 and HFU1. The best reservoir rocks from the studied wells fall under class 2 with very good porosity and fair to good permeability. The reservoir rocks that are least favourable belong to class 3 which has a low permeability and fair porosity. Class 1 type of rocks which represent the best reservoir quality have limited data.

From figures 5.24, 5.25, and 5.26 below, we can see that well E-BT1 class 1 contains a few results of HFU5. Class 2 representing packstones consists of HFU5, HFU4, HFU3 and some data points of HFU2. Class 3 representing mud fabrics consists of HFU1 and some data points of HFU2.

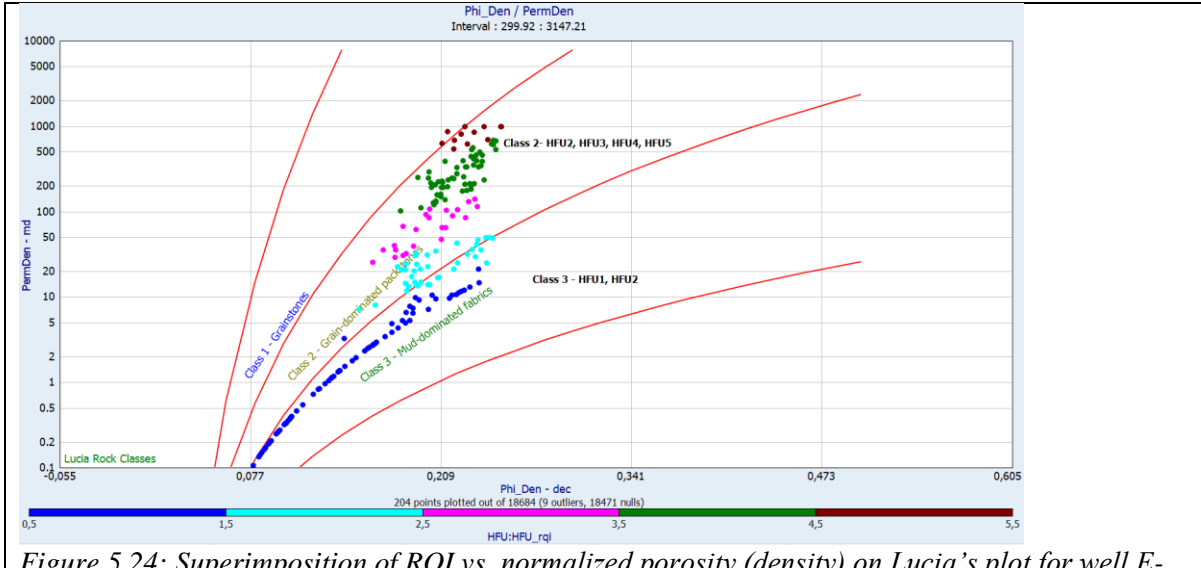


Figure 5.24: Superimposition of RQI vs. normalized porosity (density) on Lucia's plot for well E-BT1

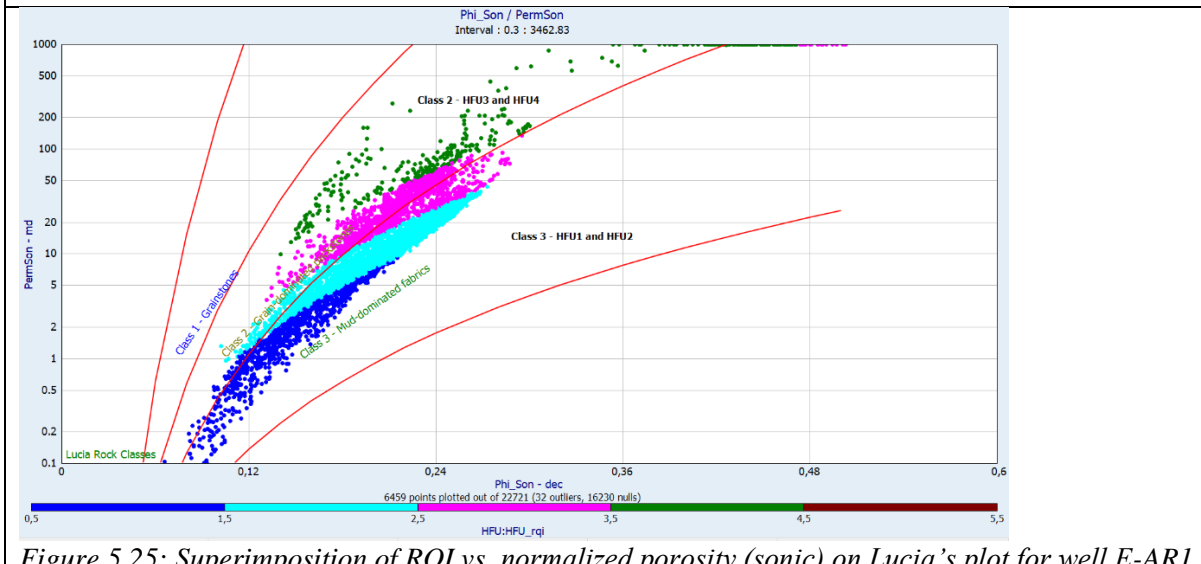


Figure 5.25: Superimposition of RQI vs. normalized porosity (sonic) on Lucia's plot for well E-ARI

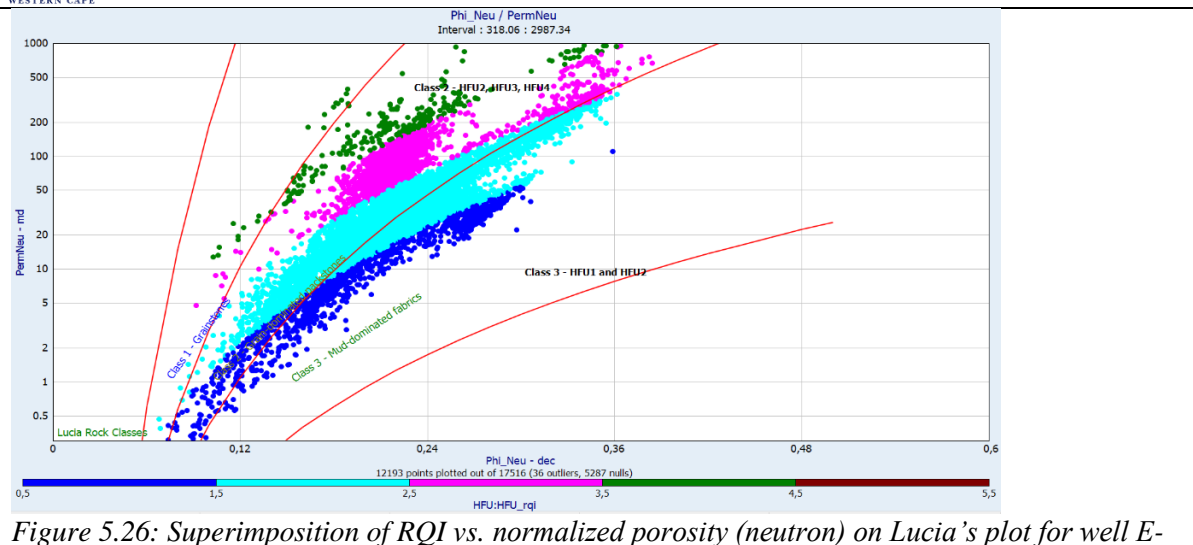


Figure 5.26: Superimposition of RQI vs. normalized porosity (neutron) on Lucia's plot for well E-AR2

5.2.4. Reservoir Rock Types (RRT) for all wells:

The mean values in the table 5.6 below have been calculated across various depth intervals of the three wells from the log plots shown below (figures 5.27, 5.28, and 5.29). The five reservoir rock types (RRT) shown below in the log plots have been identified over the three wells by integrating the Reservoir Quality Index and Winland R35 methods with core reservoir data.

The logs below show that the core FZI values correlate better with the generated RQI log over the hydrocarbon intervals. For this reason, the RQI logs have been used to create the HFU zones shown in track 6 below. Well E-BT1 have the highest permeability and therefore the highest hydraulic flow units (figure 5.27). By comparing tracks 3 and 4 below to track 5 for all wells, we can see that permeability influences the HFU logs more than the porosity logs. This means that there is a stronger relationship between permeability and Hydraulic Flow Units as seen on all three wells.

From the logs below, we can see that well E-BT1 have 5 reservoir rock types over the reservoir interval. RRT4-5 indicates the thickest intervals, thus representing a better reservoir quality for E-BT1. Both E-AR1 and E-AR2 consist of reservoir rock types 2, 3 and 4. RRT2 has the thickest intervals for both E-AR1 and E-AR2, thus representing a lower reservoir quality than E-BT1. From the logs we can also see that E-AR2 has a thicker RRT4 than E-AR1, indicating that E-AR2 has a better reservoir quality than E-AR1.

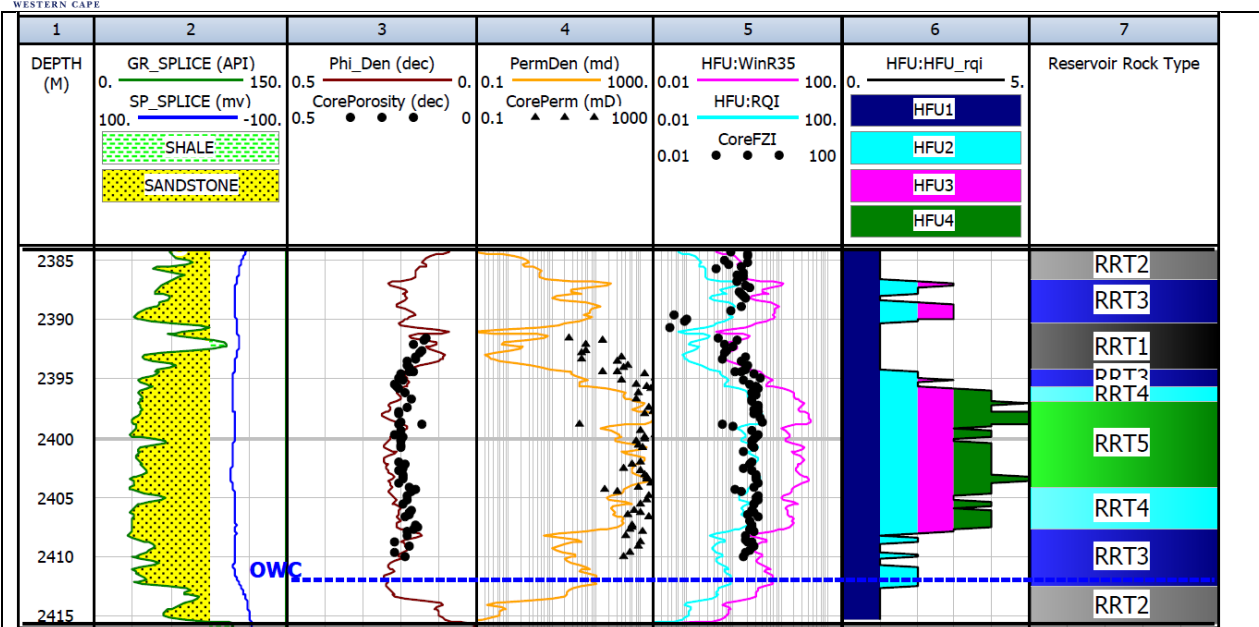


Figure 5.27: Hydraulic Flow Zones (HFU) of well E-BT1

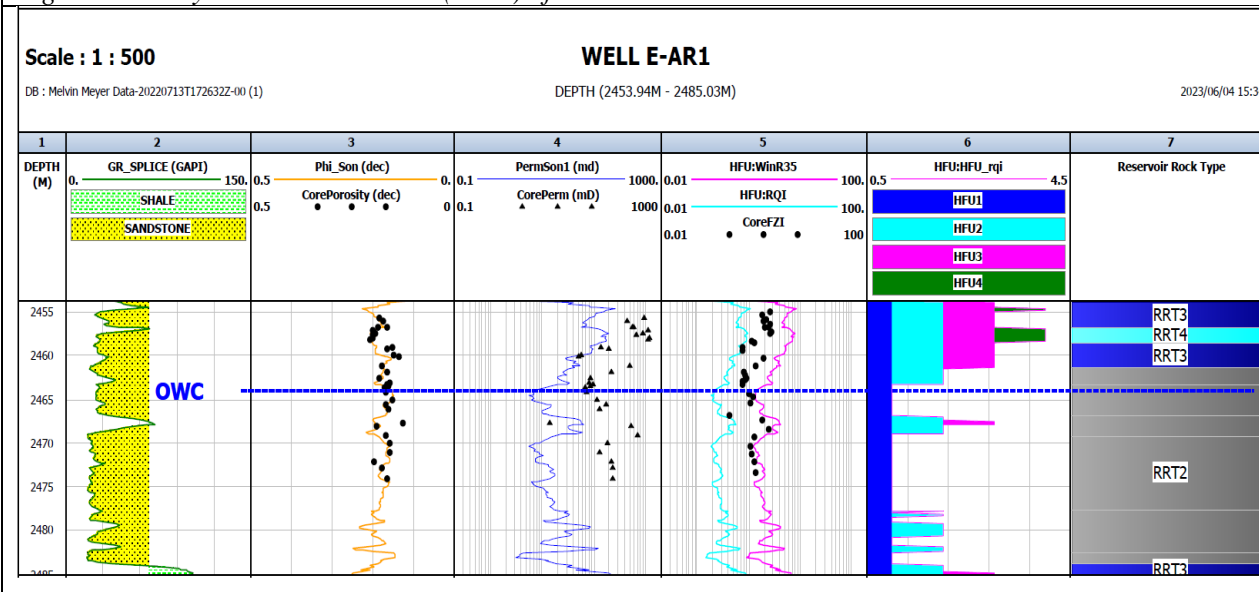


Figure 5.28: Hydraulic Flow Zones (HFU) of well E-AR1

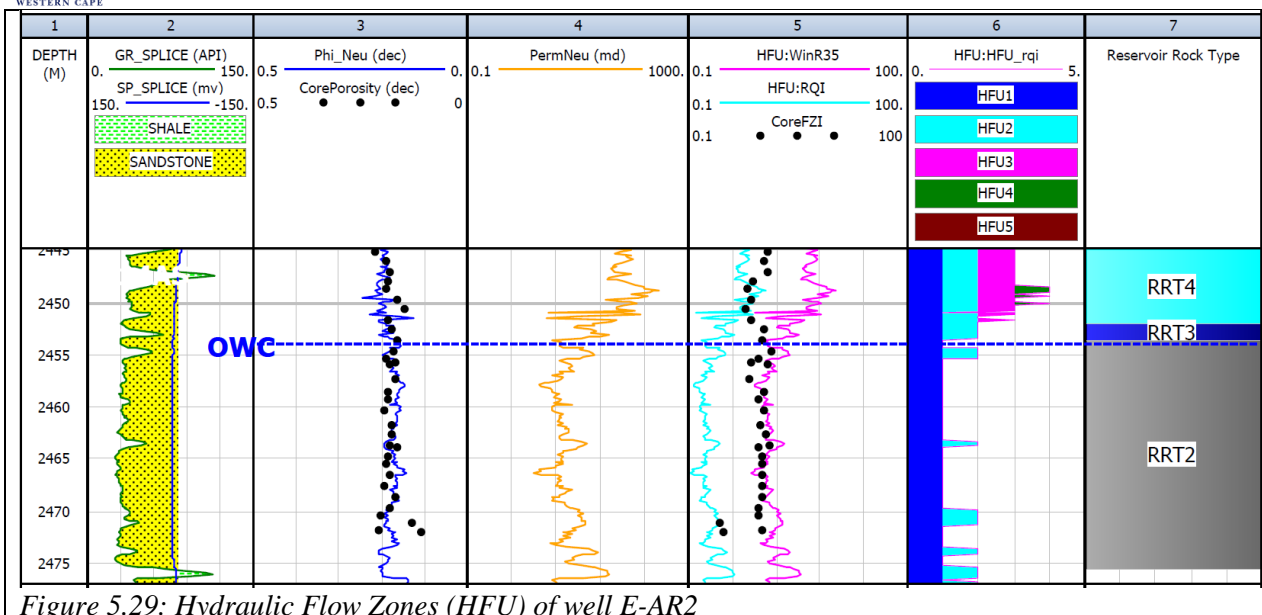


Figure 5.29: Hydraulic Flow Zones (HFU) of well E-AR2

Table 5.6: Calculated average petrophysical values used to group rock types into five reservoir rock types (RRT).

W ell	Top Depth	Bottom Depth	Thick-ness	Porosity	Permeabi-lity	HFU	Zone RRT	R35	RQI	FZI	Rock Type	Rank
				18-22	200-1000	4-5	5	>10	>1.5	5-10	Mega-porous	Very Good
				16-20	50-200	3	4	4-10	0.5-1.0	3-5	Macro-porous	Good
				14-18	10-50	2	3	2-4	0.2-0.5	2-3	Meso-porous	Fair
				12-18	2-10	1-2	2	1-2	0.1-0.2	1-2	Micro-porous	Poor
				<10	<2	1	1	<1	<0.1	<1	Nano-porous	Imper-vious
E-AR1	2452.6	2453.8		14.27	3.76	2	2	1.09	0.15	0.89	Micro	Poor
	2453.8	2456.8		18.50	22.53	3	3	2.54	0.33	1.41	Meso	Fair
	2456.8	2458.5		19.79	37.20	4	4	3.41	0.43	1.73	Macro	Good
	2458.5	2461.4		18.02	16.34	3	3	2.21	0.29	1.30	Meso	Fair
	2461.4	2463.4		18.02	6.76	2	2	1.36	0.19	0.87	Micro	Poor
	2463.4	2466.7		16.17	2.52	1	2	0.82	0.12	0.63	Micro	Poor
	2466.7	2469.3		19.10	9.14	2	2	1.49	0.21	0.88	Micro	Poor
	2469.3	2477.6		17.28	2.86	1	2	0.84	0.13	0.60	Micro	Poor
	2477.6	2482.6		19.63	8.43	2	2	1.31	0.19	0.75	Micro	Poor
	2482.6	2483.8		16.44	2.26	1	2	0.72	0.11	0.54	Micro	Poor
	2483.8	2485.0		21.84	20.86	2	3	2.03	0.28	0.97	Meso	Fair

E-AR2	2444.8	2448.3		19.54	63.6	3	4	4.66	0.56	2.28	Macro	Good
	2448.3	2450.1		20.53	141.40	4	4	6.99	0.79	3.05	Macro	Good
	2450.1	2452.0		19.34	54.42	3	4	3.85	0.47	1.88	Macro	Good
	2452.0	2453.5		18.75	18.34	2	3	2.31	0.30	1.31	Meso	Fair
	2453.5	2454.2		16.32	5.89	1	2	1.33	0.18	0.94	Micro	Poor
	2454.2	2455.6		18.01	11.87	2	2	1.84	0.25	1.12	Micro	Poor
	2455.6	2469.8		16.79	5.22	1	2	1.21	0.17	0.84	Micro	Poor
	2469.8	2471.6		18.85	11.11	2	2	1.75	0.24	1.03	Micro	Poor
	2471.6	2473.5		17.20	5.93	1	2	1.30	0.18	0.87	Micro	Poor
	2473.5	2475.4		19.45	13.24	2	2	1.84	0.25	1.03	Micro	Poor
E-BT1												
	2384.0	2386.7		13.36	2.17	1	2	0.69	0.10	0.61	Micro	Poor
	2386.7	2390.4		19.51	34.37	2	3	3.08	0.39	1.59	Meso	Fair
	2390.4	2394.2		12.93	1.84	1	1	0.64	0.09	0.59	Nano	Impervious
	2394.2	2395.7		18.53	19.63	2	3	2.43	0.32	1.38	Meso	Fair
	2395.7	2396.9		20.33	209.14	4	4	8.87	0.97	3.76	Macro	Good
	2396.9	2398.9		22.73	664.30	4	5	16.16	1.66	5.62	Mega	Very good
	2398.9	2403.0		22.58	327.97	4	5	10.44	1.14	3.87	Mega	Very good
	2403.0	2404.0		22.44	597.22	4	5	15.55	1.60	5.53	Mega	Very good
	2404.0	2407.8		21.28	178.74	3	4	7.92	0.89	3.28	Macro	Good
	2407.8	2412.6		20.87	23.30	2	3	2.31	0.31	1.17	Meso	Fair
	2412.6	2416		12.65	3.65	1	2	0.69	0.10	0.54	Micro	Poor

Detailed analysis of the different reservoir rock types (RRT):

RRT1 (black): Mainly represented by the dark blue flow unit (HFU1) in track 6 on well E-BT1 log-plot (figure 5.27). The RRT1 is composed of silty shale layers as seen in the log plot of well E-BT1 between a depth of 2390.4-2394.2m and corresponds with class 3 of the Lucia classification scheme in Figures 5.24 above. RRT1 has relatively low porosities ranging from 10-12% across reservoirs and permeabilities <2 mD. RRT1 is classified as a nano-porous rock zone with an impervious ranking. The reason for this is that the clay minerals in the silty-shale layer block the pores and therefore lead to poor reservoir conditions.

RRT2 (grey): This rock type is mainly represented by the dark and light blue flow units (HFU1, HFU2) in track 6. This rock consists of very fine-grained sandstones and falls under class 3 of the

Lucia classification scheme (mud-dominated fabrics). Poor petrophysical properties have been observed, with porosities ranging from 12-18% and permeabilities ranging from 2-10 mD. The Winland R35 pore throat sizes range between 1-2 microns and the FZI values between 1-2 microns. This rock type is classified as a micro-porous rock with poor reservoir quality. The RRT2 occurs mainly below the OWC in the water zone of the three wells. Therefore, wells E-AR1 and E-AR2 have a greater RRT2 than well E-BT1 due to their large reservoir water zones.

RRT3 (blue): This rock type is mainly represented by the pink flow units (HFU3) but in some transition stages may be represented by the light blue flow units (HFU2). This rock consists of medium-grained sandstones and falls under class 2 of the Lucia classification scheme (grain-packstones). The reservoir properties are distributed fairly and have porosities ranging between 14-18% and permeabilities from 10-50 mD. The Winland R35 pore throat radius sizes range between 2-4 microns and the FZI range between 2-3 microns. RRT3 occurs frequently over wells E-BT1 and E-AR1 as transition zones between RRT2 and RRT4. Well E-AR2 only has 1 RRT3 unit present. This reservoir rock is classified as a mesoporous rock type with a fair reservoir quality.

RRT4 (light blue): These rocks are mainly represented by the green flow units (HFU4) but also exist in the pink flow units (HFU3) as seen in well E-AR2. The reservoir rocks are composed of medium to coarse-grained sandstones that belong to class 2 of the Lucia classification scheme. The RRT4 occurs only in the oil zones, and it indicates good reservoir properties with porosities ranging between 16-20% and permeability ranging from 50-200 mD. The Winland R35 pore throat radius sizes range between 4-10 microns while the FZI values range between 3-5 microns. RRT4 is more frequently distributed in well E-AR2 with a thickness of 7.2 meters, thus indicating a good reservoir quality in the oil zone (figure 2.29). These reservoir rocks can be classified as macro-porous rocks with good reservoir quality.

RRT5 (green): The final reservoir rock is represented by only the green flow units (HFU4) and they occur only in well E-BT1. These rocks are composed of coarse-grained sandstones that belong to class 2 of the Lucia classification scheme. RRT5 is like RRT4 as they only occur within the oil zone, but they represent better reservoir quality. The petrophysical reservoir properties for RRT5 have porosities ranging between 18-22% and permeabilities ranging between 200-1000 mD thus making them more suitable for hydrocarbon exploration. The Winland R35 pore throat sizes are higher than 10 microns, and their FZI values range between 5-10 microns. In well E-BT1 this reservoir rock has

a thickness of 7.1 meters and indicates very good reservoir quality. RRT5 is classified as mega-porous rocks with very good reservoir rock quality for hydrocarbon exploration.

From the identification of the different reservoir rock types (RRT) across the reservoir interval of the three wells, it can be concluded that well E-BT1 has a very good reservoir quality, well E-AR2 has a good reservoir quality, and well E-AR1 has a good reservoir quality.

5.3. Electrical Properties: Archie and cementation factor:

The tables for each well below show the electrical properties calculated from the core plugs with an EPSA instrument. The values that were calculated are the formation factor and these values were calculated using the measured input variables of temperature (T), dry weight (Wd), saturated weights (Ws), resistivity of saturated rocks (Ro, Rt), and resistivity of brine water (Rw). These values were measured and recorded at room conditions on consecutive days on core plugs. On the spreadsheet, Archie's tortuosity constant was assumed to be 1.00. The formation factor has been calculated using the following equation:

$$F = Ro/Rw \quad (5.7)$$

Where F = Formation factor, Ro = Resistivity of brine, Rw = Resistivity of 100% saturated rock

5.3.1. Determination of Archie and cementation factor of Well E-BT1:

The electrical properties of well E-BT1 were determined from an EPSA resistivity instrument. The resistivity of the brine was found to be 0.148 Ohm-m at 20.9 °C. The brine that was used for well E-BT1 consisted of approximately 36000 ppm NaCl. The results of the formation factor of well E-BT1 are indicated in Table 5.7 below.

Table 5.7: Formation factor and Porosity of 12 different samples of well E-AR2.

Sample Name	Depth (m)	Porosity (%)	Resistivity of Brine (Rw)	Resistivity at Sw=1.0 (Ro)	Formation Factor
BX16	2402,25	19,10%	7,77	213,86	27,51
BX17	2402,55	19,30%	7,77	298,25	38,38
BX18	2402,8	20,40%	7,77	187,46	24,12
BW57	2403,05	19,60%	7,73	244,31	31,60
BX20	2403,5	19,40%	7,77	251,7	32,38
BX21	2403,75	20,30%	7,77	206,68	26,59
BX22	2404,23	16,30%	7,77	294,02	37,83
BX24	2404,87	18,20%	7,77	288,22	37,08
BX25	2405,19	18,30%	7,77	248,58	31,98
BX27	2405,69	19,40%	7,77	264,88	34,08
BX28	2406,19	17,50%	7,77	284,96	36,66
BX29	2406,47	17,60%	7,77	271,15	34,89

BX32	2407,44	15,80%	7,77	309,53	39,82
BX33	2407,69	16,60%	7,77	288,01	37,06
BX34	2407,94	18,40%	7,77	215,78	27,76
BX35	2408,19	18,10%	7,77	281,26	36,19
BX37	2408,80	21,40%	7,77	221,54	28,50
BX38	2409,08	17,70%	7,77	265,61	34,17
BX40	2409,64	21,40%	7,77	155,45	20,00
Average	18,68%		7,77	251,07	32,31

Archie and cementation exponent determination of E-BT1

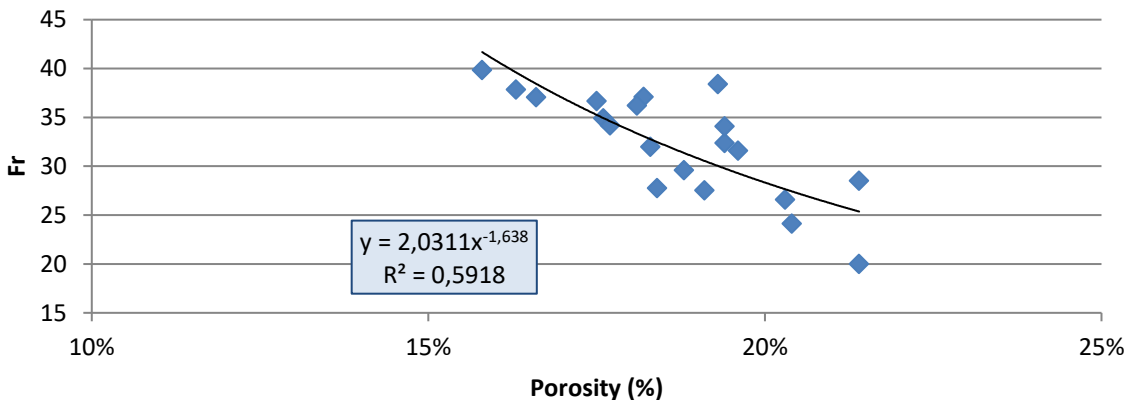


Figure 5.30: Determination of Archie and cementation exponent using the relationship between formation factor and porosity of well E-BT1.

The 18 core plug samples that were used for the calculations of well E-BT1 had an average porosity of 18.68% over the interval of 2402.25-2409.64m. The porosity and formation factor of the samples were measured at ambient conditions and are shown in table 5.7 above. By cross-plotting formation factor and porosity, we can determine both Archie's tortuosity (a) as well as the cementation exponent (m) at ambient conditions (figure 5.30).

The correlation coefficient from the measured values indicates that 59.18% variance in porosity is accounted for by the formation factor thus suggesting a relatively fair relationship between the formation factor and porosity. The cementation factor (m) of all core samples was calculated from the gradient of the best-fit trendline and was found to be 1.638 with R² being 0.71. The tortuosity

was calculated as the x-axis and was found to be 2.03. The equation below represents the relationship between formation factor and porosity:

$$Fr = \frac{a}{\phi^m} \quad (5.8)$$

$$Fr = \frac{2.03}{\phi^{1.638}} \quad (5.9)$$

Where Fr=formation factor, ϕ =Porosity, m=cementation factor (1.638). a=tortuosity (2.03)

5.3.2. Archie and cementation factor determination of Well E-AR1:

The electrical properties of well E-AR1 were determined from an EPSA resistivity instrument. The resistivity of the brine (R_{tw}) was found to be 0.154 Ohm-m at 20 °C. The brine that was used for well E-AR1 consisted of approximately 36000 pp NaCl. The results of the formation factor of well E-AR1 are indicated in Table 5.8 below.

Table 5.8: Formation factor and Porosity of 6 different samples of well E-AR1.

Sample Name	Depth (m)	Porosity (%)	Resistivity of Brine (Rw)	Resistivity at Sw=1.0 (Ro)	Formation Factor (Fr)
1A	2455,25	18,00%	7,78	241,28	31,00
1B	2458,55	17,40%	7,78	331,21	42,56
2A	2462,70	16,20%	7,78	330,72	42,50
2B	2455,25	16,30%	7,78	317,43	40,79
3A	2458,55	16,40%	7,78	276,72	35,56
3B	2462,70	16,60%	7,78	312,91	40,21
Average		16.82%	7.78	301,71	38.77

Archie and cementation exponent determination of E-AR1

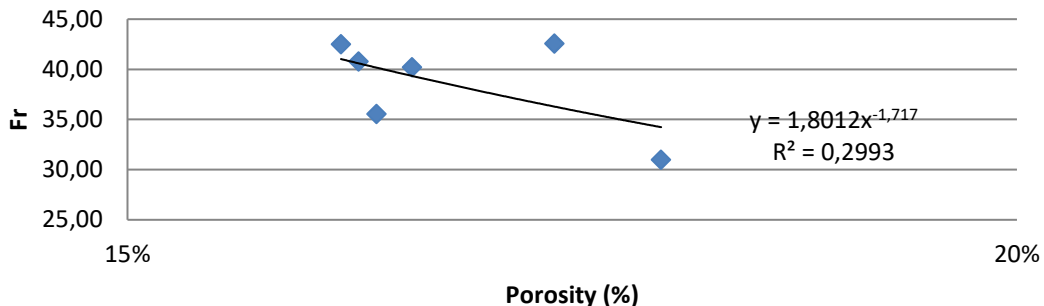


Figure 5.31: Determination of Archie and cementation exponent using the relationship between formation factor and porosity of well E-AR1.

The 6 samples that were used for the calculations of well E-AR1 had an average porosity of 16.82% over a reservoir interval between 2455.25 – 2462.70m. The porosity and formation factor of the samples were measured at ambient conditions and are shown in Table 5.8 above. By cross-plotting formation factor and porosity, we can determine both Archie's tortuosity (a) as well as the cementation exponent (m) at ambient conditions (figure 5.31).

The correlation coefficient from the measured values (blue) indicates that 29.93% variance in porosity is accounted for by the formation factor thus suggesting a relatively poor relationship between the formation factor and porosity. The average cementation factor (m) of all core samples was calculated from the gradient of the best-fit trendline and was found to be 1.72 with R^2 being 0.30. The tortuosity was calculated from the x-axis and was found to be 1.80. The equation below represents the relationship between the formation factor and porosity for well E-AR1:

$$Fr = \frac{1.80}{\phi^{1.72}} \quad (5.10)$$

Where Fr =formation factor, ϕ =Porosity, m=cementation factor (1.72). a=tortuosity (1.80)

5.3.3. Archie and cementation factor determination of Well E-AR2:

The electrical properties of well E-AR2 were determined from an EPSA resistivity instrument. The resistivity of the brine was found to be 0.156 Ohm-m at 20 °C. The brine that was used for well E-AR1 consisted of approximately 36000 ppm NaCl. The results of the formation factor of well E-AR1 are indicated in Table 5.9 below.

Table 5.9: Formation factor and Porosity of 12 different samples of well E-AR2.

Sample Name	Depth (m)	Porosity (%)	Resistivity of Brine (Rw)	Resistivity at Sw=1.0 (Ro)	Formation Factor (Fr)
4A	2442.24	18,60%	7,83	202,88	25,91
4B	2442,24	19,00%	7,83	156,25	19,97
6A	2455,91	17,10%	7,83	193,32	24,70
6B	2455,91	17,50%	7,83	186,66	23,85
7A	2453,71	17,00%	7,83	221,26	28,27
7B	2453,71	17,00%	7,83	193,47	24,72
8A	2455,80	17,10%	7,92	194,45	24,56
8B	2455,80	16,90%	7,92	173,23	21,88
9A	2463,70	17,90%	7,92	170,74	21,57
9B	2463,70	18,30%	7,92	152,55	19,27
10A	2471,85	21,20%	7,92	134,70	17,01
10B	2471,85	20,80%	7,92	138,99	17,56
<i>Average</i>		18.16%	7.88	174.15	22.12

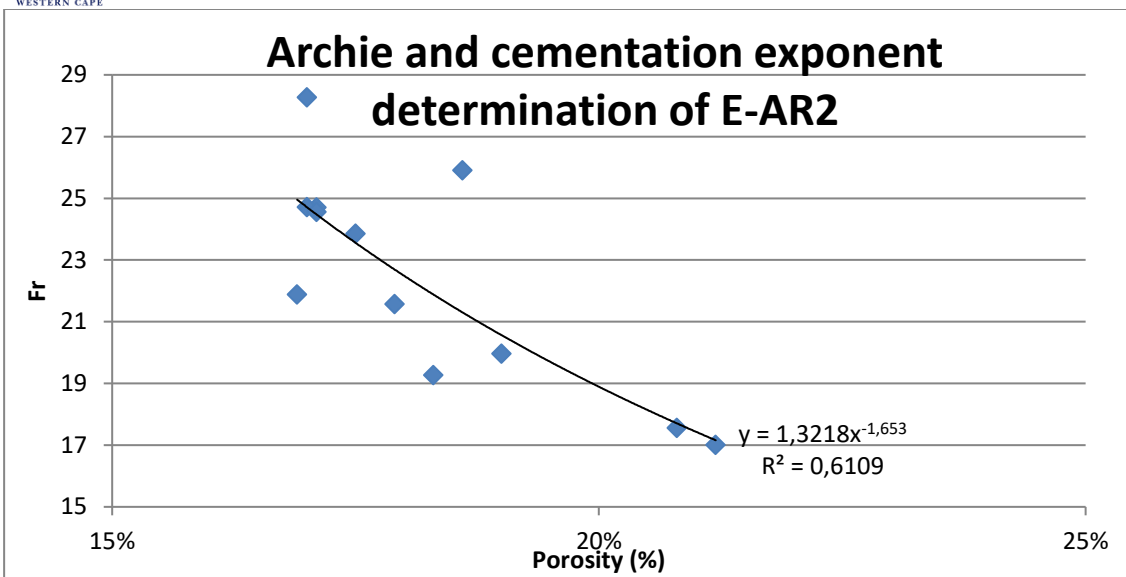


Figure 5.32: Determination of Archie and cementation exponent using the relationship between formation factor and porosity of well E-AR2.

The 12 samples that were used for the calculations of well E-AR2 had an average porosity of 18.16% over the interval of 2442.24-2471.85m. The porosity and formation factor of the samples were measured at ambient conditions and are shown in the table above. By cross-plotting formation factor and porosity, we can determine both Archie's tortuosity (a) as well as the cementation exponent (m) at ambient conditions (figure 5.32).

The correlation coefficient from the measured indicates that 61.09% variance in porosity is accounted for by the formation factor thus suggesting a relatively fair relationship between the formation factor and porosity. The cementation factor (m) of all core samples was calculated from the best-fit trendline and was found to be 1.653 with R² being 0.61. The tortuosity was found to be 1.32. The equation below represents the relationship between formation factor and porosity for well E-AR2:

$$Fr = \frac{1.32}{\phi^{1.653}} \quad (5.11)$$

Where Fr=formation factor, ϕ =Porosity, m=cementation factor (1.653). a=tortuosity (1.32)

5.3.4. Interpretation of cementation factor:

The following table indicates the type of rock corresponding to their respective cementation factors as determined by Archie in 1942. Attached to the table is also a visual representation of consolidated vs. unconsolidated reservoir rocks.

Table 5.10: Indicating the rock type corresponding to the specific cementation factor as determined by Archie.

Author	Cementation Range	Rock Type
Archie (1942)	1.8 - 2.0	Consolidated sandstone
	1.3 - 1.8	Clean unconsolidated sandstone
Primary porosity		
(a) unconsolidated well-sorted sand; high porosity		
(b) sand porosity reduced by admixture of fines or cementation		
Secondary porosity		
(c) Consolidated rock rendered porous by fracturing e.g. crystalline basement		
(d) Consolidated fractured rock with porosity increased by solution		

Figure 5.33: Representation of consolidated vs. unconsolidated reservoir rocks. (Meinzer 1923)

By comparing the reservoir rocks of the three wells to the Archie cementation range, we can see that the reservoir rocks of all three wells are characterized as unconsolidated sandstones as seen in the table below. This means that the rocks are well sorted with fair to good primary porosity as seen in the figure above. As the cementation factor increases, the cement within the rock increases. This means that rocks of E-AR1 are more cemented than the rocks of the other wells.

Table 5.11: Indicating the tortuosity and cementation factor of wells E-BT1, E-AR1 and E-AR2 with their corresponding rock types.

Well	Tortuosity factor (a)	Cementation Factor (m)	Rock Type
E-BT1	2.03	1.64	Unconsolidated Sandstone
E-AR1	1.80	1.72	Unconsolidated Sandstone
E-AR2	1.32	1.65	Unconsolidated Sandstone

5.4. Rock Physics Analysis:

The methods we will be using for the interpretation and discussion of rock physics have been previously discussed in Chapter 4 under Rock Physics Analysis. These methods include (1) the Greenberg-Castagna Method, (2) the Density Estimation Method, (3) the Fluid Substitution Method, and (4) the Elastic Impedance Method.

Both the Greenberg-Castagna and Density Estimation Methods have been used in this research to generate the necessary curves for fluid substitution modelling. The curves generated from the Greenberg-Castagna methods are V_p and V_s , whereas those created from the density estimation method are RhoAgip, RhoLind, and RhoGard which are all density curves. These curves are generated to interpret and discuss the fluid substitution modelling for each of the three wells below.

5.4.1. Shear Velocity Prediction of wells E-BT1, E-AR1 and E-AR2:

The Greenberg-Castagna method has been used in this research to predict the shear wave velocity (V_s) from the compressional wave velocity (V_p). Cross-plotting the results of shear wave vs. compressional wave velocity is important for lithology identification within the reservoir intervals. The following cross plots for all three wells indicate a positive correlation between V_p and V_s . From the cross plots, we can also see that the clustering of data points is aligned with the sandstone trendline, and this indicates that the reservoirs from all three wells are mainly sandstone. Additionally, the data is colour-coded with the Gamma Ray Log which separates the sandstones into clean sandstone, shale sandstone and shale.

From the V_p/V_s cross plot of well E-BT1 (figure 5.34), we can see that the data points are all plotted on the sandstone trendline. This cross plot also indicates that most of the data points are clean sandstone followed by shale sandstone and shale. The V_p/V_s cross plot of well E-AR1 indicates that the data points plotted on the sandstone trendline are mainly clean sandstone followed by shaly sandstone and shale (figure 5.35). Well E-AR2 appears to be mainly clean sandstone plotted on the sandstone trendline with lesser amounts of shale sand and shale (5.36).

The cross plots of all three wells indicate that the clean sandstone occurs mainly in the compressional velocity intervals of 3500-4200 m/s and in the shear velocity interval of 2000-3000 m/s. In

conclusion, we can see that the three wells have a high correlation and a uniform relationship regarding the Vp/Vs cross plots.

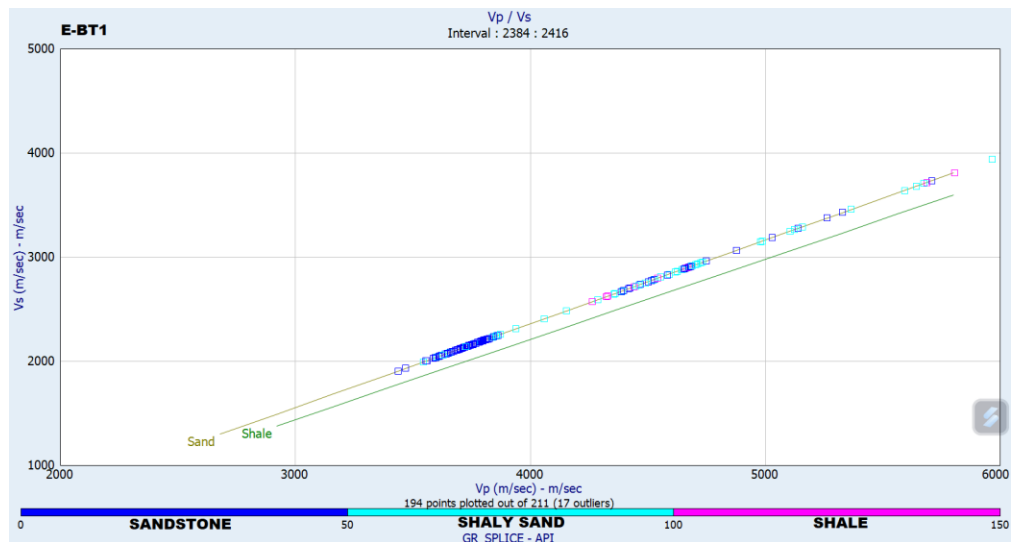


Figure 5.34: Cross plot showing the relationship between compressional and shear velocity of well E-BT1.

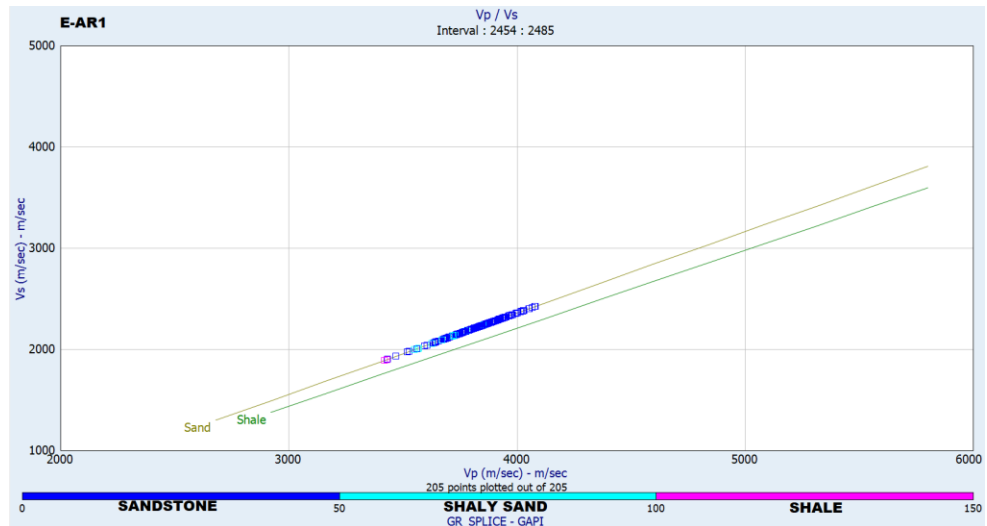


Figure 5.35: Cross plot showing the relationship between compressional and shear velocity of well E-ARI.

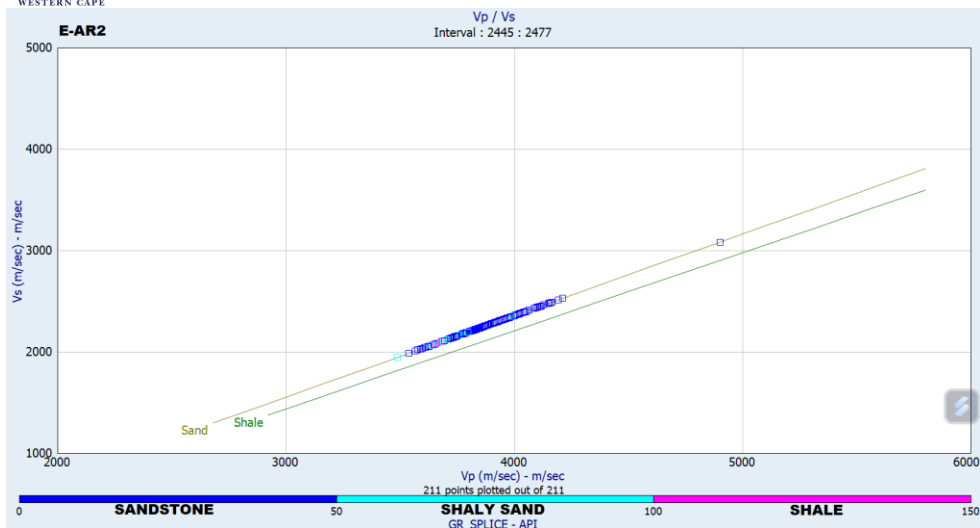


Figure 5.36: Cross plot showing the relationship between compressional and shear velocity of well E-AR2.

5.4.2. Fluid Substitution Modelling:

The data presented in the tables below have been calculated using IP software. This data is also used for the generation of the fluid substitution curves which are presented in the rock physics logs below and further explained in the fluid substitution cross plots. The fluid mixing is based on the Reuss harmonic average formula which minimizes the effect of the flushed-zone hydrocarbons on the sonic logs. The minerals that were used for the fluid substitution are quartz and wet clays and their results are presented in the tables below.

The elastic impedance log plots that are shown below for each well indicate the different calculated parameters (V_p , V_s , AI) of the different fluids across the reservoir intervals. The blue logs indicate 100% brine, the red logs indicate oil, the green logs indicate gas, and the black logs indicate the original in-situ fluids present within the well. Following the Gassmann substitution approach, we can use these different logs to indicate which fluid matches closest with the original fluid to indicate the type of fluids present within the wells.

The fluid properties that have been used for this research are from the PASA reports of well E-BT1. Wells E-AR1 and E-AR2 do not have any fluid properties available, and for that reason well E-BT1 values were used as they form part of the same pressure regime under the same conditions. The fluid properties that were used are also presented in the tables below for each well.

5.4.2.1. Fluid Substitution of Well E-BT1:

The logs that are presented in Figure 5.37 below, indicate that the different rock physical properties identified in the logs below are changed according to the different fluids that are substituted. For, well E-BT1, we can see clearly that the in-situ density log in track 4 is aligned with the density logs of oil and brine and separated from the gas density. For Vp and Vs, we can see that oil is the closest to the in-situ log, followed by gas. The brine log seems to be separated for most parts of logs Vp and Vs. However, for the poison's ratio, we can see that the brine log is closest to the in-situ log. Finally, we can see that the AI logs show a significant decrease from brine to oil to gas.

In conclusion, we can see that E-BT1 is mainly composed of oil as these logs are closer to the in-situ logs than gas and brine. We can also see that all logs are almost perfectly aligned for the first 10 meters of the reservoir interval. This can indicate that all fluids are present within the first 10 meters. As the acoustic impedance increases, the reservoir rocks become denser and stiffer and this may be due to the change in lithology, clay content, porosity, and permeability. The higher the acoustic impedance, the better the reservoir qualities for hydrocarbons. This means that the reservoir quality is highest at 2405-2410 m intervals. However, due to high clay content and lower porosity at 2390-2395 m, the increase in acoustic impedance does not necessarily indicate an increase in reservoir quality.

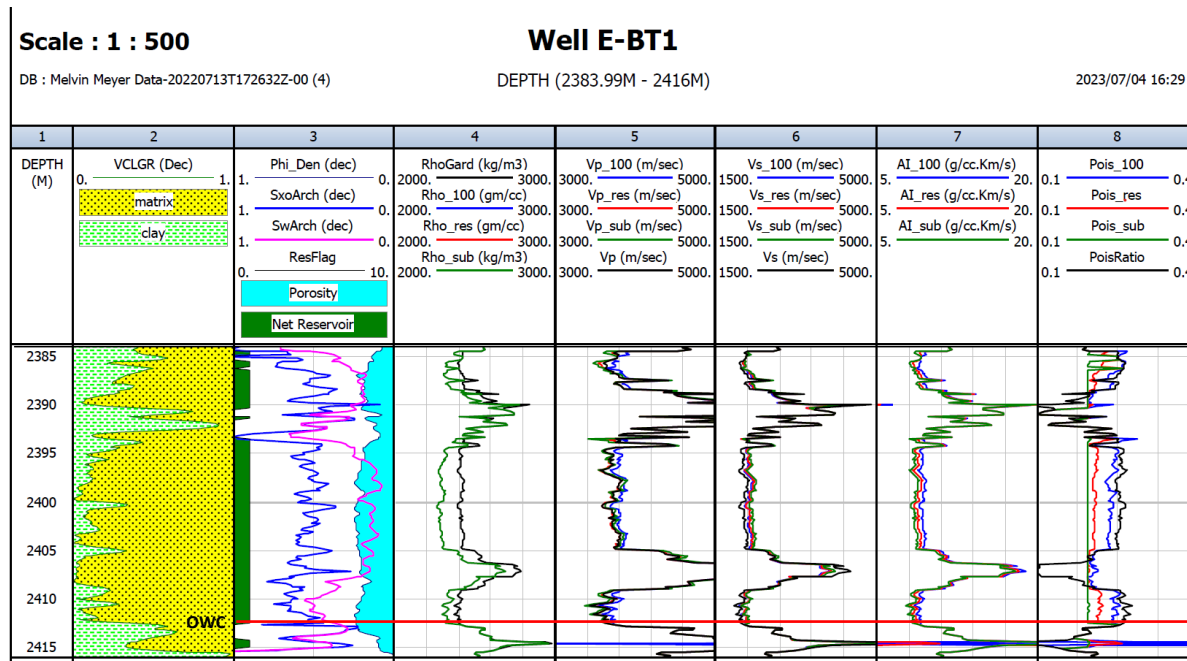


Figure 5.37: Elastic Impedance log indicating Gassmann Fluid Substitution of well E-BT1.

Table 5.12: Gassmann Fluid Substitution Results of well E-BT1.

E-BT1			
Fluid Properties			
	Brine	Oil	Gas
Density (gm/cc)	0.987	0.705	0.184
Bulk Modulus (Gpa)	2.564	0.595	0.052
Velocity (m/s)	1612	918	535
Matrix Properties			
Mineral Name	Quartz	Wet Clay	
Density (gm/cc)	2.650	2.600	
Bulk Modulus (Gpa)	37.000	21.00	
Velocity (m/s)	6050	3410	
Average Gassmann Results			
Data Interval: Reservoir			
Vp (m/s)	4298		
Vs (m/s)	2600		
Vp/Vs	1.653		
Poisson ratio	0.211		
Density (gm/cc)	2.498		
Quartz (dec)	1.000		
Wet clay (dec)	0.000		
Porosity (dec)	0.181		
SwArch (dec)	0.269		
SxoArch (dec)	0.543		
Flushed zone fluid mixture is oil/brine			
Fluid mixing using Reuss harmonic average			
Fluid Properties			
Fluid Density (gm/cc)	0.858		
Fluid Modulus (Gpa)	1.0197		
Fluid Velocity (m/s)	1090		
Dry rock properties			
Bulk modulud (Gpa)	21.783		
Shear Modulus (Gpa)	16.888		
Poisson ratio	0.192		

Modulus ratio (K/u)	1.290		

5.4.2.2. Fluid Substitution of Well E-AR1:

Figure 5.38 below, indicate that the different rock physical properties identified in the logs below are changed according to the different fluids that are substituted. For, well E-AR1, we can see that the in-situ density logs are aligned with oil within the oil zone and with water in the water zone. The in-situ logs are slightly separated from the acoustic gas logs.

For the compressional velocity, we can see that the oil and gas are the closest to the in-situ log in the oil zone over a depth of 2455-2463 m, whereas within the water zone at a depth of 2463-2485 m the water is closest with in-situ log with oil and gas being separated. This can indicate that the previously mentioned oil and water zones consist of oil and water, respectively. The shear sonic logs in track 6 indicate that water and oil are closest to the in-situ log with gas slightly separated.

The in-situ poisons ratio seems to be closer to oil over the entire reservoir interval, followed by water and finally gas. This indicates that oil is the most likely fluid that occurs within the reservoir interval. Finally, we can see that the AI logs show a slight constant decrease from water to oil to gas over the entire reservoir interval. An increase in clay content as seen at a depth of 2463 m causes the acoustic impedance to decrease (Red Arrow). However, this does not affect the reservoir quality as the argillaceous layer of rock is too thin.

In conclusion, well E-AR1 is mainly composed of oil as these logs are closest to the in-situ logs. We can also see that oil and gas are almost perfectly aligned for the first 10 meters of the reservoir interval for compressional velocity, followed by water after 10 meters. This once again confirms that there is an OWC at a depth of 2462 m.

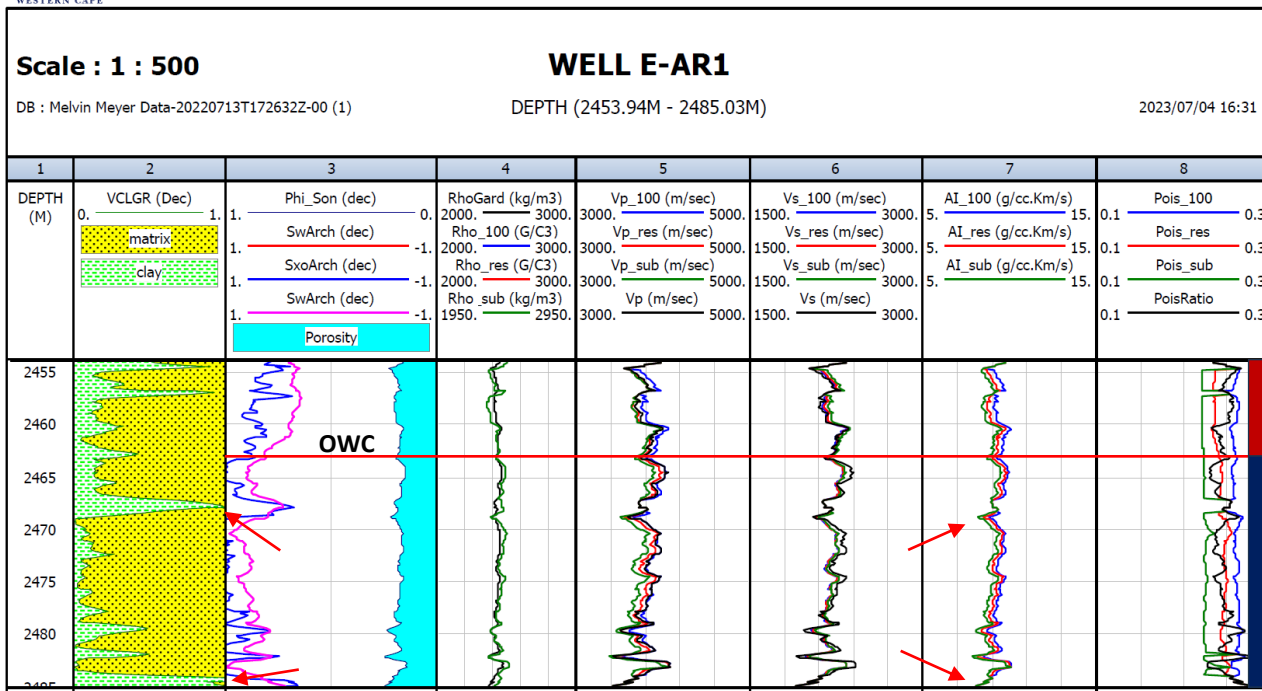


Figure 5.38: Elastic Impedance log indicating Gassmann Fluid Substitution of well E-AR1.

Table 5.13: Gassmann Fluid Substitution Results of well E-AR1.

E-AR1			
Fluid Properties			
	Brine	Oil	Gas
Density (gm/cc)	0.988	0.705	0.184
Bulk Modulus (Gpa)	2.570	0.600	0.053
Velocity (m/s)	1613	922	534
Matrix Properties			
Mineral Name	Quartz	Wet Clay	
Density (gm/cc)	2.650	2.600	
Bulk Modulus (Gpa)	37.000	21.00	
Velocity (m/s)	6050	3410	
Average Gassmann Results			
Data Interval: Reservoir			
Vp (m/s)	3307		
Vs (m/s)	1890		
Vp/Vs	1.749		
Poisson ratio	0.257		
Density (gm/cc)	2.338		

Quartz (dec)	1.000		
Wet clay (dec)	0.000		
Porosity (dec)	0.172		
SwArch (dec)	0.547		
SxoArch (dec)	0.465		
Flushed zone fluid mixture is oil/brine			
Fluid mixing using Reuss harmonic average			
Fluid Properties			
Fluid Density (gm/cc)	0.837		
Fluid Modulus (Gpa)	0.9324		
Fluid Velocity (m/s)	1056		
Dry rock properties			
Bulk modulus (Gpa)	12.143		
Shear Modulus (Gpa)	8.355		
Poisson ratio	0.220		
Modulus ratio (K/u)	1.453		

5.4.3. Fluid Substitution of Well E-AR2:

Figure 5.39 below, indicate that the different rock physical properties identified in the logs below are changed according to the different fluids that are substituted. From figure 5.39, we can see that for well E-AR2 the in-situ density curve in track 4 is aligned with the density curve of oil and separated from the density curves of water and gas. This indicates that well E-AR2 has the same density as oil within the oil zone. From the compressional velocity (V_p) curves in track 5, all three fluids are aligned with the in-situ V_p curve over the entire reservoir interval. The shear velocity and poison ratio curves show that all three fluids are separated from the in-situ curve. Lastly, we can see that the acoustic impedance curves for all three fluids are aligned.

With the use of the density curves, we can conclude that well E-AR2 is mainly composed of oil within the oil zone as the density curve is closer to the in-situ density curve than water and gas. In the water zone, both oil and gas are aligned with the in-situ load, thus indicating that both fluids are present. We can also see that an increase in clay content leads to a small decrease in acoustic impedance as indicated in the figure below (red arrows). However, due to the reservoir being

predominantly sandstone, the small clay intervals seen in the logs don't have a great effect on the reservoir quality.

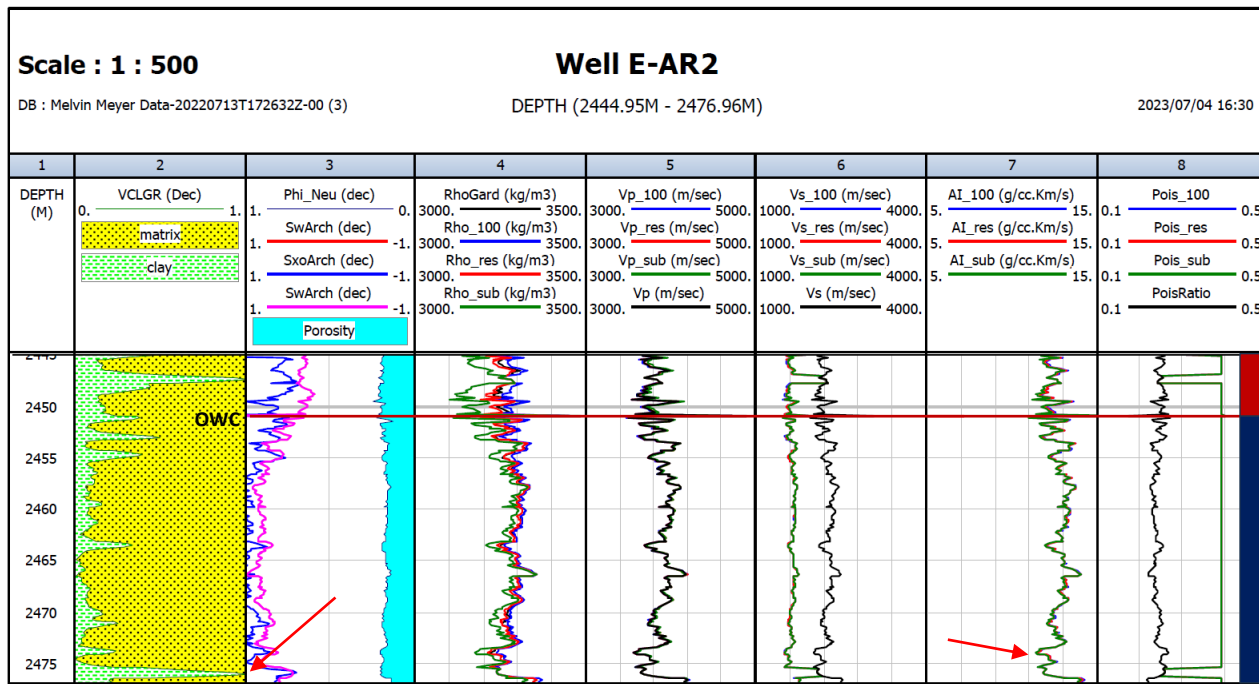


Figure 5.39: Elastic Impedance log indicating Gassmann Fluid Substitution of well E-AR2.

Table 5.14: Gassmann Fluid Substitution Results of well E-AR2.

E-AR2			
Fluid Properties			
	Brine	Oil	Gas
Flushed Zone			
Density (gm/cc)	0.987	0.704	0.186
Bulk Modulus (Gpa)	2.562	0.591	0.053
Velocity (m/s)	1611	916	532
Matrix Properties			
Mineral Name	Quartz	Wet Clay	
Density (gm/cc)	2.650	2.600	
Bulk Modulus (Gpa)	37.000	21.000	
Velocity (m/s)	6050	3410	
Average Gassmann Results			
Data Interval:			
Vp (m/s)	3148		

Vs (m/s)	1675		
Vp/Vs	1.879		
Poisson ratio	0.302		
Density (gm/cc)	3.104		
Quartz (dec)	1.000		
Wet clay (dec)	0.000		
Porosity (dec)	0.210		
SwArch (dec)	0.582		
SxoArch (dec)	0.562		

Flushed zone fluid mixture is oil/brine

Fluid mixing using Reuss harmonic average

Fluid Properties

Fluid Density (gm/cc)	0.863		
Fluid Modulus (Gpa)	1.041		
Fluid Velocity (m/s)	1098		

Dry rock properties

Bulk modulud (Gpa)	37.000		
Shear Modulus (Gpa)	8.714		
Poisson ratio	0.391		
Modulus ratio (K/u)	4.246		

Chapter 6: Multi-mineral and Petrographic Analysis

6.1. Sedimentological Interpretation of Core:

The purpose of describing the sedimentary features of the cores is to provide a detailed compilation of all results of the routine petrographic analysis performed on wells E-AR1, E-AR2, and E-BT1. Only a few selected core boxes from the three wells were carefully examined at the Petroleum Agency of South Africa and the core samples were taken from these core boxes (Table 6.1). All the cores from the three wells have been directly taken from the reservoir intervals. The cores were selected based on the differences in lithology found in the wireline logs.

Well Name	Reservoir Interval	Cores
E-BT1	Reservoir 1: 2382-2416m	Core 1: 2384-2400m Core 2: 2402-2410m Core 3: 2412-2430m
E-AR1	Reservoir 1: 2452-2484m	Core 1: 2455-2473 m
	Reservoir 2: 2802-2840m	No Cores
	Outside Reservoir	Core 2: 2849-2852m Core 3: 3116-3132m
E-AR2	Reservoir 1: 2445-2478m	Core 1: 2442-2455m Core 2: 2455-2472m
	Reservoir 2: 2804-2836m	Core 3: 2803-2820m Core 4: 2821-2826m

Table 6.1: This table indicates the cores taken from the reservoirs for each well.

6.1.1. Facies found in wells E-AR1, E-AR2 and E-BT1:

There were about 5 lithofacies recognized from the sand-dominated reservoir intervals of wells E-AR1, E-AR2 and E-BT1. Table 6.2 below shows the various lithofacies identified along with their reservoir quality in this study. A total of 5 lithofacies were identified in the three wells. The core photos in the table are used to represent the identified facies.

Table 6.2: Identified Facies with their reservoir quality and Descriptions

Facies	Description	Reservoir Quality	Facies Photos
Facies 1	Clean massive fine to coarse grained sandstones (most frequent in reservoirs)	Very Good	
Facies 2	Cross-bedded sandstones containing mud drapes	Good	
Facies 3	Heterolithic interbedded sand-shale facies	Poor	

Facies 4	Shale	Impervious	
Facies 5	Breccia	Poor	

The following figures will indicate the different sedimentary features that were observed within these identified lithofacies.

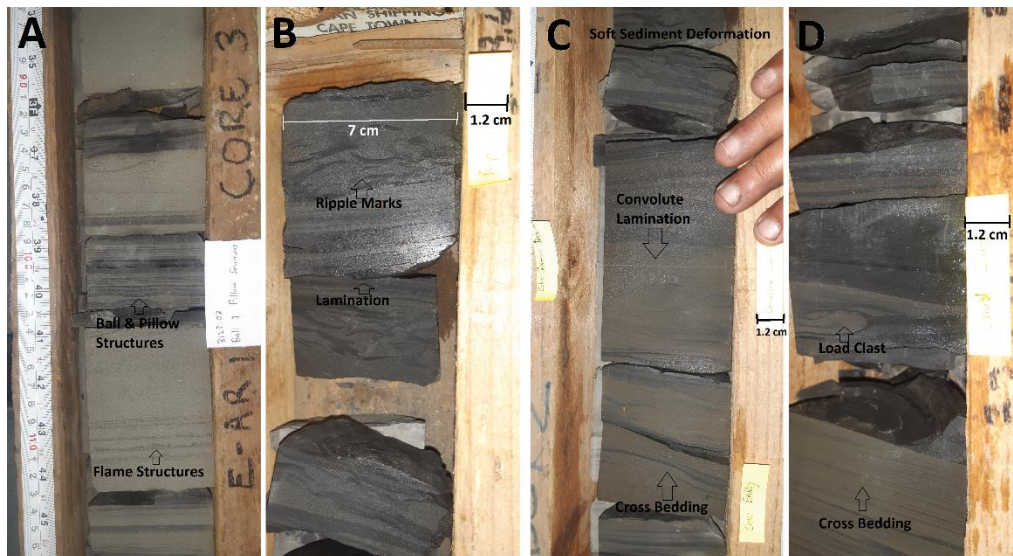


Figure 6.1: Heterolithiic sandy shales from well E-ARI which displays various types of sedimentary structures formed through soft sediment deformation. A) Ball and Pillow as well as Flame structures. B) Horizontal lamination and ripple marks. C) Convoluted lamination and cross bedding. D) Load clasts

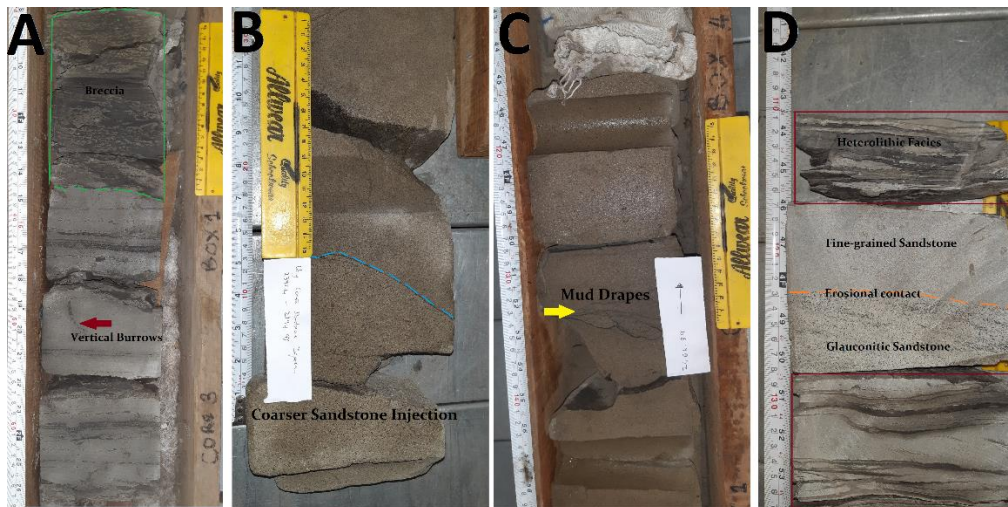


Figure 6.2: Heterolithic and massive sandstone facies of well E-BT1. A) Heterolithic shale sand with vertical burrows in the fine grained sandstone, there is also a small section of breccia (green); B) Poorly sorted coarse sandstone injection with an erosional contact (Thin section 19); C) Medium to coarse grained sandstone with some cross-bedded mud drapes (Thin Section); D) Heterolithic shale sand in red, and there an erosional contact between coarse grained glauconitic sandstone (Thin section 9) and fine-grained sandstone.

6.1.2. Cored Sections of Interest

6.1.2.1. Brief sedimentological analysis of Well E-BT1:

All five facies have been identified in the cored sections of well E-BT1 (figure 6.3). The 3 cored sections fall within the well's reservoir, which has a depth of 2382-2416m. Core 1 with a depth of 2384-2400m, contains facies 1 and 2 and consists mainly of, clean, massive fine to medium-grained sandstones that are moderately to well sorted. From the core description, the presence of quartz, feldspars, glauconite, phosphorite, and minor amounts of micas are found throughout the core. The lithology remained constant throughout, with no changes noticed. Within the core, two coarser-

grained sandstone injections with erosional contacts were also discovered as seen on the sedimentary log.

Core 2, spanning from 2402-2410m deep, displays two distinct facies types: facies 1 comprising of dense fine to medium-grained sandstone, while facies 2 is composed of cross-bedded sandstones containing mud-drapes. Glauconite and mica are found throughout, and the mud drapes within this core appear crinkled. Siderite nodules occur throughout, and at a depth of about 2409.7m, mud clasts are parallel-oriented.

The cored section for core 3 has a depth of 2412-2430m and contains facies 1, 3 and 5. The sedimentary composition of this core is mainly heterolithic sandy-shale rocks, with some fine-grained sandstone beds in between. The sandstones contain substantial amounts of glauconite throughout the core and there are also some vertical burrows and organic matter present as indicated on the sedimentary log. At a depth of 2412.36-2412.20m, breccia is formed with an interbedded claystone bed. The heterolithic facies within this core display numerous soft-sediment deformation structures, which may be the result of compaction, sliding, or liquefaction.

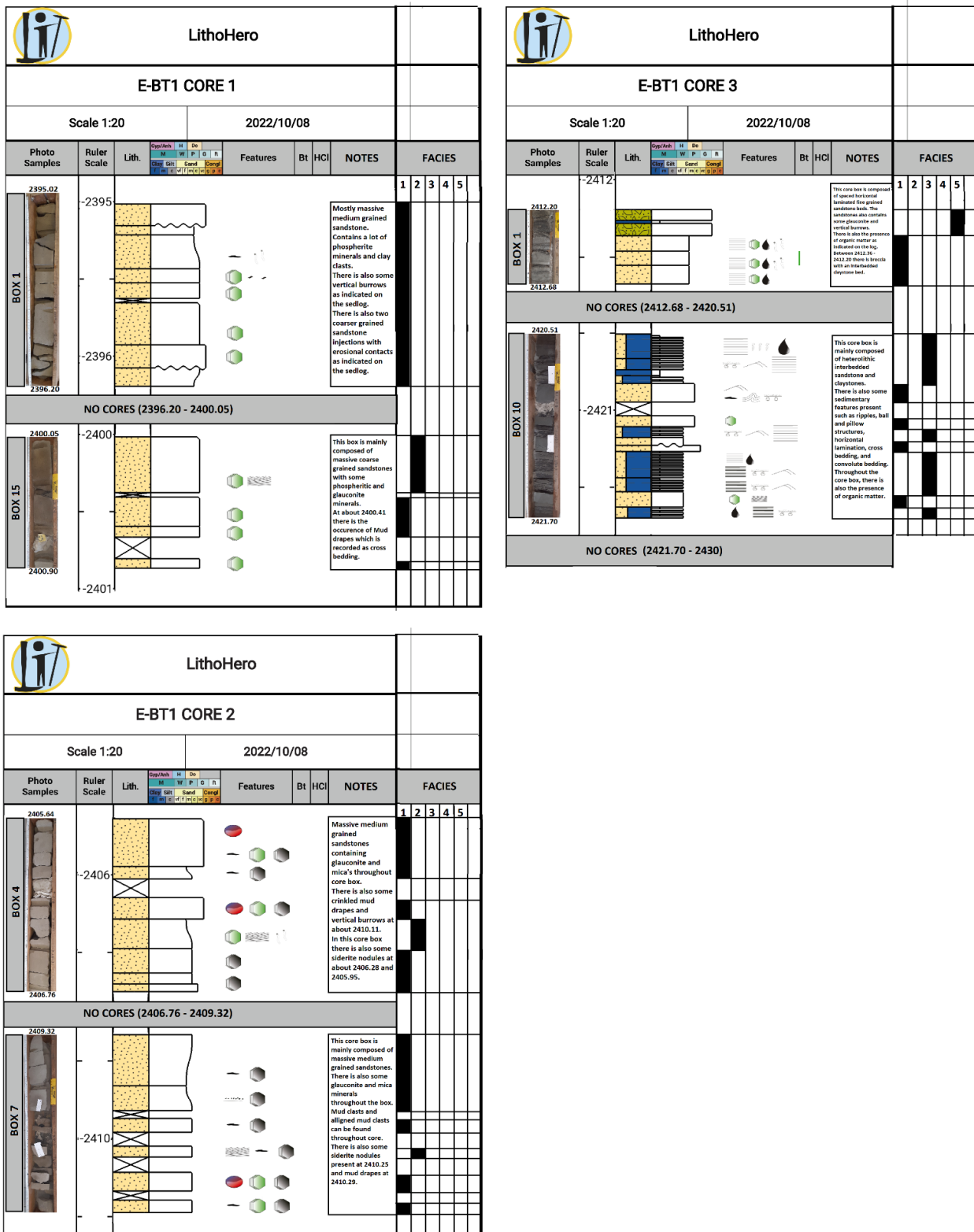


Figure 6.3: Sedimentary log plot of well E-BT1

6.1.2.2. Brief sedimentological analysis of Well E-AR1:

Four facies have been identified for the 3 cored sections of well E-AR1 (figure 6.4). Core 1 has a depth of 2455-2473 m, and it falls within the first reservoir (2452-2484m). This core is mainly composed of clean, massive fine to medium-grained sandstones that are moderately to well sorted. From the core description, there is the presence of quartz, feldspars, glauconite, phosphorite, and minor amounts of micas throughout. For core 1, the lithology doesn't change as all of them are comprised of massive sandstones with some cross-bedded features such as mud drapes and stylolites as indicated on the sedimentary logs. However, at about 2466m to 2467m, the presence of shale becomes evident, and they are interbedded within the sandstones thus representing heterolithic facies 3.

Core 2 which has a depth of 2849-2852m has 2 facies types namely, massive fine to medium-grained sandstone (facies 1) and muddy shale (facies 4). The sandstones contain clay clasts and within the muddy shale there is the appearance of a siltstone dyke. The sandstones also have sulfur stains on them which may be a result of drilling. In this core, there is also the presence of organic matter as indicated on the sedimentary log. This core falls outside the second reservoir of well E-AR1 (2802-2840m).

The cored section for core 3 has a depth of 3116-3132m and the facies occurring within this cored section are facies 1, 2, 3 and 4. This core is mainly composed of heterolithic sandy-shale rocks. These heterolithic facies contain a lot of soft-sediment deformation structures and this can be the result of either compaction, sliding, liquefaction, etc. The soft-sediment deformation features are shown in the figure above.

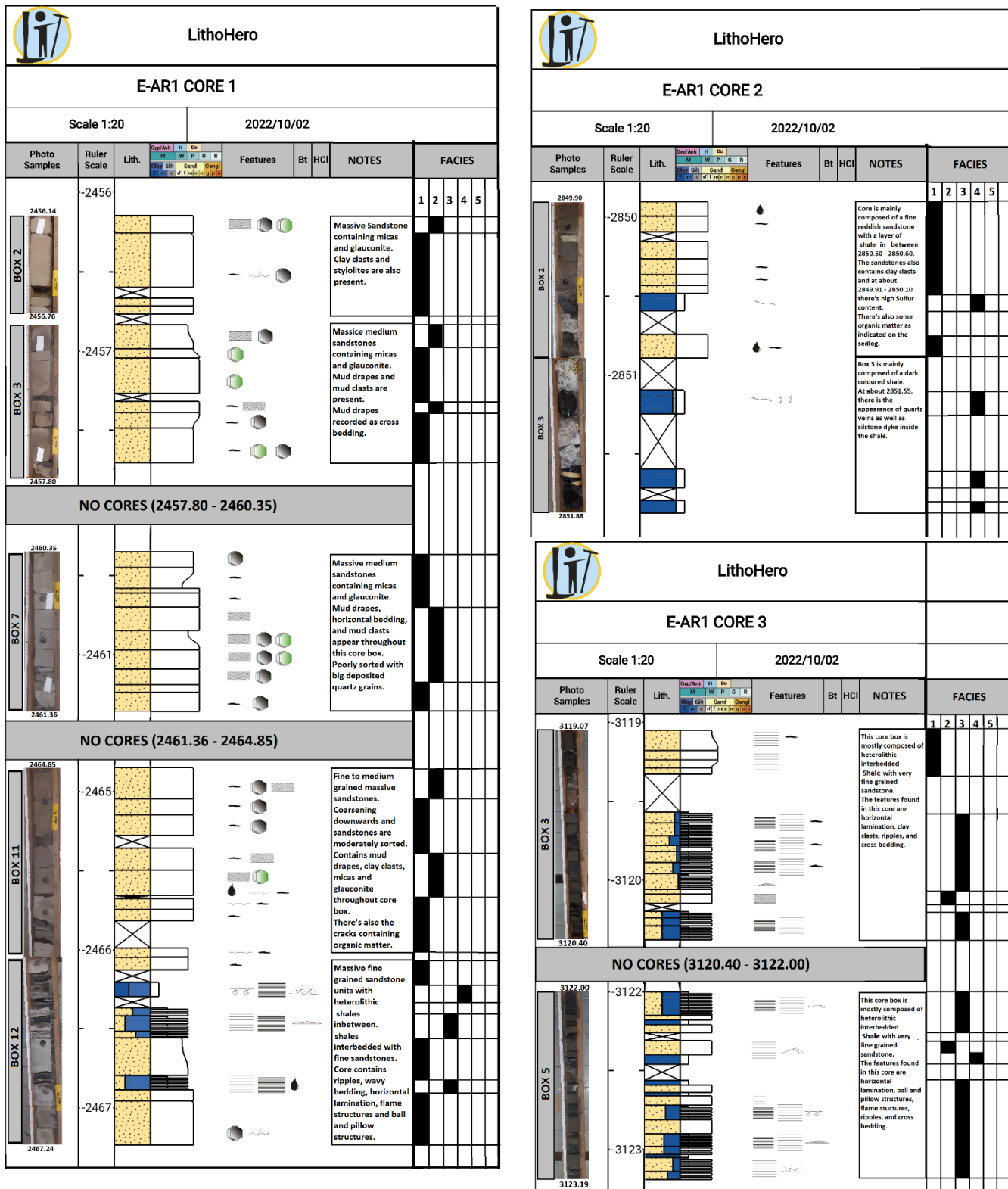


Figure 6.4: Sedimentary log plot of well E-AR1

6.1.2.3. Brief sedimentological analysis of well E-AR2:

Three facies have been identified for the 4 cored sections of well E-AR2 (figure 6.5). These facies are massive fine to coarse-grained sandstones (facies 1), cross-bedded sandstones containing mud drapes (facies 2), and interbedded sand-shale or heterolithic facies (facies 3). This well is mainly composed of massive medium to coarse-grained sandstones and contains quartz, feldspars, glauconite and minor amounts of micas.

Core 1 has a depth of 2442-2455m and falls within the first reservoir of well E-AR1 (2445-2478m). This reservoir corresponds to the first reservoir of well E-AR1 as they are part of the same horizon. This core is mainly composed of clean, massive medium to coarse-grained sandstones that are moderately to well sorted. For core 1, the lithology doesn't change as all of them are comprised of massive clean sandstones with some cross-bedded features such as mud drapes and alignment of clay clasts as indicated on the sedimentary logs. Within this core, there is also the presence of siderites throughout.

Core 2 which has a depth of 2455-2472m is comprised of massive fine to medium-grained sandstones (facies 1). This core forms part of reservoir 1 of well E-AR2 (2445-2478m). The sandstones are medium grained, moderately well sorted and contain clay clasts. These sandstones have siderite halos present which indicate high Fe content.

The cored section for core 3 has a depth of 2803-2820m and the facies occurring within this cored section are facies 1, 2, and 3. This core forms part of the second reservoir of well E-AR2 (2804-2836m). It is mainly composed of massive medium to coarse grained sandstones. Within this core there are also stylolites present as indicated on the sedimentary log. This core also shows a very sharp contact between facies 1 and facies 3 as shown on the sedimentary log.

The cored section for core 4 has a depth of 2821-2826m and falls within the second reservoir. This core has massive medium to coarse-grained sandstones that are well sorted. At 2822m there is a big siderite nodule with very high Fe content.

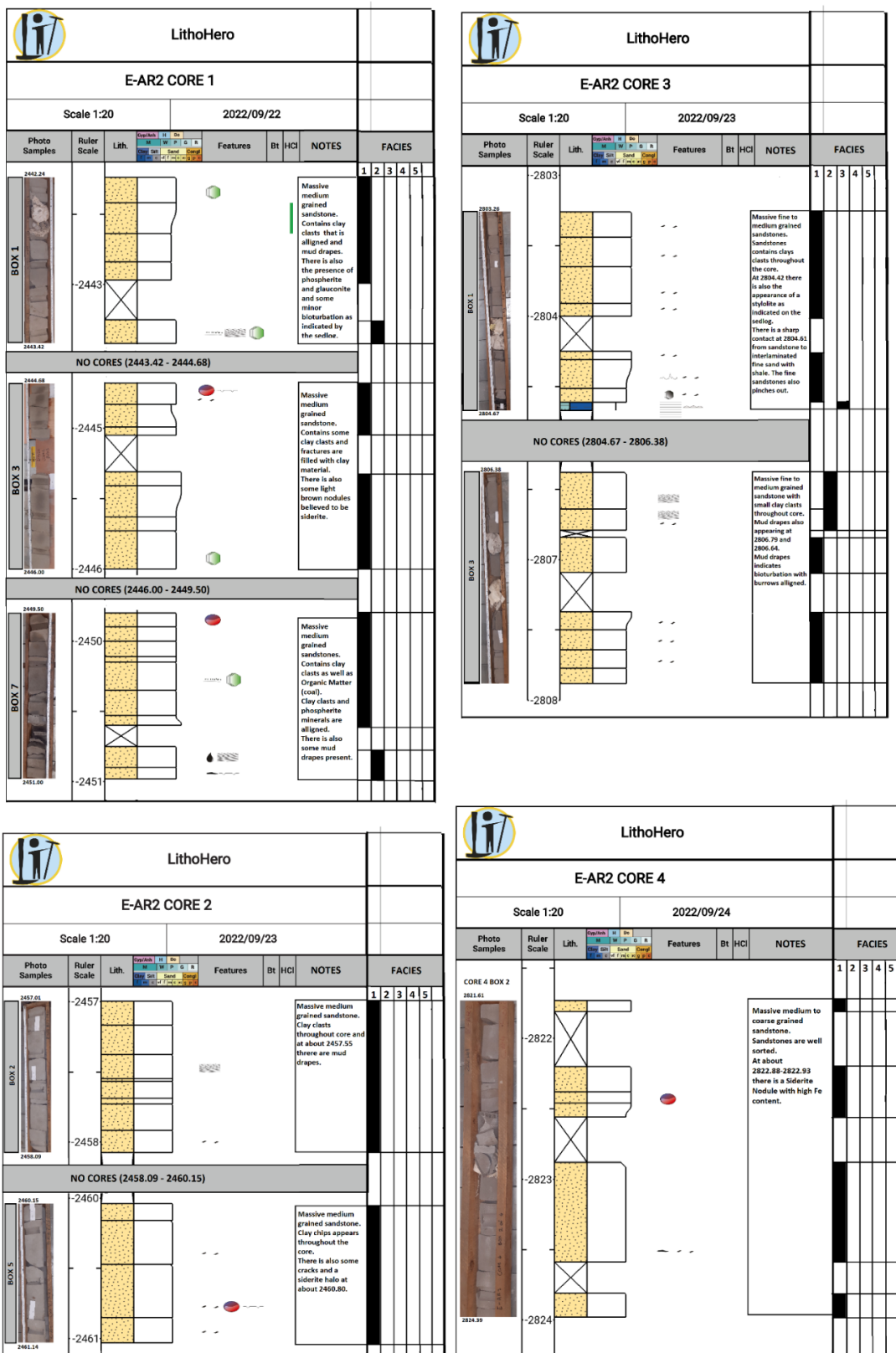


Figure 6.5: Sedimentary log plot of well E-AR2

6.2. Thin Section Analysis:

About twenty-four thin sections were made from the core samples collected at PASA from selected depths of reservoirs E-BT1, E-AR1 and E-AR2. All these samples were also analyzed through XRF analysis. These sandstones analyzed for the three wells consist of three main components namely, framework grains, pores, and cementing material.

With the use of thin sections, it is shown that the overall sandstone appears to be fine to medium to coarse-grained and shows rounded to subrounded grains with poor to well sorting. The grain contacts that occur within the thin sections are point contacts, sutural contacts (dissolution), planar contacts and interpenetrating contacts (figure 6.6). The contacts that occur can give an indication of the diagenesis that took place. The mineral grains found within these sandstones are mainly quartz, feldspars, glauconite, muscovite and biotite. The cement within these sandstones is mainly clay, calcite, quartz, and hematite cement.

6.2.1. Minerals of interest:

Table 6.3 is a representation of the common minerals with their chemical formula that are found within the reservoirs of the three wells. The chemical formula indicates the type of elements found within the mineral. The minerals found in the thin sections can be compared to the elemental composition of the XRF results.

Table 6.3: Representation of the common minerals with their respective chemical formula.

Mineral Name	Chemical Formula
Quartz	SiO_2
Alkali Feldspar	$(\text{K},\text{Na})\text{AlSi}_3\text{O}_8$
Orthoclase Feldspar	KAlSi_3O_8
Biotite	$\text{K}(\text{Mg},\text{Fe})_3\text{AlSi}_3\text{O}_{10}(\text{F},\text{OH})_2$
Muscovite	$\text{KAl}_2(\text{Si}_3\text{Al})\text{O}_{10}(\text{OH})_2$
Glauconite	$(\text{K},\text{Na})(\text{Fe},\text{Al},\text{Mg})_2(\text{Si},\text{Al})_4\text{O}_{10}(\text{OH})_2$
Hematite	Fe_2O_3
Calcite	CaCO_3

Quartz:

Quartz is the most dominant mineral within these sandstones and the quartz grains show unit extinction while some show undulose extinction. The quartz grains are mainly subrounded to subangular. The quartz minerals exist mainly as monocrystalline grains but, in some cases, they also appear as polycrystalline grains. In most of the samples, the microcrystalline quartz acts as a cement that fills up the interstitial spaces between the quartz grains. The quartz grains indicate secondary overgrowth that precipitates around the original quartz grain.

Feldspars and Lithic Fragments

The rock fragments appear to be more frequent than the feldspars in most of the thin sections making up about 3-5% in comparison to 1-2%, respectively. The feldspar grains occur mainly as Alkali feldspars and plagioclase, but it is noted that most of the feldspars do not show any twinning. The feldspar grain appears to be subrounded to subangular and is fine to medium-grained. The lithic fragments occurring within these thin sections are made up of igneous, metamorphic, and sedimentary rock clasts. These lithic fragments consist of quartz and feldspars that have undergone chemical alteration.

Micas

The common micas that occur within these thin sections are biotite and muscovite. In some thin sections the occurrence of either appears to be more abundant than the other. The reason for this could be that the abundant mica is more stable within the type of depositional environment. In these thin sections, there is also the presence of the green potassium-rich mica, named glauconite and the name comes from the fact that it is a member of the group of potassium and iron-rich phyllosilicate minerals. These minerals give an indication of the depositional environments as they mainly occur at water depths of between 50 and 500m, on the outskirts of continental shelves and upper parts of continental slopes (Nichols 2009).

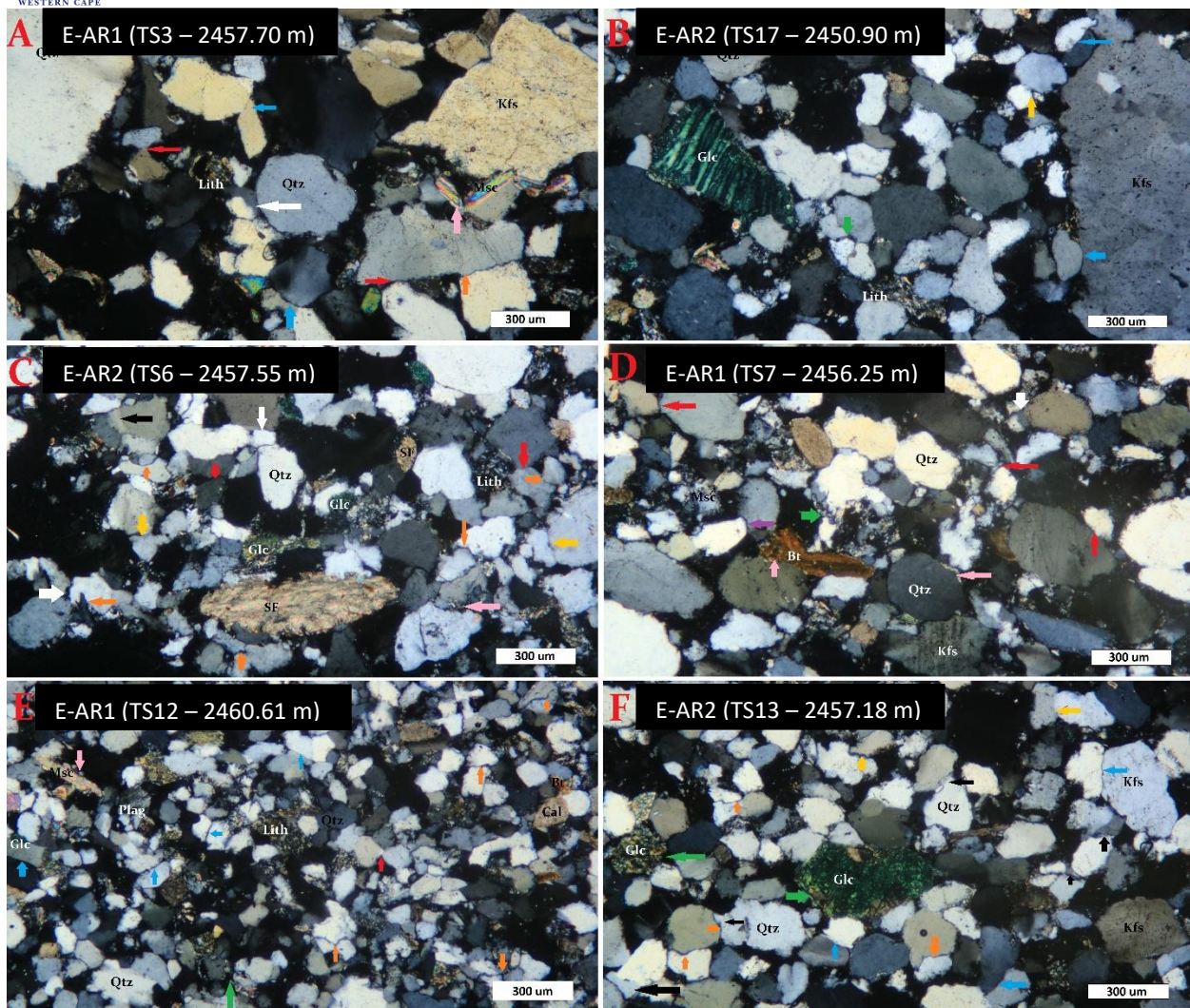


Figure 6.6: Thin section photomicrographs of sandstones showing the contacts that exist between mineral grains: (A-TS3) point contacts (red arrow), long contacts (blue), concavo-convex contacts (orange), Quartz overgrowth (white), alteration along the boundary of deformed muscovite (pink); (B-TS17) sutural contacts (green) and point contacts (yellow) ; (C-TS6) quartz cement (white), quartz overgrowth (black), sutured contacts (yellow), alteration along grain boundary (pink) ; (D-TS7) quartz overgrowth (white), alteration along grain boundary (pink), replacement minerals (green) ; (E-TS12) point contacts (red), long contacts (blue), alteration along muscovite grain boundary (pink) ; (F-TS13) glauconite being replaced by clay minerals at boundary (green), Quartz cement (black), sutured contacts (yellow). Abbreviations: Qtz=Quartz, Plag= plagioclase, Kfs= K-Feldspar, MSc= Muscovite, Bt= Biotite, Glc= Glauconite, Lith= Lithic Fragments, SF= Shell fragments

Matrix and Cement

The matrix within these samples is mainly made from clay minerals, calcite, hematite, and quartz that fill up the pore spaces between grains, thus reducing the amount of pore spaces (figure 6.7). The

clay minerals of the matrix can be either detrital or diagenetic in form. The diagenetic matrix minerals form due to the framework grains undergoing alteration, precipitation and recrystallisation.

Calcite Cement: Calcite cement occurs as a pore-filling and replacement mineral within the matrix and between the grains. As seen from the thin sections, calcite attacks and replaces most of the clay matrix and detrital grains. The figure shows how calcite surrounds the quartz grain and fills up any pore spaces available, thus reducing the porosity.

Hematite Cement: Hematite also acts as a strong replacement mineral within the cement. It occurs as a dark brown cement that fills the pore spaces and thus reduces the amount of porosity.

Quartz Cement: Quartz cement is formed mainly due to the result of precipitation of silica. The quartz cement fills the pore spaces and is also the cause of overgrowth around quartz grains. The silica which causes the quartz cement is because of the dissolution of feldspars and micas.

Clay Cement: Clay cement is the most dominant cementing material within these sandstones. They fill the matrix between the gains and act as a rim cement at the edges of the grains. The cement are formed due to the dissolution of feldspars and recrystallize within the pore spaces.

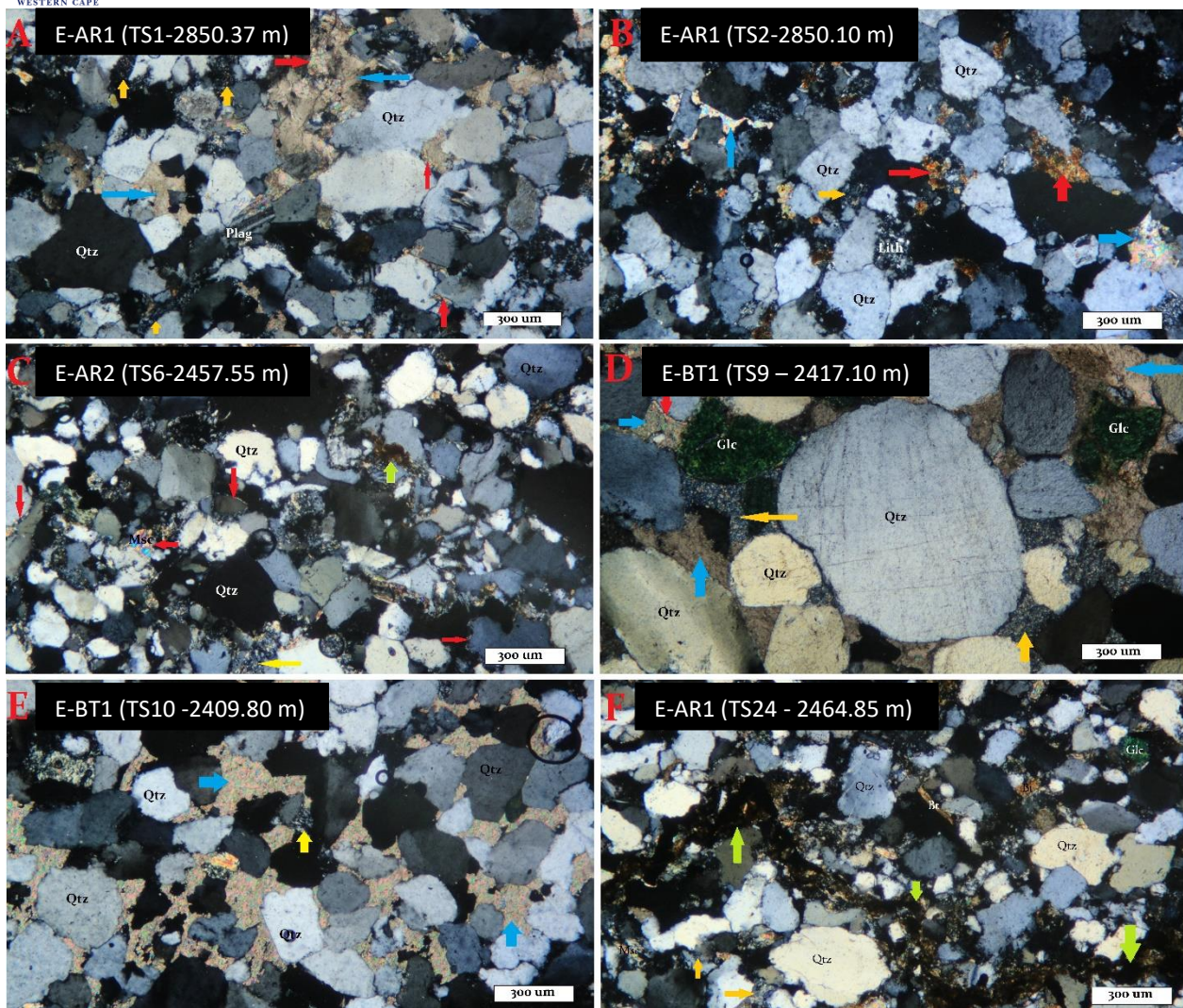


Figure 6.7.: Thin section photomicrographs of sandstones showing the cement and matrix that exists between mineral grains: (A-TS1) Clay minerals replacing calcite (red arrow), calcite cement (blue), microcrystalline quartz (yellow); (B-TS2) hematite cement (red), clay minerals replacing calcite (blue) ; (C-TS6) clay minerals replacing boundary minerals (red), hematite cement (green), microcrystalline quartz cement (yellow), (D-TS9) calcite cement in matrix (blue), microcrystalline quartz cement (yellow); (E-TS10) calcite cement altered by clay (blue), microcrystalline quartz (yellow); (F-TS24) stylolitic hematite being altered by clay minerals at boundary (green), microcrystalline quartz (yellow). Abbreviations: Qtz=Quartz, Plag=plagioclase, Kfs= K-Feldspar, MSc=Muscovite, Bt=Biotite, Glc=Glauconite, Lith=Lithic Fragments, SF= Shell fragments

6.2.2. Petrography overview of wells:

6.2.2.1. Petrography of Well E-BT1

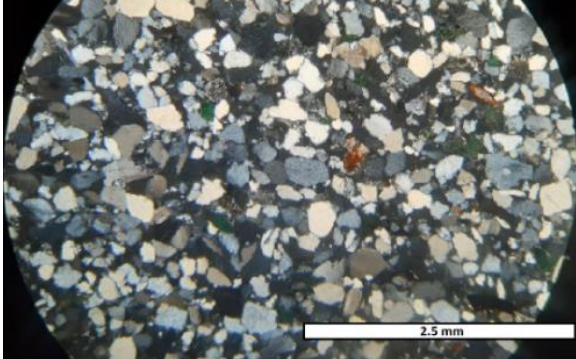
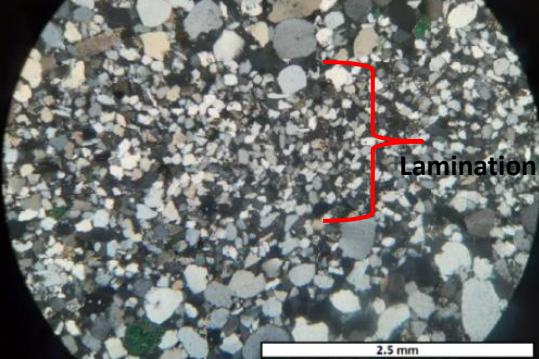
In well E-BT1 all the previously mentioned minerals are present. The sandstones of this well are medium to coarse-grained and have poor to well-sorting. In this well, there is a high concentration

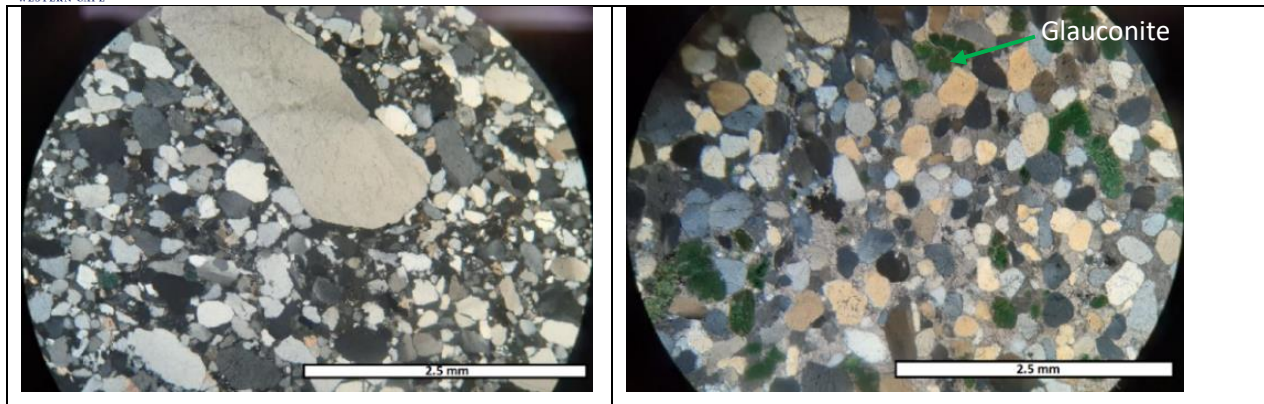
of glauconite thus suggesting that deposition took place towards the proximal parts of the submarine fan.

The sandstones are mainly cemented by clay, quartz, and calcite cement. Quartz overgrowths are the main pore filling cement within these sandstones. The poorly sorted sandstone that occurs around 2396 to 2400m may have been affected by the sandstone injection which is shown in the core logging section above.

Within these sandstones, it is evident that there has been moderate compaction due to the long planar contacts and less sutural and concave-convex contacts. The common minerals found within these sandstones are quartz with minor amounts of feldspars, glauconite, and very little amounts of muscovite and biotite. The dominant cement that occurs within these sandstones are clay, quartz, and calcite cement.

Figure 6.8: Overview of the thin sections of well E-BT1

<p>A. Thin Section 22: Well sorted sandstone at a depth of 2395.53m</p> 	<p>B. Thin Section 19: Poorly to moderately sorted laminated sandstone at a depth of 2396.08m</p> 
<p>C. Thin Section 20: Poorly sorted sandstone at a depth of 2405.93m</p>	<p>D. Thin Section 9: Well-sorted sandstone containing glauconite at a depth of 2417.10 m.</p>



6.2.2.2. Petrography of Well E-AR1

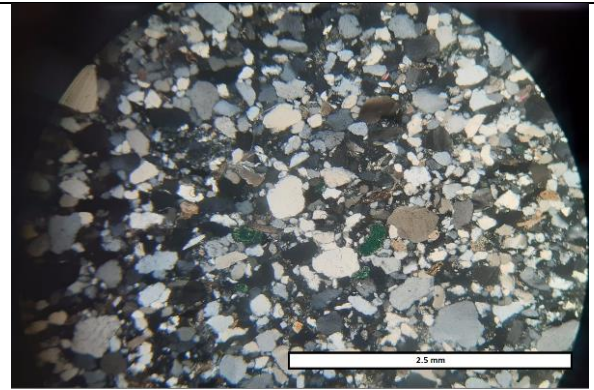
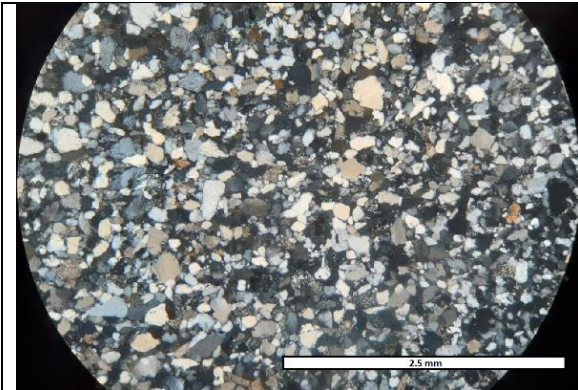
In well E-AR1 all the previously mentioned minerals are present. The sandstones of this well appear to be fine to coarse-grained and have a moderate to well-sorting. Within this well the presence of glauconite is not as dominant as in well E-BT1, thus suggesting that E-AR1 is more towards the distal parts of the fan.

The sandstones are mainly cemented by clay and quartz cement and minor amounts of calcite and hematite. However, with an increase in depth the presence of hematite cement increases as seen in XRF analysis. Quartz overgrowths are the main pore-filling cement within these sandstones. The sandstone within this well also shows very clear bedding and alignment of mineral grains. At about 2464 m there is also the presence of stylolites which are mainly filled with hematite (figure 6.5, C).

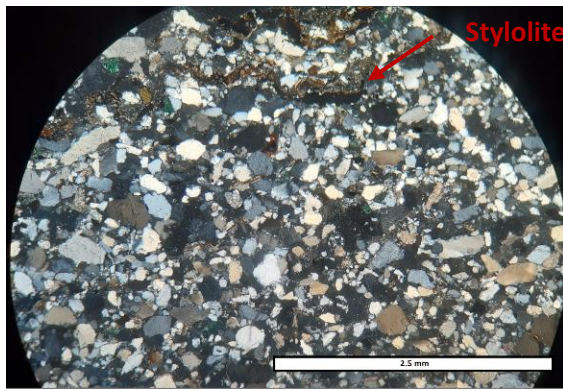
Within these sandstones, there has been moderate compaction due to the long planar contacts and less sutural and concave-convex contacts that appear. Secondary porosity is well developed for this well, after the dissolution of cements and detrital grains. For well E-AR1, most of the sandstones is dominantly composed of quartz, glauconite, feldspars, and minor amounts of muscovite and biotite.

Figure 6.9: Overview of the thin sections of well E-AR1

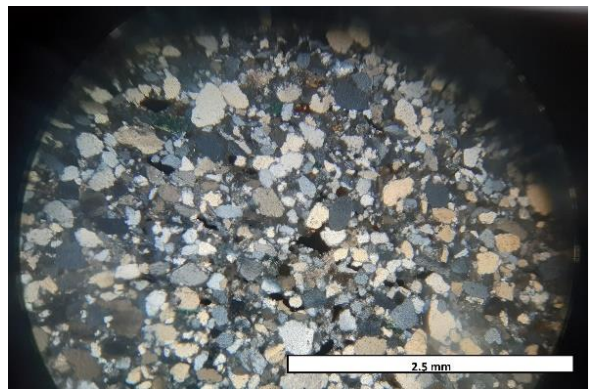
A. Thin Section 23: Well-sorted sandstone at a depth of 2456.08m	B. Thin Section 18: Moderately sorted sandstone at a depth of 2461.24m
---	---



C. Thin Section 24: Moderately-well sorted sandstone at a depth of 2464.85m



D. Thin Section 4: Moderately to well-sorted sandstone at a depth of 2465.50m



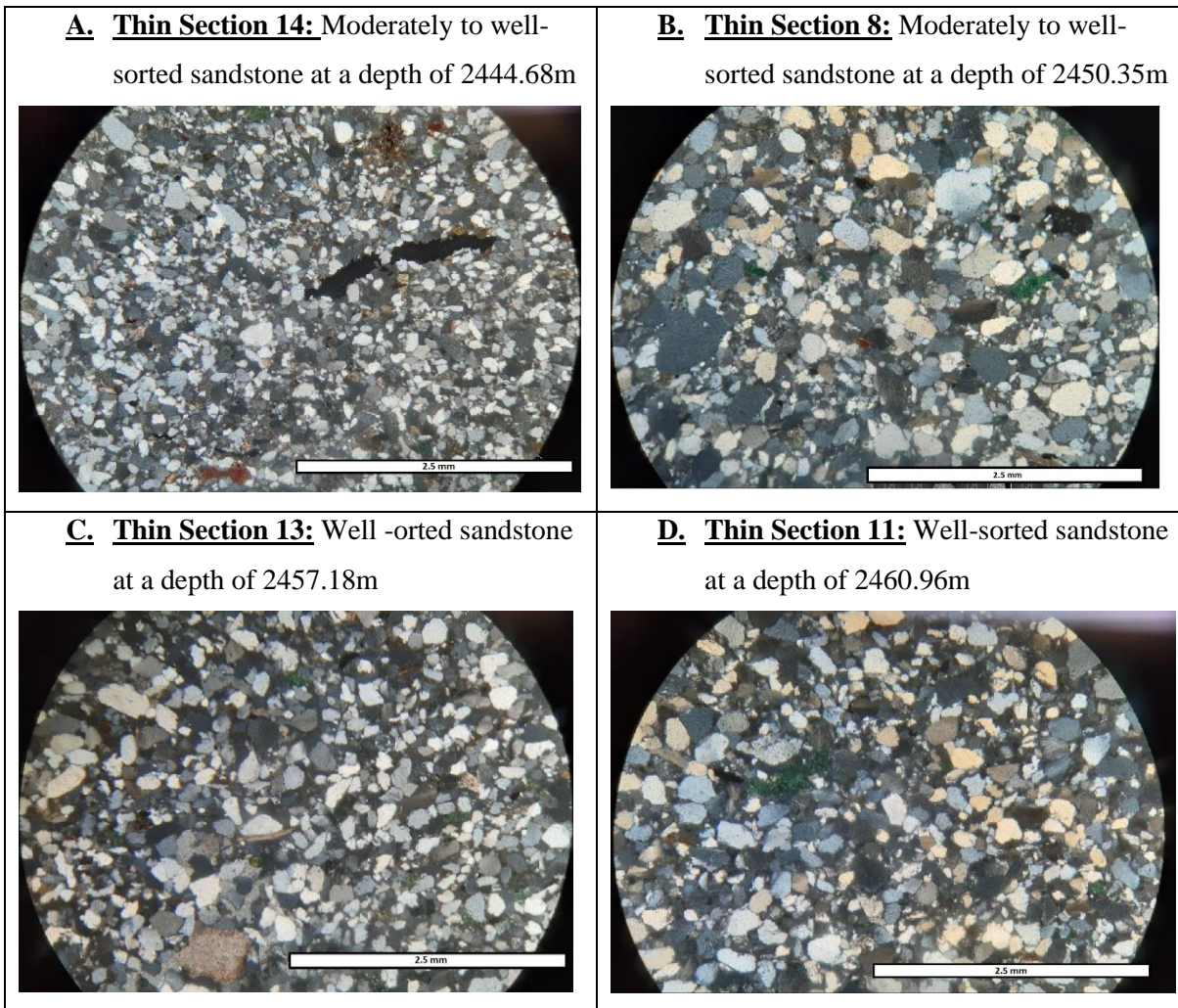
6.2.2.3. Petrography of Well E-AR2

In well E-AR2, the minerals present are quartz, glauconite, feldspars, and minor amounts of muscovite and biotite. Within this well the presence of glauconite is not as dominant as in well E-BT1, thus occurring towards the distal parts of the submarine fan.

The sandstones of this well appear to be fine to coarse-grained and have a moderately to well-sorting. The sandstones are mainly cemented by clay and quartz cement and minor amounts of calcite and hematite. However, with an increase in depth the presence of hematite cement increases. Quartz overgrowths are the main pore-filling cement within these sandstones.

Within these sandstones, it is evident that there has been moderate compaction due to the long planar contacts and less sutural and concave-convex contacts that appear. Secondary porosity is well developed for this well, after the dissolution of cements and detrital grains.

Figure 6.10: Overview of the thin sections of well E-AR2.



6.2.3. Implications of sandstone petrography on reservoir properties

The quality of a reservoir depends mainly on the relationship between porosity and permeability which can be reflected in the textural characteristics of grain shape, size, arrangement, and packing. Porosity and permeability control the fluid behaviour within rocks and therefore play a crucial role in the diagenesis of sandstones. Both primary and secondary porosity occurs within these thin sections. Primary porosity occurs directly after deposition before any changes occur after diagenesis. It exists as intergranular pore spaces between the larger grains as well as micropores inside the matrix. On the other hand, secondary porosity occurs due to the dissolution of unstable mineral grains.

The diagenetic processes that occur influence the reservoir quality and can either enhance or reduce the porosity and permeability. As these sandstones become compacted due to the overloading deposits, the pressure implied to the rock may lead to bed thinning, dewatering, grain packing and reduction in porosity. Compaction caused by overburden causes grain contacts to form. In all three wells, the overburden pressure doesn't fracture the grains thus indicating moderate compaction. Moderate compaction is also indicated by long planar contacts which are present in all three wells. Contacts such as sutured and concavo-convex contacts occur during deeper burial diagenesis. With deeper burial diagenesis there is an increase in compaction which causes changes in grain contacts and therefore a loss in porosity.

Porosity is reduced by both calcite and quartz cement which occurs frequently within these thin sections (figure 6.7). The overgrowth of quartz grains causes a reduction in porosity and permeability. Therefore, the primary porosity within these sandstones is partially reduced because of compaction and cementation. However, as the mineral grains within these thin sections continuously undergo compaction, there is an increase in the dissolution of unstable grains, and this could lead to an increase in secondary porosity. In conclusion, the initial porosity that occurred was partially reduced by compaction and cementation but increased dissolution of unstable grains and cement. Most of the porosity within these wells has been preserved due to moderate compaction, and therefore these sandstones make good reservoirs for hydrocarbon exploration.

6.3. X-Ray Fluorescence Analysis:

The following elemental concentration presented in the table 6.3 below, was recorded with a portable X-ray fluorescence analyzer (PXRF). It is a handheld instrument which records the multi-element composition of a rock sample by placing the instrument against the sample. The analytical results recorded by the instrument are transferred to a computer via a USB cable and then analyzed in an Excel spreadsheet.

Table 6.3 below, gives an overview of the average major and minor elements that were recorded over the selected cores of the three wells as discussed in the sedimentological section above. The XRF analysis for these selected cores can be found in appendixes A-C. These selected cores are further separated into an oil and water zone using the identified OWC contacts as previously discussed. The two zones are used to indicate whether the oil or water influences the elemental composition of a reservoir rock.

Table 6.4: Table showing the measured average major and trace elements recorded over oil and water zones of all three wells.

Element	E-BT1		E-AR1		E-AR2	
	Oil Zone	Water Zone	Oil Zone (2456.15 – 2461.30 m)	Water Zone (2464.90 – 2467.10 m)	Oil Zone (2442.2 – 2450.95 m)	Water Zone (2457.1 – 2461.1 m)
Mg	0.2626	0.3002	0.2203	0.0973	0.2673	0.3259
Al	1.9650	2.1482	3.4279	2.2924	1.9610	2.0994
Si	38.7164	38.6356	36.1258	39.1624	38.9318	38.5299
P	0.0517	0.0492	0.0489	0.0434	0.0675	0.0629
S	0.4715	0.3814	2.5016	0.8513	0.5250	0.3714
K	0.5790	0.6563	0.9509	0.5417	0.6174	0.6506
Ca	1.8125	1.8883	1.1455	1.2777	1.7286	2.0564
Ti	0.0460	0.0588	0.1578	0.0428	0.0371	0.0533
Cr	0.0072	0.0120	0.0132	0.0091	0.0082	0.0124
Mn	0.0080	0.0068	0.0112	0.0076	0.0112	0.0145
Fe	0.7823	0.8334	2.2689	0.8152	1.0182	1.1237

Co	0.0048	0.0042	0.0040	0.0039	0.0050	0.0053
Ni	0.0004	0.0002	0.0018	0.0002	0.0002	0.0015
Zn	0.0083	0.0075	0.0089	0.0081	0.0111	0.0072
Rb	0.0024	0.0030	0.0074	0.0030	0.0030	0.0032
Sr	0.0067	0.0067	0.0079	0.0052	0.0067	0.0088
Zr	0.0496	0.0483	0.0415	0.0337	0.0369	0.0393
Nb	0.0003	0.0002	0.0012	0.0002	0.0013	0.0012
Mo	0.0004	0.0002	0.0003	0.0002	0.0002	0.0005
Sb	0.0069	0.0057	0.0068	0.0060	0.0069	0.0067
Ba	0.0374	0.0367	0.0496	0.0322	0.0371	0.0412
Pt	0.0004	0.0007	0.0004	0.0004	0.0007	0.0006
Hg	0.0013	0.0012	0.0012	0.0011	0.0012	0.0013
Pb	0.0010	0.0012	0.0028	0.0011	0.0011	0.0012

6.3.1. XRF Analysis of E-BT1:

Figure 6.1 illustrates how the elemental composition within the sandstone reservoir of well E-BT1 changes according to depth. The depth increases as the blue bars get darker. The red highlighted area indicates the oil zone with a depth of 2395.2-2410.2 m and the white highlighted area indicates the water zone with a depth of 2412.2-2412.7 m.

From Figure 6.1, we can see that the element Silicon represents a very high concentration in relation to other elements and thus indicates the presence of silica minerals (Quartz, Feldspars, and Micas) throughout the reservoir of well E-BT1. We can also see that silicon decreases with depth; this means that silicon is more concentrated in the oil zone than water zone.

Aluminum, Potassium, Iron, and Magnesium represent the minerals feldspars, micas, and hematite from the thin sections above. The increase in these elements indicates an increase in their respective minerals over the reservoir interval. Calcium, which is the second highest element concentration of well E-BT1, represents the mineral calcite which acts as a cement within the reservoir rocks. The higher the amount of Calcium, the higher the amount of calcite cement. The concentration of calcium

does not show much variation between the two zones as seen in figure 6.8. The concentrations of the minor elements are insignificant to this research.

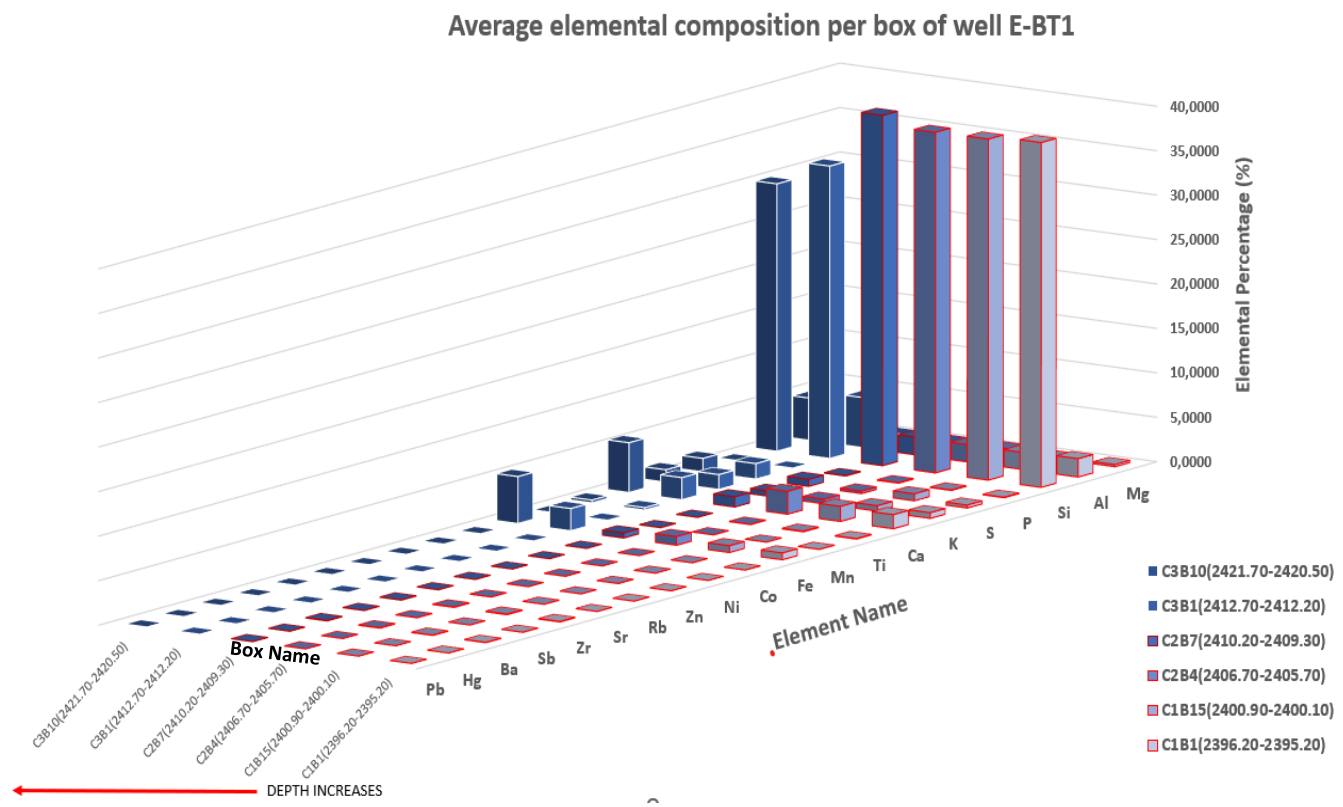


Figure 6.11: Average elemental composition over the reservoir interval of well E-BT1.

6.3.2. XRF Analysis of E-AR1:

The elemental composition of the reservoir interval of well E-AR1 is illustrated in Figure 6.9. The depth increases as the blue bars get darker. The elemental composition of the oil zone is highlighted in red, and it covers a depth of 2456.15-2461.30m, whereas the water zone is highlighted in blue and covers a depth of 2464.90-2467.10m over the reservoir interval.

For well E-AR1, we can see that the average elemental composition over both oil and water zones is different for most of the elements. This indicates that oil and water may influence on the elemental concentration of the reservoir rocks.

Figure 6.9 indicates that the element Silicon is very highly concentrated over the entire reservoir interval, thus confirming the presence of silica minerals throughout the reservoir as seen in the thin

sections above. However, we can see that there is a significant drop in silicon concentration between box C1B11 and C1B12, thus indicating that silicon decreases within the water zone.

The concentration of aluminum, iron, and magnesium remains constant with depth, except for box C1B12 where there is a significant increase in these elements. The increase in these elements can be linked to the thin section analysis, where there is a major increase in hematite cement and biotite micas towards the bottom of the reservoir. Calcium, which is less for well E-AR1 than for well E-BT1 indicates the mineral calcite which acts as a cement within the reservoir rocks. Well E-AR1 has less calcite cement than E-BT1 and therefore lower calcium concentrations. The concentration of the minor elements is insignificant for this research.

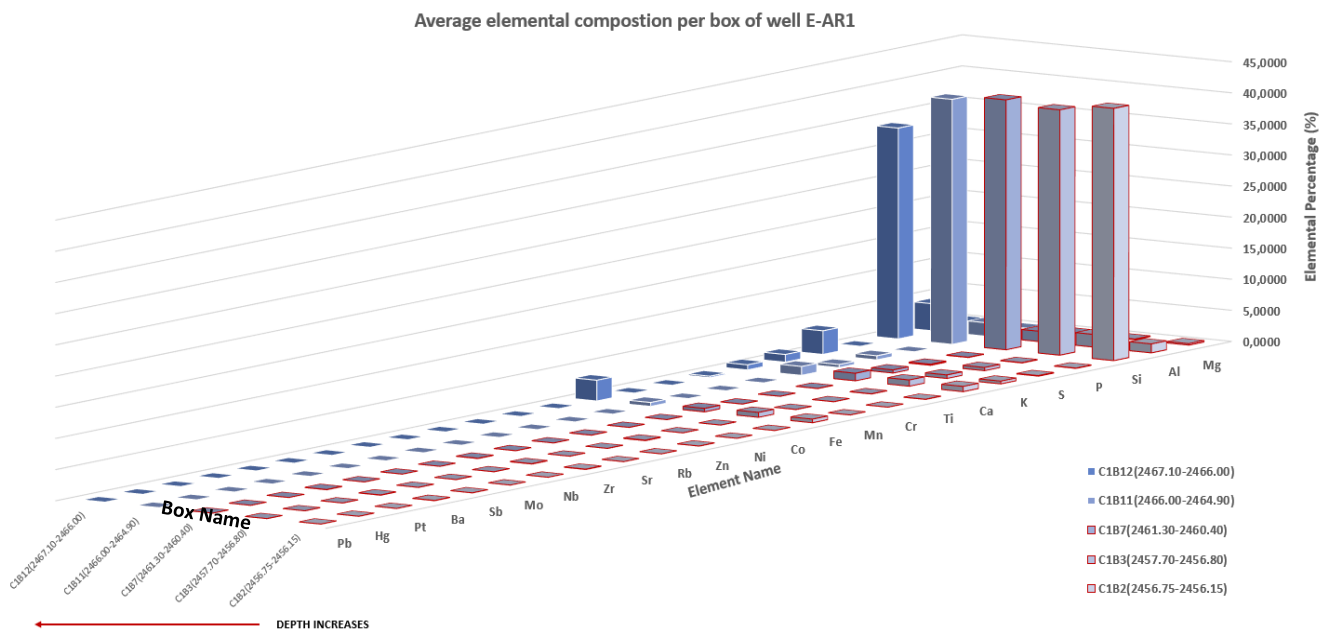


Figure 6.12: Average elemental composition over the reservoir interval of well E-AR1.

6.3.3. XRF Analysis of E-AR2:

Figure 6.10 below shows the elemental composition over the reservoir interval of well E-AR2. The depth increases as the blue bars get darker. The elemental composition of the oil zone is highlighted in red and covers a depth of 2442.2-2450.95 m. On the other hand, the elemental composition of the water zone is highlighted in blue and covers a depth of 2457.1-2461.1 m over the reservoir interval.

The average elemental composition for each element in both oil and water zones does not exhibit much variation for well E-AR2. This indicates that the type of fluid has no clear influence on the composition of the reservoir rock.

From Figure 6.10, we can see that the average concentration of silicon is very high concentrated over the entire reservoir interval, thus indicating the presence of silica throughout the reservoir of well E-AR2. The silica content also indicates that there are a lot of silica minerals present within the reservoir.

Aluminum, Potassium, Iron and Magnesium slightly decrease with depth in the reservoir. This indicates that the oil zone has a higher concentration of Fe, Mg, K, and Al than the water zone. Calcium, which is the second highest elemental concentration of well E-AR2, represents the mineral calcite which acts as a cement within the reservoir rocks. The higher the amount of calcium, the higher the amount of calcite cement. The calcium within the reservoir appears to be constant, except for box C1B1 which represents higher Ca concentrations. The concentrations of the minor elements are insignificant to this research.

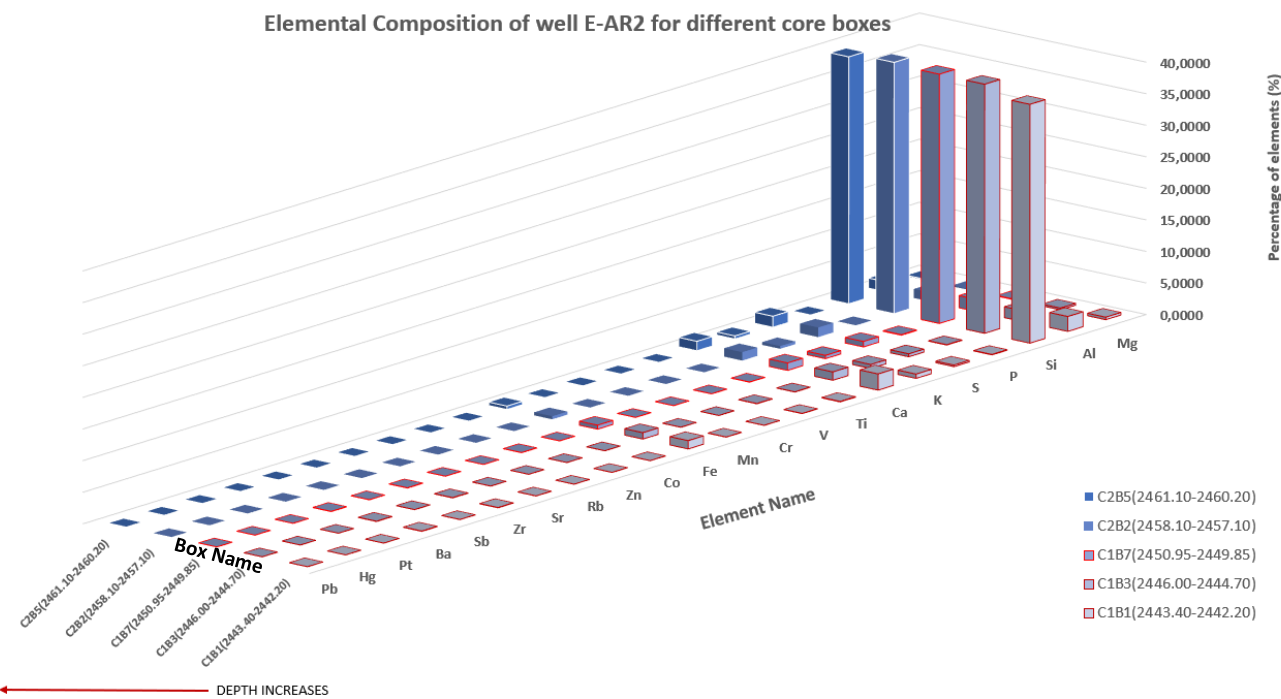


Figure 6.13: Average elemental composition over the reservoir interval of well E-AR2.

6.4. Lithological and Mineralogical Analysis:

By comparing thin sections with wireline logs, we can see whether the lithology and mineralogy correspond to a specific fluid type. The lithological wireline logs that are being used to explain the correlation between thin sections and well logs are volume of clay, spontaneous potential, volume of clay, density, and reservoir rock type. The lithological description made from the wireline logs in previous sections is correlated with the mineralogical description made from the thin sections below. The thin sections of the oil and water zones are mainly compared to see if there are any differences in mineral content within the reservoir.

6.4.1. Lithology and Mineralogy Analysis of Well E-BT1:

For well E-BT1, four different thin sections are being used to explain the differences in mineralogy between the oil zone (2384-2411.8m) and water zone (2411.8-2416 m). These thin sections are labelled, and their locations are indicated on the log below with red arrows (figure 6.14). Thin sections A (TS22) and B (TS21) are in the oil zone whereas thin sections C (TS16) and D (TS9) are within the water zone. The lithology of the oil zone is compared to the lithology of the water zone to see any mineral changes.

Through the analysis done on these thin sections, it is shown that the oil zone indicates a lower clay content compared to the water zone which is evident on the VCLGR log as well. We can also see from these thin sections that glauconite and calcite cement increase towards the water zone. The cement within the water zone is higher than the cement in the oil zone, thus indicating poorer reservoir quality. The roundness of the minerals within both oil and water zones are sub-rounded to sub-angular with a moderate to well sorting.

The thin sections also correspond well with the petrophysical properties and reservoir rock type. Thin sections of the oil zone have a higher porosity and permeability than the water zone because both clay and calcite cement increase towards the water zone. When looking at track 6, we can see that this increase in clay and calcite also corresponds to a lower RRT as thin sections C and D have lower RRT than thin sections A and B.

We can conclude that the oil zone has better reservoir quality than the water zone. The type of minerals and how they are deposited within the reservoir rocks contribute to an increase or decrease in reservoir quality. The higher the clay and calcite content, the lower the reservoir quality.

Well E-BT1

DEPTH (2383.99M - 2416M)

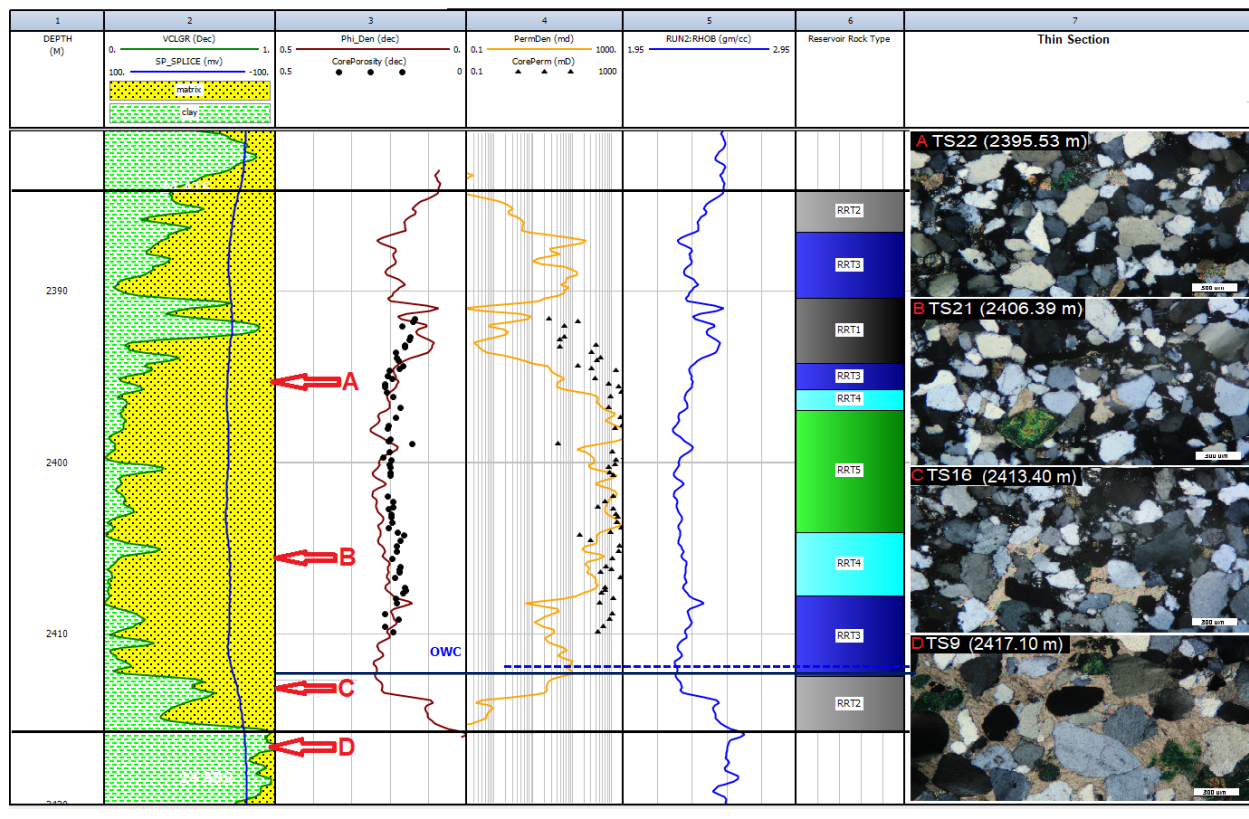


Figure 6.14: Lithological and Mineralogical log plot of well E-BT1.

6.4.2. Lithology and Mineralogy Analysis of Well E-AR1:

Four different thin sections were used to explain the differences in mineralogy between the oil zone (2454-2464m) and water zone (2464-2485m) within the reservoir interval. These thin sections are labelled, and their locations are indicated on track 4 (figure 6.15). Thin sections A (TS7) and B (TS18) are in the oil zone whereas thin sections C (TS24) and D (TS4) are in the water zone. By comparing the sandstones of the two different fluid zones (previously identified by the resistivity log in track 5), we can see whether oil or water influences the minerals present.

Through the analysis done on these thin sections, it is shown that calcite and clay minerals are more concentrated in the water zone compared to the oil zone. The thin sections in the water zone indicate a slightly higher clay content compared to the oil zone which is evident on the VCLGR log as well. We can also see that there is an increase in stylolites with depth which are filled with hematite cement in the water zones as seen in thin section C. The presence of quartz, feldspars and glauconite appears to be the same throughout the reservoir interval. The roundness of the minerals within both oil and water zones are sub-rounded to sub-angular with poor to well sorting.

The mineral identification from the thin sections also corresponds well with petrophysical and rock physics parameters. When looking at the Reservoir Rock Type (RRT), we can see from the thin sections that an increase in cement as seen in the water zones corresponds to a lower RRT, whereas the rocks of the oil zone with lower cement correspond to a higher RRT.

The thin sections also correlate with the petrophysical properties, as thin sections A and B from the oil zone have a higher permeability than thin sections C and D from the water zone. This indicates that the oil zone has a higher permeability than the water zone and this can be seen in the connected pore spaces of the thin sections.

Scale : 1 : 300
WELL E-AR1

DEPTH (2453.94M - 2485.03M)

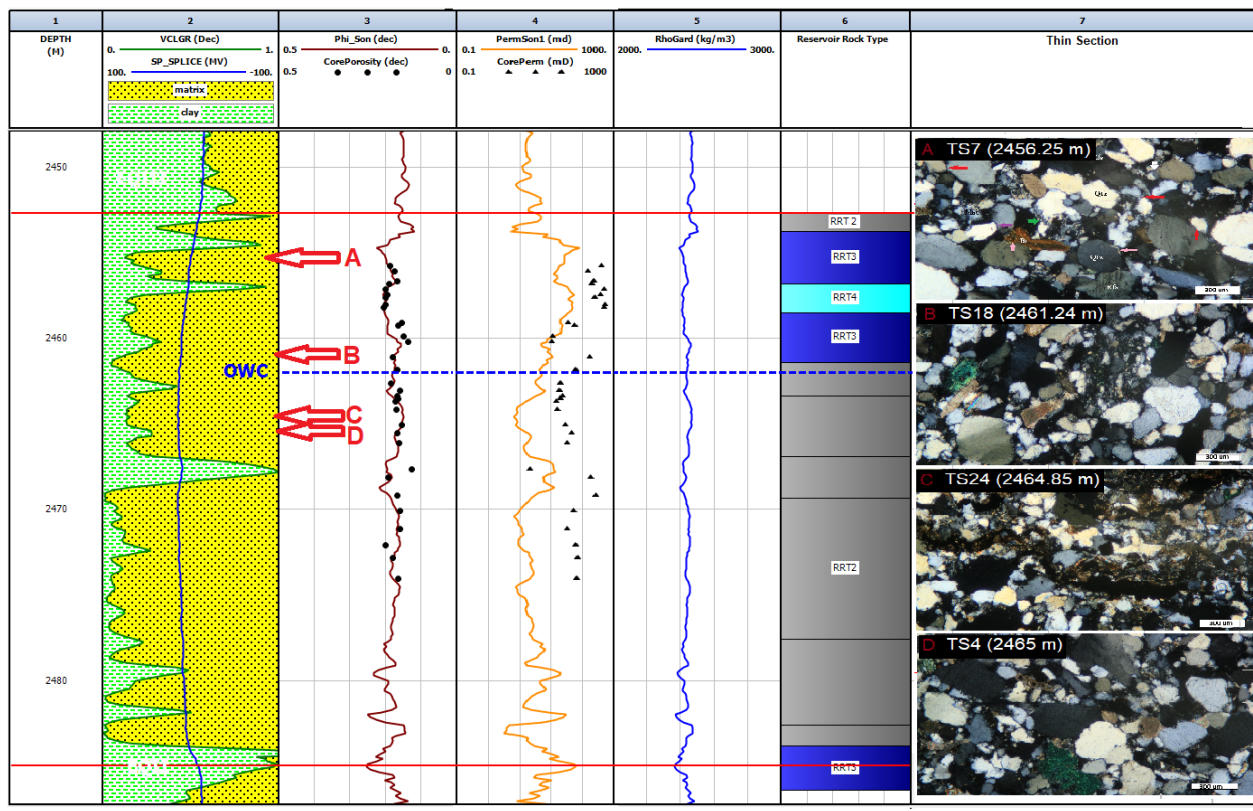


Figure 6.15: Lithological and Mineralogical log plot of well E-AR1.

6.4.3. Lithology and Mineralogy Analysis of Well E-AR2:

For well E-AR2, four thin sections are used to explain the differences in mineralogy between the oil zone (2445-2451m) and water zone (2451-2477m) within the reservoir interval. These thin sections are labelled, and their locations are indicated on track 4(figure 6.16). Thin sections A (TS8) and B (TS17) are in the oil zone whereas thin sections C (TS13) and D (TS5) are in the water zone. By comparing the sandstones of the two different fluid zones, we can see whether oil or water influences the minerals present.

Through the analysis done on these thin sections, it is shown that the clay minerals are more concentrated in the oil zone compared to the water zone. The thin sections in the oil zone indicate a slightly higher clay content compared to the water zone which is evident on the VCLGR log as well. We can also see that there is an increase in microcrystalline quartz with depth as seen in thin section

C which leads to a decrease in both porosity and permeability. The roundness of the minerals within both oil and water zones are sub-rounded with a moderately well-to-well sorting.

The mineral identification from the thin sections also corresponds well with petrophysical and rock physics parameters. When looking at the Reservoir Rock Type (RRT), we can see from the thin sections that an increase in microcrystalline quartz cement as seen in the water zones corresponds to a lower RRT, whereas the rocks of the oil zone with lower cement correspond to a higher RRT.

We can thus conclude that the oil zone has better reservoir quality than the water zone. The type of minerals and how they are deposited within the reservoir rocks contribute to an increase or decrease in reservoir quality. The higher the amount of microcrystalline quartz cement, the lower the reservoir quality.

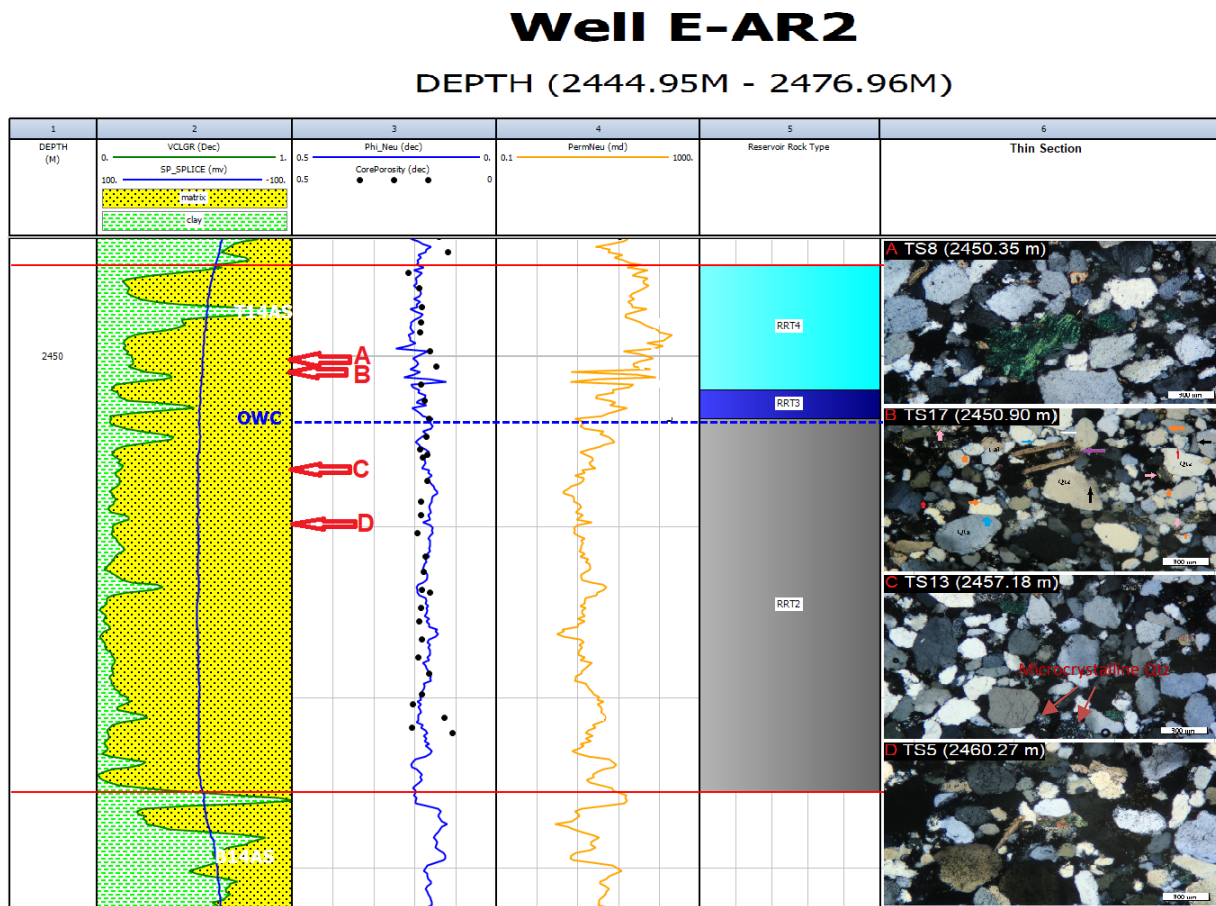


Figure 6.16: Lithological and Mineralogical log plot of well E-AR2.

Chapter 7: Conclusion and Recommendations:

7.1. Conclusion:

This research project utilized a combined approach of rock physics and petrophysics to examine the rock and fluid properties of the cretaceous sandstones in block E of the southern Bredasdorp Basin. The study focused on analysing the reservoir units encountered by several wells using wireline logs and limited core data.

From the core data, five different lithofacies were identified based on grain size and sedimentary structure. Reservoir rocks were categorized as massive sandstone facies 1 and cross-bedded sandstone facies 2, while non-reservoir rocks were labelled as heterolithic sand-shale facies 3, pure shale facies 4 and breccia facies 5. The lithological identification logs confirmed the presence and location of these lithofacies over the reservoir intervals. The Archie cementation factor indicated that all three wells contained unconsolidated rocks, suggesting they would make good reservoirs with little cement material. Shear velocity prediction is further supported by the presence of clean sandstone in all three wells, confirming them as reservoir rocks.

Additionally, a multi-mineral analysis of the wells using thin sections and XRF data confirmed the presence of the identified rock types. The sandstones in the wells were found to be predominantly composed of silica according to XRF data. Accessory minerals such as glauconite and cements such as quartz, hematite, and calcite were confirmed in the thin sections. These cements reduced the porosity and permeability of the reservoir rocks to some extent.

Petrophysical parameters such as shale volume, porosity, permeability, and water saturation were determined using core data and wireline logs. The core data was used to calibrate the wireline logs, and the results indicated that well E-BT1 had the most favourable reservoir conditions with high porosities and permeabilities. Well E-AR1 and E-AR2 also showed indications of good reservoir conditions.

Furthermore, five hydraulic flow units were identified based on core porosity and permeability, which were then used to predict flow units from wireline logs in uncored intervals. This allowed for consideration of the complex variation in pore geometry in different rock types. A total of five

reservoir rock types was identified, ranging from RRT1 to RRT5 based on reservoir quality, with well E-BT1 exhibiting the best reservoir rocks and quality.

Lastly, the fluid types and contacts were analysed using resistivity logs, RFT graphs, and the Gassmann fluid substitution method. By examining the resistivity logs and RFT graphs, the fluid contacts were determined to be oil-water contacts (OWC), where the oil zones form part of the upper reservoir section. The Gassmann fluid substitution method indicated the presence of oil based on the acoustic impedance logs, with the in-situ logs closely matching those of oil for all three wells. The acoustic impedance logs also indicate that oil mainly forms within the oil zone. Additionally, both the compressional and shear velocity logs for all fluid types increased significantly in high density layers.

7.2. Recommendations:

This integrated study could have been more efficient if the following unnecessary issues were not encountered. The issues encountered are as follows:

- Missing and incomplete core analysis reports, with no depth recorded on some core measurements.
- Incomplete NPHI logs and DST data for wells E-AR1 and E-AR2. Alternative porosity logs had to be used to compensate for incomplete logs. The DST data of well E-BT1 were used to calculate the data for the other wells as all three wells in this research form part of the same pressure regime and environmental conditions.
- Missing and unevenly cut core plugs for wells E-AR1 and E-AR2, which created difficulties and delays in measuring porosity, permeability, and water saturation through PoroPerm and EPS-A.
- Unnecessary delays in acquiring data from PASA. These unplanned delays can cause major delays in research.
- No available institutions in South Africa for conducting measurements of geomechanical data for rock physics analysis.

I would recommend that before planning the research, students must ensure that the wells they work on have all the data available. This includes all necessary core reports, core logs, and las files. If this data is missing, the interpretation of your work can be delayed and create unnecessary difficulties. I would also recommend that more wells be used for research to avoid having to depend on one or two wells if other wells are incomplete. Finally, I would recommend that students are in close contact with PASA as soon as research starts.

References

- Abe, James S, Paul I Edigbe, and Samuel G Lawrence. 2018. "Rock physics analysis and Gassmann's fluid substitution for reservoir characterization of "G" field, Niger Delta." *Arabian Journal of Geosciences* 1-10.
- Acho, Collins B. 2015. *Assessing hydrocarbon potential in cretaceous sediments in western Bredasdorp sub-basin in the Outeniqua Basin South Africa*. Cape Town: University of the Western Cape.
- Alamooti, Amirhossein M, and Farzan K Malekabadi. 2018. "An introduction to Enhanced Oil Recovery." *Fundamentals of Enhanced Oil and Gas Recovery from Conventional and Unconventional Resources*.
- Alyafei, Nayef. 2021. *Fundamentals of Reservoir Rock Properties*. 2nd Edition. Hamad Bin Khalifa University Press.
- Amaufule, J.O, M Altunbay, D Tiab, D.G Kersey, and D.K Keelan. 1993. "Enhanced reservoir description: using core and log data to identify hydraulic flow units and predict permeability in uncored intervals/wells." *Society of Petroleum Engineers, Annual Technical Conference and Exhibition* 205-220.
- Aminzadeh, Fred, and Shivaji N Dasgupta. 2013. "Geophysics for Petroleum Engineers." *Developments in Petroleum Science*.
- Anal.Methods. 2019. "Hand-held X-ray fluorescence spectrometry." *The Royal Society of Chemistry* 2498–2501.
- Avseth, Per, and Knut Bjørlykke. 2010. "Explorational Rock Physics – The Link Between Geological Processes and Geophysical Observables." *ResearchGate*.
- Bellotti, P, V Di Lorenzo, and D Giacca. 1979. "Overburden gradient from sonic log ." *SPWLA, London March* .
- Beniest, Anouk . 2017. *From continental rifting to conjugate margins: Insights from analogue and numerical modelling*. Thesis, Paris: Université Pierre et Marie Curie/IFP Energies nouvelles.
- Boukadi, F, A Bemani, M Rumhy, and M Kalbani. 1998. "Threshold pressure as a measure of degree of rock wettability and diagenesis in consolidated Omani limestone cores." *Marine and Petroleum Geology* 15 33-39.
- Broad, D.S, E.H.A Jungslager, I.R McLachlan, and J Roux. 2006. "Offshore Mesozoic Basin." *Geological Society of South Africa, Johannesburg/Council for Geosciences* 553-571.
- Broad, E.H.A Jungslager, McLachlan, and Roux. 1996. "Geology of offshore Mesozoic basins: Contribution to a text book on the geology of Africa." *Geological Society of South Africa* 6-10, 15-19.

- Brown, L.F, J.M Benson, G.J Brink, S Doherty, A Jollands, E.H.A. Jungslager, J.H.G. Keenan, A Muntingh, and N.J.S Van Wyk. 1995. "Sequence stratigraphy in offshore South African divergent basins. An atlas on exploration for Cretaceous lowstand traps. Soekor (pty) Ltd." *Studies in Geology, American Association Petroleum Geology* 41, 184.
- Bruker, AXS. 2006. "X-ray Diffraction From a Crystal Lattice, Bragg's Equation." In *Introduction to X-Ray Fluorescence*, 19. Karlsruhe, West Germany: West Germany.
- Cornford, C. 2005. "Petroleum Geology: The Petroleum System." *Encyclopedia of Geology*.
- Cullity, C.D. 1978. *Elements of X-RAY DIFFRACTION*. 2nd Edition . Edited by Morris Cohen. Addison-Wesley Publishing Company Inc.
- Dandekar, Abhijit Y. 2006. *Petroleum Reservoir Rock and Fluid Properties*. United States: CRC Press: Taylor & Francis Group.
- Darling, Toby. 2005. "Chapter 2 - Quicklook Log Interpretation." In *Well Logging and Formation Evaluation*, 29-48. Science Direct.
- Darling, Toby. 2005. "Well Logging and Formation Evaluation." In *Chapter 2 - Quicklook Log Interpretation* , by Toby Darling, 29-48. Gulf Professional Publishing. doi://doi.org/10.1016/B978-075067883-4/50002-4.
- Davies, C.P.N. 1988. "Bredasdorp Basin-south flank hydrocarbon expulsion," *SOEKOR unpubl. Rept.* 17.
- Davies, C.P.N. 1997. *Hydrocarbon Evolution of the Bredasdorp Basin, offshore South Africa: from Source to Reservoir*. PhD thesis, Cape Town: University Stellenbosch.
- de Jager, Jan. 2020. "Chapter 24: Concepts of conventional petroleum systems ." In *Regional Geology and Tectonics*, 687-720. Netherlands: Elsevier B.V.
- de Viguerie, L, V.A Sole, and P Walter. 2009. "Multilayer quantitative X-ray fluorescence analysis applied to easel paintings." *Springer-Verlag*.
- De Wit, M.J, and I.G.D Ransome. 1992. "Inversion Tectonics of the Cape Fold Belt, Karoo and Cretaceous Basins of the Southern Africa." *A.A Balkem, Nederlands* 49.
- Dingle, R.V, W.G Siesser, and A.R Newton. 1983. "Mesozoic and Tertiary Geology of Southern Africa." *A.A. Balkema, Rotterdam* 375.
- Dutrow, B.L, and M.C Clark. n.d. *X-ray Powder Diffraction (XRD)*. Accessed 07 20, 2020.
https://serc.carleton.edu/research_education/geochemsheets/techniques/XRD.html.
- Earle, Steven. 2012. *20.3 Fossil Fuels*. Accessed June 2, 2022. <https://opentextbc.ca/geology/chapter/20-3-fossil-fuels/>.

- Ebanks, W.J, M Scheihing, and C Atkinson. 1993. "Flow units for reservoir characterization ." *Development geology reference manual: American Association of Petroleum Geologists: Methods in Exploration Series* 282-285.
- Emmanuel, N, and P Carey. 2011. "Sequence stratigraphic characterisation of petroleum reservoir in blk 11b/12b of the southern Outeniqua basin." *Inkaba yeAfrica; annual workshop*, [Online] www.inkaba.org/publication/workshops.
- Engelbrecht, S.F, A Honiball, M Morris, and W McAlloon. 1991. *Well Completion-Borehole E-BT1 (SOE-EXP-WCR-269)*. SOEKOR.
- Engelbrecht, S.F, L.A Willis, M Morris, and W McAlloon. 1990. *Geological Well-Complteion Report of Borehole E-AR2*. SOEKOR.
- eserc.stonybrook.edu. n.d. <http://www.eserc.stonybrook.edu/ProjectJava/Bragg/>.
- Fadipe, Oluwaseun A. 2012. *Reservoir quality, structural architecture, fluid evolution and their controls on reservoir performance in block 9, F-O gas field, Bredasdorp Basin, offshore South Africa*. Cape Town: University of the Western Cape.
- Gardner, G.L.F, L.W Gardner, and A.R Gregory. 1974. "Formation velocity and density - the diagnostic basics for stratigraphic traps." *Geophysics* 39 770-780.
- Grote, Wiebke. 2020. *Qualitative and Quantitative XRD (mineralogy)*. Pretoria : University of Pretoria.
- Haldar, Swapan Kumar. 2018. "Chapter 6 - Exploration Geophysics." In *Mineral Exploration (Second Edition)*, 103-122. Elsevier.
- Hussien, T.M.H. 2014. *Formation Evaluation of Deep-water Reservoirs in the 13A and 14A Sequences of the Central Bredasdorp Basin, offshore South Africa*. MSc. Thesis, Cape Town: University of the Western Cape.
- Hyne , N. 2012. "Nontechnical Guide to Petroleum Geology, Exploration, Drilling and Production." *Tulsa: PennWell Corporation*.
- IHS. 2014. "Map of South Africa's current activity ." *The Source for critical Information and Insight, Global Exploration and Production Service*. <http://www.ihs.com/energy>.
- ILE, Anthony. 2013. *Petrophysics and fluid mechanics of selected wells in Bredasdorp Basin*. MSc Thesis, Cape Town: University of the Western Cape.
- Johari, Arash, and Mohammad E Niri. 2020. "Rock physics analysis and modelling using well logs and seismic data for characterising a heterogeneous sandstone reservoir in SW of Iran." *Eploration Geophysics*.
- Kadkhodaie, Ali, and Rahim Kadkhodaie. 2022. "Chapter 7 - Tight gas petrophysical evaluation." In *Reservoir characterization of Tight Gas Sandstones*, 145-170. Elseriver.

- Khan, N, and K Rehman. 2018. "Petrophysical evaluation and fluid substitution modeling for reservoir depiction of Jurassic Datta Formation in the Chanda oil field, Khyber Pakhtunkhwa, northwest Pakistan." *J Pet Explor Prod Technol* 9 1-18.
- Li, Yanran, Zhiming Hu, Changhong Cai, Xiangui Liu, Xianggang Duan, Jin Ghang, Yalong Li, et al. 2021. "Evaluation method of water saturation in shale: A comprehensive review." *Marine and Petroleum Geology* 128 105017.
- Lindseth, R.O. 1979. "Synthetic Sonic Logs - a process for stratigraphic interpretation." *Geophysics* v.44 no.1 3-26.
- Magoba, Moses, and Mimonitu Opuwari. 2019. "Petrophysical interpretation and fluid substitution modelling of the upper shallow marine sandstone reservoirs in the Bredasdorp Basin, offshore South Africa." *Journal of Petroleum Exploration and Production Technology (2020)* 10 783-803.
- Magobiyane, N.V. 2014. *Sedimentological re-interpretation of zone 3 (Upper Shallow Marine) of selected wells, Bredasdorp Basin (Offshore South Africa)*. MSc Minithesis on Petroleum Geology, Cape Town: The University of the Western Cape .
- Magoon, Leslie B. 2004. "Petroleum System: Nature's Distribution System for Oil and Gas ." *Enclopedia of Energy* .
- Maseko, Phindile Pearl. 2016. *Petrophysical evaluation and characterization of sandstone reservoirs of the western Bredasdorp Basin, South Africa for well D-D1 and E-AP1*. MSc Research Paper, Cape Town: University of the Western Cape.
- McMillan, I.K, G.J Brink, D.S Broad, and J.J Maier. 1997. "Late-Mesozoic sedimentary basins off the south coast of South Africa ." In: Shelley, R.C, *Sedimentary Basins of the World: The African Basins* 319-376.
- Meinzer, O.E. 1923. "Outline of ground-water hydrology with definitions." *US Geological Survey Water Supply, Paper 494*.
- Mondol, N.H. 2015. "Well Logging: Principles, Application and Uncertainties." Chap. Chapter 16 in *Petroleum Geoscience- From Sedimentary Environments to Rock Physics*, 385-425. Springer-Verlag Berlin Heidelber.
- MyScope. 2014. *Output*. 04 07. Accessed 07 12, 2020.
<https://myscope.training/legacy/xrd/background/machine/output/>.
- Nasrollahzadeh, M, M Atarod, M Sajjadi, S.M Sajadi, and Z Issaabadi. 2019. "Chapter 6.8.7.1 X-Ray Diffractometer." In *Interface Science and Technology*, Vol. 28. Elsevier.
- Nichols, Gary. 2009. *Sedimentology and Stratigraphy*. 2nd. United Kingdom: Wiley Blackwell.

Ojongoekpoko, H.M. 2006. *Porosity and Permeability distribution in the Deep Marine Play of the Central Bredasdorp Basin, Block 9, Offshore South Africa*. MSc Thesis, Cape Town: University of the Western Cape.

Opwuari, M, and N Dominick. 2021. "Sandstone reservoir zonation of the north-western Bredasdorp Basin South Africa using core data." *Journal of Applied Geophysics* 193 1-14.

Opwuari, Mimonitu, Blessing Afolayan, Saeed Mohammed, Paschal Amaechi, Youmssi Bareja, and Tapas Chatterjee. 2022. "Petrophysical core-based zonation of OW oilfield in the Bredasdorp Basin South Africa." *Scientific Reports* 12-510.

Parker, Irfaan. 2014. *Petrophysical Evaluation of Sandstone reservoirs of the central Bredasdorp Basin, Block 9, Offshore South Africa*. MSc Thesis, Cape Town: University of the Western Cape.

PASA. 2017. *Petroleum Exploration in South Africa*. Brochure, Petroleum Agency SA.

Petroleum Agency SA. 2004/2005/2010. "Petroleum exploration information and opportunities in South Africa." *Petroleum Agency brochure*.

Petroleum Agency SA; 2004/5. *South African Exploration Opportunities*. Brochure, Cape Town: South African Agency for Promotion of Petroleum Exploration and Exploitation, 27.

Ramiah, K, K.D Trivedi, and M Opwuari. 2019. "A 2D geochemical model of an offshore gas field in the Bredasdorp Basin, South Africa." *Journal of Petroleum Exploration and Production Technology* 9: 207-222.

Rider, M. 2002. "Reservoir Characterization with Borehole Geophysics." In *The Geological Interpretation of Well Logs*, by K.M Strack. Whittles Publishing Strack, K.M.

Rollinson, Hugh R. 1993. *Using geochemical data- evaluation, presentation, interpretation*. United Kingdom: Longman Scientific & Technical.

Rudolf, Muller. 2012. *Spectrochemical Analysis by X-Ray Fluorescence*. United States: Springer US.

Schalkwyk, H.J. 2005. *Assessment control on reservoir performance and the effects of granulation seam mechanics in the Bredasdorp Basin, South Africa*. MSc. Thesis, Cape Town: University of the Western Cape.

Sheardown, Ashley, and Jason Donev. 2022. *Energy Education - Source Rock*. Accessed June 2, 2022.
https://energyeducation.ca/encyclopedia/Source_rock.

Sonibare, W.A, J Sippel, M Scheck-Wenderoth, and D Mikes. 2014. "Crust-scale 3D model of the Western Bredasdorp Basin (Southern South Africa): Data-based insights from combined isostatic and 3D gravity modelling." *Basin Research* 27 125-151.

Speakman, Scott A. n.d. "Introduction to X-Ray Powder Diffraction Data Analysis." Accessed 07 12, 2020.
<http://prism.mit.edu/xray>.

2023. *Thermo Fisher Scientific*. August 1.

<https://www.thermofisher.com/uk/en/home/industrial/spectroscopy-elemental-isotope-analysis/spectroscopy-elemental-isotopeanalysis-learning-center/elemental-analysis-information/xrf-technology.html>.

Thompson, K. 1998. "When did the falklands rotate?" *Marine and petroleum geology* 15 723-736.

Tiab, Djebbar, and Erle C Donaldson. 2012. "Chapter 4 - Formation Resistivity and Water Saturation ." In *Petrophysics (Third Edition)*, 221-326. Elsevier .

Turner, J.R, N Grobber, and S Sontundu. 2000. "Geological modelling of the Aptian and Albian sequences within Block 9, Bredasdorp Basin, Offshore South Africa." *Journal of African Earth Sciences, Geocongress 2000: A new millenium on ancient crust, 27th Earth Science Congress of the Geological Society of South Africa, edited by Kisters, AFM and Thomas RJ* 80.

Van der Merwe, R.F. 1992. "Inversion tectonics in the Bredasdorp Basin, offshore South Africa." In *Ransome (eds) Inversion tectonics of the Cape Fold Belt,Karoo and Cretaceous Basis of Southern Africa , by M.J De Wit, 49-59.*

VINCI-Technologies. 2022. *Routine Core Analysis*. <https://www.vinci-technologies.com/rocks-and-fluids/routine-core-analysis/electrical-properties/eps-a-electrical-properties-system-a-ambient-conditions/113435/>.

Wahl, J.S., W.B. Nelligan, A.H. Frentrop, C.W. Johnstone, and R.J. Schwartz . 1964. "The thermal neutron decay time log." *SPE Journal* 10 364-379.

Wheaton, Richard. 2016. "Chapter 2 - Basic Rock and Fluid Properties." In *Fundamentals of Applied Reservoir Engineering*, 5-57. United Kingdom: Appraisal, Economics and Optimization.
doi:<https://doi.org/10.1016/B978-0-08-101019-8.00002-8>.

Wood, E.M. 1995. "Oil and gas development potential in Block 9, the Bredasdorp Basin, offshore South Africa." *Oil & Gas Journal*.

XOS. 2020. *X-Ray Diffraction (XRD)*. Accessed 07 12, 2020. <https://www.xos.com/XRD#>.

Zhang, Baoying, and Jingling Xu. 2016. "Methods for the evaluation of water saturation considering TOC in shale reservoirs." *Journal of Natural Gas Science and Engineering* 36 800-810.

APPENDIX LIST:

APPENDIX A: XRF results of well E-BT1 for selected core boxes.

	Name	Depth (m) Core and Box	Date	Time	Duration	Mg	Al	Si	P	S	K	Ca	Ti	Mn	Fe	Co	Ni	Zn	Rb	Sc	Zr	Sn	Ba	Hf	Th
E-BT1.57	2395.2	3.0/2022 08:56:52	10	06:58:00	2,395.2	38,213.80	0.0522	2,020.7	0.7805	2,029.4	0.0655	0.0108	0.9046	0.0058	0.0000	0.0056	0.0853	0.0063	0.0466	0.0047	0.0342	0.0010	0.0000		
E-BT1.58	2395.3	3.0/2022 08:57:53	10	06:58:00	2,394.0	36,886.03	0.0400	3,019.0	0.5755	1,510.0	0.0651	0.0105	0.8716	0.0055	0.0000	0.0057	0.0073	0.0056	0.0456	0.0042	0.0346	0.0014	0.0007		
E-BT1.56	2395.4	3.0/2022 08:58:07	10	06:58:00	2,396.1	31,953.57	0.0461	0.4926	0.6582	2,023.9	0.0651	0.0104	1,019.5	0.0000	0.0000	0.0010	0.0012	0.0053	0.0067	0.0465	0.0040	0.0298	0.0012	0.0011	
E-BT1.54	2395.5	3.0/2022 08:58:29	10	06:58:00	2,107.5	36,321.12	0.0418	0.6858	0.5859	1,636.8	0.1149	0.0070	0.6848	0.0055	0.0000	0.0108	0.0028	0.0052	0.0453	0.0056	0.0420	0.0015	0.0015		
E-BT1.53	2395.6	3.0/2022 08:58:51	10	06:58:00	1,889.4	30,597.9	0.0466	0.5298	1,212.3	0.0000	0.0137	0.6957	0.0050	0.0000	0.0059	0.0021	0.0057	0.0579	0.0059	0.0300	0.0010	0.0000			
E-BT1.52	2395.7	3.0/2022 08:59:23	10	06:58:00	1,944.1	36,946.0	0.0455	0.7200	0.6935	1,472.8	0.0000	0.0056	0.6934	0.0044	0.0000	0.0056	0.0024	0.0056	0.0592	0.0056	0.0300	0.0013	0.0016		
E-BT1.51	2395.8	3.0/2022 08:59:54	10	06:58:00	2,121.0	1,787.3	0.3487	0.0557	0.3186	0.5398	1,411.1	0.0931	0.0059	0.6466	0.0058	0.0000	0.0052	0.0041	0.0545	0.0041	0.0278	0.0011	0.0017		
E-BT1.50	2395.9	3.0/2022 08:59:57	10	06:58:00	1,551.7	36,564.1	0.0478	0.3509	0.5895	1,400.1	0.0000	0.0135	0.6976	0.0055	0.0000	0.0051	0.0027	0.0059	0.0583	0.0059	0.0285	0.0016	0.0014		
E-BT1.49	2396	3.0/2022 08:59:57	10	06:58:00	1,389.1	31,775.8	0.0541	0.5741	0.5741	1,052.1	0.0000	0.0101	0.6437	0.0126	0.0000	0.0054	0.0024	0.0055	0.0474	0.0051	0.0281	0.0011	0.0000		
E-BT1.48	2396.1	3.0/2022 08:59:49	10	06:58:00	1,861.4	36,834.9	0.0455	0.5242	0.6061	1,691.3	0.0000	0.0080	0.6828	0.0070	0.0000	0.0052	0.0054	0.0107	0.0487	0.0114	0.0381	0.0014	0.0015		
E-BT1.47	2396.2	3.0/2022 08:59:25	10	06:58:00	1,817.1	2,896.6	0.3497	0.0453	0.7688	0.4983	1,854.0	0.1457	0.0055	0.6953	0.0055	0.0000	0.0059	0.0056	0.0569	0.0051	0.0314	0.0013	0.0012		
AVERAGE PER BOX																									
E-BT1.46	2400.1	3.0/2022 09:07:09	10	06:58:00	1,929.9	31,651.0	0.0600	0.8040	0.8272	1,737.7	0.0589	0.0178	0.8804	0.0059	0.0000	0.0152	0.0082	0.0067	0.0505	0.0106	0.0461	0.0016	0.0118		
E-BT1.45	2400.2	3.0/2022 09:07:53	10	06:58:00	1,682.6	36,617.9	0.0588	0.4548	0.5482	1,565.2	0.0000	0.0106	0.7873	0.0117	0.0000	0.0114	0.0017	0.0056	0.0452	0.0042	0.0252	0.0016	0.0017		
E-BT1.44	2400.3	3.0/2022 09:08:16	10	06:58:00	2,033.4	31,589.0	0.0589	0.5642	0.8705	1,801.1	0.0016	0.7398	0.0079	0.0000	0.0071	0.0021	0.0049	0.0088	0.0081	0.0325	0.0018	0.0018			
E-BT1.43	2400.4	3.0/2022 09:08:34	10	06:58:00	2,552.4	36,175.38	0.0521	0.5645	0.6434	2,475.9	0.1113	0.0000	0.8842	0.0059	0.0000	0.0104	0.0026	0.0061	0.0394	0.0056	0.0378	0.0022	0.0016		
E-BT1.42	2400.5	3.0/2022 09:07:55	10	06:58:00	2,025.1	2,129.8	0.3486	0.0385	1,199.1	0.5781	1,664.2	0.0000	0.0000	0.8531	0.0000	0.0000	0.0072	0.0024	0.0047	0.0356	0.0042	0.0333	0.0021	0.0000	
E-BT1.41	2400.6	3.0/2022 09:07:45	10	06:58:00	2,095.6	31,955.8	0.0444	0.1966	0.5969	1,549.2	0.0883	0.0000	0.9779	0.0101	0.0000	0.0057	0.0023	0.0046	0.0413	0.0085	0.0316	0.0011	0.0014		
E-BT1.40	2400.7	3.0/2022 09:07:21	10	06:58:00	1,782.3	40,052.2	0.0352	0.2988	0.5137	1,329.1	0.0000	0.0000	0.8561	0.0047	0.0000	0.0426	0.0026	0.0040	0.0342	0.0009	0.0000	0.0000	0.0000		
E-BT1.39	2400.9	3.0/2022 09:07:42	10	06:58:00	1,000.0	1,725.8	0.0577	0.0522	0.1053	1,601.2	0.1224	0.0000	0.6934	0.0055	0.0000	0.0356	0.0025	0.0051	0.0390	0.0059	0.0452	0.0110	0.0010		
AVERAGE PER BOX																									
E-BT1.38	2405.7	3.0/2022 09:25:52	10	06:58:00	1,390.1	40,716.2	0.0465	0.1822	0.3738	1,128.9	0.0000	0.0000	0.3206	0.0000	0.0000	0.0043	0.0026	0.0051	0.0362	0.0076	0.0279	0.0011	0.0012		
E-BT1.37	2405.8	3.0/2022 09:27:24	10	06:58:00	1,318.1	2,499.5	36,731.1	0.0688	0.2653	0.5253	1,529.8	0.0595	0.7114	0.0000	0.0000	0.0054	0.0024	0.0044	0.0367	0.0057	0.0394	0.0023	0.0008		
E-BT1.36	2405.9	3.0/2022 09:27:44	10	06:58:00	2,020.6	2,253.7	0.5953	0.0426	0.5622	0.6145	1,597.3	0.0417	0.0138	0.6566	0.0048	0.0000	0.0303	0.0022	0.0045	0.0463	0.0054	0.0348	0.0010	0.0000	
E-BT1.35	2406	3.0/2022 09:27:57	10	06:58:00	2,414.8	1,946.7	0.0827	0.3071	0.5920	2,018.2	0.0479	0.0138	0.8888	0.0045	0.0000	0.0885	0.0016	0.0080	0.0255	0.0056	0.0367	0.0015	0.0015		
E-BT1.34	2406.2	3.0/2022 09:27:58	10	06:58:00	4,033.7	1,771.6	0.0522	0.6070	0.5374	0,5374	0.0648	0.0006	0.8669	0.0000	0.0000	0.0055	0.0017	0.0088	0.0492	0.0056	0.0300	0.0000	0.0018		
E-BT1.33	2406.3	3.0/2022 09:28:05	10	06:58:00	3,044.0	2,046.4	0.0605	0.9468	0.4561	1,621.1	1,831.1	0.0653	0.0727	0.8137	0.0000	0.0000	0.0052	0.0029	0.0064	0.0469	0.0060	0.0313	0.0016	0.0000	
E-BT1.32	2406.4	3.0/2022 09:28:08	10	06:58:00	3,573.5	2,004.4	0.0506	0.0535	0.1194	0.5373	3,214.3	0.0000	0.0152	1,257.7	0.0054	0.0000	0.0055	0.0021	0.0052	0.0370	0.0009	0.0000	0.0012	0.0000	
E-BT1.31	2406.5	3.0/2022 09:28:09	10	06:58:00	1,970.4	36,353.8	0.0574	0.1244	0.5230	0.0000	0.0132	1,5014	0.0058	0.0000	0.0084	0.0023	0.0043	0.0417	0.0052	0.0347	0.0017	0.0013			
E-BT1.30	2406.6	3.0/2022 09:28:09	10	06:58:00	2,084.6	3,015.0	0.0687	0.1467	0.5623	0.0000	0.0106	0.0492	0.0000	0.0000	0.0078	0.0023	0.0053	0.0473	0.0054	0.0364	0.0010	0.0011			
E-BT1.29	2406.7	3.0/2022 09:28:09	10	06:58:00	3,020.4	1,928.2	0.0729	0.0522	0.3983	0.0000	0.0131	1,286.7	0.0057	0.0000	0.0056	0.0025	0.0053	0.0474	0.0056	0.0365	0.0016	0.0016			
AVERAGE PER BOX																									
E-BT1.28	2409.3	3.0/2022 09:56:02	10	06:58:00	1,316.1	30,574.74	0.0729	0.7294	0.7494	0,629.0	0.5391	0.0197	0.4865	0.0054	0.0000	0.0056	0.0019	0.0223	0.0162	0.0133	0.0127	0.0033	0.0011	0.0011	
E-BT1.27	2409.4	3.0/2022 09:56:05	10	06:58:00	1,016.0	40,380.02	0.0265	0.3327	0.4749	0.6750	0.0000	0.0106	0.3882	0.0076	0.0000	0.0057	0.0021	0.0021	0.0240	0.0047	0.0240	0.0013	0.0000		
E-BT1.26	2409.5	3.0/2022 09:56:15	10	06:58:00	1,983.8	36,736.56	0.0340	2,531.9	1,533.8	1,596.1	0.0000	0.0108	0,4545	0.0068	0.0000	0.0057	0.0022	0.0022	0.0240	0.0047	0.0240	0.0013	0.0000		
E-BT1.25	2409.6	3.0/2022 09:56:08	10	06:58:00	1,977.2	40,575.3	0.0463	0.0000	0.5448	0.0000	0.0061	0.4864	0.0055	0.0000	0.0057	0.0021	0.0021	0.0232	0.0047	0.0232	0.0013	0.0000			
E-BT1.24	2409.7	3.0/2022 09:56:15	10	06:58:00	2,000.0	32,859.73	0.0531	0.0544	0.6746	0.0767	0.0790	0.0111	0.2722	0.0056	0.0000	0.0057	0.0023	0.0023	0.0232	0.0047	0.0232	0.0013	0.0000		
E-BT1.23	2409.8	3.0/2022 09:56:26	10	06:58:00	1,265.0	32,826.56	0.0506	0.0526	0.5914	0.7970	1,453.7	0.0106	0.0000	0.0057	0.0023	0.0023	0.0232	0.0047	0.0232	0.0013</					



APPENDIX B: XRF results of well E-AR1 for selected core boxes.

Name	Depth(m)	Core & Core box	Date	Time	Duration	M ₃	A ₁	S ₁	P ₁	S ₂	K ₁	C ₁	T ₁	C ₂	Mn	Fe	C ₃	Ni	Zn	Rb	Si ₁	Si ₂	Na	Mo	Se	Ba	Pr	Hg	Pb
Core Box 2																													
E-AR1102	2455.15		3.10.2022	04:22:28	10	0.0795	1.294	40:28:07	0.0704	0.0778	0.392	0.5757	0.0000	0.0000	0.4877	0.0000	0.0095	0.0015	0.0229	0.0053	0.0000	0.0066	0.0000	0.0045	0.0000	0.0017	0.0021	0.0011	
E-AR1101	2455.25		3.10.2022	04:20:04	10	0.0502	1.850	39:46:08	0.6513	0.0650	0.5461	0.0958	0.0640	0.0000	0.0005	0.7621	0.0000	0.0051	0.0021	0.0034	0.0081	0.0000	0.0045	0.0000	0.0017	0.0021	0.0011		
E-AR1100	2455.35		3.10.2022	04:14:06	10	0.0000	1.524	40:45:00	0.6331	0.0000	0.4208	0.5672	0.0620	0.0000	0.0005	0.5515	0.0000	0.0056	0.0000	0.0033	0.0053	0.0000	0.0051	0.0000	0.0017	0.0021	0.0014		
E-AR1199	2455.45		3.10.2022	04:04:45	10	0.0732	40:26:01	0.5740	0.0285	0.4807	0.0656	0.0482	0.0000	0.0002	0.0956	0.0045	0.0000	0.0085	0.0021	0.0031	0.0093	0.0000	0.0026	0.0000	0.0016	0.0022	0.0014		
E-AR1198	2455.55		3.10.2022	04:04:45	10	0.0000	1.349	40:33:35	0.6211	0.0000	0.4901	0.4071	0.0707	0.0000	0.0000	0.0958	0.0000	0.0001	0.0000	0.0023	0.0045	0.0000	0.0019	0.0000	0.0014	0.0023	0.0014		
E-AR1197	2455.65		3.10.2022	04:04:45	10	0.0158	1.397	40:26:76	0.6050	0.0000	0.4598	0.7119	0.0289	0.0000	0.0000	0.5388	0.0039	0.0006	0.0056	0.0021	0.0046	0.0000	0.0004	0.0019	0.0004	0.0014	0.0023	0.0014	
E-AR1196	2455.75		3.10.2022	04:04:59	10	0.0032	1.048	40:56:09	0.6211	0.0000	0.4119	0.4657	0.0558	0.0000	0.0000	0.0925	0.0021	0.0000	0.0065	0.0004	0.0109	0.0000	0.0011	0.0054	0.0000	0.0011	0.0003		
AVERAGE OF BOX																													
E-AR1195	2455.8		3.10.2022	04:56:34	10	0.0000	1.807	40:17:49	0.6767	0.0000	0.5204	0.9001	0.0501	0.0000	0.0000	0.7291	0.0000	0.0067	0.0023	0.0039	0.0194	0.0000	0.0049	0.0000	0.0012	0.0027	0.0017		
E-AR1194	2455.9		3.10.2022	04:56:08	10	0.0840	16:489	38:37:33	0.0447	0.0000	1.203	0.980	0.1126	0.0000	0.0001	0.0684	0.0000	0.0001	0.0220	0.0026	0.0324	0.0000	0.0041	0.0000	0.0012	0.0021	0.0016		
E-AR1193	2456.0		3.10.2022	04:56:53	10	0.0000	3.170	38:42:00	0.0415	0.0000	1.484	0.946	0.1292	0.0000	0.0000	0.0646	0.0000	0.0001	0.0204	0.0024	0.0308	0.0000	0.0042	0.0000	0.0012	0.0021	0.0016		
E-AR1192	2456.1		3.10.2022	04:56:50	10	0.0850	1.907	39:58:00	0.6468	0.0000	0.8827	0.5194	0.0271	0.0000	0.0000	0.7859	0.0000	0.0001	0.0201	0.0021	0.0301	0.0000	0.0043	0.0000	0.0012	0.0021	0.0014		
E-AR1191	2456.2		3.10.2022	04:56:50	10	0.0000	1.930	39:49:55	0.0485	0.0000	0.9421	0.0000	0.0000	0.0444	0.0000	0.0001	0.0656	0.0000	0.0203	0.0000	0.0031	0.0000	0.0001	0.0000	0.0001	0.0003			
E-AR1190	2456.3		3.10.2022	04:56:48	10	1.6769	40:16:56	0.6613	0.0000	0.762	0.7841	0.0000	0.0000	0.0000	0.7226	0.0000	0.0001	0.0075	0.0021	0.0303	0.0000	0.0043	0.0000	0.0012	0.0021	0.0016			
E-AR1189	2456.4		3.10.2022	04:54:34	10	0.0864	1.3755	37:09:33	0.6870	0.0000	0.8882	0.1388	0.0191	0.0000	0.0001	0.7024	0.0000	0.0001	0.0204	0.0024	0.0313	0.0000	0.0045	0.0000	0.0012	0.0021	0.0016		
E-AR1188	2456.5		3.10.2022	04:56:37	10	0.0000	1.4931	40:33:35	0.0437	0.0045	0.3935	0.8671	0.0000	0.0000	0.0000	0.7813	0.0000	0.0001	0.0057	0.0016	0.0306	0.0000	0.0044	0.0000	0.0012	0.0021	0.0016		
E-AR1187	2456.6		3.10.2022	04:56:36	10	0.0000	1.6965	40:34:01	0.6559	0.0000	0.9253	0.0448	0.0253	0.0000	0.0000	0.5558	0.0000	0.0001	0.0015	0.0026	0.0076	0.0000	0.0045	0.0000	0.0012	0.0021	0.0016		
E-AR1186	2456.7		3.10.2022	04:56:36	10	0.0000	1.8495	39:58:05	0.6766	0.0000	0.7626	0.0766	0.0000	0.0000	0.0000	0.6275	0.0000	0.0001	0.0075	0.0026	0.0305	0.0000	0.0045	0.0000	0.0012	0.0021	0.0016		
AVERAGE OF BOX																													
E-AR1184	2456.8		3.10.2022	04:56:56	10	0.0893	2.084	39:52:29	0.0417	0.0083	0.6355	1.755	0.054	0.0000	0.0082	0.5985	0.0000	0.0001	0.0204	0.0028	0.0347	0.0000	0.0049	0.0000	0.0012	0.0021	0.0016		
E-AR1183	2456.9		3.10.2022	04:56:59	10	0.0772	1.5555	40:25:57	0.6112	0.0000	0.653	0.5633	0.0000	0.0000	0.0001	0.5177	0.0000	0.0001	0.0204	0.0025	0.0329	0.0000	0.0042	0.0000	0.0012	0.0021	0.0016		
E-AR1182	2456.10		3.10.2022	04:56:59	10	0.0000	1.583	40:32:59	0.0415	0.0000	0.9422	1.834	0.0087	0.0000	0.0000	0.5944	0.0000	0.0001	0.0204	0.0025	0.0333	0.0000	0.0043	0.0000	0.0012	0.0021	0.0016		
E-AR1181	2456.11		3.10.2022	04:56:59	10	0.0861	40:33:33	0.6089	0.0000	0.6629	1.6868	0.0085	0.0000	0.0000	0.5063	0.0000	0.0001	0.0207	0.0026	0.0345	0.0000	0.0043	0.0000	0.0012	0.0021	0.0016			
E-AR1180	2456.12		3.10.2022	04:56:59	10	0.0000	1.1321	41:39:23	0.0434	0.0000	0.8404	1.384	0.0100	0.0000	0.0000	0.4733	0.0000	0.0001	0.0204	0.0026	0.0345	0.0000	0.0043	0.0000	0.0012	0.0021	0.0016		
E-AR1179	2456.13		3.10.2022	04:56:59	10	0.0826	1.5485	40:55:77	0.0434	0.0000	0.7482	0.5781	0.0059	0.0000	0.0000	0.4519	0.0000	0.0001	0.0204	0.0025	0.0346	0.0000	0.0043	0.0000	0.0012	0.0021	0.0016		
E-AR1178	2456.14		3.10.2022	04:56:59	10	0.0611	1.6777	39:58:56	0.6698	0.0000	0.9252	1.2066	0.0000	0.0000	0.0000	0.6761	0.0000	0.0001	0.0202	0.0026	0.0346	0.0000	0.0043	0.0000	0.0012	0.0021	0.0016		
E-AR1177	2456.15		3.10.2022	04:56:59	10	0.0000	1.9201	39:53:05	0.0484	0.0000	0.9795	1.5133	0.0000	0.0000	0.0000	0.6081	0.0000	0.0001	0.0202	0.0027	0.0347	0.0000	0.0043	0.0000	0.0012	0.0021	0.0016		
E-AR1176	2456.16		3.10.2022	04:56:59	10	0.0000	2.4277	39:49:29	0.6484	0.0000	0.7955	1.924	0.0067	0.0000	0.0000	0.4745	0.0000	0.0001	0.0202	0.0026	0.0348	0.0000	0.0043	0.0000	0.0012	0.0021	0.0016		
E-AR1175	2456.17		3.10.2022	04:56:59	10	0.0000	2.3077	39:51:25	0.0456	0.0000	0.5213	1.3801	0.0051	0.0000	0.0000	0.4781	0.0000	0.0001	0.0202	0.0026	0.0349	0.0000	0.0043	0.0000	0.0012	0.0021	0.0016		
E-AR1174	2456.18		3.10.2022	04:56:59	10	0.0412	21:84	38:17:00	0.0449	0.0000	0.2641	0.8428	0.1048	0.0000	0.0000	0.0681	0.0000	0.0001	0.0203	0.0026	0.0350	0.0000	0.0043	0.0000	0.0012	0.0021	0.0016		
E-AR1173	2456.19		3.10.2022	04:56:59	10	0.0000	2:31	39:59:08	0.0416	0.0000	0.3833	0.8466	0.0446	0.0000	0.0000	0.4655	0.0000	0.0001	0.0202	0.0026	0.0351	0.0000	0.0043	0.0000	0.0012	0.0021	0.0016		
E-AR1172	2456.20		3.10.2022	04:56:59	10	0.0508	1.5386	39:43:30	0.0404	0.0000	0.1048	0.9044	0.0252	0.0000	0.0000	0.6135	0.0000	0.0001	0.0202	0.0026	0.0352	0.0000	0.0043	0.0000	0.0012	0.0021	0.0016		
E-AR1171	2456.21		3.10.2022	04:56:59	10	0.0000	1.9202	39:53:05	0.0484	0.0000	0.9795	1.5607	0.0000	0.0000	0.0000	0.6081	0.0000	0.0001	0.0202	0.0026	0.0353	0.0000	0.0043	0.0000	0.0012	0.0021	0.0016		
E-AR1170	2456.22		3.10.2022	04:56:59	10	0.0000	2.4277	39:49:29	0.6484	0.0000	0.7955	1.924	0.0067	0.0000	0.0000	0.4745	0.0000	0.0001	0.0202	0.0026	0.0354	0.0000	0.0043	0.0000	0.0012	0.0021	0.0016		
E-AR1169	2456.23		3.10.2022	04:56:59	10	0.0000	2.3081	38:58:55	0.6613	0.0000	0.5213	1.4824	0.0067	0.0000	0.0000	0.4723	0.0000	0.0001	0.0202	0.0026	0.0355	0.0000	0.0043	0.0000	0.0012	0.0021	0.0016		
E-AR1168	2456.24		3.10.2022	04:56:22	10	0.0000	1.6722	40:27:02	0.0401	0.0000	0.1245	0.7038	0.0141	0.0000	0.0000	0.4947	0.0000	0.0001	0.0202	0.0026	0.0356	0.0000	0.0043	0.0000	0.0012	0.0021	0.0016		
E-AR1167	2456.25		3.10.2022	04:56:22	10	0.0000	1.6722	40:27:02	0.0401	0.0000	0.1245	0.7038	0.0141	0.0000	0.0000	0.4947	0.0000	0.0001	0.0202	0.0026	0.0356	0.0000	0.0043	0.0000	0.0012	0.0021	0.0016		
E-AR1166	2456.26		3.10.2022	04:56:22	10	0.0000	1.5325	39:54:45	0.6613	0.0000	0.3235	1.0																	

UNIVERSITY OF THE
WESTERN CAPE

APPENDIX C: XRF results of well E-AR1 for selected core boxes.

Name	Depth (m) CORE and BOX	Date	Duration (s)	Mg	Al	Si	P	S	K	Ca	Ti	Cr	Mn	Fe	Co	Zn	Rb	Sc	Zr	Sh	Ba	Pt	Hg	Pb
E-AR2.33	2442.20	3.10.2022	10	0.2627	2.3227	36.9201	0.0809	0.4049	0.8122	3.4365	0.0436	0.0000	0.0235	1.8716	0.0073	0.0048	0.0037	0.0173	0.0391	0.00083	0.0527	0.0000	0.0000	0.0013
E-AR2.32	2442.36	3.10.2022	10	0.4651	2.2556	37.1280	0.0822	0.2438	0.6723	3.3103	0.0790	0.0327	0.0153	1.5661	0.0042	0.0050	0.0030	0.0155	0.0472	0.0034	0.0551	0.0000	0.0003	0.0016
E-AR2.31	2442.40	3.10.2022	10	0.4422	2.1059	38.1394	0.0500	0.0000	0.5676	2.6829	0.0801	0.0315	0.0160	1.3101	0.0047	0.0047	0.0000	0.0136	0.0346	0.0038	0.0493	0.0000	0.0009	0.0000
E-AR2.30	2442.50	3.10.2022	10	0.2898	2.0904	37.8932	0.0564	0.1700	0.5810	0.0900	0.0798	0.0000	0.0172	1.5193	0.0040	0.0115	0.0055	0.0028	0.0155	0.0030	0.0205	0.0524	0.0000	0.0000
E-AR2.29	2442.56	3.10.2022	10	0.5451	2.3451	37.6562	0.0662	0.2307	0.5518	1.5581	0.0947	0.0000	0.0146	1.5530	0.0038	0.0055	0.0026	0.0110	0.0324	0.0037	0.0355	0.0000	0.0009	0.0000
E-AR2.28	2442.60	3.10.2022	10	0.4126	2.2497	37.8930	0.0560	0.1555	0.6432	2.7059	0.0972	0.0000	0.0146	1.5294	0.0038	0.0055	0.0026	0.0110	0.0324	0.0037	0.0355	0.0000	0.0009	0.0000
E-AR2.27	2442.80	3.10.2022	10	0.7422	1.7304	37.2151	0.1257	0.1052	0.9521	3.3441	0.0000	0.0247	0.0489	1.5382	0.0103	0.0081	0.0038	0.0121	0.0343	0.0028	0.0155	0.0500	0.0147	0.0026
E-AR2.26	2442.90	3.10.2022	10	0.0000	2.1743	39.4627	0.0530	0.2397	0.5575	1.5848	0.1136	0.0000	0.0139	1.6838	0.0047	0.0055	0.0027	0.0147	0.0325	0.0021	0.0652	0.0009	0.0009	0.0012
E-AR2.25	2442.30	3.10.2022	10	0.3796	3.4448	37.5627	0.0621	0.5632	0.8320	1.7610	0.1110	0.0000	0.0086	1.8457	0.0040	0.0050	0.0026	0.0146	0.0246	0.0000	0.0842	0.0000	0.0038	0.0023
E-AR2.24	2442.40	3.10.2022	10	0.0000	2.8213	38.9235	0.0531	0.3608	0.6160	1.4413	0.0000	0.0084	0.6646	0.0033	0.0050	0.0023	0.0051	0.0240	0.0005	0.0836	0.0002	0.0012	0.0013	
E-AR2.23	2442.50	3.10.2022	10	0.1922	2.3589	37.8413	0.0686	0.2776	0.6748	2.5609	0.0659	0.0110	0.0181	1.3079	0.0053	0.0070	0.0030	0.0119	0.0394	0.0005	0.0454	0.0005	0.0002	0.0011
E-AR2.22	2442.70	3.10.2022	10	0.1220	1.9787	38.5302	0.0694	0.7511	0.8653	1.5475	0.0300	0.0362	1.2521	0.0514	0.0313	0.0000	0.7918	0.0030	0.0048	0.0413	0.0052	0.0234	0.0000	0.0014
E-AR2.21	2442.80	3.10.2022	10	0.0000	1.8883	39.8836	0.0476	0.2360	0.6079	2.5268	0.0000	0.0087	1.2083	0.0111	0.0065	0.0000	0.0050	0.0021	0.0047	0.0104	0.0038	0.0020	0.0019	
E-AR2.20	2442.90	3.10.2022	10	0.5532	1.7933	39.3855	0.0379	0.6873	0.6210	1.3720	0.0524	0.0000	0.0145	0.8399	0.0059	0.0062	0.0031	0.0046	0.0316	0.0042	0.0515	0.0014	0.0019	
E-AR2.19	2442.50	3.10.2022	10	0.0000	2.1516	39.5440	0.0456	0.2635	0.6146	1.1346	0.0836	0.0000	0.0057	0.8678	0.0035	0.0085	0.0032	0.0042	0.0326	0.0041	0.0441	0.0019	0.0016	
E-AR2.18	2442.40	3.10.2022	10	0.1658	1.2411	39.8384	0.0359	0.6935	0.4748	1.3027	0.0000	0.0115	0.8835	0.0207	0.0063	0.0033	0.0034	0.0363	0.0005	0.0394	0.0000	0.0032	0.0012	
E-AR2.17	2442.60	3.10.2022	10	0.0000	1.6446	39.2771	0.0502	0.0635	0.9623	1.0964	0.0000	0.0000	0.0082	0.8343	0.0036	0.0030	0.0036	0.0030	0.0343	0.0006	0.0395	0.0000	0.0016	
E-AR2.16	2442.70	3.10.2022	10	0.3768	1.4004	37.9581	0.0686	2.1048	0.5741	2.5268	0.0000	0.0087	1.2083	0.0111	0.0065	0.0000	0.0051	0.0021	0.0047	0.0104	0.0324	0.0000	0.0014	
E-AR2.15	2442.70	3.10.2022	10	0.4223	1.6402	39.9835	0.0521	0.1295	0.5457	0.9308	0.0000	0.0000	0.8942	0.0065	0.0000	0.0000	0.9263	0.0037	0.0025	0.0454	0.0038	0.0025	0.0012	
E-AR2.14	2442.80	3.10.2022	10	0.0000	40.4347	0.0457	0.2635	0.6146	1.1366	0.0000	0.0000	0.9268	0.0048	0.0000	0.0000	0.0084	0.0026	0.0046	0.0043	0.0043	0.0014	0.0019		
E-AR2.13	2442.90	3.10.2022	10	0.6788	1.8086	39.3239	0.0385	0.0000	0.0001	0.0719	0.9438	0.0000	0.0000	0.1462	0.0000	0.0000	0.0000	0.0289	0.0006	0.0026	0.0420	0.0000	0.0012	0.0000
E-AR2.12	2442.60	3.10.2022	10	0.3989	2.0788	38.7642	0.0426	0.0084	0.7255	1.4914	0.0758	0.0000	0.0149	1.6492	0.0052	0.0041	0.0031	0.0653	0.0050	0.0041	0.0032	0.0000	0.0000	0.0000
E-AR2.11	2442.70	3.10.2022	10	0.2756	1.7164	39.4712	0.0510	0.4637	0.6330	1.3188	0.0219	0.0082	0.1038	0.0061	0.0033	0.0047	0.0038	0.0071	0.0052	0.0038	0.0006	0.0014		
E-AR2.10	2442.80	3.10.2022	10	0.2616	2.4556	38.4845	0.1375	0.6602	0.7053	1.3118	0.0000	0.0085	0.8235	0.0040	0.0040	0.0016	0.0028	0.0210	0.0067	0.0247	0.0000	0.0002	0.0019	
E-AR2.9	2442.50	3.10.2022	10	0.0000	1.7933	40.6500	0.0470	0.0000	0.6620	0.6620	0.0302	0.0133	0.6789	0.0072	0.0031	0.0019	0.0050	0.0050	0.0050	0.0050	0.0050	0.0008	0.0000	
E-AR2.8	2450.05	3.10.2022	10	0.0000	2.1210	39.7501	0.0489	0.3792	0.5320	0.9454	0.0637	0.0000	0.0082	0.5346	0.0040	0.0040	0.0016	0.0157	0.0016	0.0026	0.0257	0.0000	0.0013	
E-AR2.7	2450.15	3.10.2022	10	0.0000	1.4115	38.2392	0.0400	0.2868	0.5611	2.2816	0.0000	0.0000	0.7447	0.0081	0.0045	0.0035	0.0035	0.0035	0.0044	0.0025	0.0015	0.0023		
E-AR2.6	2450.25	3.10.2022	10	0.0000	3.0948	2.0935	38.7486	0.0618	1.5544	1.5240	0.0534	0.0000	0.6748	0.0333	0.0040	0.0040	0.0023	0.0322	0.0289	0.0073	0.0298	0.0004	0.0016	
E-AR2.5	2450.35	3.10.2022	10	0.0000	1.8139	40.3372	0.0500	0.7121	0.4279	0.9324	0.0000	0.0000	0.3849	0.0000	0.0026	0.0026	0.0021	0.0264	0.0048	0.0039	0.0000	0.0000		
E-AR2.45	2450.45	3.10.2022	10	0.0000	1.8749	40.6785	0.0356	0.1874	0.3042	1.0793	0.0000	0.0000	0.4449	0.0049	0.0000	0.0000	0.0021	0.0236	0.0058	0.0039	0.0000	0.0011		
E-AR2.44	2450.55	3.10.2022	10	0.0000	1.3779	3.0772	38.7483	0.0457	1.1308	0.4018	0.3915	0.0000	0.0000	0.7105	0.0050	0.0000	0.0000	0.0021	0.0236	0.0073	0.0039	0.0000	0.0013	
E-AR2.43	2450.60	3.10.2022	10	0.0000	2.6417	39.4662	0.0501	0.3770	0.6539	1.2123	0.0533	0.0000	0.0000	0.7864	0.0000	0.0038	0.0041	0.0000	0.0223	0.0046	0.0056	0.0059	0.0008	0.0012
E-AR2.42	2450.55	3.10.2022	10	0.0000	2.0538	40.4518	0.0332	0.1744	0.4531	1.2166	0.0000	0.0000	0.0633	0.5136	0.0000	0.0000	0.0019	0.0238	0.0059	0.0073	0.0059	0.0009	0.0009	
E-AR2.41	2450.50	3.10.2022	10	0.0000	1.9688	1.9259	0.0767	0.8634	1.1751	0.0000	0.0000	0.0197	0.0055	0.0089	0.6282	0.0029	0.0075	0.0025	0.0330	0.0058	0.0289	0.0007	0.0009	
E-AR2.40	2450.50	3.10.2022	10	0.0000	1.9259	1.9259	0.0767	0.8634	1.1751	0.0000	0.0000	0.0197	0.0055	0.0089	0.6282	0.0029	0.0075	0.0025	0.0330	0.0058	0.0289	0.0007	0.0009	
E-AR2.39	2451.10	3.10.2022	10	0.2981	1.1933	39.5001	0.0489	0.2959	0.3229	1.1428	0.0000	0.0000	0.0621	0.4230	0.0052	0.0000	0.0017	0.0334	0.0052	0.0055	0.0059	0.0016		
E-AR2.38	2451.20	3.10.2022	10	0.0000	1.2503	37.3433	0.0514	0.3227	0.3229	1.1262	0.0000	0.0000	0.0727	0.4239	0.0055	0.0000	0.0016	0.0334	0.0052	0.0055	0.0059	0.0016		
E-AR2.37	2451.30	3.10.2022	10	0.0000	1.5945	38.2979	0.0628	0.2397	0.3045	1.1723	0.0000	0.0000	0.0447	0.0000	0.0047	0.0000	0.0047	0.0334	0.0052	0.0055	0.0059	0.0016		
E-AR2.36	2451.40	3.10.2022	10	0.0000	2.3297	37.3784	0.0397	0.8128	0.5656	1.1521	0.0000	0.0000	0.0111	0.762	0.0060	0.0000	0.0021	0.0334	0.0052	0.0055	0.0059	0.0016		
E-AR2.35	2451.50	3.10.2022	10	0.0000	2.3875	1.5078	0.0295	0.8128	0.5656	1.1521	0.0000	0.0000</												